DESIGN AND IN SITU CHARACTERIZATION OF NOVEL NANOSTRUCTURED MATERIALS FOR FUEL CELLS

A Dissertation

Presented to the Faculty of the Graduate School

of Cornell University

In Partial Fulfillment of the Requirements for the Degree of

Doctor of Philosophy

by

Yin Xiong

August, 2019

DESIGN AND IN SITU CHARACTERIZATION OF NOVEL NANOSTRUCTURED MATERIALS FOR FUEL CELLS

Yin Xiong, Ph. D.

Cornell University 2019

Abstract

The depletion of fossil fuels and global warming require the application of highly efficient and sustainable energy conversion devices, like fuel cells. However, the sluggish kinetics of the oxygen reduction reaction (ORR) on the cathode has significantly hindered the widespread implementation of fuel cells, which stimulates the development of highly active and durable electrocatalysts. Enormous progress has been made on both precious metal and non-precious metal catalysts, including Pt/Pd alloyed nanoparticles, transition metal oxides and nitrogen doped carbon materials.

In this thesis, a bifurcated strategy involving the rational design and *in situ* mechanistic investigation has been proposed and conducted. Via different synthetic routes, a variety of nano-structured materials has been prepared, including Pt-based structurally ordered intermetallics, core-shell structured nanoparticles with Pt surface decoration, tri-metallic spinel oxides, bimetallic organic framework (BMOF) derived carbon materials and nitrogen-doped BMOF-derived Pt-Co nanoparticles. They are featured with distinctive properties to adapt various working conditions, for the ground transportation or stationary applications, for proton exchange membrane fuel cells (PEMFCs) or alkaline exchange membrane fuel cells (AEMFCs). For example, Pt-based catalysts exhibit excellent electrocatalytic activities with a relatively high Pt utilization efficiency, making them suitable as promising candidates in the acidic electrolyte for fuel cell vehicles. Precious-

metal-free catalysts demonstrate high activity, robust durability and cost effectiveness, which can be potentially applied in alkaline media for stationary applications.

The *in situ* mechanism analysis of these materials consists of two parts: the first reveals the structural evolution of structurally ordered bimetallic intermetallics at high temperature, from both microscopic and macroscopic levels to determine the optimized synthesis condition for the Pt_3Co intermetallic nanoparticles. The second part couples the electrochemical reaction with X-ray adsorption spectroscopy to elucidate the working and degradation mechanism of trimetallic oxides, which indicates the synergistic catalysis by Co and Mn, with Fe serving as the stabilizing agent. These analyses, in return, provide valuable insights for designing and optimizing related materials in the future.

BIOGRAPHICAL SKETCH

Yin Xiong received her B.S. from Nanjing University, China, right after which she joined Prof. Abruña lab at Cornell University in 2014. Yin has always held a passion for energy applications, and she found the analytical electrochemistry studied in Prof. Abruña team fit for her vision. Through the past five years, she has focused on the novel nano-structured electrocatalysts for the electrochemical energy generation and understanding their formation and degradation mechanism using in situ characterization tools. In addition to striving for scientific discovery, she also works closely with industrial partners to apply her findings to practical use.

Dedicated to my parents and friends

ACKNOWLEDGEMENT

'*None of us is as smart as all of us*'

--Kenneth H. Blanchard

I would like to express my sincere gratefulness for all inspirations, encouragements, guidance and help from my advisor, committee, colleagues and friends.

I am deeply grateful to my research advisor, Prof. Héctor Abruña for his patience and guidance that are extremely helpful. He is one of the most generous, kind and knowledgeable scientists I have ever met, and I have received uncountable encouragement and suggestions from him throughout this five-year journey. He helped me to grow up as an independent researcher and build my confidence and horizon. My gratefulness also goes to Prof. Francis DiSalvo, who kindly serves in my special committee, and has provided great insights that make my research fruitful. His deep knowledge in inorganic materials and crystallography always shed light on my projects, and his permission to use his lab greatly conveniences my research. My third committee member, Prof. Tobias Hanrath, should receive my sincere gratitude as well, for his kind, constant support and interesting ideas through our constructive discussions.

As an experimentalist, my research heavily relies on the advanced techniques and instruments that are available in multiple facility centers at Cornell. I have received extensive help from a group of excellent managers at Cornell. My projects on unique nanomaterials cannot be successful without the help from Mick Thomas on SEM, from

John Grazul and Mariena Silvestry Ramos on TEM, Rong Huang on synchrotron, and many other individuals in CCMR.

My thanks go to my collaborators, Prof. Li Xiao from Wuhan University, Yao Yang, Elliot Padgett, Howie Joress, Xinran Feng, Xin Huang, Unmukt Gupta and Anusorn Kongkanand from General Motors, for their valuable contribution and assistance.

I always feel at home during the past five years even though I am far away from my hometown. This is because I have always been warmly surrounded by friends and colleagues at Cornell, who selfishlessly share their joy, opinions, and great experience with me. I was never alone both in life and at work.

I would also like to take this opportunity to thank my parents and family. They have been supporting through my entire life and their love have always been my inspiration, passion and encouragement.

Last but not least, I want to thank Energy Materials Center at Cornell, the Center for Alkaline-based Energy Solutions, US Department of Energy and other funding agencies to for financially supports.

Table of Contents

LIST OF FIGURES

show the crystal lattice on the [1-10] zone axis. (E) Fourier transform of lattice images in (D) shows the diffraction spots corresponding to the lattice d-spacing of (111) and (110) facets (PDF# 04-003-3875).

Figure 4.5 (A). STEM image of Pd-Fe@Pt. (B-D). EELS elemental maps of Pd (red), Fe (green) and composite map of Pd vs. Fe (D). (E). EELS elemental line profiles of Pd and Fe extracted from white dashed boxes from EELS mapping in (B) and (C), respectively

Figure 4.6 EELS spectra corresponding to the EELS elemental mapping in Figure 4.4. Pd $M_{4,5}$ and Fe $L_{2,3}$ edges were used to extract EELS maps from spectrum images. The inset exhibits the Pd $M_{4,5}$ edge (white line) after the background subtraction from the raw EELS spectra (black line) using the linear combination of power laws (LCPL) method. The background noise was filtered using principal component analysis (PCA).

Figure 4.7 EDX spectra of PdFe@Pt. Pt Mα, Pd Lα, β, Fe Kα were selected to process the spectrum image and generated EDX maps. It should be noted that the strong Cu K edges are from the Cu TEM grid

Figure 4.8 (A). STEM image of a PdFe@Pt nanoparticle. (B-D). EDX elemental maps of Pd (red), Fe (green) and Pt (yellow). (E). EDX line profiles of Pd (red), Fe (green) and Pt (blue) extracted from white dashed boxes from EDX mapping in (B-D). (F). Schematic model of a core-shell spherical particle and the theoretical projected intensity profiles

Figure 4.9 Electrocatalytic properties of synthesized Pd-Fe/C and Pd-Fe@Pt/C nanoparticles. (A). Cyclic voltammetry (CV) profiles of synthesized Pd-Fe/C NPs in Ar-saturated 0.1 M $HClO_4$ solution, scanned at a rate of 50 mV/s at room temperature. (B). ORR polarization curves in O_2-saturated 0.1 M $HClO_4$ at a scan rate of 5 mV/s and

rotation rate of 1600rpm. (C). CV profiles of Pd/C, $Pd_{0.58}Fe_{0.42}$/C and $Pd_{0.58}Fe_{0.42}$@Pt/C in Ar-purged 0.1 M $HClO_4$ solution at a sweep rate of 50 mV/s. (D). Comparison of ORR polarization curves for Pt/C and $Pd_{0.58}Fe_{0.42}$@Pt/C in O_2-saturated 0.1 M $HClO_4$ solution at a scan rate of 5 mV/s and 1600rpm rotation rate. (E). Tafel plots. Mass activities of different catalysts normalized to the total mass of Pd and Pt. (F). Tafel plots. Mass activity of Pt/C and $Pd_{0.58}Fe_{0.42}$@Pt/C, normalized to the mass of Pt. (G). Comparison of mass activity between Pt/C and $Pd_{0.58}Fe_{0.42}$@Pt/C, at 0.9V vs RHE

Figure 4.10 The CO stripping voltammetry of Pd/C, Pt/C and Pt-decorated $Pd_{0.58}Fe_{0.42}$/C at a scan rate of 50 mV/s in an Ar-saturated 0.1 M $HClO_4$ solution. Dosing potential of CO adsorption was 0.05 V vs. RHE

Figure 4.11 (A). Cyclic voltammetry profiles (B). and ORR polarization profiles of Pt decorated $Pd_{0.58}Fe_{0.42}$/C nanoparticles before and after stability test

Figure 4.12 Theoretical calculations of the Pd/Pt atomic ratio as a function of the particle size (Diameter, D) and the shell thickness (**x**). The insert shows the magnified diagram with a focus on lower Pd/Pt atomic ratio, i.e., higher relative Pt content. Solid lines are Pd@Pt core-shell particles while dashed lines are PdFe@Pt. The crossing point of the two dashed green lines is for PdFe@Pt with D=10 nm, which has to have a Pt/Pd ratio larger than 1:2.7 to achieve a complete Pt monolayer (3 Å). n_{Pd}% in the equation is the mole fraction of Pd in the core materials (e.g., n_{Pd}%=0.5 in PdFe). Details of the equation derivation can be found in the supporting information.

Table 4.1 Detailed information of reports regardining about Pt monolayer-coating NPs

Table 5.1 All of the following reported catalysts are nanoparticles supported on carbon substrate.

Figure 5.1 (A) Schematic illustration of the home-made device for the *in situ* synchrotron-based, X-ray diffraction (XRD) study. (B) XRD patterns of the as-synthesized Pt_3Co/C alloy and Pt_3Co/C after further annealing at 700 ^oC in the in-situ heating cell. (C) Quantitative analysis of the peak integral of the (110) ordering peak, and the (111) and (200) major peaks. Inset: illustration of background subtraction. (D) Quantitative calculations of the relative content of ordered intermetallic based on the assumption of a linear relationship between the ratio of the integrated areas of the ordered intermetallic peak at (110) to the sum of the (111) and (200) peaks

Figure 5.2 (A) Temperature calibration of the *in situ* heating stage (Si substrate). The Y axis is the theoretical melting temperature of metals and the X axis is the measured melting temperature from the heating stage. The plot shows a linear offset between the measured temperature and the actual temperature (B) XRD pattern of as-synthesized annealed Pt_3Co collected from 2D detector

Figure 5.3 (A) *In situ* heating XRD patterns of Pt_3Co/C annealed at various temperatures. The dashed line represents the as-synthesized Pt_3Co/C alloy. (B) Calculated relative content of ordered intermetallic Pt_3Co/C formed and particle size (calculated from the width of the (111) peak). (C) *In situ* heating XRD patterns of Pt_3Co/C at 750 ^oC, the optimal temperature, as a function of annealing time. (D) Calculated relative content of ordered Pt_3Co/C formed, and particle size

Figure 5.4 Powder XRD patterns of Pt_3Co/C annealed at various temperatures for 2h in a flow furnace in the lab. The change in ordering peak at ~33^o is fairly consistent with Figure 5.3 A.

Figure 5.5 (A) Measured d-spacing of Pt_3Co/C after 2 h annealing at various temperatures. (B) Measured d-spacing of Pt_3Co/C at different annealing times at 750 ^oC

Figure 5.6 (A) Simulation results for the SROP (red, dashed line) and LROP (blue, solid line) as a function of temperature for bulk (N=864, no marker) and spherical NPs with diameter d=2.9 nm (N=800, circles) and d=5.2 nm (N=4800, squares, with snapshots shown at temperatures just before the ODT on the left, and just after the ODT on the right). The temperatures are rigidly shifted so as to match the simulation results to the experimental Bulk order-disorder transition (ODT) temperature. As the size of the NP is reduced, the ODT temperature for the NPs also decreases. Snapshots of the bulk trajectory taken at increasing temperatures showing (B) ordered intermetallic phase, $L1_2$, (C) $D0_{22}$ state with global long-range order and lower crystal symmetry, and (D) disordered solid solution phase. The green and red atoms represent Pt and Co, respectively

Figure 5.7 (A) *In situ* heating XRD patterns of Pt_3Co/C annealed from 620 ^oC to 830 ^oC at a slow temperature ramping rate of 0.5 ^oC/min (B) Relative peak integral ratio of the (110) to (111) peaks (with the maximum ratio normalized to 100%) at a series of temperatures

Figure 5.8 (A) XRD patterns of Pt_3Co after annealing at 715 ^oC for 2 h, and after cooling down to room temperature. (B) Relative contents of ordered intermetallic Pt_3Co/C under two different cooling rates. X-axis represents the monitored temperatures during the cooling process

Figure 5.9 *In situ* heating STEM enabling tracking of the morphological changes of Pt_3Co/C annealed at 750°C. (A-C) Pt_3Co/C before annealing, annealed for 22 min, and annealed for 2h, respectively. (D-I) A specific region was magnified to illustrate particle

migration and coalescence during a continuous 2 h annealing process. (J) Measured distribution of particle sizes of thousands of particles from Figure 5.7A at different annealing times at 750°C. Cross marks on the X-axis represent the corresponding average particle sizes. (K) Volume-weighted, particle size distribution, which reflects the relative contribution of larger particles more clearly, as shown by the more pronounced tails for particle sizes above 8 nm. Cross marks on the X-axis represent the corresponding volume-weighted, average particle sizes. (L) Specific surface area (SSA) (m^2/g_{Pt}) estimated from STEM images of three different regions at different annealing times. Inset: Electrochemical surface area (ECSA) for Pt_3Co/C before and after annealing at 750 °C for 2 h, measured from the coulometric charge associate with hydrogen adsorption (H_{ads}) regions in the cyclic voltammograms. Details of statistical analysis of particle sizes and SSA calculations can be found in the experimental section. Scale bars in Figures A-C are 50 nm, and scale bars in Figures D-I are 5 nm

Figure 5.10 Atomic-scale *ex situ* HAADF-STEM images of Pt_3Co/C after annealing. (A) An ordered intermetallic Pt_3Co particle on the [100] zone axis. Brighter atoms at corners of squares are Pt, and dimmer atoms at the center are Co. (B) A partially ordered intermetallic particle on the [100] zone axis. Both brighter and dimmer atoms exist at the center of the squares. (C) Corresponding projected crystal model along [100]. Red and green atoms are Pt and Co, respectively. Crystal models were built based on the ordered intermetallic Pt_3Co (PDF # 01-072-9179)

Figure 5.11 (A) Calculated ECSA, mass-specific activity (MA) and surface-specific activity (SA) at 0.9V vs. RHE of Pt_3Co/C before and after stability tests, after a series of annealing temperatures for 2h. (B) Normalized retention of mass-specific activity (MA),

surface area-specific activity (SA), and electrochemical surface area (ECSA) on the left axis, and half-wave potential shift on the right axis of Pt_3Co/C after annealing at different temperatures. Normalized retention was calculated based on the ratio of the initial activity/surface areas to that after durability tests (2000 cycles in cyclic voltammetry at 100 mV/sec in 0.1M $HClO_4$ over the potential at the range from 0.6 to 1.0 V vs RHE). The best durability was achieved at around 750 ^oC, corresponding to the optimal degree of ordering

Figure 5.12 CV profiles of as-synthesized Pt_3Co/C and Pt_3Co/C annealed at different temperatures, before and after stability tests. (All CV profiles were obtained at a sweep rate of 50 mV/sec in oxygen-saturated a 0.1M $HClO_4$ solution over the potential range from 0.05 to 1.1 V vs RHE.)

Figure 5.13 RDE polarization curves of as-synthesized Pt_3Co/C and Pt_3Co/C annealed at different temperatures, before and after stability tests. (All RDE polarization curves were obtained at a sweep rate of 5 mV/sec in oxygen-saturated a 0.1M $HClO_4$ solution at a rotation rate of 1600 rpm.)

Table 5.2 The calculated ECSA, MA, SA at 0.9 V and half-wave potential ($E_{1/2}$) for different Pt_3Co/C samples before and after stability tests. ECSA and Mass activity retentions were calculated from the ratio of hydrogen adsorption region between its initial values to that after stability test. Since all the catalysts have the same mass loading of Pt_3Co, SA will have a value of MA divided by ECSA

Figure 5.13 Fuel cell performance comparison of disordered and annealed Pt_3Co/C before and after stability testing. BOL and EOL represent beginning-of-life (initial performance) and end-of-life (after 30,000 cycles), respectively. (A) MEA performance

at Pt loadings of 0.025 and 0.10 mg_{Pt}/cm^2 on anode and cathode, respectively. Cell operation conditions are in the order of anode/cathode: H_2/air, 94 °C, 65/65%RH, 250/250 $kPa_{abs,outlet}$, stoichiometries of 1.5/2. (B) Mass-specific activity (MA) measured at 0.9 V vs. RHE; ECSA of Pt measured by CO stripping in MEA; Voltage measured at a high current density of 2 A/cm^2. (C) Power density at 0.67 V under the same condition as (A)

Figure 6.1 STEM images process. (A-B) raw atomic-scale STEM images. (C-D) images in (A-B) filtered by using the Richard-Lucy deconvolution (3 iterations). The deconvolution was processed in ImageJ software assuming an Airy disk (100 kV, α_{max}=28 mrad) convolved with a 0.8 Å Gaussian source

Figure 6.2 EELS spectrum of MCF-0.8 acquired from the particle shown in Figure 6.6A

Figure 6.3 Schematic of the *in situ* XAS electrochemical cell. Working electrode (WE, catalyst on carbon paper) and counter electrode (CE, carbon rod) were immersed in 1M NaOH solution. Reference electrode (RE, Ag/AgCl in saturated KCl) was connected to the cell by a salt bridge and the distance between the RE and the catalysts at the end of the carbon paper was minimized to reduce IR drops caused by the resistance in the thin electrolyte layer (≤ 200 μm) in the X-ray window. Details of the cell design and operation was reported in our previous study

Figure 6.4 XRD patterns of as-synthesized MCF cubic spinel nanoparticles: $CoFe_2O_4$, $Mn_{0.3}(CoFe_2)_{0.9}O_4$, $Mn_{0.6}(CoFe_2)_{0.8}O_4$, $Mn_{0.8}(CoFe_2)_{0.73}O_4$, $Mn_1(CoFe_2)_{0.66}O_4$ and $Mn_{1.2}(CoFe_2)_{0.6}O_4$. The red and black vertical lines correspond to standard $CoFe_2O_4$ (PDF # 01-077-0426) and $MnFe_2O_4$ (PDF # 01-073-3820) XRD patterns, respectively; inset represents the enlarged region of the $CoFe_2O_4$ (440) diffraction peak

Figure 6.5 (A) STEM image of as-synthesized MCF-0.8 catalysts. (B) STEM image from one region magnified in (A) (red dashed box), showing particles composed of smaller sub-domains with domain sizes of around 15 nm

Figure 6.6 Atomic-scale HAADF-STEM images of MCF-0.8. (A-B) atomic-scale image and the corresponding crystal model on the $[11\bar{2}]$ zone axis. Two lattice d-spacings were measured to be 4.9 and 3.0 Å, which matched well with the theoretical values of (111), 4.85 Å and $(2\bar{2}0)$, 2.97 Å, respectively. Atom columns, **a**, at the corner of the lattice image, exhibit a brighter intensity than atom columns, **b**, on the side, because **a** has higher atom density than that of **b** and **c** in the crystal model. Atom columns, **c**, at the center of the lattice image, are elongated in the (111) direction, which are actually composed of three atom columns next to each other. (C) The crystal model on the $[11\bar{2}]$ zone axis slightly tilted to reveal the underneath atom columns. (D-E) Another atomic-scale image and the corresponding crystal model on the [110] zone axis. Hexagonal repeating unit cells with two nearby sides of 3.7 and 2.2 Å were observed, which matched the theoretical values of 3.66 and 2.15 Å, respectively, in the crystal model. Atom columns, **a**, at the center of the lattice image, exhibit a brighter intensity than that of columns **b** and **c** on the side, because **a** has a higher atom density than **b** and **c**. Atom columns, **b** and **c** show little difference in the image intensity, since they are Co and Fe atoms, with very similar atomic numbers, 27 and 26, respectively. The crystal model was established based on the cubic spinel structure of $CoFe_2O_4$. (F) The crystal model on the [110] zone axis was slightly tilted to reveal the underneath atom columns

Figure 6.7 EELS elemental maps of MCF-0.8. (A) HAADF-STEM image of a typical nanoparticle composed of smaller sub-domains. The lattice image in the dashed box was

magnified in (E) to show (220) and ($2\bar{2}0$) with same d-spacing values of 3.1 Å on the zone axis of [001]. (B-D) EELS elemental maps of Mn (red), Fe (green) and Co (blue), respectively. (F-H) EELS elemental composite maps of Mn vs. Fe, Mn vs. Co and Fe vs. Co, respectively

Figure 6.8 Electrocatalytic properties of as-synthesized MCF nanoparticles. (A) Cyclic voltammetry (CV) profiles of synthesized MCF NPs in Ar-saturated 1 M NaOH solution, scanned at a rate of 5 mV/s at room temperature. (B) ORR polarization curves in O_2-saturated 1 M NaOH at a scan rate of 5 mV/s and rotation at a rate of 1600 rpm. (C) Comparison of mass activity and half-wave potential of different MCFs at 0.9 V vs. RHE. (D) Polarization profiles of MCF-0.8 after 10,000 cycles of stability testing

Figure 6.9 Cyclic voltammetric profiles of $CoFe_2O_4$, $MnFe_2O_4$ and $Mn_{0.8}(CoFe_2)O_4$ in Ar-saturated 1M NaOH, at 5 mV/s scan rate

Figure 6.10 Cyclic voltammetric profiles between 0.15 to 1.2V of MCF-0.8 ($Mn_{0.8}(CoFe_2)_{0.73}O_4$) in Ar-saturated 1M NaOH, at 5 mV/s scan rate. The black line is the initial CV, and the red and blue lines are after stability testing of 6,000 and 10,000 cycles, respectively, at 100 mV/s between 0.6 to 1.0 V vs. RHE

Figure 6.11 STEM image of MCF-0.8 catalyst after 10,000 electrochemical cycles. The observed particle aggregation is likely responsible, at least input, for the degradation in electrochemical activity

Figure 6.12 EDX spectra of MCF-0.8 before and after electrochemical cycles. The X-ray intensities were normalized to the value of Fe Kα edge for comparisons. It should be noted that the Mn major Kα edge is at 5.89 keV and the Mn minor Kβ edge at 6.49 keV overlaps with Fe's major Kα edge(6.40 keV). Fe's minor Kβ edge at 7.05 keV overlaps

with Co's major Kα edge at 6.93 keV, which explains why Fe and Co peaks have small shoulder peaks on the right side of their peaks

Table 6.1 EDX quantitative analysis of MCF_0.8 catalysts before and after electrochemical cycles. Relative amounts of Mn, Co and Fe are average results from seven different regions in EDX measurements. The relative error using one standard deviation (Sd) was estimated to around 1 at.%. Accurate calculations of relative contents of Mn, Co and Fe were discussed as below

Table 6.2 EDX quantitative analysis of MCF_0.8 catalysts before and after electrochemical cycles without considering the overlap between Mn Kβ and Fe Kα and between Fe Kβ and Co Kα

Figure 6.13 *In situ* XANES spectra of the Mn, Co and Fe K-edges of MCF-0.8 and the evolution of the average metal valence and metal-oxygen atomic distance at a series of applied potentials. (A) *In situ* XANES spectra at the Mn K-edge of the MCF-0.8 (solid lines) and the reference manganese oxides (dashed lines). Inset shows the selected applied potential from the CV profile at a scan rate of 1mV/s in the home-made electrochemical cell at which signals were detected. (B) *In situ* XANES spectra at the Co K-edge of the MCF-0.8 (solid lines) and the reference cobalt oxides (dashed lines). Inset shows the gradual shift of the Co K-edge to lower photon energies with changing in intensity. (C) *In situ* XANES spectra at the Fe K-edge of the MCF-0.8 (solid lines) and the reference iron oxides (dashed lines). Inset shows the incremental shift of Fe K-edge to lower photon energies with a change in intensity. (D) Calculated average metal valence (solid lines, left Y-axis) as a function of potential based on the linear combination fitting using XANES

spectra of reference metal oxides. Measured metal-oxygen (M-O) atomic distance as a function of potential (dashed lines, right Y-axis) based on the *in situ* EXAFS analysis

Figure 6.14 (A) Valence analysis of Mn K-edge at 1.2 V vs. RHE. Linear combination fitting (LCF) (red dashed line) indicates the relative content of MnO (22%), Mn_3O_4 (56%), Mn_2O_3 (8.1%) and MnO_2 (14%) at 1.2 V. This LCF has a small R-factor of 0.00276 and reduced χ^2 of 0.000710, indicating a good fitting quality. (B) Average Mn valence at a series of applied potential, which was calculated from the relative contribution of four manganese oxide references. (C) Valence analysis of Co K-edge at 1.2 V. Linear combination fitting (LCF) (red dashed line) indicates the relative content of CoO (75.5%), Co_3O_4 (0%) and Co_2O_3 (24.5%) at 1.2 V. This LCF has a small R-factor of 0.0179 and reduced χ^2 of 0.00517, indicating a reasonable fitting quality. (D) Average Co valence at a series of applied potential, which was calculated from the relative contribution of three cobalt oxide references

Figure 6.15 *In situ* EXAFS of Mn (A) and Co (B) at a series of applied potential. The Metal-oxygen (M-O) bond distance increases as the applied potential decreased from 1.2 to 0.2 V, corresponding to a lower metal valence and weaker binding strength to oxygen. EXFAS spectra were processed by setting the background value (Rbkg) to 1.2 in Athena software with the FT-window set to 3 to 10 $Å^{-1}$ and no phase correction

Figure 6.16 Valence analysis of Fe K-edge at 1.2 V. Linear combination fitting (LCF) (red dashed line) indicates the relative content of FeO (0%), Fe_3O_4 (0%) Fe_2O_3 (100%) at 1.2 V. This LCF has a small R-factor of 0.00317 and reduced χ^2 of 0.000922, indicating a good fitting quality. The Fe valence is thus +3 and stays the same when E decreases from 1.2 to 0.2 V, based on the LCF analysis

Figure 6.17 Periodic changes of the relative X-ray intensities ($ln(I_1/I_2)$) at 6553 eV (Mn K-edge, red lines), 7225 eV (Co K-edge, green lines) and 7131 eV (Fe K-edge, blue lines), respectively, as a function of the cyclic potential sweep at 1 mV/s from 1.2 to 0.15 V vs. RHE. Intensity variations at 6553, 7225 and 7131 eV reflect the conversion among Mn(IV), Mn(III) and Mn(II), between Co(III) and Co (II), and Fe(III) and Fe(II), respectively. Relative X-ray intensity increases, suggesting a conversion of the metal from higher valence to lower valence as the applied potential goes from 1.2 to 0.15 V, and reach a maximum value at 0.28 V. Concomitantly, the relative X-ray intensity decreased as the applied potential goes from 0.15 to 1.2 V and reach a maximum value at 1.12 V. The upper inset shows the corresponding CV at 1 mV/s over the potential range of 0.15-1.2 V vs. RHE. Oxidation and reduction currents in the CV are divided by two boundary potentials, 0.28V and 1.12 V vs. RHE

Figure 7.1 X-ray diffraction patterns of as-synthesized BMOFs with different ratios of Co and Zn precursors

Figure 7.2 SEM images of as-prepared BMOFs synthesized at room temperature (A) BMOF_Co (B) BMOF_$ZnCo_3$ (C) BMOF_ZnCo (D) BMOF_Zn_3Co (E) BMOF_Zn_6Co (F) BMOF_$Zn_{11}Co$ (G) BMOF_$Zn_{20}Co$ (H) BMOF_Zn

Figure 7.3 TEM images of pyrolyzed BMOFs at 800^oC under forming gas (A) BMOF_Co (B) BMOF_$ZnCo_3$ (C) BMOF_ZnCo (D) BMOF_Zn_3Co (E) BMOF_Zn_6Co (F) BMOF_$Zn_{11}Co$ (G) BMOF_$Zn_{20}Co$ (H) BMOF_Zn

Figure 7.4 (A-H) SEM images of pyrolyzed BMOF_Co, BMOF_$ZnCo_3$, BMOF_ZnCo, BMOF_Zn_3Co, BMOF_Zn_6Co, BMOF_$Zn_{11}Co$, BMOF_$Zn_{20}Co$ and BMOF_Zn at 800^oC in forming gas (95% N_2 and 5% H_2) (I) TEM image of the pyrolyzed Zn_6Co (J)

SEM image of the pyrolyzed Zn_6Co_Fe (K) XRD patterns of Zn_6Co and Zn_6Co_Fe (L) Raman spectrum of Zn_6Co and Zn_6Co_Fe

Figure 7.5 Powder XRD patterns of BMOFs after pyrolysis at 800^{o}C in forming gas

Figure 7.6 (A) TGA results of annealed BMOFs before and after acid wash, in air and (B) BET N_2 adsorption/desorption isotherms of BMOFs derived carbon nanocomposites

Figure 7.7 Morphology and structural characterization of BMOFs. (A) SEM image of the as-prepared BMOF_Zn_6Co (B) SEM image of the pyrolyzed Zn_6Co

Figure 7.8 HAADF-STEM images of $Co_{0.9}Fe_{0.1}$ bimetallic nanoparticles embedded in a MOF-derived porous carbon matrix (BMOF). (A) low-magnification STEM image of BMOF (B) particle size distribution (PSD) histogram of about 300 particles analyzed from (A) and Figure S4. (C) Atomic-scale STEM image of a single crystal with a d-spacing value of 0.20 nm, indicating {111} facets of Co0.9Fe0.1. (D) Atomic-scale STEM image of a nanoparticle with five sub-domains on the [110] zone axis and the domain boundaries indicated as the red dashed lines. Inset shows the corresponding Fourier transform with five pairs of {111} diffraction spots; Chemical composition of a $Co_{0.9}Fe_{0.1}$ bimetallic nanoparticle. (E-H) STEM image and the corresponding EELS elemental maps of Co (red), Fe (green) and the composite map (Co vs. Fe). (I) Processed EELS spectrum with pronounced Fe and Co L3,2 edges (J) STEM-EDX spectrum with Fe Kα and Co Kα,β edges. Quantitative EDX analysis suggests Fe, Co contents of 89.2 at.% and 10.8 at.%, respectively.

Figure 7.9 Collection of low-magnification STEM images of $Co_{0.9}Fe_{0.1}$ bimetallic nanoparticles embedded in a MOF-derived porous carbon matrix (BMOF) (scale bar, 20

nm). Around 300 nanoparticles were counted and analyzed for the PSD histogram in Figure 7.8B. Very few particles larger than 15 nm were not included in the PSD histogram

Figure 7.10 STEM image of a $Co_{0.9}Fe_{0.1}$ bimetallic nanoparticle and the corresponding EELS maps of Co (red), Fe (green) and the composite map (Co vs. Fe)

Figure 7.11 (A-D) and (E-H) STEM images of $Co_{0.9}Fe_{0.1}$ bimetallic nanoparticles and the corresponding EDX elemental maps of Co (red), Fe (green) and the composite map (Co vs. Fe), extracted using Co and Fe Kα edges from spectrum images. The corresponding EDX spectra can be found in Fig. 4D. Co and Fe had X-ray counts of no less than 50 and 10 counts/pixel, respectively, and the beam dose was ~ 0.8 e/(Å·s). Large nanoparticles were selected for mitigating sample drift during long-time high-quality EDX elemental mapping acquisition

Figure 7.12 Degradation mechanism investigation of BMOF electrocatalysts during durability tests. (A) ORR polarization profiles of BMOF electrocatalysts at 1600 rpm and 5 mV/s after 10,000, 20,000 and 30,000 potential cycles from 0.6 to 1.0 V at 100 mV/s. (B) EDX spectra of BMOF at the initial state and after 30,000 cycles, showing a relatively stable Fe/Co atomic ratio. (C) STEM image of BMOF after 30,000 cycles, showing a majority of small particles as well as aggregated larger particles. (D) PSD histogram of BMOF after 30,000 cycles, analyzed from (C) and Figure 7.13, showing an increasing number of larger particles, relative to the initial state in Figure 7.12B

Figure 7.13 STEM image processing. (A) raw atomic-scale STEM image of a $Co_{0.9}Fe_{0.1}$ bimetallic nanoparticle. (B) image in (A) filtered using Richard-Lucy deconvolution (3 iterations). The deconvolution was processed in ImageJ software assuming an Airy disk (100 kV, α_{max}=28 mrad) convolved with a 0.8 Å Gaussian source

Figure 7.14 Degradation mechanism investigation of BMOF electrocatalysts during durability tests. (A) ORR polarization profiles of BMOF electrocatalysts at 1600 rpm and 5 mV/s after 10,000, 20,000 and 30,000 potential cycles from 0.6 to 1.0 V at 100 mV/s. (B) EDX spectra of BMOF at the initial state and after 30,000 cycles, showing a relatively stable Fe/Co atomic ratio. (C) STEM image of BMOF after 30,000 cycles, showing a majority of small particles as well as aggregated larger particles. (D) PSD histogram of BMOF after 30,000 cycles, analyzed from (C) and Figure 7.13, showing an increasing number of larger particles, relative to the initial state in Figure 7.12B

Figure 7.15 (A-B) low-magnification STEM images of BMOFs after 30000 potential cycles. Around 300 nanoparticles were counted and analyzed for the PSD histogram in Figure 7.9

LIST OF ABBREVIATIONS

ORR, oxygen reduction reaction

BMOF, bimetallic organic framework

PEMFC, proton exchange membrane fuel cell

AEMFC, alkaline exchange membrane fuel cell

ICE, internal combustion engine

FCV, fuel cell powered vehicle

DMFC, direct methanol fuel cell

PAFC, phosphoric acid fuel cell

MCFC, molten carbonate fuel cell

SOFC, solid oxide fuel cell

HOR, hydrogen oxidation reaction

DOE, Department of Energy

XRD, X-ray diffraction

XPS, X-ray photoelectron spectroscopy

TEM, transmission electron microscopy

UHV, ultrahigh vacuum

M/N/C, Metal/Nitrogen/Carbon

XANES, X-ray absorption near edge structure

XAFS, X-ray Absorption Fine Structure

PGM, precious-group-metal

NC, nitrogen-doped carbon

MOF, metal-organic-framework

CNT, carbon nanotube

OER, oxygen evolution reaction

MEA, membrane electrode assembly

RHE, reversible hydrogen electrode

WE, working electrode

CE, counter electrode

CV, cyclic voltammetry

ECSA, electrochemical surface area

$E_{1/2}$, half-wave potential

I_d, diffusion limiting current

I_k, kinetic current

TGA, thermogravimetric analysis

RDE, rotating disk electrode

SAED, selected area electron diffraction

EDX, energy-dispersive X-ray spectroscopy

EELS, electron energy loss spectroscopy

BF, bright field

HAADF, high angle annular dark field

ICP-AES, inductively coupled plasma atomic emission spectroscopy

LCPL, linear combination of power laws

ODPT, order-disorder phase transition

TCS, tetragonal crystal structure

PFSA, perfluorosulfonic acid

AST, accelerated stability tests

GDE, gas diffusion electrode

LROP, long-range order parameter

SROP, short-range order parameter

FCC, face-centered cubic

ODT, order-disorder transition

STEM, scanning transmission electron microscope

SSA, specific surface area

SA, area-specific activity

MA, mass-specific activity

BOL, beginning-of-life

EOL, end-of-life

HCD, high-current-density

MCF, Mn-promoting/doping cobalt ferrite

PCA, principal component analysis

LCF, linear combination fitting

ZIF, zeolitic imidazolate framework

SEM, scanning electron microscopy

PSD, particle size distribution

BET, Brunauer–Emmett–Teller

CHAPTER 1

INTRODUCTION

1.1 Motivations

Fossil fuels have been dominating energy sources for decades, and their continuous depletion and deleterious environmental issues necessitate the complementary regenerative alternatives.[1-3] A report from NASA indicated that the CO_2 levels before the 1950s had never exceeded 300 ppm, after which it had increased dramatically due to the rapid development of modern industries, where tremendous level of fossil fuels are utilized.[4] With the aspirational objection of clean and renewable fuels, together with the ever-increasing global energy demands, fuel cells have attracted a great deal of attention from both industry and academia.[5-6] The fuel cell is an energy conversion device, transforming the energy from chemicals, directly to electricity. It stands out from its peers with the highest energy density as shown in the Ragone plot listed as Figure 1.1[7]. The figure compares various electrochemical energy conversion/storage technologies including the conventional internal combustion engine (ICE), which shows that fuel cells, regarded as a high-efficiency energy-conversion technologies, are able to provide with continuous power. Other systems such as supercapacitors can perform charge/discharge processes at very high rates but low energy densities while batteries can deliver high energy but low power. In reality, a combined strategy of renewable energy generation/storage technologies will be regarded to supplement if not completely replace conventional internal combustion engines[8].

Compared to turbines and internal combustion engines, fuel cells have numerous advantages. First, their energy conversion efficiency is not limited by the Carnot cycle, which typically restricts that of ICEs to 20-30%. Thus, fuel cells can be more efficient and produce high power density required for start-up. Second, fuel cells are environmentally friendly, dramatically lowering pollution related to energy technologies using fossil fuels. Thirdly, unlike batteries, fuel cells can be refueled rapidly, typically within minutes, making them suitable for ground transportation. Fuel cells are generally considered as one of the key technologies for sustainable power sources with extensive applications. For example, in 2014, Toyota commercialized the first fuel cell powered vehicle (FCV) the Mirai, followed by Clarity from Honda and Tucson from Hyundai. The application of fuel cells is not limited in the field of the automotive, they have also been employed by NASA as engines for their aircrafts, even date back to the Apollo program in the 1960s.

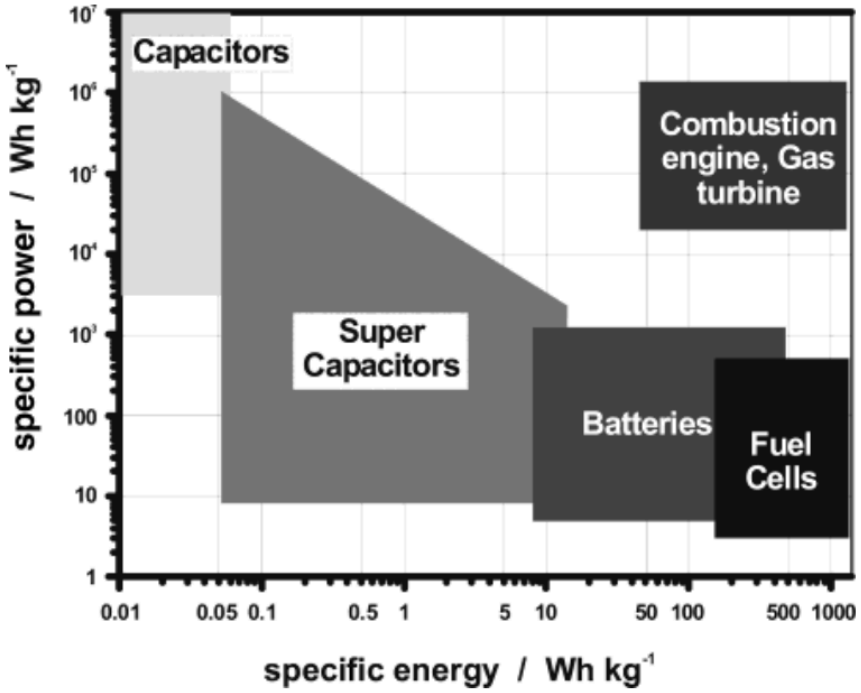

Figure 1.1. Ragone plot of specific power vs specific energy for various renewable energy conversion/storage systems in comparison to the traditional internal combustion engine. Figure reproduced from reference 7.

1.2 Introduction to Fuel Cells

A fuel cell consists of two electrodes (namely anode and cathode), A membrane, and gas diffusion layers. Its energy conversion performance is predominately dependent on the overpotentials at the two electrodes. The working mechanism of fuel cells is shown in Figure 1.2, where O_2 is reduced at the cathode, fuels are oxidized at the anode, and electrons transfer through the external circuit to supply the load. Fuel cells can be categorized into various kinds based on their working conditions and fuels, where the last three types in the figure are mostly operated at high temperatures and only suitable for large scale stationary applications. The most commonly used low-temperature fuel cells are polymer electrolyte membrane fuel cells (PEMFCs), and alkaline exchange membrane fuel cell (AEMFCs), where hydrogen serves as the fuel (oxidant) in acidic or basic media, respectively. The working efficiency and half-reactions occurring at each electrode are indicated below:

Anode: $H_2 \rightarrow 2H^+ + 2e^-$ / $H_2 + 2OH^- \rightarrow 2H_2O$ (PEMFCs / AEMFCs) $E^o = 0V$

Cathode: $O_2 + 4e^- + 4H^+ \rightarrow 2H_2O$;

$O_2 + 2H_2O + 4e^- \rightarrow 4OH^-$ (PEMFCs/AEMFCs) $E^o = 1.23V$

Overall: $O_2 + 2H_2 \rightarrow 2H_2O$ $E^o = 1.23V$

Cell efficiency = $\frac{E°cathode - E°anode}{1.23V} \times 100\%$

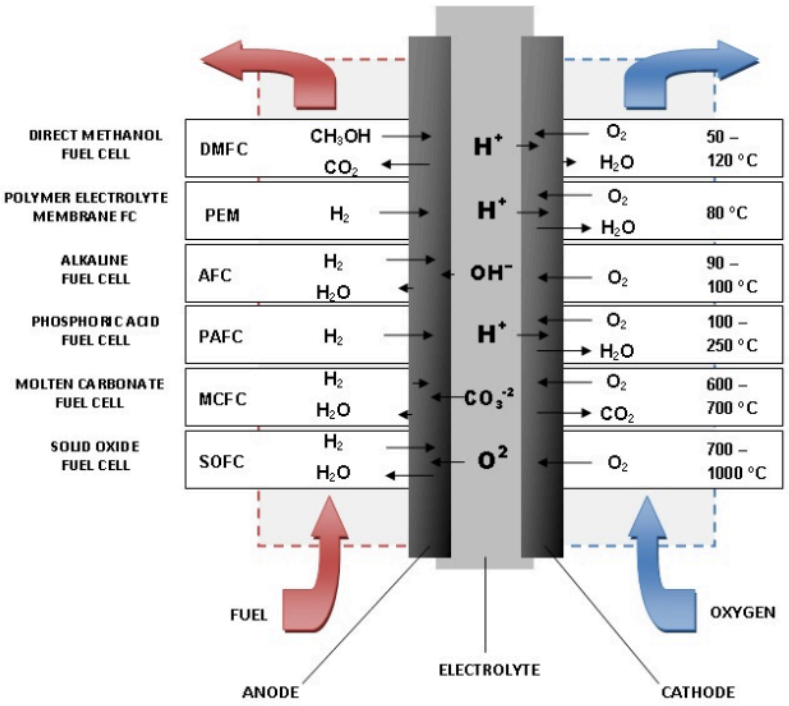

Figure 1.2. Schematic of different types of fuel cells: direct methanol fuel cells (DMFCs), polymer electrolyte membrane fuel cells (PEMFCs), alkaline exchange membrane fuel cell (AEMFCs), phosphoric acid fuel cells (PAFCs), molten carbonate fuel cells (MCFCs) and solid oxide fuel cells (SOFCs). Figure reproduced from reference 9.

As shown in the equation, the cell efficiency is dictated by the potential difference between cathode and anode so that overpotentials need to be minimized. Fuel cell anodes, now always had small overpotentials, on the order of 20 mV, due to the fast kinetics of H_2 oxidation at Pt. The voltage/efficiency loss comes mostly from the cathode where overpotentials over 300 mV are typically observed. It is generally recognized that the sluggish kinetics of the oxygen reduction reaction (ORR) are largely responsible for such limitation. In order to achieve a satisfactory full cell performance, Various catalysts has been developed, and the most successful example, namely Pt-based nanoparticles, has been commercialized to promote the reaction rates at both electrodes. The amount of Pt needed for the hydrogen oxidation reaction (HOR) at the anode is relatively low, typically at a level near 0.05 mg/cm^2 while a much higher amount (0.2 mg/cm^2) of Pt is required to catalyze the sluggish kinetics of oxygen reduction reaction (ORR) at the cathode[10-11].

The 2017 annual report from the United States Department of Energy (DOE) shown in Figure 1.3 presents the estimated cost to manufacture FCEs at the production level of 1000, 100,000 and 500,000 units per year, where the contribution from the catalysts always accounts for the largest portion[11]. The high cost of the electrocatalyst is due to the scarcity of Pt, and consequently leads to the high market prices of FCVs (~57,000 dollars for Toyata Miari). In order to lower cost, tremendous efforts have been devoted into the development of more cost-effective precious metal based electrocatalysts and non-precious metal alternatives, with robust durability and high precious-metal utilization efficiencies.

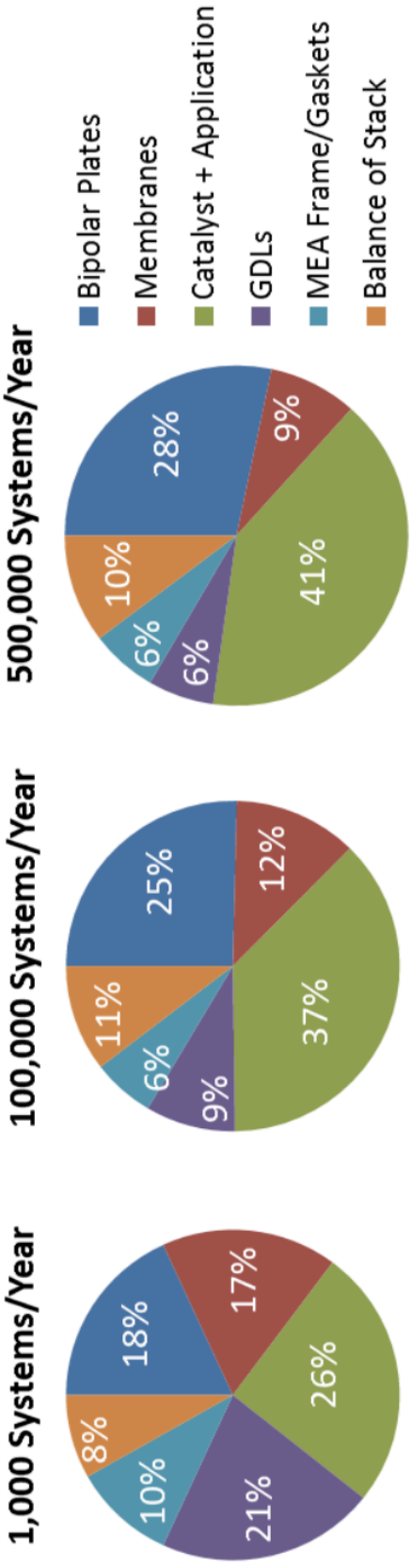

Figure 1.3. Breakdown of the 2017 projected fuel cell stack cost at 1,000, 100,000, and 500,000 systems per year. Figure reproduced from reference 11.

1.3 Current Situation of ORR Electrocatalysts

Ideally, an electrocatalyst should meet three criteria, high activity, robust durability and acceptable cost. The design principles of catalysts for PEMFCs and AEMFCs vary significantly due to their distinct working conditions. Briefly, PEMFCs can typically provide high power densities and durability, with a mature supply chain of Nafion membranes and assembly techniques. However, their low operating pH electrolyte requires catalysts that can survive such an aggressive environment. Currently, only precious metals can operate under such conditions. AEMFCs operate under a less corrosive working environment and anions have weaker adsorption on the surface of electrocatalysts, contributing to less sluggish ORR kinetics. The constraints have triggered tremendous efforts in the field to develop more efficient electrocatalysts and membranes. The following section present a review on current state-of-art electrocatalysts for PEMFCs and AFCs, respectively, covering materials properties, synthesis approaches, and their pro/cons for practical applications.

1.3.1 Electrocatalysis in PEMFCs

The oxygen reduction reaction (ORR) mechanism in acidic media can be divided into four steps, which together, with the corresponding free energy changes, are illustrated in Figure 1.4A[12]. These steps include: (1), the oxygen molecule is adsorbed on the surface of the electrode where subsequently, one of the oxygen atoms receives a proton and an electron; (2), the protonated oxygen atom gets a second proton and electron pair, followed by the breaking of the O-O bond forming one water molecule on the surface; (3), proton and electron transfer to the remaining single oxygen atom adsorbed on the surface; (4),

the newly-formed hydroxyl obtains another proton and electron pair and desorbs from the electrode surface as water. The first and last steps involve a gain in the Gibbs free energy, and thus one of them is likely to be the rate-determining step. The first protonation step slows down the kinetics due to the weak binding strength of oxygen molecules to the surface of the electrode and lower O_2 coverage. In contrast, the last step can slow down the process due to the possibility that oxygen molecules may bind too strongly to the electrode and occupy active sites with intermediate species.

In order to promote the sluggish ORR, electrocatalysts are utilized. Scientists have calculated the energy barriers of various electrocatalysts toward the ORR, as shown in Figure 1.4B. The dashed line is the standard reduction potential of oxygen molecules, and two solid lines are calculated Gibbs free energies for the first and last steps. The ideal electrocatalyst should be located on the summit of the plot, with the shortest distance away from the standard potential which means minimal overpotential. Platinum (Pt) is the most active elemental electrocatalyst, located on the left side where the desorption process is rate-limit. When Pt is alloyed with transition metals or it exposes a specific facet, the electronic and ligand effects modify the surface structure, lowering the binding energy. Although some discrepancy exists between the calculated and experimental results, there is at least a semi-quantitative correlation between the enhancement of the ORR activity and the regulation of the electrocatalyst surface.

Pt/Pd-based nanoparticles are generally regarded as the most active electrocatalysts in acidic media. Considerable research has involved the structural modification of Pt/Pd binary or ternary materials. 3d-transition metals, including Ni, Co, Fe, Mn, Cu and others,

have been alloyed with Pt to improve the ORR activity and lower the cost which is mostly associated with the loading of precious metals[13-17]

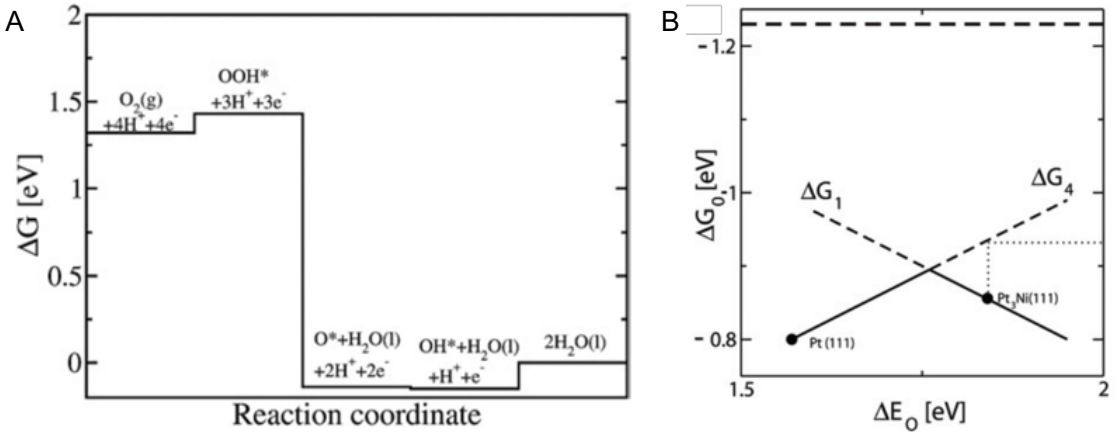

Figure 1.4. (A) The mechanism and calculated changes in the Gibbs free energy for the ORR on the surface of Pt (111); (B) The correlation of the free energy and adsorption energy of oxygen for the first and the last steps. The vertical dashed line indicates the standard redox potential. The distance from the solid volcano profile to the horizontal dashed line represents the ORR overpotential at the limiting exchange current. Figure reproduced from reference 12.

Previously, our group has designed Pd-Co bimetallic nanoparticles with optimized chemical composition and Pt_3Co with the ordered intermetallic structure for the ORR[18-19]. In the case of Pt_3Co, the improved activity and durability were attributed to the lattice contraction and downshift of the d-band center, caused by the small atomic radius and electronic structure of Co, respectively, which influence the surface binding energy with oxygenated species[20-21]. Based on these observations, nanoparticles with a Pt/Pd shell on the surface were prepared. Due to the relatively larger adsorption enthalpy of H on Pt/Pd than on Co, Pt/Pd nanocatalysts significantly maintain their structural and electrochemical integrity[22-23]. Tuning the surface and morphology of nanoparticles is also an approach to improve the activity and utilization efficiency of precious metal based electrocatalysts. Our group has also systematically analyzed the effects from different dealloying conditions using $PtCu_3$ as a model. The results have demonstrated the chemical leaching process generates spongy and porous structures, which exhibit superior activity compared with the electrochemically leached counterparts. The gradual leaching-out of Cu in the acidic working conditions produced a high Pt surface area, yielding essentially the same specific activity but much higher mass activity[24-25].

Other researchers have also made significant progress on screening more effective electrocatalysts. Specific surfactants and reaction conditions are utilized to synthesize shape-selective nanoparticles, which have been further analyzed by X-ray diffraction (XRD), X-ray photoelectron spectroscopy (XPS) and transmission electron microscopy (TEM) in either ultrahigh vacuum (UHV) or near-ambient conditions to understand their growth/nucleation processes. A variety of computation methods and models have also been built to elucidate the mechanism of the enhancement. For example, the Strasser

group and the Stamenkovic have studied shape-selective Pt-Ni nanoaprticles, where the crystal facet is exclusively controlled to be (111)[26-27]. The enhanced electrocatalytic activity of the octahedral nanoparticles was associated with the low coverage of hydroxyl species and the high density of active sites for O_2 adsorption. Yang et al., have prepared nanocrystals with a more complex architecture, with tetrahexahedral or rhombic dodecahedral frames[28-29]. Their enhanced activity was attributed to the atomic scale compositional segregation and minimal number of buried Pt sites.

Besides high catalytic activity, robust durability is also of paramount importance. To pursue this goal, several strategies have been implemented to modify the crystal and/or electronic structure. For instance, the Pt-Fe and Pt-Co intermetallic systems have recently drawn a great deal of interest due to their ability to retain their high stability under working conditions[19, 30-31]. Compared with the disordered alloys, the improvement is believed to come from the stable intermetallic arrangement of two elements in the core, together with the spontaneously formed Pt-rich shell.

The degradation of the electrocatalyst and the concomitant performance degradation mainly come from the loss of the transition metal and the fact that the leached transition metal ions in the electrolyte can, in turn, contaminate the Pt surface. The intermetallic nanoparticles with the ordered lattice have a uniform and regular atomic structure, so the transition metal is mostly bonded to and surrounded by Pt, dramatically mitigating degradation. Intermetallic phases are traditionally synthesized via high temperature annealing, in order to overcome the thermal barrier, namely slow kinetics and diffusion rates of solid-solid reactions. However, the intensive thermal movement in return, leads to coalescence and aggregation of catalyst particles, lowering their surface area and

deteriorating their electrocatalytic performance. The DiSalvo and Sun groups employed KCl matrix and MgO coating, respectively, to partially retard the intense thermal movement of atoms, in order to the mitigate the aggregation during the structural evolution[32-34]. In their cases, the inert shell can help achieve a good balance between electrocatalytic activity and durability for practical applications. Apart from the degradation due to agglomeration, the distortion of shape-controlled nanoparticles can also result in activity losses. To address this, the Strasser and the Huang groups reported that doping in a relatively low content of a third metal, like Rh and Mo, can stabilize the atomic structure. Rh is preferentially located at the edge of the octahedral crystals and Mo forms strong binding with Pt and Ni, to suppress the diffusion and dissolution of Pt and Ni atoms[35-36].

In addition to precious metal based electrocatalysts that are extensively used for PEMFCs, nitrogen doped carbon materials have emerged as a way to bring down cost since 1964, when Jasinski discovered the catalysis of ORR by Co-phthalocyanine[37]. The Zelenay and Dodlet groups have reported a class of Metal/Nitrogen/Carbon (M/N/C) catalysts for the ORR, where Co/Fe is coordinated with doped nitrogen ($Fe\text{-}N_4$/$Co\text{-}N_4$) encapsulated in a carbon matrix, obtained from the pyrolysis from organic macromolecules, most likely serving as active sites[38-40].

Assorted macromolecules and metal-organic-frameworks have been used as precursors of N and metals, with optimized thermal and acid-treatments to control the architecture and composition. The resulting M/N/C-catalysts commonly have a high N content, high graphitization degree and both meso- and micro- porosity, that are designed to achieve sufficient active site density, high electronic conductivity and O_2 transport, respectively.

However, despite of extensive efforts, the relatively low volumetric activity of the M/N/C catalysts has impeded their technical and commercial feasibility. To address this challenge and uncover complex working mechanisms, various techniques, including Mössbauer spectroscopy, TEM, XPS and X-ray absorption near edge structure/X-ray Absorption Fine Structure (XANES/XAFS) have been employed, to either directly visualize active sites or unravel the correlation among electrochemical properties of M/N/C catalysts, their catalytic activities, and durability.

1.3.2 Electrocatalysis in AEMFCs

Along with the development of PEMFCs, AEMFCs have also drawn a great deal of attention recently. The alkaline electrolyte in AEMFCs provides milder working conditions for the electrocatalyst, that enables the use of less expensive non-precious-group-metal (PGM) based catalysts. The implementation of PGM-free-catalysts can circumvent the obstacle of high price caused by the scarcity of precious metals. At the same time, the adsorption energy of anions is weakened in the basic media, which promotes the kinetics of the ORR.

Although Pt and Pd based nanoparticles are still among the best candidates applied to AEMFCs, spinels (AB_2O_4), perovskites (ABO_3) and nitrogen-doped carbon (NC) materials have been reported recently to exhibit promising activity in ORR electrocatalysis[41]. In the category of spinel oxides, Co and Mn based oxides have generated extensive interest due to their variable valence states and, unique crystal and electronic structures. Dai et al. has performed a comprehensive investigation of Co_3O_4 monometallic oxides, and later substituted Co partially with Mn loaded on a nitrogen-doped reduced graphene oxide support. Compared with the conventional Vulcan carbon

supported catalysts, CoMnO exhibited improved activity that was attributed to the synergistic behavior arising from the covalent coupling between nanoparticles and supports[42-43]. Moreover, Chen group has reported facile, general and mild condition synthesis methodologies to prepare a series of $Mn_xCo_{3-x}O_4$ spinel nanocrystallites with controllable compositions and crystal phases. The correlation between structural properties and electrocatalytic activity of $Mn_xCo_{3-x}O_4$ was established by virtue of the selective synthesis for $Mn_xCo_{3-x}O_4$ nanoparticles, exclusively in cubic or tetragonal spinel structures[44-45].

Nano-structured carbon materials, doped with heteroatoms or single metallic atoms, have also been demonstrated to be promising electrocatalysts for ORR. Besides traditional organic molecules/polymers, such as polyaniline, cyanamide, phenanthroline and others, metal-organic-frameworks (MOFs) have also recently stimulated interest in the field as precursors/templates to fabricate PGM free catalysts. This family of materials feature high surface areas (1000-10000 m^2/g), homogenous distribution and high content of nitrogen, as well as the tunable 3D geometry; all favorable for electrochemical reactions. The Lou group has utilized ZIF-67 (Co as central metallic atoms and imidazole as organic ligands) as a single source for the carbon, nitrogen and transition metal[46]. Under optimized thermal treatment conditions, a significant amounts of interconnected carbon nanotubes (CNTs) grow in the skeleton of polyhedral carbon crystals, forming hollow-structured hierarchical frameworks. They represented remarkable bifunctional electrocatalytic activities for both ORR and the oxygen evolution reaction (OER), with robust chemical and structural architectures. Liang et al. have further enhanced the activity of MOF-based catalysts by combining ZIF-67 and ZIF-8 to form bimetallic

organic frameworks (BMOFs) as self-sacrificial template, and subsequently doping with additional phosphorus, to simultaneously obtain high graphitization, high heteroatom dopant content and hierarchical porosity[47]. The optimized material exhibited extraordinary long-term durability and high tolerance to methanol over the working potential window.

1.4 Research Overview

Inspired by previous works, my PhD dissertation can be divided into two categories. The first one is related to the design and development of novel nanostructured materials for the energy applications, together with structural characterizations. The start point is the high-loading Pt_3Co intermetallic, which is a practical ORR electrocatalytic material that has received extensive attention from major auto manufacturing collaborators such as General Motors and Nissan. To better utilize Pt_3Co in industrial applications, I have optimized the structure of the carbon support, varied the loading of precious metal and modified the chemical and atomic structures of the nanoparticle, so as to optimize power density in MEAs. In addition to the structurally ordered Pt-based intermetallics, I have also studied surface modified nanoparticles with a compositionally-optimized core, to enhance the intrinsic activity with a high Pt utilization efficiency. Precious-metal-based materials are still the best candidates for PEMFCs, although they are also responsible for the high cost. Several kinds of non-precious-metal catalysts, including ternary spinel oxides and BMOF derived nanoporous carbon materials, have also been rationally designed fo application in alkaline media. Their low cost, promising activity and robust

durability, provide design guidance for the development of more cost-effective alternatives.

The second aspect of my research has been the *in situ* study on the formation and degradation processes of the prepared nanomaterials described above. A series of *in situ* techniques were combined to learn the atomic and morphological changes during the structural evolution of bimetallic nanoparticles at high temperatures. A particular focus has been the coupling of synchrotron-based X-ray methods with electrochemical technologies to track catalytic processes under working conditions. These two directions have yielded deep and detailed information on nanocatalysts at the micro/macroscopic level. These results now yielded valuable insights for the development and preparation of next-generation high performance fuel cell electrocatalysts.

1.5 Reference

1. Debe, M. K., Electrocatalyst approaches and challenges for automotive fuel cells. *Nature* **2012**, 486, 43-51.
2. Lewis, N. S.; Nocera, D. G., Powering the planet: Chemical challenges in solar energy utilization. *Proc. Natl Acad. Sci.* **2006**, 103, 15729-15735.
3. Winter, M.; Brodd, R. J., What are batteries, fuel cells, and supercapacitors? *Chem. Rev.* **2004**, 104, 4245-4269.
4. https://climate.nasa.gov/climate_resources/24/graphic-the-relentless-rise-of-carbon-dioxide/

5. Banham, D.; Ye, S.; Current status and future development of catalyst materials and catalyst layers for PEMFCs: An industrial perspective. *ACS Energy Lett*. **2017**, 2, 629-638.
6. Kongkanand, A.; Mathias, M.; The priority and challenge of high-power performance of low-platinum proton-exchange membrane fuel cells. *J. Phys. Chem. Lett*. **2016**, 7, 1127-1137.
7. Bacon, F. T., *Ind. Eng. Chem*.**1960**, 52 (4), 301–303.
8. Winter, W.; Brodd R. J., What Are Batteries, Fuel Cells, and Supercapacitors? *Chem. Rev*. **2004**, 104 (10), 4245-4270.
9. www.isondopm.com/technology
10. Shao, M.; Chang, Q.; Dodelet, J. P.; Chenitz, R., Recent Advances in Electrocatalysts for Oxygen Reduction Reaction. *Chem. Rev*. **2016**, 116, 3594-3657.
11. DOE Hydrogen and Fuel Cells Program Record, 2017.
12. Rossmeisl, J.; Karlberg, G. S.; Jaramillob, T.; Nørskov, J. K., Steady state oxygen reduction and cyclic voltammetry. *Faraday Discuss*. **2018**, 140, 337-346.
13. Stamenkovic, V. R.; Bongjin, S. M.; Arenz, M.; Mayrhofer, K. J. J.; Lucas, C. A.; Wang, G.; Ross, P. N.; Markovic, N. M., Trends in electrocatalysis on extended and nanoscale Pt-bimetallic alloy surfaces. *Nature Mater.* **2007**, 6, 241-247.
14. Wu, J. B., Truncated octahedral Pt_3Ni oxygen reduction reaction electrocatalysts. *J. Am. Chem. Soc*. **2010**, 132, 4984-4985.
15. Zhang, J.; Yang, H. Z.; Fang, J. Y.; Zou, S. Z., Synthesis and oxygen reduction activity of shape-controlled Pt_3Ni nanopolyhedra. *Nano Lett.* **2010**, 10, 638-644.

16. Srivastava, R.; Mani, P.; Hahn, N.; Strasser, P., Efficient oxygen reduction fuel cell electrocatalysis on voltammetrically dealloyed Pt-Cu-Co nanoparticles. *Angew. Chem. Int. Ed*. **2007**, 46, 8988-8991.

17. Kang, Y.; Murray, C. B., Synthesis and electrocatalytic properties of cubic Mn-Pt nanocrystals (nanocubes). *J. Am. Chem. Soc*. **2010**, 132, 7568-7569.

18. Wang, D.; Xin, H.; Wang, H.; Yu, Y.; Rus, E.; Muller, D.; DiSalvo, F.; Abruña, H.; Facile synthesis of carbon-supported Pd-Co core-shell nanoparticles as oxygen reduction electrocatalysts and their enhanced activity and stability with monolayer Pt decoration. *Chem. Mater*. **2012**, 24, 2274-2281.

19. Wang, D.; Xin, H.; Hovden, R.; Wang, H.; Yu, Y.; Muller, D.; DiSalvo, F.; Abruña, H., Structurally ordered intermetallic platinum-cobalt core-shell nanoparticles with enhanced activity and stability as oxygen reduction electrocatalysts. *Nat. Mater*. **2012**, 12, 81-87.

20. Mavrikakis, M.; Hammer, B.; Norskov, J. K. Effect of strain on the reactivity of metal surfaces. *Phys. Rev. Lett*. **1998**, 81, 2819.

21. Hammer, B.; Hansen, L. B.; Norskov, J. K., Improved adsorption energetics within density-functional theory using revised Perdew-Burke-Ernzerhof functionals. *Phys. Rev. B* **1999**, 59, 7413.

22. Popova, N. M.; Babenkova, L. V., *React. Kinet. Catal. Lett.* **1979**,

23. Johansson, M.; Lytken, O.; Chorkendorff, I., The sticking probability for H_2 on some transition metals at a hydrogen pressure of 1 bar. *J. Chem. Phys.* **2008**, 128, 034706.

24. Wang, D.; Yu, Y.; Xin, H.; Hovden, R.; Ercius, P.; Mundy, J.; Chen, H.; Richard, J.; Muller, D.; DiSalvo, F.; Abruña, H., Tuning oxygen reduction reaction activity via

controllable dealloying: a model study of ordered Cu_3Pt/C intermetallic nanocatalysts. *Nano Lett.* **2012**, 12, 5230-5238.

25. Wang, D.; Yu, Y.; Zhu, J.; Liu, S.; Muller, D.; Abruña, H.; Morphology and activity tuning of Cu_3Pt/C ordered intermetallic nanoparticles by selective electrochemical dealloying. *Nano Lett*. **2015**, 15, 1343-1348.
26. Stamenkovic, V.; Fowler, B.; Mun, B.; Wang, G.; Ross, P.; Lucas, C.; Markovic, N., Improved oxygen reduction activity on Pt_3Ni(111) via increased surface site availability. *Science* **2007**, 315, 493-497.
27. Cui, C.; Gan, L.; Heggen, M.; Rudi, S.; Strasser, P., Compositional segregation in shaped Pt alloy nanoparticles and their structural behavior during electrocatalysis. *Nat. Mater*. **2013**, 12, 765-771.
28. Ding, J.; Bu, L.; Guo, S.; Zhao, Z.; Zhu, E.; Huang, Y.; Huang, X., Morphology and phase controlled construction of Pt-Ni nanostructures for efficient electrocatalysis. *Nano Lett.* **2016**, 16, 2762-2767.
29. Becknell, N.; Son, Y.; Kim, D.; Li, D.; Yu, Y.; Niu, Z.; Lei, T.; Sneed, B.; More, K.; Markovic, N.; Stamenkovic, V.; Yang, P., Control of architecture in rhombic dodecahedral Pt–Ni nanoframe electrocatalysts. *J. Am. Chem. Soc*. **2017**, 139, 11678-11681.
30. Cui, Z.; Fu, G.; Li, Y.; Goodenough, J., Ni 3 FeN‐Supported Fe 3 Pt Intermetallic Nanoalloy as a High-performance Bifunctional Catalyst for Metal-Air Batteries. *Angew. Chem*. **2017**, 129, 10033-10037.

31. Du, X.; He, Y.; Wang, X.; Wang, J., Fine-grained and fully ordered intermetallic PtFe catalysts with largely enhanced catalytic activity and durability. *Energy Environ. Sci.* **2016**, 9, 2623-2632.

32. Cui, Z.; Chen, H.; Zhou, W.; Zhao, M.; DiSalvo, F., Structurally ordered Pt_3Cr as oxygen reduction electrocatalyst: ordering control and origin of enhanced stability. *Chem. Mater*. **2015**, 27, 7538-7545.

33. Chen, H.; Yu, Y.; Xin, H.; Newton, K.; Holtz, M.; Wang, D.; Muller, D.; Abruña, H.; DiSalvo, F., Coalescence in the thermal annealing of nanoparticles: an in Situ STEM study of the growth mechanisms of ordered Pt–Fe nanoparticles in a KCl matrix. *Chem. Mater*. **2013**, 25,1436-1442.

34. Li, Q.; Wu, L.; Wu, G.; Su, D.; Lv, H.; Zhang, S.; Zhu, W.; Casimir, A.; Zhu, H.; Mendoza-Garcia, A.; Sun, S., New approach to fully ordered fct-FePt nanoparticles for much enhanced electrocatalysis in acid. *Nano Lett.* **2015**, 15, 2468-2473.

35. Beermann, V.; Gocyla, M.; Willinger, E.; Rudi, S.; Heggen, M.; Dunin-Borkowski, R.; Willinger, M.; Strasser, P., Rh-Doped Pt–Ni octahedral nanoparticles: understanding the correlation between elemental distribution, oxygen reduction reaction, and shape stability. *Nano Lett.* **2016**, 16, 1719-1725.

36. Huang, X.; Zhao, Z., Cao, L.; Chen, Y.; Zhu, E.; Lin, Z.; Li, M.; Yan, A.; Zettl, A.; Wang, Y.; Duan, X.; Mueller, T.; Huang, Y., High-performance transition metal-doped Pt3Ni octahedra for oxygen reduction reaction. *Science* **2015** 348, 1230-1234.

37. Jasinski, R., A new fuel cell cathode catalyst. *Nature* **1964**, 201, 1212-1213.

38. Lefèvre, M.; Proietti, E.; Jaouen, F.; Dodelet, J., Iron-based catalysts with improved oxygen reduction activity in polymer electrolyte fuel cells. *Science* **2009**, 324, 71-74.

39. Proietti, E.; Jaouen, F.; Lefèvre, M.; Larouche, N.; Tian, J.; Herranz, J.; Dodelet, J., Iron-based cathode catalyst with enhanced power density in polymer electrolyte membrane fuel cells. *Nat. Comm*. **2011**, 2.

40. Chung, H.; Cullen, D.; Higgins, D.; Sneed, B.; Holby, E.; More, K.; Zelenay, P., Direct atomic-level insight into the active sites of a high-performance PGM-free ORR catalyst. *Science* **2017**, 357, 479-484.

41. Suntivich, J.; Gasteiger, H.; Yabuuchi, N.; Nakanishi, H.; Goodenough, J.; Shao-Horn, Y., Design principles for oxygen-reduction activity on perovskite oxide catalysts for fuel cells and metal-air batteries. *Nat. Chem*. **2011**, 3, 546-550.

42. Liang, Y.; Li, Y.; Wang, H.; Zhou, J.; Wang, J.; Regier, T.; Dai, H., Co_3O_4 nanocrystals on graphene as a synergistic catalyst for oxygen reduction reaction. *Nat. Mater*. **2011**, 10, 780-786.

43. Liang, Y.; Wang, H.; Zhou, J.; Li, Y.; Wang, J.; Regier, T.; Dai, H., Covalent hybrid of spinel manganese-cobalt oxide and graphene as advanced oxygen reduction electrocatalysts. *J. Am. Chem. Soc*. **2012**, 134, 3517-3523.

44. Cheng, F.; Shen, J.; Peng, B.; Pan, Y.; Tao, Z.; Chen, J., Rapid room-temperature synthesis of nanocrystalline spinels as oxygen reduction and evolution electrocatalysts. *Nat. Chem*. **2010**, 3, 79-84.

45. Li, C.; Han, X.; Cheng, F.; Hu, Y.; Chen, C.; Chen, J., Phase and composition controllable synthesis of cobalt manganese spinel nanoparticles towards efficient oxygen electrocatalysis. *Nat. Comm*. **2015**, 6, 1.

46. Xia, B.; Yan, Y.; Li, N.; Wu, H.; Lou, X.; Wang, X., A metal-organic framework-derived bifunctional oxygen electrocatalyst. *Nat. Energy* **2016**, 1, 15006.

47. Chen, Y.; Wang, C.; Wu, Z.; Xiong, Y.; Xu, Q.; Yu, S.; Jiang, H. Metal-organic frameworks: from bimetallic metal-organic framework to porous carbon: high surface area and multicomponent active dopants for excellent electrocatalysis. *Adv. Mater*. **2015**, 27, 5009-5009.

CHAPTER 2

METHODOLOGY

2.1 Electrochemical Instrumentations

2.1.2 Potentiostats

All electrochemical characterizations were performed using several potentiostats, including a Solartron model 1280 B and a Pine AFRDE5 bipotentiostat with data collected by LABVIEW software. ORR polarization profiles (RDE experiments), cyclic voltammetry and rotating ring-disk electrode (RRDE) characterizations were performed on a Pine AFRDE5 bipotentiostat equipped with a Pine Instruments AFMSRX analytical rotator. All CO-stripping experiments were carried out on the Solartron potentiostats.

2.1.3 Working, Reference and Counter Electrodes

Two kinds of working electrodes (rotating disk electrodes) were used in the electrochemical experiments. One was homemade and the other was a commercial product from Pine Instruments. A glassy carbon rod (d=5 mm, 5 mm in length) was inserted into a Telfon rod shroud, with carbon fiber wool filled in the back side of the electrode to make electrical contact. A stainless-steel rod used to connect the electrode to rotator, was fixed at the bottom of the Telfon rod with epoxy (double/bubble). The glassy carbon disk Pt ring rotating ring-disk electrode was purchased from Pine Instruments (E6R2 fixed-disk RRDE tips peek), with disk OD = 5.5mm, ring OD = 8.5mm and ring ID = 6.5mm. The collection efficiency (N) was measured to be 38% in $K_3Fe(CN)_6$

electrolyte. Before each electrochemical measurement, electrodes have polished with the finest sandpaper (1200/P2500) followed by 1 μm diamond paste (METADI-Buehler) and aluminum oxide powders (Φ = 0.2 μm) on a Buehler polishing clothing.

1M KCl or saturated KCl Ag/AgCl electrodes were used as reference electrodes purchased from CH instruments. All measured potentials were converted to the reversible hydrogen electrode (RHE) scale using the following equation:

$$E_{RHE} = E_{Ag/AgCl} + 0.197 \text{ (sat KCl)}/0.235 \text{ (1M KCl)} + 0.0592\times \text{ pH}$$

A large area Pt wire was used as the counter electrode in the measurement of precious metal catalysts while a graphite rod was used for non-precious-metal catalysts to avoid any contamination from the precious metal. A home-made glass cell was used, with a main chamber in the center and two side chambers. A fine porosity glass frit separated the main chamber and two side chambers to prevent the electrolyte mixing but maintaining sufficient ionic conductivity.

2.2 Customized Setup

2.2.1 *In situ* Heating X-ray Setup

To track the structural evolution of bimetallic nanoparticles at high temperatures, a custom-designed setup was used to mimic the real synthesis conditions and record changes in the XRD pattern during the annealing process. The *in situ* heating setup was modified based on a SabreTube furnace (Absolute Nano, Wixom, MI), where a piece of Si single crystal strip was used as the heating stage, fixed in the center of a quartz tube, as shown in Figure 2.1A with a photo of the setup shown in Figure 2.1B[1]. The main quartz chamber had two windows that were covered with Kapton films and had a tilt angle near

5 degrees. Another piece of Si single crystal with a 200 μm thick depression was used as the sample holder and placed on the heating stage with a thermocouple underneath to control the heating temperature during the test. XRD patterns were directly measured as d spacings by a Pilatus 100K (Dectris, Switzerland) pixel array detector and calibrated with CeO_2 powder. The XRD patterns of Pt_3Co/C, before and after the annealing process, prepared in a regular flow furnace, have been measured *ex situ* to test the reliability of the setup, as shown in Figure 2.2. All XRD patterns were measured on an X-ray energy of 19.6 keV with a wavelength of 0.63 Å in the unit of d spacing, and further converted to 2θ using Cu Kα radiation keV at the wavelength of 1.5406 Å. After the conversion, they were well consistent with those measured with powder XRD, which demonstrated that results from the *in situ* heating setup properly reflected the crystal structural evolution of annealed materials.

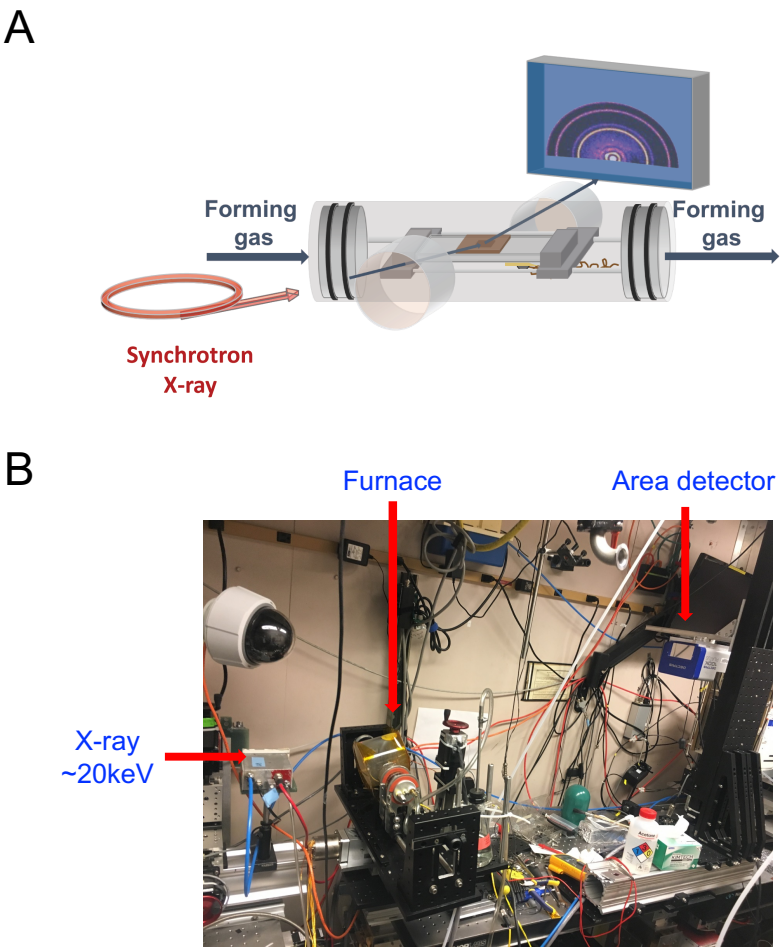

Figure 2.1. (A). Schematic figure of the *in situ* heating setup (modified based on SabreTube furnace). Figure reproduced from reference 1. (B). Photo of the *in situ* heating setup in the synchrotron. Figure reproduced from reference 1.

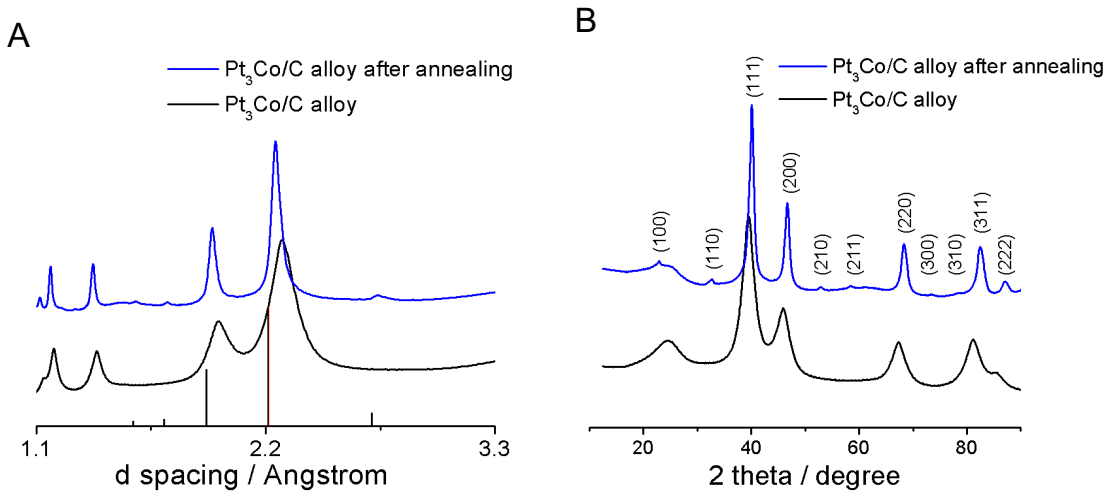

Figure 2.2 The measured XRD patterns of non-annealed/annealed (alloy/intermetallic) Pt_3Co/C in the synchrotron (A) measured directly in d spacing (B) converted to 2θ using Cu Kα radiation. Figure reproduced from reference 1.

2.2.2 *In situ* XANES/XAS Setup

To analyze *in situ* the electrocatalytic mechanism of ternary metallic spinel oxides under real working conditions, a custom-designed *in situ* XANES/XAS setup was fabricated to couple the electrochemical reaction with the XANES/XAS measurements. A schematic figure is shown in Figure 2.3A. The setup consists of two Teflon blocks, with a hole at the center of each of them. The holes are covered with Kapton film allowing X-rays to go through with minimal attenuation. The working electrode (WE) was made of carbon paper with catalysts loaded on its tip (1cm×1cm), and placed right between the two Kapton-covered holes. A graphite rod served as the counter electrode (CE) immersed in 1M NaOH electrolyte next to the WE. The reference electrode (RE, Ag/AgCl in saturated KCl) was connected to the cell by a salt bridge and the distance between the RE and the catalyst layer at the end tip of the carbon paper was minimized to reduce the IR drop. The thickness of the electrolyte layer between two Kapton films was near 100-200 μm, to guarantee that the X-ray can penetrate it and the signal can be collected by the detector downstream. A Teflon cap on the top fixed by four screws at the four corners to help maintain airtightness, while a gas inlet and a gas outlet were at two sides of the cap to saturate the electrolyte with Ar or O_2.

The reliability of the setup was tested by obtaining the cyclic voltammetric profiles of a trimetallic cubic spinel oxide for three successive cycles, shown in Figure 2.3B. There are essentially no difference between the CV obtained in the *in situ* analysis setup and a conventional electrochemical cell. Several redox couples can be observed in the CV with negligible degradation during the first 3 cycles. Detailed descriptions about the setup can be found in references 2 and 3.

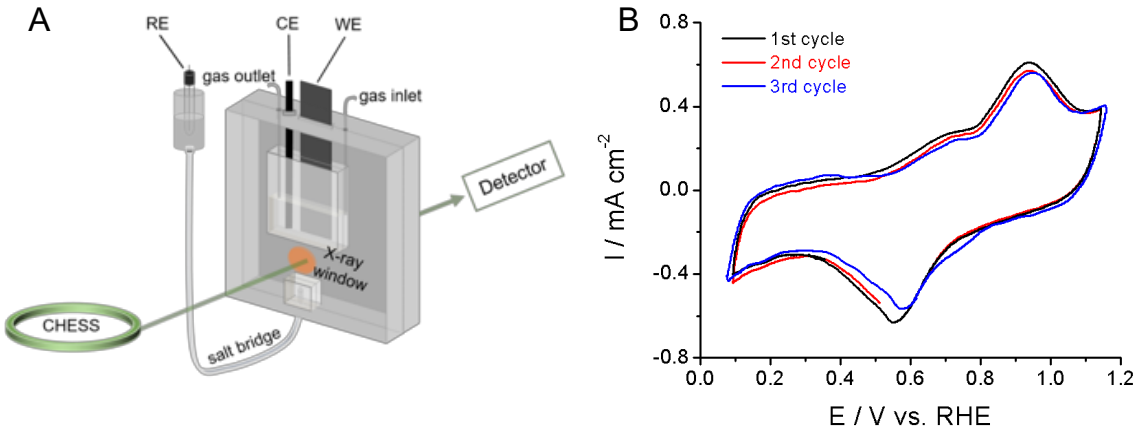

Figure 2.3 (A) Schematic of the *in situ* XANES/XAS electrochemical cell. Working electrode (WE, catalyst on carbon paper) and counter electrode (CE, carbon rod) were immersed in 1M KOH solution. Reference electrode (RE, Ag/AgCl in saturated KCl) was connected to the cell by a salt bridge and the distance between RE and catalysts at the end of the carbon paper was minimized to reduce IR drops caused by the resistance in the thin electrolyte layer ($\leq$ 200 μm) in the X-ray window. (B) Three cyclic voltammetry profiles that were collected during X-ray measurements for a trimetallic cubic spinel oxide. Figure reproduced from references 2 and 3.

2.3 Electrochemical Characterizations

2.3.1 Cyclic Voltammetry

For most materials, cyclic voltammetric profiles were obtained at 50 mV/s until the material subject to test was stabilized (typically 50 cycles) on the potential window of 0.05-1.1 V vs. RHE for precious-metal catalysts or 0.15-1.2 V vs. RHE for non-precious-metal catalysts, respectively. After the material exhibited a stable response, the cyclic voltammetric profiles was recorded at a rate of 20 mV/s for Pt-based catalysts to measure the electrochemical surface area (ECSA). The ECSA is calculated by integrating the area under the hydrogen adsorption region, between 0.05 to 0.4 V with a conversion factor of 200 μC cm^{-2} [4-5]. For non-precious-metal catalysts, like spinel oxides, the potential window was positively shifted by 0.1 V to 0.15-1.2 V vs. RHE to avoid the possible reduction of the metal oxides and keep the integrity of the crystal structure. For the bimetallic-organic-frameworks (BMOFs) derived carbon materials, the potential window was 0.05 -1.1 V. Due to the high surface area and pseudocapacity from the carbon support (carbon nanotubes for spinel oxides), the cyclic voltammetric profiles at 5 mV/s was also recorded to subtract the background signal when comparing the electrocatalytic activity.

There are two protocols used in the stability testing, one involved scanning between 0.05-1.0 V at 50 mV/s and the other involved scanning between 0.6-1.0 V at 100 mV/s. The second one is more practical since the cathodic reaction is always taking place at potentials higher than 0.6 V vs. RHE.

2.3.2 ORR Polarization Curves

RDE and RRDE experiments were performed to compare the ORR catalytic activity of different materials. Typically, the polarization curve was recorded over the potential

window between 0.2-1.1 V at a scan rate of 5 mV/s at a rotation rate of 1,600 rpm. There are two metrics used for comparison, one is the half-wave potential ($E_{1/2}$) and the other is the diffusion limiting current (I_d), where $E_{1/2}$ reflects the activity and I_d shows the selectivity of the reaction. For the ORR, the more positive the $E_{1/2}$ is, the more active the catalyst is and the enhancement in the mass/specific activity can be in an order of magnitude. Kinetic activities (I_k) can be calculated through the Koutecky–Levich equation, as below[6, 7]:

$$\frac{1}{I} = \frac{1}{I_k} + \frac{1}{I_d}$$

Here, I is the measured current density at different voltages, I_k is kinetic current density and I_d is the diffusion limited current density. The theoretical I_d should be equal to the value calculated from Levich equation:

$$I_d = 0.62nFAD^{2/3}\nu^{-1/6}\omega^{1/2}C_{O_2}$$

In this case, we assume that O_2 has been completely reduced to water via the 4-electron transfer route. However, if the measured diffusion limited current is obviously smaller than the theoretical value, RRDE experiments are required to identify the production of peroxide over the working potential window. The rotating Pt-ring GC-disk electrode was used with the catalyst ink dropped on the central disk and the potential scanned from 0.2 to 1.1 V. The potential of the ring is kept at 1.2 V, where any produced peroxide from the disk will be re-oxidized at the ring electrode. The average electron transfer number and the peroxide yield can be calculated with the equation below[8], where N is the collection efficiency of the electrode:

$$n\ (electron\ transfer\ number) = \frac{4I_d}{I_d + I_r/N}$$

$$\%H_2O_2\ (peroxide\ yield) = \frac{\frac{2I_r}{N}}{I_d + \frac{I_r}{N}} \times 100\%$$

The Pt-based system is well-established and always has a peroxide yield lower than a few percent at a catalyst loading of 20 μg/cm^2. For non-precious metal oxides, the higher the loading is, the lower the peroxide yield becomes due to the thicker catalyst layer rendering a higher possibility for them to be reduced by nearby sites rather than fleeing into the electrolyte[9]. Based on the report by Dodelet and Dahn, when the catalyst loading is high enough (>800 μg/cm^2), the peroxide yield could be controlled to be below 5%.

2.3.3 CO Stripping

The setup for CO stripping experiment is similar to the one for cyclic voltammetry and RDE experiments, except that the electrode is first dosed with CO, enabling a monolayer adsorption of CO molecules on the surface of the electrocatalysts. For Pt based catalysts, the dosing process is conducted at 0.05 V vs RHE for 10 mins while for Pd based materials, the dosing potential is fixed at 0.2 V vs RHE due to a stronger binding strength between Pd and CO. Subsequently, the bubbling gas is switched to Ar for 10-20 mins to remove any remaining CO dissolved in the electrolyte. The scan rate during CO stripping experiments can be varied from 5 to 50 mV/s over the potential range between 0.05 V to 1.2 V, with a conversion factor of 420 μC/cm^2 [10].

2.4 References

1. Xiong, Y.; Yang, Y.; Joress, H.; Padgett, E.; Gupta, U.; Yarlagadda, V.; Agyeman-Budu, D.; Huang, X.; Moylan, T.; Zeng, R.; Kongkanand, A.; Escobedo, F. A.; Brock,

J. D.; DiSalvo, F. J.; Muller, D. A.; Abruña, H. D., Revealing the atomic ordering of binary intermetallics using *in situ* heating techniques at multilength scales. *Proc. Natl. Acad. Sci.* **2019**, *116*, 1974-1983.

2. Yang, Y.; Wang, Y.; Xiong, Y.; Huang, X.; Shen, L.; Huang, R.; Wang, H.; Pastore, J.; Yu, S.; Xiao, L.; Brock, J. D.; Zhuang, L.; Abruña, H. D., *In situ* X-ray absorption spectroscopy of a synergistic Co-Mn oxide catalyst for the oxygen reduction reaction. *J. Am. Chem. Soc.* **2019**, 141, 1463-1466.
3. Xiong, Y.; Yang, Y.; Feng, X.; DiSalvo, F.; Abruña, H. A., Strategy for increasing the efficiency of the oxygen reduction reaction in Mn-doped cobalt ferrites. *J. Am. Chem. Soc.* **2019**, 141, 4412-4421.
4. Vidal-Iglesias, F. J.; Aran-Ais, R. M.; Solla-Gullon, J.; Herrero, E.; Feliu, J. M., Electrochemical characterization of shape-controlled Pt nanoparticles in different supporting electrolytes. *ACS Catal.* **2011**, 2, 901-910.
5. Chen, Q-S.; Solla-Gullon, J.; Sun, S-G.; Feliu, J. M., The potential of zero total charge of Pt nanoparticles and polycrystalline electrodes with different surface structure: The role of anion adsorption in fundamental electrocatalysis. *Electrochim. Acta.* 2010, 55, 7982-7994.
6. Bard, A. J.; Faulkner, L. R., Electrochemical methods: fundamentals and applications. New York: *J. Wiley and Sons*. **2010**, ISBN 0-471-04372-9.
7. Levich, V. G., Physicochemical hydrodynamics. Englewood Cliffs, N.J: Prentice-Hall. **1962**, ISBN 0136744400.
8. Chang, S.; Wang, C.; Du, H.; Hsu, H.; Kang, C.; Chen, C.; Wu, J.; Yen, S.; Huang,

W.; Chen, L., Vitalizing fuel cells with vitamins: pyrolyzed vitamin B12 as a non-precious catalyst for enhanced oxygen reduction reaction of polymer electrolyte fuel cells. *Energy Environ. Sci.* **2012**, *5*, 5305-5314.

9. Bonakdarpour, A.; Lefevre, M.; Yang, R.; Jaouen, F.; Dahn, T.; Dodelet, J.; Dahn, J., Impact of loading in RRDE experiments on Fe-N-C catalysts: two- or four-electron oxygen reduction?. *Electrochem. Solid State Lett.* **2008**, *11*, B105.
10. Shao, M.; Odell, J.; Choi, S.; Xia, Y., Electrochemical surface area measurements of platinum- and palladium-based nanoparticles. *Electrochem. Comm*. **2013**, 31, 46-48.

CHAPTER 3

HIGH-LOADING INTERMETALLIC PT3CO/C CORE-SHELL NANOPARTICLES AS ENHANCED ACTIVITY ELECTROCATALYSTS TOWARDS THE OXYGEN REDUCTION REACTION (ORR)

Reproduced from *Chem. Mater.* **2018**, 30, 5, 1532-1539

3.1 Abstract

A facile, seed-mediated, growth method and post-annealing treatment have been employed to synthesize a single-phase 40% mass-loading intermetallic Pt_3Co/Vulcan electrocatalyst, which can make the electrocatalytic layer thinner, thus lowering the mass transport resistance for the ORR in proton exchange membrane fuel cells (PEMFCs). These 40% Pt_3Co/C nanocatalysts exhibited superior kinetics towards the ORR, relative to a 20% Pt_3Co/C catalyst, and only showed a slight degradation in the half-wave potential and electrochemical surface area after a 4,000-cycle stability test. The high activity and stability are attributed to a stable intermetallic Pt_3Co core with a 2-3 atomic-layer-thick Pt-shell, as well as its good dispersion on the support. This seed-mediated growth approach and post-annealing treatment provide a new strategy to ensure single-phase formation and uniform particle size distribution for other high mass-loading binary intermetallic/alloy electrocatalyst systems and can contribute to the practical commercialization of PEMFCs, especially in high current density applications, like automotive.

3.2 Introduction

Proton exchange membrane fuel cells (PEMFCs) are regarded as one of the most promising energy conversion technologies owing to their high efficiency, of around 90%, and environmental sustainability. A significant hurdle that prevents the large-scale deployment of PEMFC stems from the oxygen reduction reaction (ORR) at the cathode, where the sluggish kinetics need to be addressed with carefully designed electrocatalysts.[1-3] Extensive studies have been carried out on Pt-based catalysts,

followed by investigations of Pt-M alloys in which M can be Fe, Cu, Cr, Co or other 3d transition metals, mostly emphasizing the Pt_3M stoichiometry (M=transition metal).[4-12] These alloys exhibit superior electrocatalytic activity compared to pure Pt, due to electronic modifications, as well as ligand and strain effects, which are known to weaken the adsorption strength of intermediate species, resulting in enhanced kinetics.[13] These materials also offer a cost advantage due to the high abundance of first row transition metals. There has also been some work on Pt-coated nanoparticles,[14-17]and nitrogen-doped non-precious metal catalysts, such as graphene and carbon nanotubes complexes.[18-20] Among all reported catalysts, Pt-Co and Pt-Ni alloys are generally regarded as having the highest electrocatalytic activity, especially in fuel cell applications requiring high current densities.

Previously, we reported on a family of Pt/Pt_3Co nanocatalysts, composed of a 2-3 atom thick Pt shell, and an ordered intermetallic Pt_3Co core, which exhibited exceptional electrocatalytic activity after high temperature annealing. However, the low loading of most state-of-the-art catalyst materials on carbonaceous support matrices, limits their practical application, especially at high current densities, where even for the best, Pt-based catalysts, around a 0.4 mg/cm^2 Pt loading is required. This usually results in a thick catalyst layer, which increases the mass transfer resistance and deteriorates MEA performance.[21] This dilemma could, in principle, be solved by using higher mass loadings, which would make the catalyst layer thinner and thus enhance mass transport. However, because of the enthalpies of mixing involved during the formation of ordered intermetallics, the synthesis process requires high-temperature treatments, especially for Pt_3Co, whose ordering temperature is above 700 ^oC. Electroactive nanoparticles tend to

undergo aggregation/sintering during high temperature annealing processes, forming large particles, thus lowering the specific surface area which, in turn, compromises electrocatalytic activity.

To prevent aggregation at high temperatures and obtain small particle sizes, Sun and coworkers used MgO as a protective coating during the synthesis of structurally disordered PtFe nanoparticles, and then employed a high temperature heat-treatment. After annealing, the MgO protective layer was dissolved in dilute nitric acid. This process yielded small, carbon supported, intermetallic fct-PtFe with small particle sizes.[22] Similarly, Hyeon and coworkers reported on the use of carbonized polydopamine as both, the carbon source, and protective layer. Dopamine has a strong affinity for metal atoms and prevents them from aggregating. It was polymerized on the pre-synthesized disordered PtFe nanoparticles and then annealed at 700^{o}C to carbonize the polydopamine and facilitate the conversion to the ordered fct-PtFe.[23] Lee and co-workers took advantage of the interaction between a metal precursor and a mesoporous aluminosilicate to suppress aggregation of nanoparticles.[24] They incorporated Pt-based nanoparticles on the surface of the ordered mesoporous aluminosilicate support, and used HF to remove the frame before electrochemical characterization. Alumina interacts strongly with Pt-group metals and induces a relatively small particle size and good dispersion of the loaded metal. It also limits aggregation during high temperature treatments/annealing.

However, most of the reported intermetallic nanoparticles used as electrocatalysts in fuel cells, employ a loading of 20 wt% on carbon supports. Significant aggregation has been observed when the metal mass loading is increased, since metal atoms have a strong affinity for each other and, thus, are more likely to agglomerate.

Herein, we report a facile, seed-mediated impregnation method to synthesize high loading (40%) Pt_3Co/C intermetallic electrocatalysts dispersed on a carbon matrix, effectively doubling the mass loading compared with state-of-the-art materials, without sacrificing its mass activity or specific activity.[25] One clear advantage of the method is the elimination of the need for energy-consuming filtering and washing procedures, making it suitable for large-scale production.[26] The use of seeds helps to obtain high dispersions at high metal mass loading.[27, 28] The high loading electrocatalysts are well-dispersed with no signs of particle segregation or phase separation, and offer exceptional electrocatalytic activity and durability, and represent attractive candidates for high current density operation.

3.3 Experimental Section

3.3.1 Sample Preparation

The 20% carbon supported Pt_3Co seeds were synthesized by the impregnation method we reported previously. Briefly, 46.5 mg (0.09 mmol) $H_2PtCl_6 \bullet 6H_2O$, 7.1 mg $CoCl_2 \bullet 6H_2O$ (0.03 mmol) were dissolved in 2 mL of deionized water and 77.3 mg of vulcan-72R support were dispersed in it. The suspension was ultrasonicated for 30 mins, and then evaporated by heating with magnetic stirring to form a smooth slurry. After leaving the as-obtained slurry overnight, the slurry was dried in an oven at 60°C. The black powder was gently ground in an agate mortar, and was subsequently placed in a flowing furnace at 300°C under H_2/N_2 for 2 hrs, then annealed at 600°C for 2 hrs. Finally, the product was cooled down under an N_2 atmosphere. 44 mg of the uniformly-distributed 20% Pt_3Co/C, synthesized before, were used as seed and added to 26.5 mg of H_2PtCl_6

and 4.1 mg of $CoCl_2 \bullet 6H_2O$, ultrasonicated for 15 mins to blend them, and gently heated to evaporate the solvent. The formed slurry was thick and smooth and was subsequently dried in an oven at 60°C. A free-flowing powder was obtained after grinding. It was subsequently transferred into a tube furnace and heated at 200 °C for 2 hrs, and then at 700 °C for another 2 hrs, both under H_2/N_2.

3.3.2 Structural Characterization

The crystal structure of the synthesized Pt_3Co/C was confirmed by XRD using a Rigaku Ultima VI X-ray diffractometer, measured from 10° to 90°. An FEI T12 - Spirit TEM was used to image the Pt_3Co/C nanoparticles, dispersed on carbon, before and after stability testing. Samples were thoroughly ultrasonicated in ethanol before being drop cast on carbon-laced copper grids. The accelerating voltage was 120 kV for bright field TEM imaging. Size distributions were obtained from TEM images using ImageJ software. Thermogravimetric analysis (TGA) was used to verify the intermetallic loading on the carbon matrix.

High-resolution TEM and SAED were performed using an FEI Tecnai F-20 operated at 200 kV. STEM images and elemental EELS maps were acquired on a fifth-order aberration-corrected STEM (Cornell Nion UltraSTEM) operated at 100kV with a beam convergence semi-angle of 30 mrad. Subångström resolution is achievable under such operating conditions.[29] Pt and Co maps were extracted using Co L-edge and Pt M-edge transitions as described in a previous publication.[30]

3.3.3 Electrochemical Characterization

Electrochemical measurements were performed in 0.1M $HClO_4$ on a Solartron electrochemical analyzer at room temperature. 5 mg of the 40% Pt_3Co intermetallic

catalyst were mixed with 2 mL of 0.05 wt% Nafion/ethanol solution and subsequently sonicated. 10 uL of the resulting catalyst ink were loaded onto a 5 mm glassy carbon electrode, followed by thermal evaporation of the solvent. A coiled Pt wire was used as the counter electrode and a Ag/AgCl, in saturated KCl, served as the reference electrode. ORR measurements were carried using a rotating disk electrode (RDE) in oxygen-saturated 0.1M $HClO_4$ solution at rotation rates from 100 rpm to 1600 rpm, and IR correction was performed based on the resistance of the RDE. The ORR profiles were obtained after 50 potential cycles in 0.1M $HClO_4$ over the potential range from 0.05 to 1.1 V at 50 mVs^{-1} to remove surface contamination. Cyclic voltammetry was performed to calculate the electrochemical surface area (ECSA), by integrating the charge under the hydrogen adsorption/desorption region from 0 V to +0.4 V. Durability tests were carried out by continuous scanning cyclic voltammetry for 2000 and 4000 cycles. ECSA measurements and ORR profiles were also obtained after cycling so as to evaluate stability. The intrinsic resistivity of Vulcan 72R, 20% Pt_3Co/C and 40% Pt_3Co/C were measured to be 0.033, 0.022 and 0.013 ohm•cm, respectively, via Cascade CP06 Four Point Probe Setup.

3.4 Results and Discussion

The synthesis route of the seed mediated growth of the 40% Pt_3Co/C intermetallic is schematically presented in Figure 3.1. The structure of the 20% Pt_3Co/C metal-loading seeds and final products were controlled by heat-treatment of the Pt_3Co/C alloys synthesized via an impregnation method at different temperatures in a forming gas (5% H_2 and 95% N_2) atmosphere. The X-ray diffraction (XRD) patterns of the 40% Pt_3Co/C

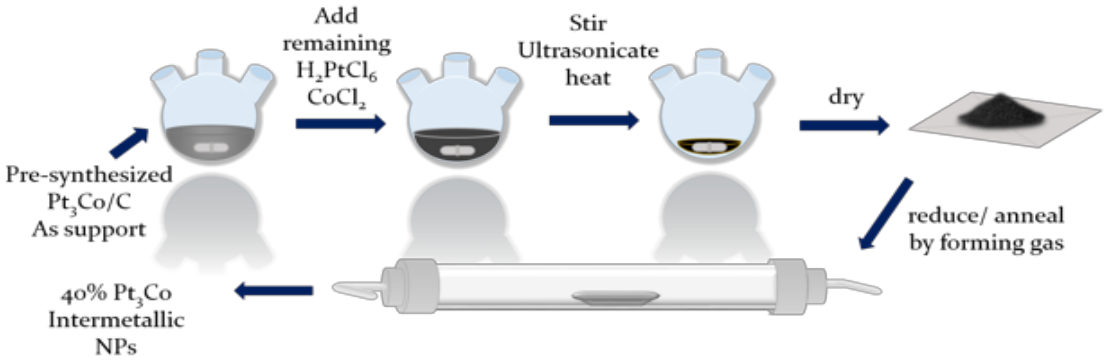

Figure 3.1 Schematic illustration of the synthesis procedure of the 40% Pt_3Co/C electrocatalyst.

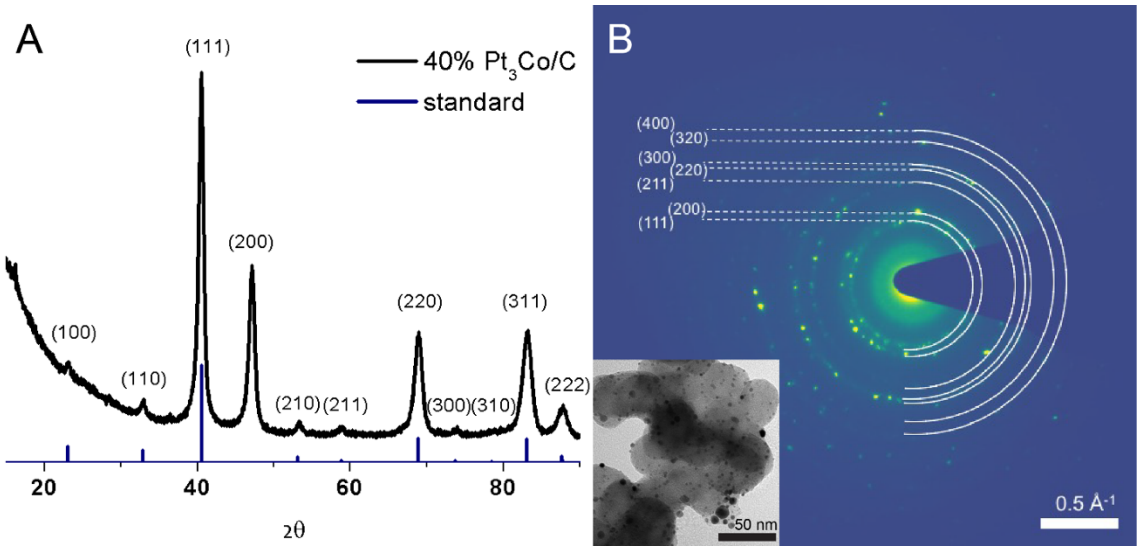

Figure 3.2 XRD and SAED patterns of 40% Pt_3Co/C. **(A)** XRD pattern of Pt_3Co/C compared with the standard Pt_3Co reflections (PDF card # 04-006-8057). **(B)** Selected area electron diffraction (SAED) of Pt_3Co/C nanoparticles in the inset.

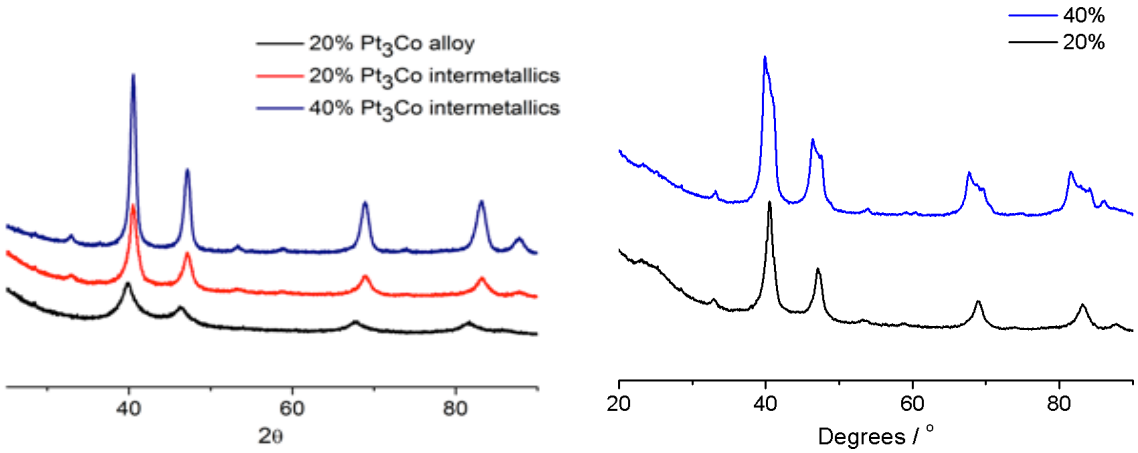

Figure 3.3 left: XRD pattern of 20% Pt_3Co/C alloy, intermetallics, and 40% Pt_3Co/C intermetallics prepared by seed-mediated growth method; right: 20% and 40% Pt_3Co/C nanoparticles prepared via conventional one-step impregnation method, after high-temperature annealing.

alloys and structurally ordered seeds, as well as that of a 20% loading intermetallic Pt_3Co/C product are shown in Figure 3.2A and Figure 3.3, respectively. The 20% mass loading sample, reduced at 300°C, exhibited the features typical of a face-centered cubic (fcc) lattice. As shown in Figure 3.2A, the 40% Pt_3Co/C sample exhibited the typical Pt face-centered cubic (fcc) structure, corresponding to (111), (200), (220) and (311) facets. The XRD peak positions are shifted to higher angles ((111) peak at 40.72°), relative to the standard Pt XRD ((111) at 39.76°, PDF # 00-004-0802), indicating that Co, with a smaller atomic radius, is incorporated into the Pt lattice to form an alloy with a resulting lattice contraction. After heat-treatment, the 20% and 40% intermetallic Pt_3Co/C samples exhibited pronounced (110) and (210) peaks, confirming the ordered structure of the Pt_3Co intermetallic phase (Figure 3.3). In contrast to materials prepared by the conventional one-step impregnation method at the same loading, which generally phase segregate (Figure S1), the 40% intermetallics from the seed-mediated growth method exhibited a single phase. Using the full-width at half-maximum (FWHM) of the (220) peak and the Debye-Scherrer equation, the average particle size of the 40% Pt_3Co/C sample was calculated to be 7.1 ± 0.8 nm, which is similar to that of the 20% Pt_3Co/C (6.5 ± 1 nm) shown in Figure 3.3. The selected area electron diffraction (SAED) pattern unambiguously established the crystal structure to be that of the 40% Pt_3Co/C (Figure 3.2B). The angular distribution of the diffraction spots of Pt_3Co/C, in reciprocal space, showed the existence of major facets, such as (111) and (200), as well as intermetallic facets, such as (211) and (300), which are all consistent with the XRD data. The successful synthesis of the 40% Pt_3Co/C intermetallic is attributed to the use of 20% Pt_3Co/C intermetallics as mediating seeds, which largely prevents the phase segregation

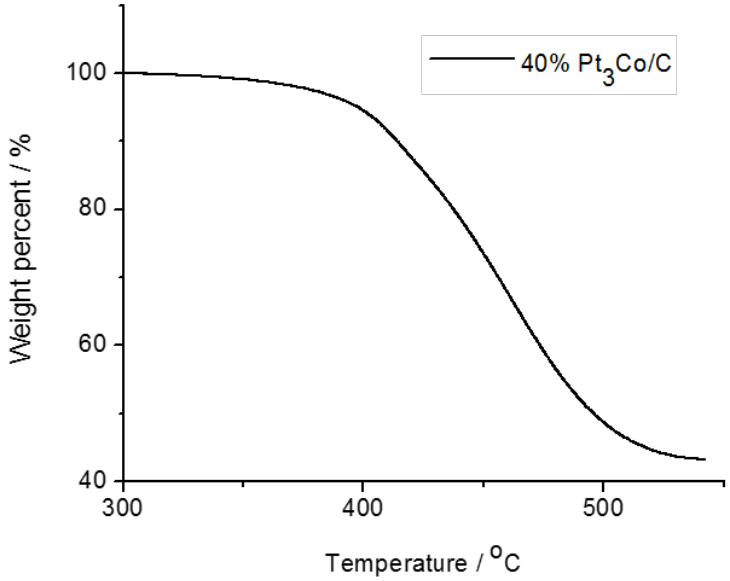

Figure 3.4 TGA of 40% Pt_3Co/C in N_2/O_2 (80% N_2 and 20% O_2) atmosphere.

Element	Series	Atom at. %	Weight wt. %
Cobalt	L-series	1.14	3.57
Platinum	M-series	3.42	35.49
Carbon	K-series	95.44	60.94

Table 3.1 EDX of Elemental information of Pt and Co

caused by the possible redistribution of impregnated species and lattice mismatch during the particle formation process, and also promotes the even distribution of the constituent metals, even after high temperature treatment. [31, 32]

The loading of the product was established by thermo gravimetric analysis (TGA) and energy-dispersive X-ray spectroscopy (EDX). As shown in Figure 3.4, the weight loss of a Pt_3Co/C nanocomposite sample, after being heated to 550°C, is attributed to both the removal of the carbon support and the oxidation of the metals. Assuming that all metals formed oxides, the theoretically determined remaining weight should be 47%, which is very close to the experimental result of 45% (43%). Table 3.1 shows that the atomic ratio of Pt to Co is 3:1 and that carbon represents around 60% of the total weight. These values are all consistent with expectation.

The chemical composition of the surface of the Pt_3Co nanoparticles was investigated using electron energy loss spectroscopy (EELS) employing an aberration-corrected STEM operated at 100 kV. The TEM image shows that most of the Pt_3Co particles are evenly distributed on the Vulcan carbon support, as shown in Figure 3.5. The narrow size distribution of the particles in Figure 3.5B, which was obtained from over 300 particles, exhibits an average particle size of around 5 nm in diameter, which is slightly smaller than the value calculated from XRD. XRD gives volumetric-weighted measurements, which may overestimate the geometric particle size.[33] The average particle size of the 40% Pt_3Co/C catalyst is comparable to that of the 20% Pt_3Co/C, as determined from TEM images in Figure 3.6 (about 4.5 nm from the histogram in Figure 3.7, statistics based on counting over 200 particles). This indicates that 40% Pt_3Co/C can be grown with small particle size and thus large electrochemical surface area, although the mass loading has

been doubled. Figures 3.5C and D present bright field (BF) and high angle annular dark field (HAADF) images of Pt_3Co/C acquired with a fifth-order aberration-corrected scanning transmission microscope (STEM) operated at 100 kV. Atomic-resolution BF and HAADF images of two 5 nm nanoparticles clearly show the (111) lattice spacing along the [000] zone axis.

The surface chemical composition of the Pt_3Co nanoparticles was explored using electron energy loss spectroscopy (EELS).[34] Figure 3.8A shows the atomic-scale HAADF-STEM image of a Pt_3Co nanoparticle. Figures 3.8B and 3.8C show the color mapping of the Pt (red) and Co (green) projected elemental distributions within the particle. The Pt (red) versus Co (green) composite image indicates that the Pt_3Co core (yellow) is surrounded by a thin pure Pt shell. The line profiles (Figure 3.8C) across the (111) facet in Figures 3.8B and 3.8C show that the Pt shell thickness is about 0.6 nm, or about 2-3 atomic layers. The image also shows that the outside of the Pt_3Co particles is decorated by a small amount of Co/CoO_x. This layer of Co/CoO_x, however, will not influence the electrochemical activity of Pt_3Co/C, since it will quickly dissolve under acidic conditions. The cyclic voltammetric (CV) profiles of 40% Pt_3Co/C were obtained in O_2-saturated 0.1M $HClO_4$ solution at various scan rates, from 5 mVs^{-1} to 50 mVs^{-1}(Figure 3.9A). Figure 3.9D shows the CV profiles of 20% and 40% intermetallic nanoparticles, evaluated at a scan rate of 20 mV s^{-1}. The electrochemically active surface area (ECSA) of the Pt_3Co/C catalysts was calculated by measuring the average charge in the H_{upd} adsorption/desorption region from 0-0.4V after double-layer correction, with a conversion factor of 200 μC cm^{-2} for the adsorption of a hydrogen monolayer.[35, 36] When normalized to the amount of Pt present on the catalyst layer, the 20% loading had a

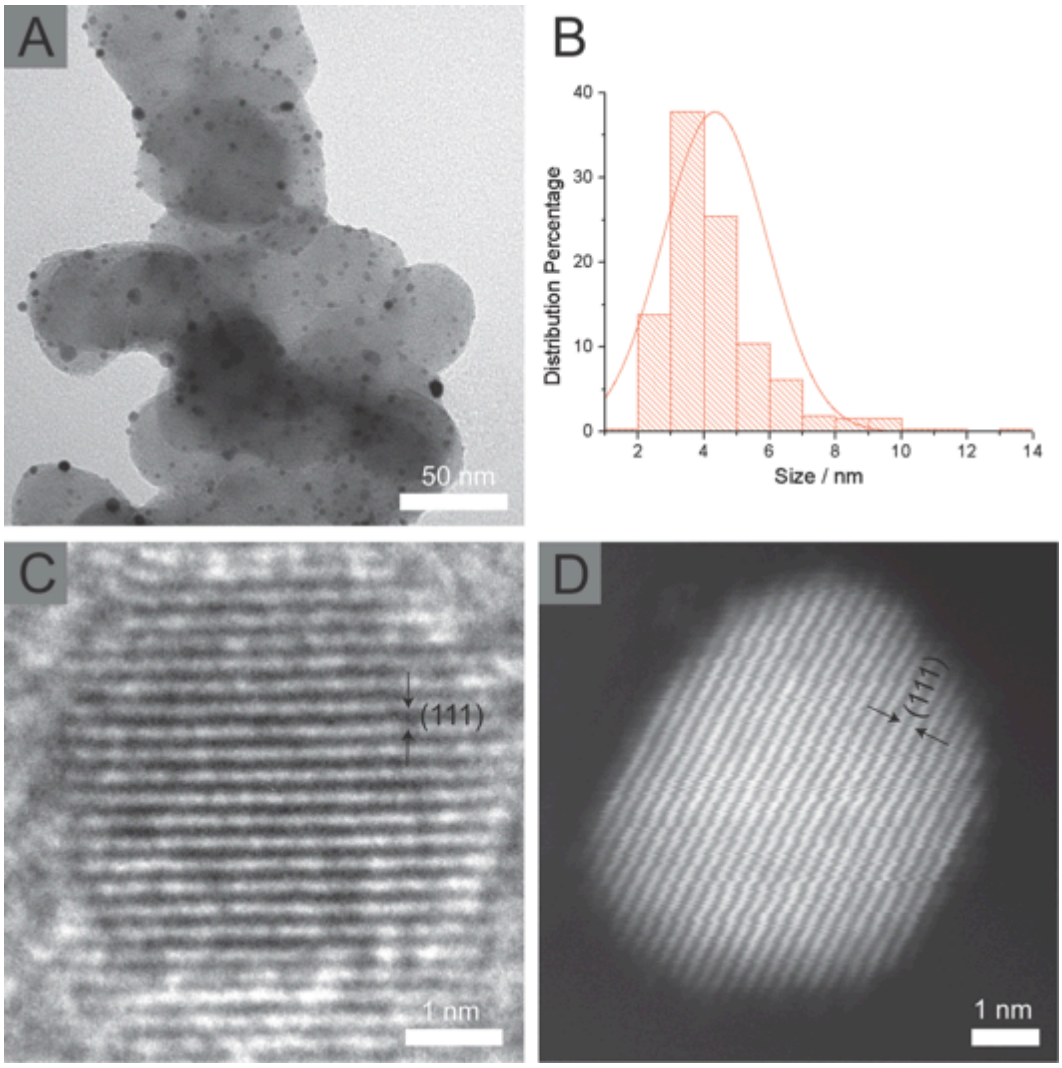

Figure 3.5 BF-TEM and HAADF-STEM images of 40% Pt_3Co/C. (A) BF-TEM image of Pt_3Co/C. (B) Particle size distribution of Pt_3Co nanoparticles in Figure 3.5A. (C, D) Atomic-resolution BF-TEM image (C) and HAADF-STEM image (D) of Pt_3Co/C with arrow marks indicating the (111) lattice spacing.

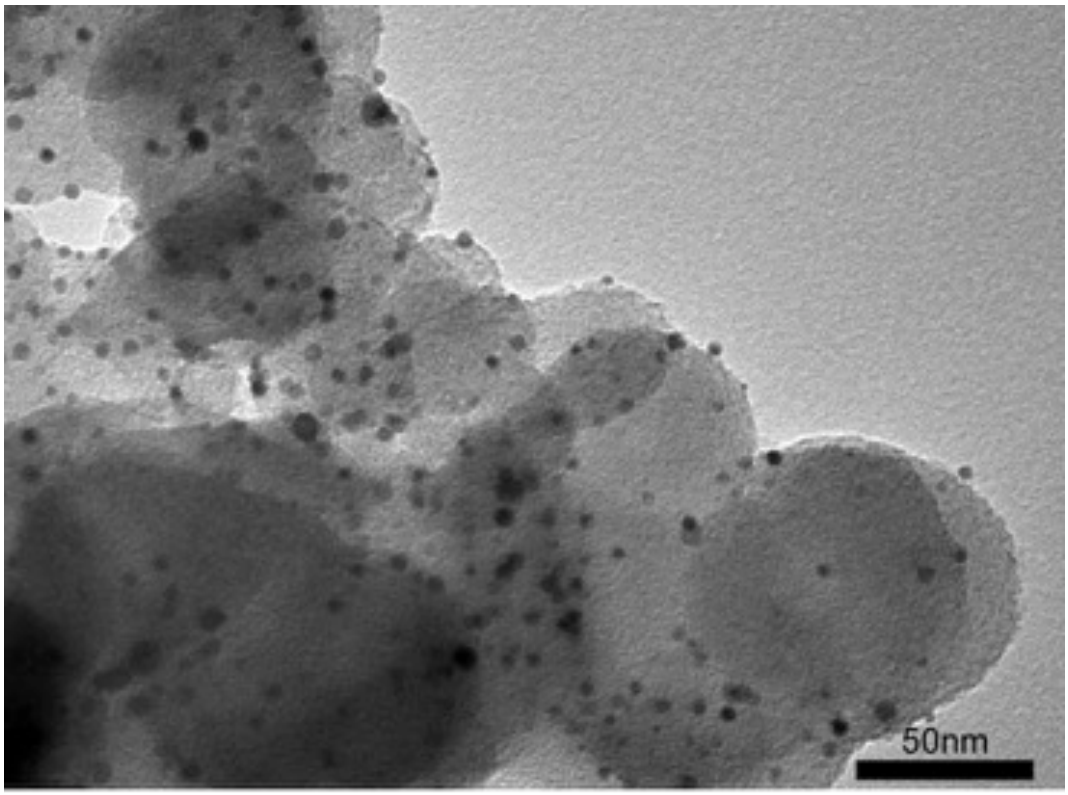

Figure 3.6 20% Pt_3Co/C intermetallic nanoparticles low-magnification TEM image.

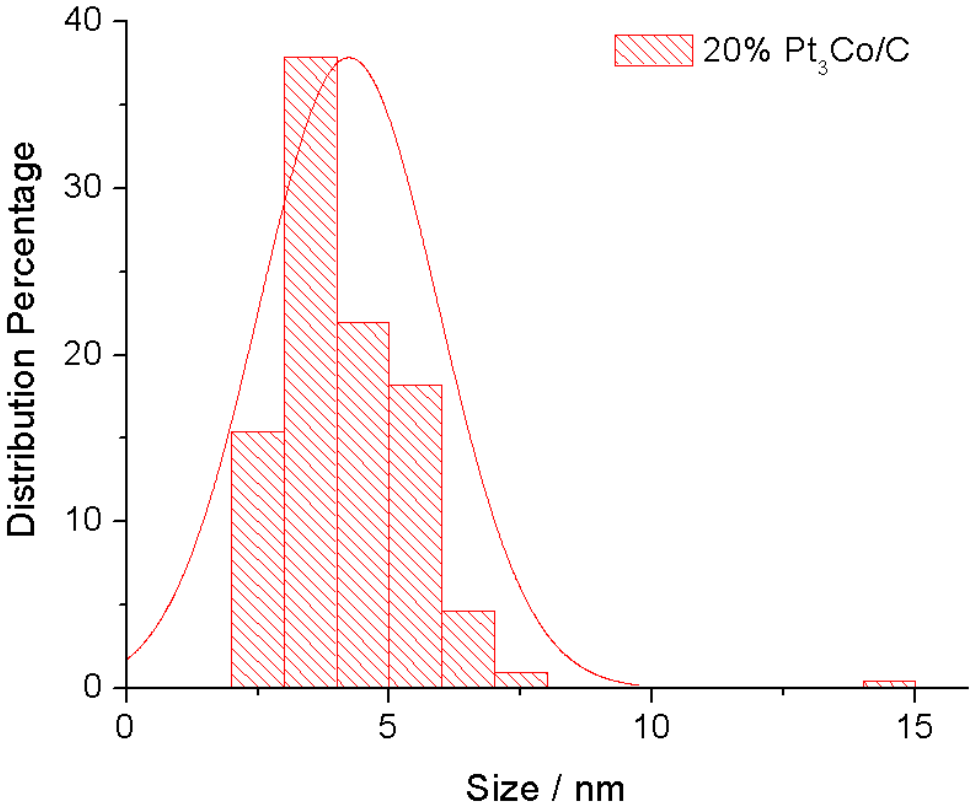

Figure 3.7 Particle size histogram of 20% Pt_3Co/C intermetallic nanoparticles.

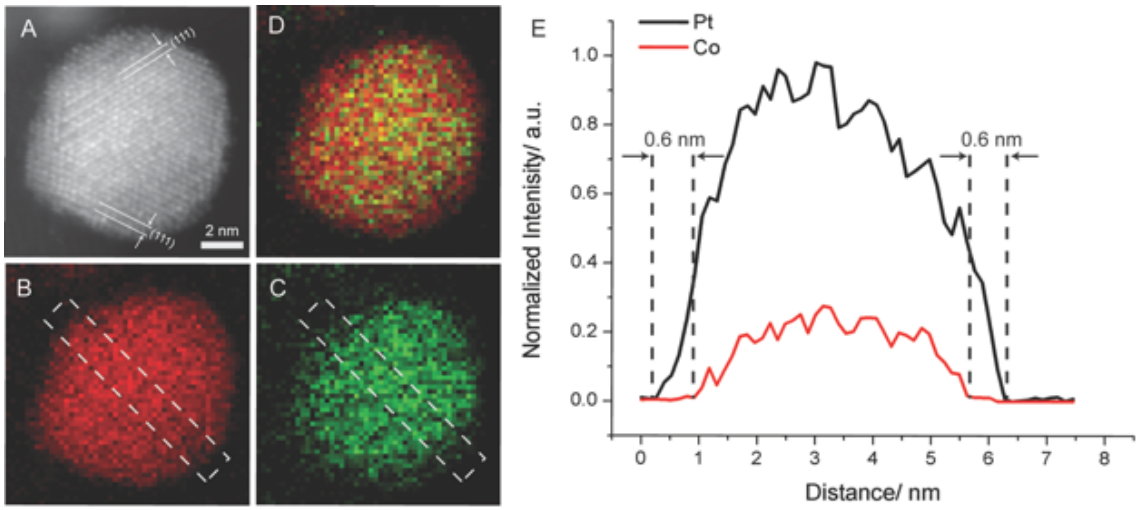

Figure 3.8 HAADF-STEM image of Pt_3Co/C and EELS elemental mapping of 40% Pt_3Co/C. (A) HAADF-STEM image of a Pt_3Co/C nanoparticle with parallel lines and arrow marks indicating (111) lattice spacing. (B-D) EELS maps of Pt (B), Co (C) and the composite Pt versus Co (D). (E) Line profiles extracted from the boxed areas in (B), (C) across the facet showing that the Pt shell is ~ 0.6 nm thick.

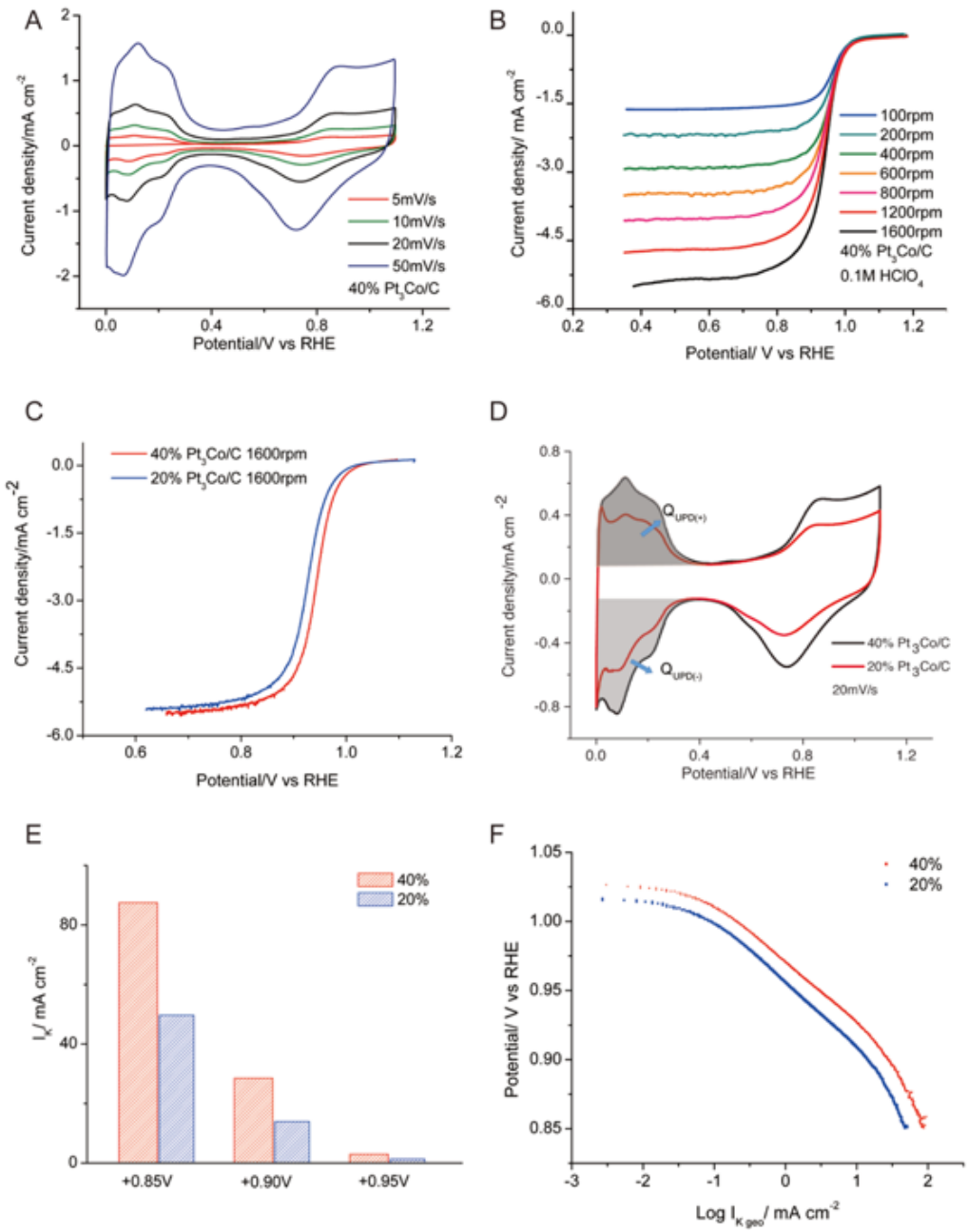

Figure 3.9 (A) Cyclic voltammetry at various scan rates of 40% Pt_3Co/C in 0.1M $HClO_4$. (B) RDE measurement of 40% Pt_3Co/C at various rotation rates. (C). Comparison of the RDE curves of 20% and 40% Pt_3Co/C at 1600rpm. (D) Cyclic voltammetry curve of 20% (red) and 40% (black) Pt_3Co/C electrocatalysts scanned at 20mV/s, with the shaded regions representing the ECSA of the catalyst. (E) Comparison of specific activities for

20% and 40% Pt_3Co/C at 0.85 V, 0.90 V, and 0.95 V, respectively, normalized to geometric area. (F) Intrinsic current density for 20% and 40% loading Pt_3Co/C electrocatalysts from RDE measurements at 1600 rpm, normalized to the geometric area.

slightly higher ECSA (ca 20%) than the 40% loading. However, they both exhibited virtually identical electrochemical activity when normalized to ECSA and mass (Figure 3.10).

The ORR activity and durability of the 20% and 40% intermetallic Pt_3Co/C catalysts were further investigated using RDE in 0.1 M $HClO_4$ at room temperature. All electrodes were conditioned before testing by cycling the potential from 0.05 V to 1.0 V at a rate of 50 mVs^{-1} to remove any surface contamination. Figure 3.9B presents the ORR polarization curves of a 40% Pt_3Co/C intermetallic catalyst at various rotation rates ranging from 100 to 1600 rpm. The current exhibits kinetic control at the most positive potentials. At more-negative potentials, as anticipated, the current eventually becomes controlled by mass transport. The current density reached 5.6 mA cm^{-2} in the diffusion-limited region, which is a typical value for the $4e^-$ reduction of oxygen in 0.1M $HClO_4$ saturated with O_2 at 1600 rpm based on the Levich equation.[37] The current onset potential for the 40% intermetallic Pt_3Co/C catalyst was ~1.07 V, and the half-wave potential was ~0.943V, around 17 mV higher than that of the 20% material, as shown in Figure 3.9C, indicating its high electrocatalytic activity. This catalyst is among the best reported ORR catalysts in acid media.[38-43] The kinetic current (I_k) was calculated using the Koutecky−Levich equation $\frac{1}{I} = \frac{1}{I_k} + \frac{1}{I_d}$, where I is the measured current, I_d is the diffusion-limited current and I_k is the kinetic current. I_k values for the 20% and 40% intermetallic nanoparticles were then normalized to the geometric area of the catalyst and presented in Figure 3.9F. The kinetic current of the 40% Pt_3Co/C nanoparticles was about 2 times that of the 20% Pt_3Co/C catalyst over the active voltage range. Figure 3.9E compares the specific activity normalized to geometric area for the 20% and the 40%

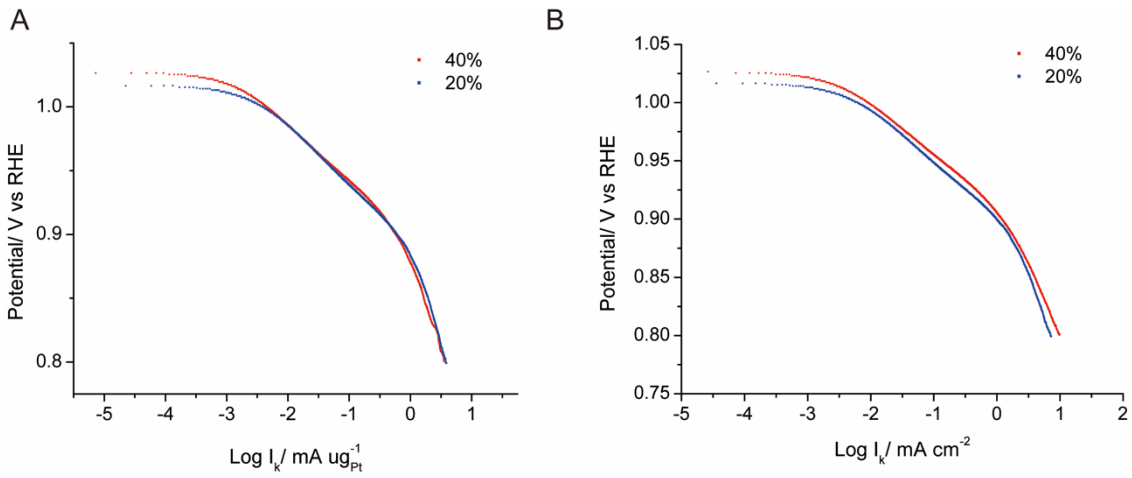

Figure 3.10 (A) Mass activity normalized to Pt weight of 20% and 40% Pt_3Co/C (B) Specific activity normalized to ECSA of 20% and 40% Pt_3Co/C.

Pt_3Co/C at various potentials indicating inherently higher activity of the 40% Pt_3Co/C material as catalyst. In addition, Figure 3.10 indicates that the mass activity, normalized to both Pt mass and ECSA, are around the same for the 20% and 40% Pt_3Co/C intermetallic materials, despite the fact that the average particle size is larger for the latter, which suggests that the excellent electrochemical performance of the 40% Pt_3Co catalyst can be largely attributed to its controlled single-phase intermetallic structure with a Pt-rich shell, and the high ECSA coming from the lattice contraction and uniform distribution of nanocatalysts. At 0.9V vs RHE, as is shown in Figure 3.10B, the normal cathode working potential, its mass activity is 0.51 mA/ug_{Pt} and specific activity is $1.1mA/cm^2_{Pt,}$ demonstrating its high catalytic activity, even at such a high metal loading. This property makes this material especially promising for high current density MEA applications since it helps decrease the catalyst layer thickness, promoting O_2 diffusion in the ORR process while maintaining the high intrinsic electrocatalytic activity [42, 44, 45]

The stability/durability of the high-loading Pt_3Co/C intermetallic electrocatalyst was evaluated by potential cycling between 0.05V and 1V at $50mVs^{-1}$ in 0.1M $HClO_4$ solution under an N_2 atmosphere. The cyclic voltammetric profiles of the 20% and 40% Pt_3Co/C obtained after 2,000 and 4,000 cycles are shown in Figure 3.11A. The ECSA was calculated by taking the average of the integrated area of the hydrogen adsorption and desorption regions, from 0.05V to 0.4V, as reported in Table 3.2. With continued cycling, the 40% intermetallic nanoparticles still yield well-defined hydrogen adsorption/desorption peaks, which are the characteristic features of the Pt skin. After 2,000 cycles, it maintained around 99% of its initial surface area and 97% after 4,000 cycles. Such high durability can be ascribed to the Pt-rich shell and the stable Pt_3Co

intermetallic core as supported by STEM-EELS mapping. For the 20% intermetallic nanoparticles, Figure 3.12 shows the cyclic voltammetry curves during the cycling process. The ECSA was calculated from the integrated charge between 0.05V to 0.4V vs RHE, which is always used for 20% Pt-based catalysts, to avoid the influence of the hydrogen evolution reaction. The 20% Pt_3Co/C catalyst maintained 98.4% of its ECSA after the first 2,000 cycles and 95.3% after 4,000 cycles. Both materials showed highly stable behavior during electrochemical cycling processes.

After 4,000 cycles, RDE measurements were conducted and are shown in Figure 3.11B. There is negative shift in the half wave potential of around 25mV, which may come from the detachment and aggregation of the catalyst. However, after stability testing, the 40% loading catalyst still exhibited an electrocatalytic activity that was comparable to that exhibited by the 20% loading state-of-art catalyst. The geometric current density at 0.95 V was measured before and after the stability test, as shown in Table 3.2. For better comparison, the 20% and 40% Pt/C have been tested under the same conditions, as shown in Figure 3.13 (about 38 mV negative shift in half-wave potential), which support the conclusion that the Pt_3Co/C intermetallics exhibit better stability. Figure 3.11C shows the TEM image of the catalyst after long-term operation, and the particle size histogram, based on over 200 particles, is presented in Figure 3.11D. After stability testing, there is some aggregation taking place. The peak position in the histogram has shifted slightly to larger values with the average nanoparticle size being about 7-8 nm. However, the particles remain evenly distributed on the carbon support.

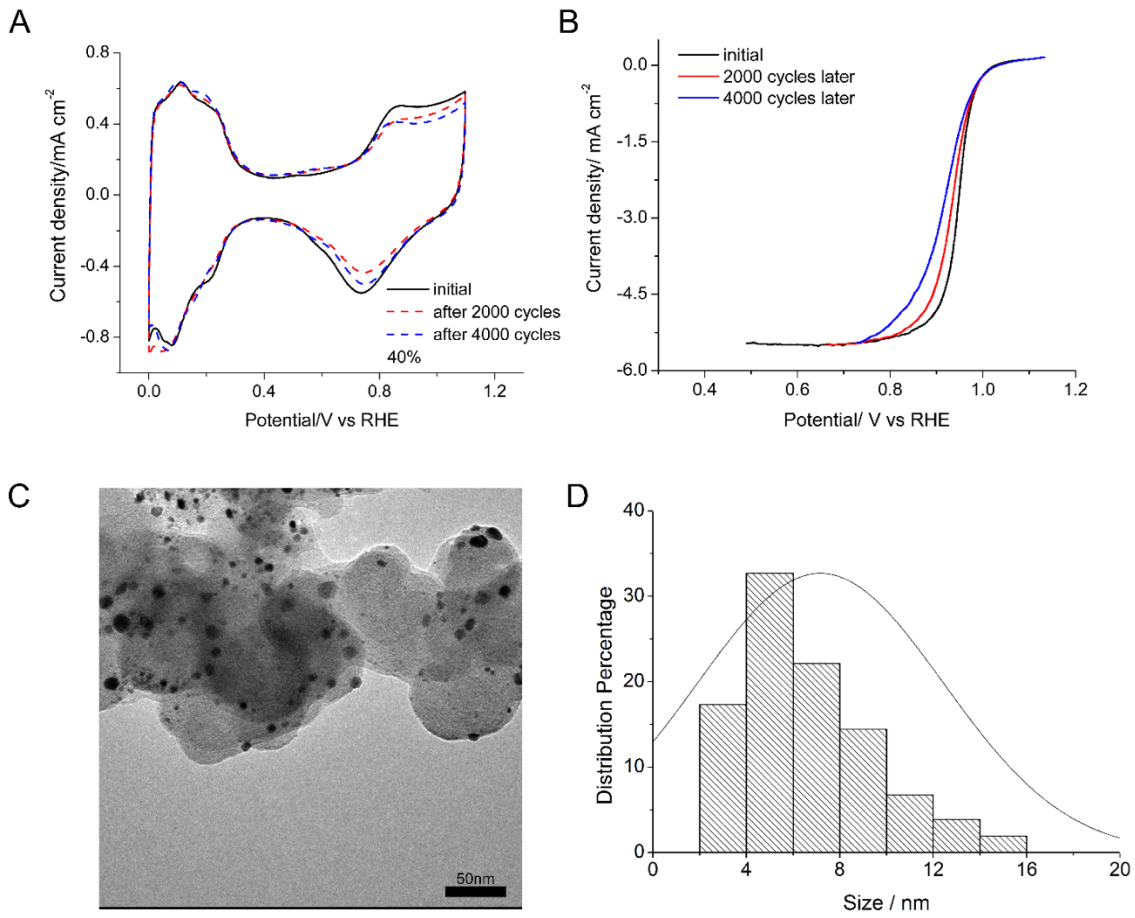

Figure 3.11 (A) Cyclic voltammetry of 40% Pt_3Co/C before cycling, after 2000 cycles, and 4000 cycles, respectively. (B) RDE curves for 40% Pt_3Co/C before cycling, after 2000 cycles, and 4000 cycles, respectively (C) TEM image of 40% Pt_3Co/C after 4000 cycles in the stability test. (D) Size distribution histogram of 40% Pt_3Co/C after stability testing.

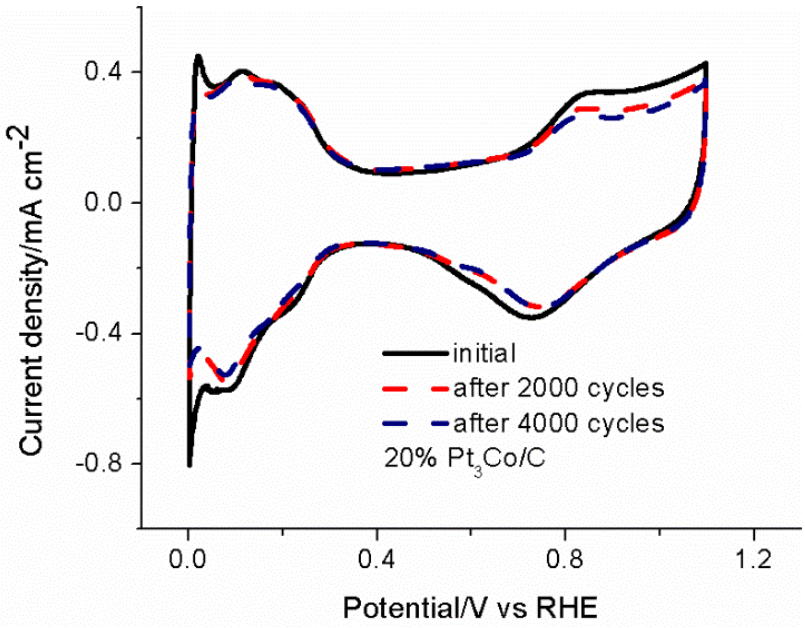

Figure 3.12 Cyclic voltammetry of 20% Pt_3Co/C during stability test after 2000 and 4000 cycles.

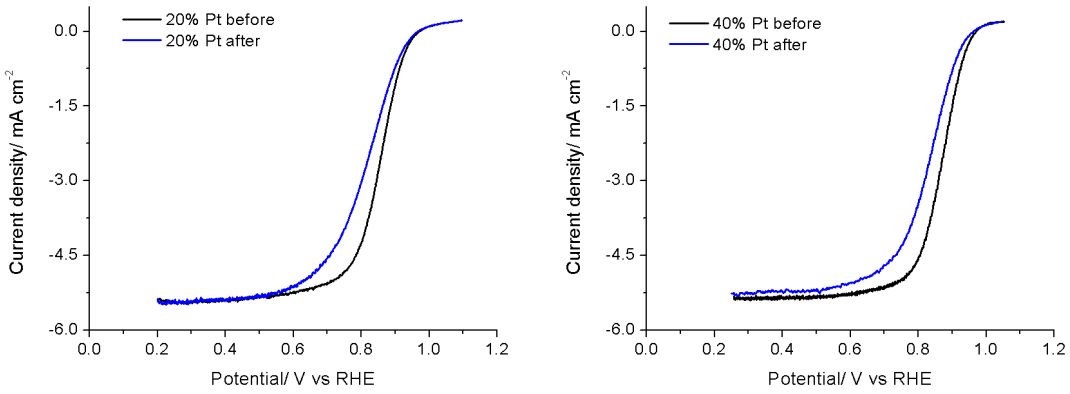

Figure 3.13 RDE profiles of 20% Pt/C and 40% Pt/C before and after stability test.

		20% Pt_3Co/C	40% Pt_3Co/C
ECSA (m^2/g_{Pt})	before	61	51
	after	58	49
Geometric current density at 0.95V (mA/cm_{geo}^2)	before	1.33	2.94
	after	0.7	1.43

Table 3.2 ECSA and geometric current density of 20% and 40% Pt_3Co/C before and after stability test

3.5 Conclusion

In summary, a 40% mass-loading core-shell intermetallic Pt_3Co/C has been successfu lly synthesized through a seed-mediated impregnation approach using a 20% Pt_3Co/C in termetallic as the seed. The 40% Pt_3Co/C was able to maintain the single-phase intermet allic structure despite the high mass loading and showed superior ORR activity when co mpared to a 20% Pt_3Co/C catalyst. It also exhibited high durability with minimal degrad ation after 4,000 cycles. The high activity and durability of Pt_3Co/C are ascribed to the s table intermetallic Pt_3Co core with 2-3 atomic-layers Pt shell, even at high metal loadin g. These results highlight the promising application of high loading intermetallic nanopa rticles for high current density PEM fuel cell applications, and possible extension of the seed-mediated approach to other binary intermetallic systems.

3.6 References

1. Gasteiger, H. & Markovic, N. M. Just A Dream-or Future Reality? *Science* **2009**, 324, 48–49.
2. Greeley, J.; Stephens, I.; Bondarenko, A.; Johansson, T.; Hansen, H.; Jaramillo, T.; Rossmeisl, J.; Chorkendorff, I.; Nørskov, J. Alloys of Platinum and Early Transition Metals as Oxygen Reduction Electrocatalysts, *Nat. Chem.* **2009**, *1*, 552-556.
3. Debe, M. Electrocatalyst Approaches and Challenges for Automotive Fuel Cells. *Nature* **2012**, *486*, 43-51.
4. Antolini, E.; Salgado, J.; Gonzalez, E. The Stability of Pt–M (M = First Row Transition Metal) Alloy Catalysts and Its Effect on the Activity in Low

Temperature Fuel Cells—A Literature Review and Tests on A Pt–Co Catalyst. *J. Power Sources* **2006**, *160*, 957-968.

5. Cui, Z.; Chen, H.; Zhao, M.; DiSalvo, F. High-Performance Pd3Pb Intermetallic Catalyst for Electrochemical Oxygen Reduction. *Nano Lett.* **2016**, 16, 2560-2566.
6. Yano, H.; Kataoka, M.; Yamashita, H.; Uchida, H.; Watanabe, M. Oxygen Reduction Activity of Carbon-Supported Pt–M (M = V, Ni, Cr, Co, and Fe) Alloys Prepared by Nanocapsule Method. *Langmuir* **2007**, *23*, 6438-6445.
7. Venkateswara Rao, C.; Viswanathan, B. ORR Activity and Direct Ethanol Fuel Cell Performance of Carbon-Supported Pt–M (M = Fe, Co, and Cr) Alloys Prepared by Polyol Reduction Method. *J. Phys. Chem. C* **2009**, *113*, 18907-18913.
8. Malheiro, A.; Perez, J.; Villullas, H. Well-Alloyed PtFe/C Nanocatalysts of Controlled Composition and Same Particle Size: Oxygen Reduction and Methanol Tolerance. *J. Electrochem. Soc.* **2009**, 156, B51-B58.
9. Kim, J.; Lee, Y.; Sun, S. Structurally Ordered FePt Nanoparticles and Their Enhanced Catalysis for Oxygen Reduction Reaction. *J. Am. Chem. Soc.* **2010**, *132*, 4996-4997.
10. Mani, P.; Srivastava, R.; Strasser, P. Dealloyed Pt-Cu Core–Shell Nanoparticle Electrocatalysts for Use in PEM Fuel Fell Cathodes. *J. Phys. Chem. C* **2008**, *112*, 2770-2778.
11. Stephens, I.; Bondarenko, A.; Grønbjerg, U.; Rossmeisl, J.; Chorkendorff, I. Understanding the Electrocatalysis of Oxygen Reduction on Platinum and Its

Alloys. *Energ. Environ. Sci.* **2012**, *5*, 6744.

12. Stamenkovic, V.; Mun, B.; Arenz, M.; Mayrhofer, K.; Lucas, C.; Wang, G.; Ross, P.; Markovic, N. Trends in Electrocatalysis on Extended and Nanoscale Pt-Bimetallic Alloy surfaces. *Nat. Mat.* **2007**, *6*, 241-247.
13. Escudero-Escribano, M.; Verdaguer-Casadevall, A.; Malacrida, P.; Grønbjerg, U.; Knudsen, B.; Jepsen, A.; Rossmeisl, J.; Stephens, I.; Chorkendorff, I. Pt5Gd as Highly Active and Stable Catalyst for Oxygen Electroreduction. *J. Am. Chem. Soc.* **2012**, *134*, 16476-16479.
14. Wang, J.; Inada, H.; Wu, L.; Zhu, Y.; Choi, Y.; Liu, P.; Zhou, W.; Adzic, R. Oxygen Reduction on Well-Defined Core–Shell Nanocatalysts: Particle Size, Facet, and Pt Shell Thickness Effects. *J. Am. Chem. Soc.* **2009**, *131*, 17298-17302.
15. Gong, K.; Su, D.; Adzic, R. Platinum-Monolayer Shell on $AuNi_{0.5}Fe$ Nanoparticle Core Electrocatalyst with High Activity and Stability for the Oxygen Reduction Reaction. *J. Am. Chem. Soc.* **2010**, *132*, 14364-14366.
16. Wang, G.; Huang, B.; Xiao, L.; Ren, Z.; Chen, H.; Wang, D.; Abruña, H.; Lu, J.; Zhuang, L. Pt Skin On AuCu Intermetallic Substrate: A Strategy to Maximize Pt Utilization for Fuel Cells. *J. Am. Chem. Soc.* **2014**, *136*, 9643-9649.
17. Wang, D.; Xin, H.; Yu, Y.; Wang, H.; Rus, E.; Muller, D.; Abruña, H. Pt-Decorated PdCo@Pd/C Core−Shell Nanoparticles with Enhanced Stability and Electrocatalytic Activity for the Oxygen Reduction Reaction. *J. Am. Chem. Soc.* **2010**, *132*, 17664-17666.

18. Chung, H.; Cullen, D.; Higgins, D.; Sneed, B.; Holby, E.; More, K.; Zelenay, P. Direct Atomic-Level Insight into the Active Sites of A High-Performance PGM-Free ORR Catalyst. *Science* **2017**, *357*, 479-484.
19. Wang, Q.; Zhou, Z.; Lai, Y.; You, Y.; Liu, J.; Wu, X.; Terefe, E.; Chen, C.; Song, L.; Rauf, M.; Tian, N.; Sun, S. Phenylenediamine-Based FeN_x/C Catalyst with High Activity for Oxygen Reduction in Acid Medium and Its Active-Site Probing. *J. Am. Chem. Soc.* **2014**, *136*, 10882-10885.
20. Lin, L.; Zhu, Q.; Xu, A. Noble-Metal-Free Fe–N/C Catalyst for Highly Efficient Oxygen Reduction Reaction Under Both Alkaline and Acidic Conditions. *J. Am. Chem. Soc.* **2014**, *136*, 11027-11033.
21. Qi, Z.; Kaufman, A. Low Pt Loading High Performance Cathodes for PEM Fuel Cell. *J. Power Sources* **2003**, *113*, 37-43.
22. Li, Q.; Wu, L.; Wu, G.; Su, D.; Lv, H.; Zhang, S.; Zhu, W.; Casimir, A.; Zhu, H.; Mendoza-Garcia, A.; Sun, S. New Approach to Fully Ordered Fct-FePt Nanoparticles for Much Enhanced Electrocatalysis in Acid. *Nano Lett.* **2015**, *15*, 2468-2473.
23. Chung, D.; Jun, S.; Yoon, G.; Kwon, S.; Shin, D.; Seo, P.; Yoo, J.; Shin, H.; Chung, Y.; Kim, H.; Mun, B.; Lee, K.; Lee, N.; Yoo, S.; Lim, D.; Kang, K.; Sung, Y.; Hyeon, T. Highly Durable and Active Ptfe Nanocatalyst for Electrochemical Oxygen Reduction Reaction. *J. Am. Chem. Soc.* **2015**, *137*, 15478-15485.
24. Mun, Y.; Shim, J.; Kim, K.; Han, J.; Kim, S.; Ye, Y.; Hwang, J.; Lee, S.; Jang, J.; Kim, Y.; Lee, J. Direct Access to Aggregation-Free and Small Intermetallic

Nanoparticles In Ordered, Large-Pore Mesoporous Carbon For An Electrocatalyst. *RSC Adv.* **2016**, *6*, 88255-88264.

25. Wang, D.; Xin, H.; Hovden, R.; Wang, H.; Yu, Y.; Muller, D.; DiSalvo, F.; Abruña, H. Structurally Ordered Intermetallic Platinum–Cobalt Core–Shell Nanoparticles with Enhanced Activity and Stability as Oxygen Reduction Electrocatalysts. *Nat. Mat.* **2013**, *12*, 81-87.
26. McNicol, B.; Rand, D.; Williams, K. Direct Methanol–Air Fuel Cells for Road transportation. *J. Power Sources* **1999**, *83*, 15-31.
27. Watzky, M.; Finke, R. A New Mechanism When Hydrogen Is the Reductant: Slow, Continuous Nucleation and Fast Autocatalytic Surface Growth. *J. Am. Chem. Soc.* **1997**, *119*, 10382-10400.
28. Chayen, NE. Methods for Separating Nucleation and Growth in Protein Crystallisation. *Prog. Biophys. Mol. Bio.* **2005**, *88*, 329-337.
29. Huang, P.; Ruiz-Vargas, C.; van der Zande, A.; Whitney, W.; Levendorf, M.; Kevek, J.; Garg, S.; Alden, J.; Hustedt, C.; Zhu, Y.; Park, J.; McEuen, P.; Muller, D. Grains and Grain Boundaries in Single-Layer Graphene Atomic Patchwork Quilts. *Nature* **2011**, *469*, 389-392.
30. Xin, H.; Mundy, J.; Liu, Z.; Cabezas, R.; Hovden, R.; Kourkoutis, L.; Zhang, J.; Subramanian, N.; Makharia, R.; Wagner, F.; Muller, D. Atomic-Resolution Spectroscopic Imaging of Ensembles of Nanocatalyst Particles Across the Life of a Fuel Cell. *Nano Lett.* **2012**, *12*, 490-497.
31. Niu, W.; Zhang, L.; Xu, G. Seed-Mediated Growth of Noble Metal Nanocrystals: Crystal Growth and Shape Control. *Nanoscale* **2013**, *5*, 3172-

3181.

32. Cacciuto, A.; Auer, S.; Frenkel, D. Onset of Heterogeneous Crystal Nucleation in Colloidal Suspensions. *Nature* **2004**, *428*, 404-406.
33. Warren, R. X-Ray Diffraction, Dover: New York, 1990.
34. Muller, D.; Kourkoutis, L.; Murfitt, M.; Song, J.; Hwang, H.; Silcox, J.; Dellby, N.; Krivanek, O. Atomic-Scale Chemical Imaging of Composition and Bonding by Aberration-Corrected Microscopy. *Science* **2008**, *14*, 132-133.
35. Chen, Q.; Solla-Gullón, J.; Sun, S.; Feliu, J. The Potential of Zero Total Charge of Pt Nanoparticles and Polycrystalline Electrodes with Different Surface Structure: The role of Anion Adsorption in Fundamental Electrocatalysis. *Electrochim. Acta.* **2010**, *55*, 7982-7994.
36. Vidal-Iglesias, F.; Arán-Ais, R.; Solla-Gullón, J.; Herrero, E.; Feliu, J. Electrochemical Characterization of Shape-Controlled Pt Nanoparticles in Different Supporting Electrolytes. *ACS Catal.* **2012**, *2*, 901-910.
37. Bard, A. J. & Faulkner L. R. Electrochemical Methods: Fundamentals and Applications, Wiley: New York, 2001.
38. Watanabe, M.; Tsurumi, K.; Mizukami, T.; Nakamura, T.; Stonehart, P. Activity and Stability of Ordered and Disordered CoPt Alloys for Phosphoric Acid Fuel Cells. *J. Electrochem. Soc.* **1994**, *141*, 2659-2668.
39. Wang, D.; Yu, Y.; Xin, H.; Hovden, R.; Ercius, P.; Mundy, J.; Chen, H.; Richard, J.; Muller, D.; DiSalvo, F.; Abruña, H. Tuning Oxygen Reduction Reaction Activity via Controllable Dealloying: A Model Study of Ordered Cu_3Pt/C Intermetallic Nanocatalysts. *Nano Lett.* **2012**, *12*, 5230-5238.

40. Seo, S.; Joh, H.; Kim, H.; Moon, S. Properties of Pt/C Catalyst Modified by Chemical Vapor Deposition of Cr as A Cathode of Phosphoric Acid Fuel Cell. *Electrochim Acta.* **2006**, *52*, 1676-1682.
41. Jeon, M.; McGinn, P. Co-alloying Effect of Co and Cr with Pt for Oxygen Electro-Reduction Reaction. *Electrochim. Acta.* **2012**, *64*, 147-153.
42. Cui, Z.; Chen, H.; Zhou, W.; Zhao, M.; DiSalvo, F. Structurally Ordered Pt3Cr as Oxygen Reduction Electrocatalyst: Ordering Control and Origin of Enhanced Stability. *Chem. Mat.* **2015**, *27*, 7538-7545.
43. Yang, H.; Alonso-Vante, N.; Léger, J.; Lamy, C. Tailoring, Structure, and Activity of Carbon-Supported Nanosized Pt-Cr Alloy Electrocatalysts for Oxygen Reduction in Pure and Methanol-Containing Electrolytes. *J. Phys. Chem. B* **2004**, *108*, 1938-1947.
44. Mukerjee, S.; Srinivasan, S. Enhanced Electrocatalysis of Oxygen Reduction on Platinum Alloys in Proton Exchange Membrane Fuel Cells. *J. Electroanal. Chem.* **1993**, *357*, 201-224.
45. Colón-Mercado, H.; Popov, B. Stability of Platinum Based Alloy Cathode Catalysts in PEM Fuel Cells. *J. Power Sources* **2006**, *155*, 253-263.

CHAPTER 4

PT-DECORATED COMPOSITION-TUNABLE PD-FE@PD/C CORE-SHELL NANOPARTICLES WITH ENHANCED ELECTROCATALYTIC ACTIVITY TOWARDS THE OXYGEN REDUCTION REACTION

Reproduced from *J. Am. Chem. Soc.* **2018**, 140, 23, 7248-7255

4.1 Abstract

Design of electrocatalysts with both a high-Pt-utilization efficiency and enhanced electrochemical activity is still the key challenge in the development of proton exchange membrane fuel cells. In the present work, Pd-Fe/C bimetallic nanoparticles (NPs) with an optimal Fe composition and decorated with Pt are introduced as promising catalysts towards the oxygen reduction reaction. These bimetallic nanoparticles have a Pd-Fe@Pd core-shell structure with a surface Pt decoration as established through the use of electron energy loss spectroscopy (EELS) and energy-dispersive X-ray (EDX) spectroscopy. These catalysts exhibit excellent electrocatalytic activity ($E_{1/2}$ = 0.866 V vs RHE), increasing the mass activity by more than 70% over that of pure Pt in terms of the total mass of Pt and Pd and by 14 times if only Pt is considered. Simple geometrical calculations based on spherical core-shell models indicate that Pd-Fe@Pt has a surface Pt decoration rather than a complete Pt monolayer. Such calculations applied to other examples in the literature point out the need for careful and rigorous arguments about claimed 'Pt monolayer/multilayers. Such calculations must be based on not only elemental mapping data but also on the Pt/Pd and other metal atomic ratios in the precursors. Our analysis predicts a minimal Pt/Pd atomic ratio in order to achieve a complete Pt monolayer on the surface of the core materials.

4.2 Introduction

Proton exchange membrane fuel cells (PEMFCs) represent one of the most attractive energy conversion technologies suitable for automotive applications, due to their high power density, high energy conversion efficiency and potential environmental

friendliness[1-3]. However, the large-scale deployment of PEMFCs will require a large amount of Pt for catalysts in order to accelerate the sluggish kinetics of the oxygen reduction reaction (ORR) at the cathode[4-6]. The high-cost and scarcity of Pt, thus becomes one of the major hurdles that preclude the broad-based application of PEMFCs, about 35 % of total cost of the fuel cell.

Over the past decades, great efforts have focused on minimizing the Pt loading and increasing its utilization efficiency. A considerable amount of work has been concentrated on developing Pt-based core/ Pt-rich shell structures or less expensive core materials with a monolayer of Pt covering the surface[7-12]. A Pt-surface enrichment can be achieved by the thermal treatment in a H_2 gas environment as well as by the selective dealloying of transition-metal-rich PtM bimetallic alloys[13-17]. For example, Wang and co-workers synthesized the intermetallic Pt_3Co with about 2-3 atomic-layer Pt shell via annealing at 700^{o}C, boosting both the mass and specific activity of the catalyst by 10 times[7]. Gan et al. utilized an acid leaching process to activate a Ni-rich Pt alloy, forming Ni-rich core/ Pt shell nanoparticles with high electrocatalytic activity[12]. Hu et al. and Wang et al. prepared a class of non-Pt core NPs with a monolayer Pt shell to further boost the electrochemical activity with higher Pt utilization efficiency[18, 19].

However, Pt mono/multilayer coated core-shell catalysts can still require a relatively high content of Pt due to the high specific area of nano-sized particles. The amount of Pt used in the electrocatalyst can be further lowered by the adoption of electrocatalysts with other metal-based core materials. Pd-based catalysts are attractive alternatives since Pd possesses promising catalytic properties but has a lower cost than Pt. Many efforts have focused on designing Pd-based nanocrystals, with various composition, structure, and

morphology, such as Pd-Cu alloys with different atomic ratios, Pd-Cu nanocubes and ultrathin one-dimensional Pd-Ni nanowires[20-22]. (Convention: if structure is ordered then use chemical formulas such as Pd_3Fe. Nevertheless, the incorporation of alloying transition metals with Pd, still has lower electrocatalytic activity than that of Pt/C. Careful design of new materials with desirable structure and surface properties is urgently required for next-generation ORR electrocatalysts.)

Herein, we report a novel solution-phase synthesis method, that provides the flexibility to control the composition of the PdFe bimetallic core with dramatically improved electrocatalytic activity via a minimal Pt decoration of the surface. The incorporation of Fe in the Pd enhances its catalytic activity perhaps due to the lattice strain. Indeed, the electrochemical activity follows a 'volcano curve' with increasing amounts of Fe. Moreover, through facile galvanic replacement reactions, a small amount of Pt will decorate the surface of Pd-Fe, and enhances its activity, surpassing that of the state-of-art Pt NPs. Structures of Pd-Fe@Pt/C have been extensively investigated by scanning transmission electron microscopy equipped with electron energy loss spectroscopy and energy-dispersive X-ray spectroscopy, we show how simple geometric model can be used to determine the Pt shell thickness from the Pt/Pd atomic ratio.

4.3 Experimental Section

4.3.1 Chemicals

Palladium acetylacetonate ($Pd(acac)_2$), iron acetylacetonate ($Fe(acac)_3$), triethylene glycol, 1,2-hexadecanediol, sodium hydroxide, potassium tetrachloroplatinate(II) (K_2PtCl_4) and Nafion (5% wt) were purchased from Sigma-Aldrich. All chemicals were

used as received without further purification. Vulcan XC-72 carbon black was from Cabot Corporation.

4.3.2 Synthesis of Pd-Fe@Pd/C and Pt-decorated Pd-Fe@Pd Nanoparticles

In a typical synthesis, the carbon supported Pd-Fe@Pd/C was prepared in two steps. First, 0.1 mmol of $Pd(acac)_2$ and a pre-determined amount of $Fe(acac)_3$, were dissolved in 30 mL of triethylene glycol solution in a three-neck flask. 120 mg of 1,2-hexadecanediol were added to the solution. The solution was then stirred magnetically and ultrasonicated for 15 mins with suspended carbon powder (Vulcan-72R) to achieve a 20 wt% metal loading on the carbon support. The well-distributed suspension was purged with Ar for 15 mins, heated at 130 ^oC for 10 mins and then the temperature ramped up to 230 ^oC for 1 hr. After cooling down, the mixture was washed with ethanol, acetone and NaOH/ ethanol (1g NaOH/10 mL ethanol) three times, respectively, to remove any remaining surface surfactant. The resulting product was collected by centrifugation and dried at room temperature. The prepared Pd-Fe/C NPs were subsequently annealed under forming gas (95% N_2 and 5% H_2) for 2 h at 500 ^oC to form Pd-Fe@Pd/C core shell NPs [9]. Finally, a Pt-decorated Pd-Fe@Pd/C structure was obtained via a galvanic replacement reaction of part of the surface Pd with Pt. Specifically, 20 mg of the Pd-Fe@Pd/C NPs was suspended in 10 mL of 0.04 mmol K_2PtCl_4 solution, followed by 30 mins of ultrasonication and magnetic stirring at 60 ^oC for an additional 5 h. The final product was obtained by filtration and dried under room temperature overnight in air. The composition of the Pd-Fe/Pt NPs was determined using ICP-AES (Inductively coupled plasma atomic emission spectroscopy), after dissolving the nanoparticles in an aqua regia ($HCl+HNO_3$) solution. Pt loading of the Pt-decorated Pd-Fe@Pd/C NPs was determined by the

difference between the initial mass of K_2PtCl_4 and the residual K_2PtCl_4 in the filtrate after reaction.

4.3.3 Structural Characterization

The crystal structure of all the synthesized NPs was confirmed by XRD using a Rigaku Ultima IV Diffractometer. Diffraction patterns were collected at a scan rate of 3^o min^{-1} at 0.02 ^{o} steps from 10 ^{o} to 90 ^{o}. STEM images and EELS maps were acquired on a fifth-order aberration-corrected STEM (FEI Titan Themis) operated at 300 keV and with a beam convergence semi-angle of 30 mrad. Pd-$M_{4,5}$ and Fe L_2 edges were used to extract Pd and Fe EELS maps. STEM-EDX elemental maps were acquired using an FEI Tecnai F-20 microscope operated at 200 keV and an Oxford X-Max detector. The beam dose during EDX mapping was about 4 e/($Å^2 \cdot s$) to achieve more than 10 counts/pixel for the Pt map and more than 70 counts/pixel for the Pd and Fe maps, without a noticeable sample drift. It should be noted that the signal-to-noise (S/N) ratio in EDX map is the square root of x-ray counts/pixel so that S/N of Pd and Fe is larger than 8 and S/N of Pt is larger than 3. Pt-Mα, Pd-Lα, β and Fe-Kα were used to extract Pt, Pd and Fe EDX maps, respectively from the spectrum image.

4.3.4 Electrochemical Characterizations

Electrochemical measurements were performed in 0.1M $HClO_4$ on a Solartron potentiostat at room temperature. In all electrochemical measurements, 5 mg of the prepared catalyst were mixed with 2 mL of 0.05 wt% Nafion/ethanol solution and subsequently sonicated for approximately 30 minutes. 10 µL of the resulting catalyst ink were loaded onto the end of a 5 mm diameter glassy carbon electrode, followed by thermal evaporation of the solvent under infrared light. A coiled Pt wire was used as the

counter electrode and Ag/AgCl, in a saturated KCl solution, served as the reference electrode. ORR measurements were carried a rotating disk electrode (RDE) in oxygen-saturated 0.1M $HClO_4$ solution at a rotation rate of 1600 rpm. (Bubbling with O2 for 15 mins before scanning and re-bubbling for 7 mins before the next scan) The ORR profiles were obtained after 50 cycles in 0.1M $HClO_4$ over the potential range from 0.05 to 1.1 V at 50 mVs^{-1} to remove surface contamination[23-25]. All cyclic voltammetry curves were obtained between 0.05 V to 1.1 V at 50 mV/s and ORR polarization curves were measured at 5 mV/s, from the negative to the positive direction. Durability tests were carried out by continuous scanning cyclic voltammetry from 0.05 V to 1 V at 100 mV/s for 4000 cycles. CO stripping experiments were conducted by dosing at 0.05 V vs. RHE for 10 mins with CO purging, then switched to Ar for another 10 mins to remove any remaining CO dissolved in the electrolyte. The scan rate during CO stripping experiments was 50 mV/s over the potential range between 0.05 V to 1.2 V.

4.3.5 Derivation of Equations for Calculating Pd/Pt Atomic Ratio

Derivation of equations to calculate the Pd/Pt atomic ratio as a function of particle size (D) and shell thickness (x). Take PdFe@Pt as an example:

Assume particle is spherical and has a diameter D, with a uniform surface Pt distribution.

Step1: Calculate number of moles of Pd in the core material.

Volume of core: $V_{core} = \frac{4}{3} \times \pi \times (\frac{D}{2} - x)^3$

Mass of core: $m_{Pd} = V_{core} \times \rho_{core} \times m_{Pd}\%$

Average density of core: $\rho_{core} = 0.5\ \rho_{Pd} + 0.5\ \rho_{Fe}$; $\rho_{Pd} = 11.9\ g/cm^3$; $\rho_{Pd} = 7.87\ g/cm^3$

$m_{Pd}\%$ is the mass fraction of Pd in PdFe

Number of moles of Pd:

$$n(Pd) = \frac{mPd}{MPd} = \frac{4}{3} \times \pi \times (\frac{D}{2} - x)^3 \times (0.5\ \rho_{Pd} + 0.5\ \rho_{Fe}) \times 0.5/(0.5\ M_{Pd} + 0.5\ M_{Fe})$$

$M_{Pd} = 106$ g/mol; $M_{Fe} = 56$ g/mol

Step2: Calculate number of moles of Pt in the shell material.

Volume of shell: $V_{shell} = \frac{4}{3} \times \pi \times [(\frac{D}{2})^3 - (\frac{D}{2} - x)^3]$

Mass of core: $m_{Pd} = V_{shell} \times \rho_{shell}$

Average density of core: $\rho_{shell} = \rho_{Pt} = 21.45$ g/cm^3

Number of moles of Pt:

$$n(Pd) = \frac{mPd}{MPd} = \frac{4}{3} \times \pi \times [(\frac{D}{2})^3 - (\frac{D}{2} - x)^3]\ \rho_{Pt}/M_{Pt}\ ;\ M_{Pt} = 195 \text{ g/mol.}$$

Step3: Calculate atomic ratio Pd/Pt

$$\text{Atomic ratio Pd/Pt} = \frac{nPd}{nPt} = 0.5 \times \frac{\frac{\rho core}{Mcore}}{\frac{\rho shell}{Mshell}} \times \frac{(\frac{D}{2} - x)3}{(\frac{D}{2})3 - (\frac{D}{2} - x)3} = 0.5 \times \frac{\frac{0.5\rho Pd + 0.5\rho Fe}{0.5MPd + 0.5Fe}}{\frac{\rho Pt}{MPt}} \times \frac{(\frac{D}{2} - x)3}{(\frac{D}{2})3 - (\frac{D}{2} - x)3}$$

$$= 0.5534 \times \frac{(\frac{D}{2} - x)3}{(\frac{D}{2})3 - (\frac{D}{2} - x)3};\ \text{(0.5 is the mole fraction of Pd in PdFe)}$$

Similar derivations can be done as follows:

Pd@Pt core-shell spherical particle:

$$\text{Atomic ratio Pd/Pt} = 1.0326 \times \frac{(\frac{D}{2} - x)3}{(\frac{D}{2})3 - (\frac{D}{2} - x)3}$$

Au@Pt core-shell spherical particle:

$$\text{Atomic ratio Au/Pt} = 0.8920 \times \frac{(\frac{D}{2} - x)3}{(\frac{D}{2})3 - (\frac{D}{2} - x)3}$$

AuCu@Pt core-shell spherical particle:

$$\text{Atomic ratio Au/Pt} = 0.4927 \times \frac{\left(\frac{D}{2}-x\right)3}{\left(\frac{D}{2}\right)3-\left(\frac{D}{2}-x\right)3}$$

4.4 Results and Discussion

The Pd-Fe/C bimetallic NPs were prepared via a two-step solution-phase method. First, $Pd(acac)_2$ and $Fe(acac)_3$ were thermally decomposed to form a Pd-Fe alloy in the triethylene glycol solution at 230 °C (further content details can be found in the experimental section). The amount of $Pd(acac)_2$ was fixed to 0.1 mmol and the amount of $Fe(acac)_3$ was varied from 0.05 mmol to 0.2 mmol, to achieve Pd-Fe/C with various compositions. The as-prepared Pd-Fe/C NPs were annealed at 500 °C for 2 h under forming gas. Due to the high adsorption energy of H on Pd, the surface-segregation in an H_2 atmosphere at high temperature leads to the formation of a Pd-Fe@Pd core-shell structure.[18, 19] The composition of the synthesized Pd-Fe/C NPs was determined by inductively coupled plasma atomic emission spectroscopy (ICP-AES), and the relative content of Fe in the final products were consistent with the amount of Fe precursor initially added (Figure 4.1). While the incorporation of transition metals into Pd has been widely reported in previous studies to facilitate the ORR kinetics[7, 13-17], we later discovered that the activity could be further enhanced by minimal surface decoration with Pt. The process can be simply achieved through a galvanic replacement reaction of Pd with Pt in a very dilute $PtCl_4^{2-}$ solution (detailed information in the experimental section).

The XRD patterns of post-annealed Pd-Fe/C NPs and control Pd/C are shown in Figure 4.2. The broad peak at around 25 ° is ascribed to the carbon support. The remaining peaks, from left to right, correspond to the (111), (200), (220), (311) and (222) planes,

respectively, in a face-centered cubic (fcc) alloy structure. The XRD patterns also showed tiny (110) at 33 º and (210) at 53º peaks in Pd-Fe/C, which are consistent with the standard database (PDF # 04-003-3875). Figure 4.2B clearly shows that, with higher fraction of Fe in Pd-Fe/C alloy NPs, the diffraction peaks shift to higher angles, which is due to thelarger smaller size of Fe relative to Pd. Figure 4.2C shows the dependence of Pd composition to the d spacing, which indicates the linear relationship between them. The domain size was calculated to be about 10 nm from the (220) peak width via the Scherrer equation. This is similar to the particle size observed in TEM images. Since the domain size and the particle size are similar, the nanoparticles are single crystals, not polycrystalline aggregates.

Single-phase Pd-Fe NPs with a uniform size distribution are suitable for Pt surface decoration. Figure 4.3 compares the morphology and particle size of Pd-Fe/C and Pt decorated Pd-Fe/C, from low-magnification TEM images. Both of them exhibited an average particle size of about 10 nm and a uniform distribution on the carbon support, with no discernible differences in morphology. The spontaneous, yet mild, replacement reaction provides a controllable approach for surface decoration without causing damage to the structure. Here, we decorated the Pd-Fe/C bimetallic NPs with a composition of $Pd_{0.58}Fe_{0.42}$/C due to their optimal electrochemical properties, which will be discussed in detail later (*vide infra*).

A

$Fe(acac)_3$/mmol	Atomic percent from ICP-AES	
	Pd / %	Fe / %
0	100	0
0.05	74	26
0.1	63	37
0.125	58	42
0.2	52	48

B

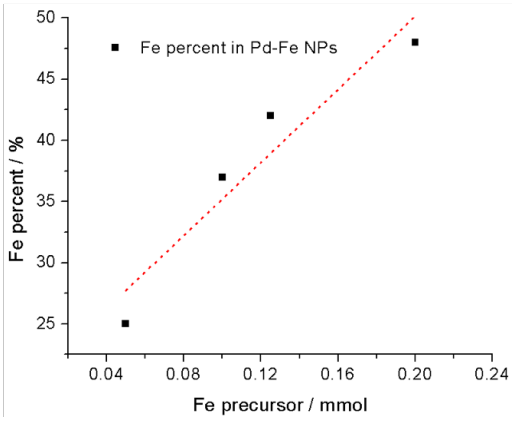

Figure 4.1 (A). Table showing the atomic percentage of Pd and Fe measured by ICP-AES with different amounts of $Fe(acac)_3$ added in the system (B). The relatively linear relationship (R^2=0.9) of $Fe(acac)_3$ precursor added and measured Fe percentage in the synthesized Pd-Fe/C NPs (relative error=±1.25%).

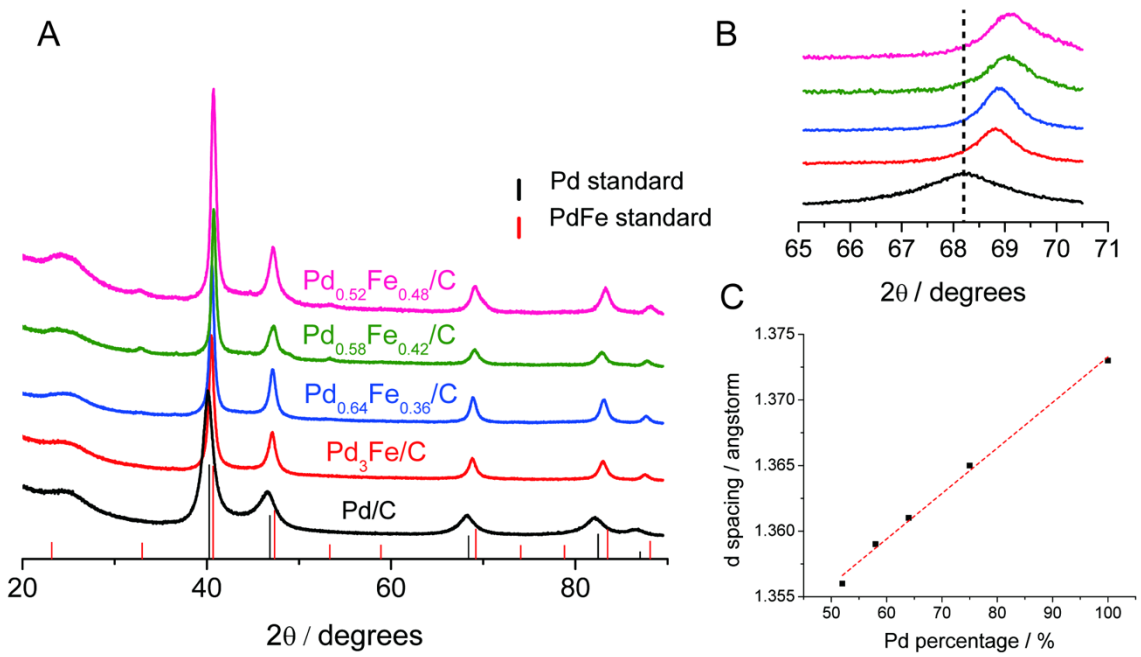

Figure 4.2 (A) XRD patterns of synthesized Pd-Fe/C bimetallic nanoparticles: Pd/C, Pd_3Fe/C, $Pd_{0.64}Fe_{0.36}/C$, $Pd_{0.58}Fe_{0.42}/C$ and $Pd_{0.52}Fe_{0.48}/C$ after annealing at 500 °C for 2 h. The red and black vertical lines correspond to Pd (PDF # 5-681) and PdFe (PDF # 04-003-3875) standard XRD. (B) Inserted graph is the enlarged region of the Pd (220) diffraction peak. (C) Plot of d-spacing of (220) peak for Pd-Fe/C with different composition.

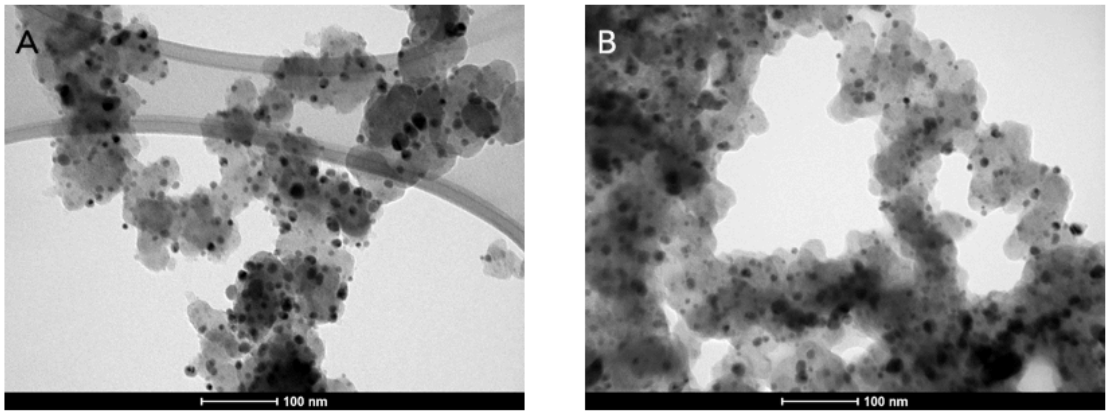

Figure 4.3 Low-magnification bright-field TEM images of as-prepared (A) $Pd_{0.58}Fe_{0.42}$/C and (B) $Pd_{0.58}Fe_{0.42}$@Pt/C

The crystallographic and chemical information of Pt decorated $Pd_{0.58}Fe_{0.42}$/C (simplified as PdFe@Pt/C in the following discussions) have been further explored using an aberration-corrected scanning transmission electron microscope (STEM) equipped with an electron energy loss spectrometer (EELS) operated at 300 keV. STEM images in Figures 4.4A-B show PdFe@Pt/C nanoparticle with a narrow size distribution and an average particle size of around 10 nm in diameter, which is consistent with the grain size calculated from XRD. In Figures 4.4C-E, the atomic-scale STEM image of a single particle, and the corresponding Fourier transform, reveal the lattice d-space of the (111) (2.2 Å) and (110) (2.7 Å) plane projected on the [1-10] zone axis, which match the (111) (2.22 Å) and (110) (2.71 Å) in the standard PdFe XRD (PDF # 04-003-3875). The (110) plane is recognized as the characteristic diffraction feature of ordered intermetallics, which is consistent with the (110) intermetallic peak at 33 ° in the XRD profile in the Figure 4.2. The chemical composition information was obtained using EELS elemental mapping in STEM model. Figures 4.5B-D show the Pd (red), Fe (green) and their composite maps, extracted from the Pd $M_{4,5}$ edge and the Fe L_2 edge in the EELS spectra (Figure 4.6). The presence of a thin Pd shell can be clearly distinguished from the thin red region in the Pd vs. Fe composite map. The precise thickness of the Pd shell was quantitatively analyzed by extracting EELS line profiles from the Pd and Fe maps. Figure 4.5E indicates a Pd shell thickness of about 1 nm, which corresponds to a three atomic-layer thick Pd shell on the surface. The thin Pd shell could serve as a protection layer to prevent the dissolution of Fe in the acid media during the electrochemical cycling while being thin enough to maintain the superior ORR electrocatalytic activity of the PdFe intermetallic core.

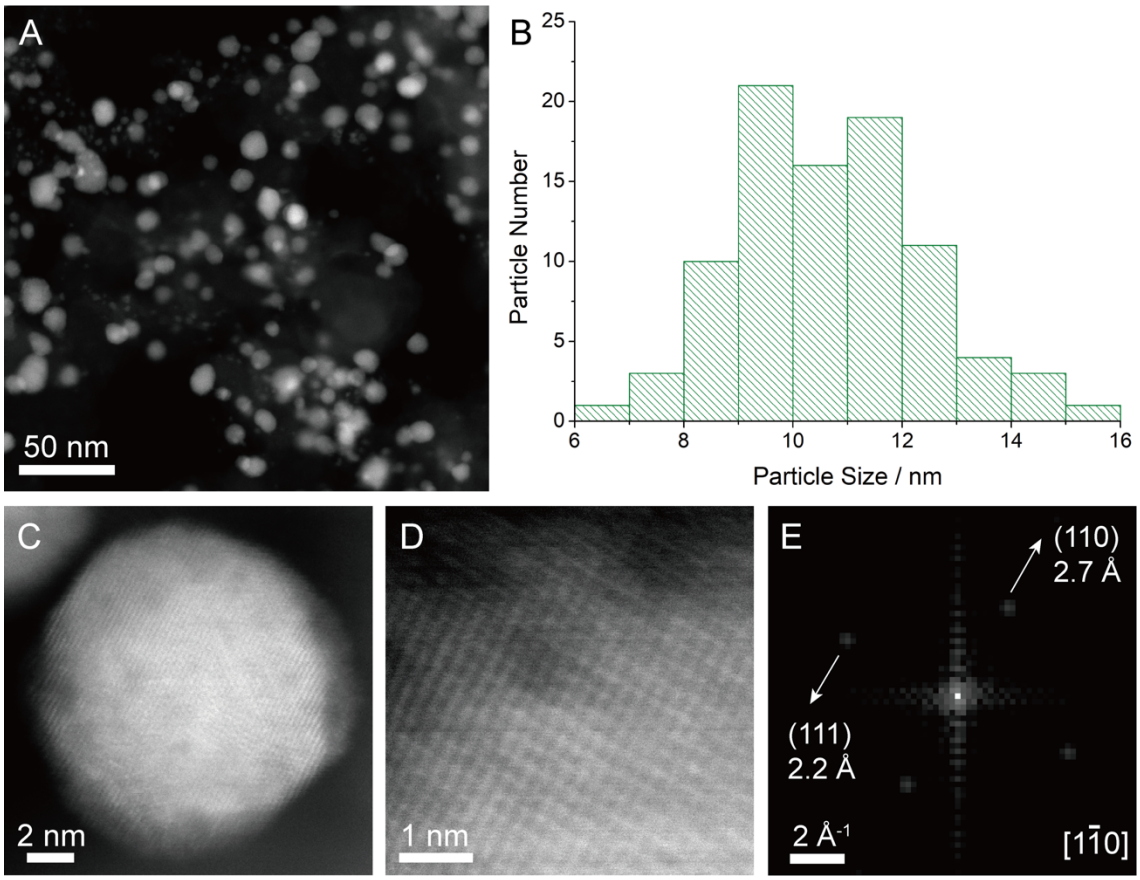

Figure 4.4 (A-B) HAADF-STEM image of Pd-Fe@Pt nanoparticles and the corresponding histogram of the particle size distribution. (C-D) Atomic-scale STEM image of a particular Pd-Fe@Pt nanoparticle (C) with a magnified region that clearly show the crystal lattice on the [1-10] zone axis. (E) Fourier transform of lattice images in (D) shows the diffraction spots corresponding to the lattice d-spacing of (111) and (110) facets (PDF# 04-003-3875).

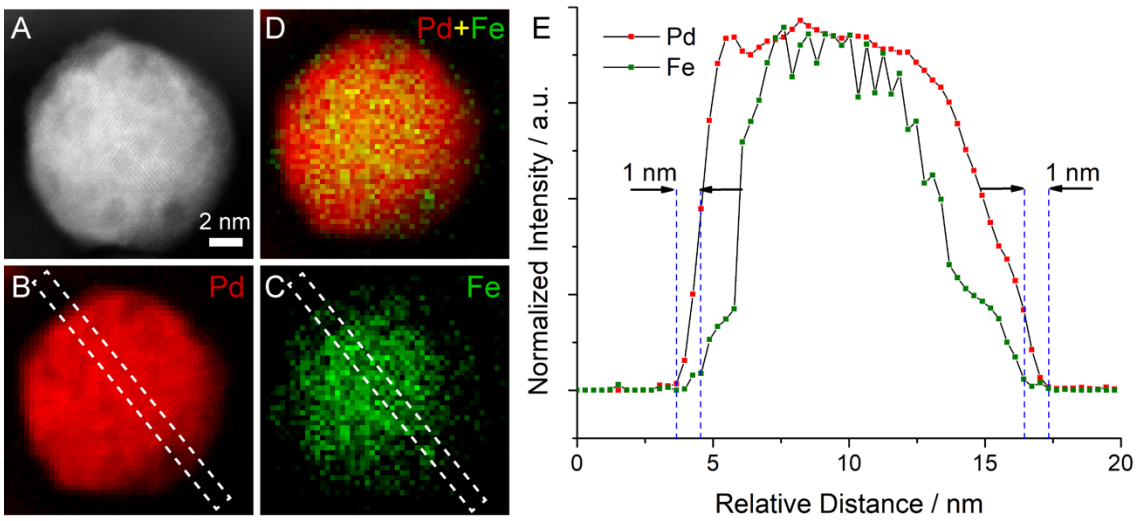

Figure 4.5 (A). STEM image of Pd-Fe@Pt. (B-D). EELS elemental maps of Pd (red), Fe (green) and composite map of Pd vs. Fe (D). (E). EELS elemental line profiles of Pd and Fe extracted from white dashed boxes from EELS mapping in (B) and (C), respectively

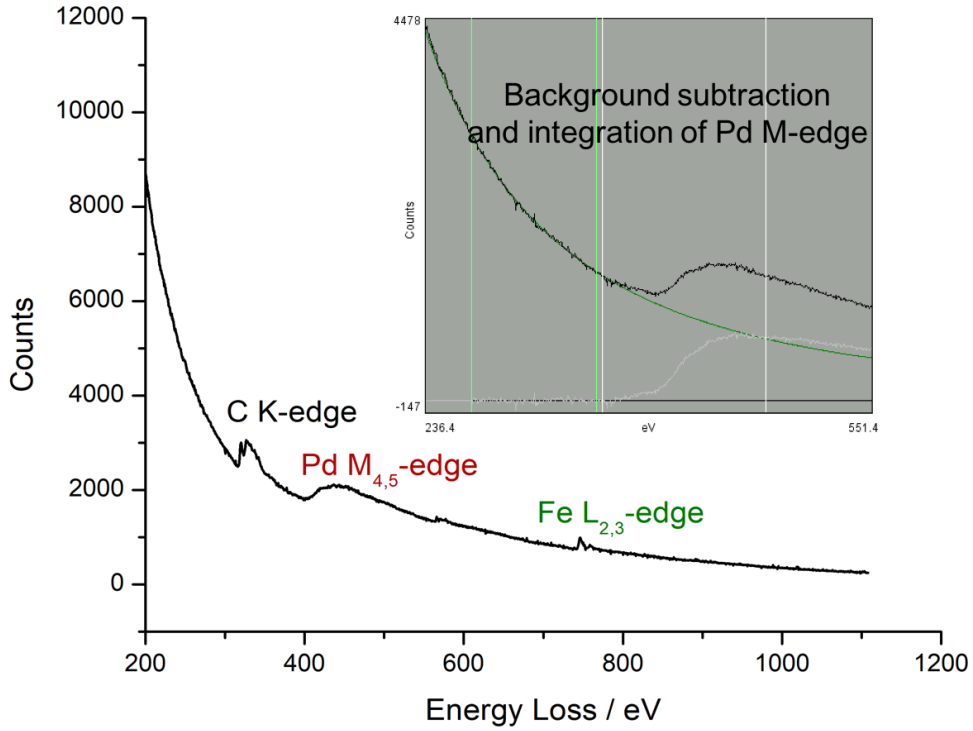

Figure 4.6 EELS spectra corresponding to the EELS elemental mapping in Figure 4.4. Pd $M_{4,5}$ and Fe $L_{2,3}$ edges were used to extract EELS maps from spectrum images. The inset exhibits the Pd $M_{4,5}$ edge (white line) after the background subtraction from the raw EELS spectra (black line) using the linear combination of power laws (LCPL) method. The background noise was filtered using principal component analysis (PCA).

Because of the low Pt content in PdFe@Pt (Pt: Pd = 1:70), the EELS signal-to-noise ratio of Pt $M_{4,5}$ edges were not high enough to get a reliable Pt map. Instead, energy-dispersive X-ray (EDX) spectroscopy served as a reliable tool to detect the trace amount of Pt on the nanoparticles.

To demonstrate the presence of surface decoration, we employed EDX spectroscopy in STEM mode to study the elemental distribution of Pt vs. Pd and Fe in Pd-Fe@Pt. The EDX spectrum in Figure 4.7 shows a strong Pt Mα edge, which, together with the Pd Lα, β and Fe Kα edges, can be used for EDX elemental mapping. Figures 4.8A-D present the STEM image of a typical Pd-Fe@Pt nanoparticle and the corresponding EDX elemental maps of Pd (red), Fe (green) and Pt (yellow). In order to quantitatively study the elemental distribution, we extracted EDX elemental line profiles (Figure 4.8E) from the corresponding elemental maps (white dashed boxes in Figures 4.8B-D). Pd and Fe exhibit bell-shaped line profiles whereas Pt shows a plateau with two distinguishable edges. The schematic in Figure 4.8F illustrates the theoretical projected intensity profile of core-shell particles, indicating that Pd and Fe will ideally present a semi-circular intensity profile while the surface Pt layer will exhibit a slightly lower intensity in the middle with two noticeable sharp edges. The differences between the experimental data and the schematic are likely due to the blurring effects from the larger electron beam size employed in EDX mapping. That means the experimental EDX line profiles can be rationalized as the combined result of the intensity profile in the schematic and a Gaussian blurring (smoothing) function. However, the key features of the EDX line profiles and the schematic are quite similar and indicates that Pt decorates the surface of the Pd-Fe@Pd core-shell nanoparticles.

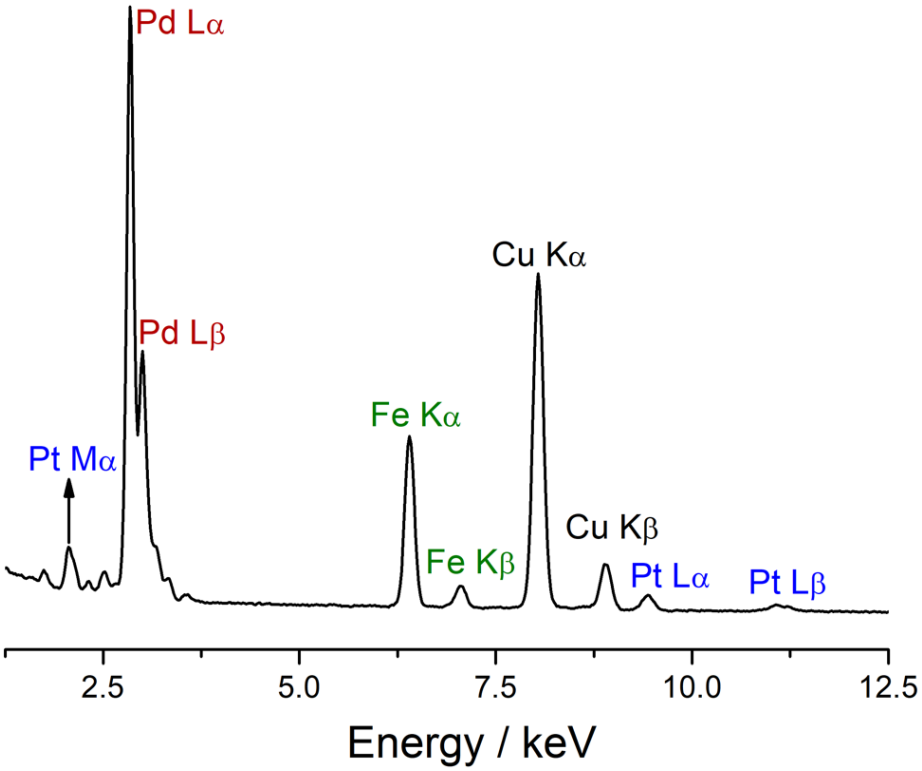

Figure 4.7 EDX spectra of PdFe@Pt. Pt Mα, Pd Lα, β, Fe Kα were selected to process the spectrum image and generated EDX maps. It should be noted that the strong Cu K edges are from the Cu TEM grid.

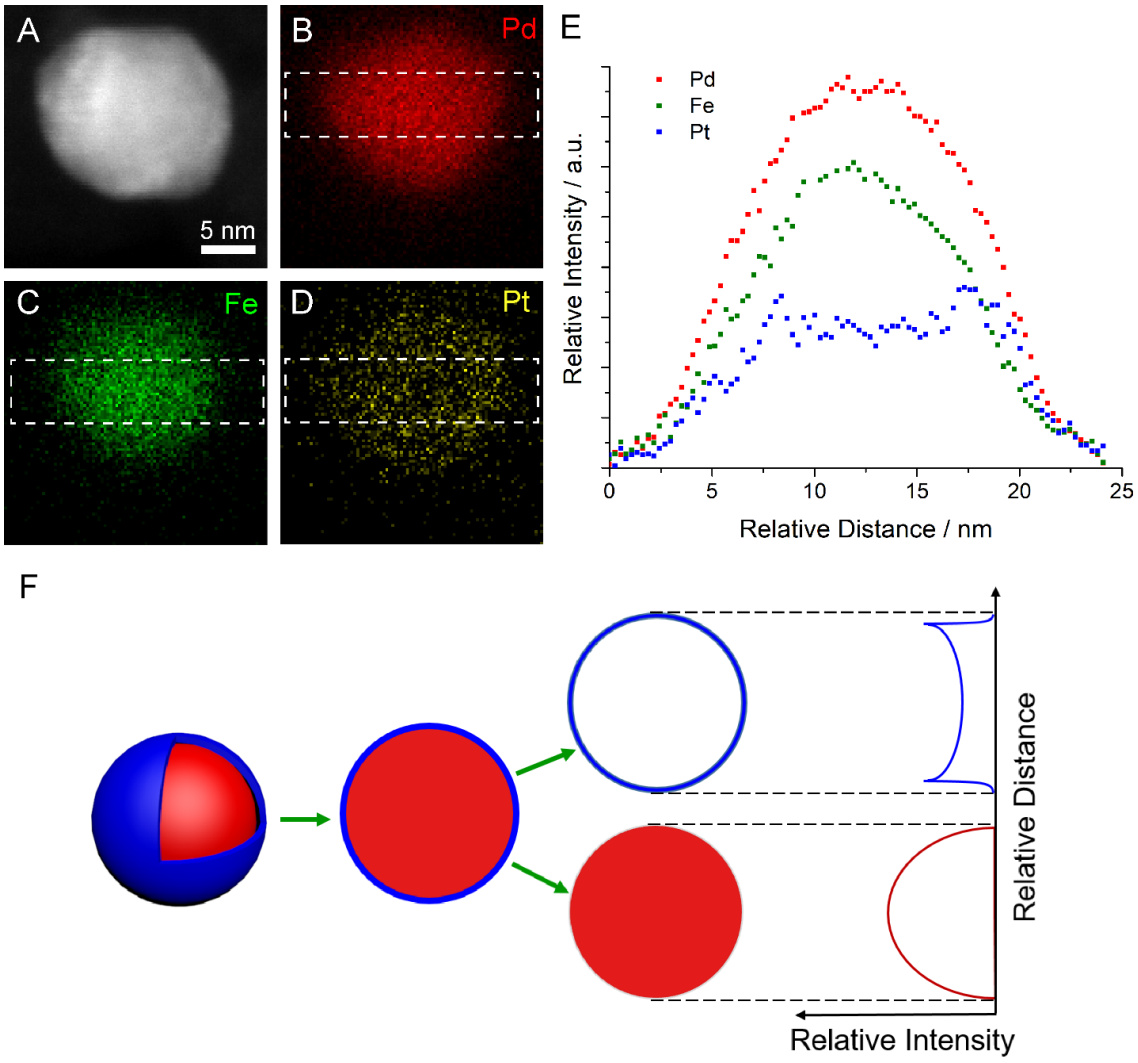

Figure 4.8 (A). STEM image of a PdFe@Pt nanoparticle. (B-D). EDX elemental maps of Pd (red), Fe (green) and Pt (yellow). (E). EDX line profiles of Pd (red), Fe (green) and Pt (blue) extracted from white dashed boxes from EDX mapping in (B-D). (F). Schematic model of a core-shell spherical particle and the theoretical projected intensity profiles.

The cyclic voltammetric profiles (CVs) of the Pd-Fe/C bimetallic NPs, with different Fe content were obtained in an Ar-saturated 0.1 M $HClO_4$ solution at a scan rate of 50 mV/s, and all shown in Figure 4.9A. These distinct hydrogen regions are observed the incorporation of Fe partially alters the electronic properties of Pd, and modifies the adsorption of hydrogen. Compared to Pd/C, the cathodic peak (around 0.7V) of the Pd-Fe/C bimetallic catalysts, exhibits a positive shift, which indicates a decreased adsorption free energy for the oxygen-containing species and faster rate of reduction of the Pd surface oxide[26-28]. To better understand the relationship between lattice strain and electrochemical activity, the catalytic performance, towards the ORR of different catalysts was characterized by rotating disk electrode (RDE) in O_2-saturated 0.1 M $HClO_4$ solution at 1600rpm. The polarization curves are profiled in Figure 4.9B. The diffusion limited current of about -5.5 mA/cm^2 at 1600 rpm indicates that all of the Pd-Fe/C bimetallic NPs are effective the four-electron transfer reduction process[29, 30]. Compared to Pd/C, Pd-Fe/C bimetallic NPs exhibit a positive shift in the onset potential, indicating that alloying of Pd with Fe enhances the ORR kinetics and lowers the overpotential. The half-wave potentials ($E_{1/2}$) of the Pd-Fe/C NPs are also positively shifted, to different extent, depending on composition, following the order: Pd/C < Pd_3Fe/C < $Pd_{0.52}Fe_{0.48}$/C < $Pd_{0.64}Fe_{0.36}$/C < $Pd_{0.58}Fe_{0.42}$/C. The electrocatalytic performance of the series of Pd-Fe/C NPs shows a 'volcano trend' with increasing Fe content, which could be explained via Norskov's d-band center theory[31, 32]. The surface electronic structure of the NPs will be affected by two main aspects: the lattice constant (strain) and the ligand effect. Initially, as Fe content increases, the lattice constant contraction (strain) is dominated. This weakens the adsorption energy of the oxygen-containing intermediate species, and thus

enhances the electrocatalytic activity. Subsequently, with further increases in the amount of Fe, the ligand effect becomes more pronounced and plays a more important role, lowering the electrochemical activity. Overall, those two opposite influences might contribute to the 'volcano trend' in the electrocatalytic performance.

Taking this into account, $Pd_{0.58}Fe_{0.42}$/C NPs with the highest ORR activity were decorated with Pt in an effort to further enhance its ORR activity. Pt decoration, or monolayer surface-covering, has been extensively recognized as an effective approach to promote ORR kinetics with low Pt loading. The CVs of Pd/C, $Pd_{0.58}Fe_{0.42}$/C before and after Pt decoration are shown in Figure 4.9C. The cathodic peak of $Pd_{0.58}Fe_{0.42}$/C exhibits a positive shift when compared to Pd/C, and shifts further positive after Pt decoration, demonstrating faster hydroxyl adsorption/ desorption after the incorporation of Fe and surface Pt decoration. The polarization profiles of Pt-decorated $Pd_{0.58}Fe_{0.42}$/C and Pt/C are profiled in Figure 4.9D.

The half-wave potential of Pt-decorated $Pd_{0.58}Fe_{0.42}$/C surpassed that of Pt/C by 7mV. To quantitatively evaluate the electrochemical activity, the kinetic currents of $Pd_{0.58}Fe_{0.42}$@Pt/C and Pt/C were calculated using the Koutecky−Levich equation[37], normalized to the total mass of Pt and Pd (Figure 4.9E), and Pt (Figure 4.9F), respectively. The mass activity of the Pt-decorated $Pd_{0.58}Fe_{0.42}$/C, normalized to all noble metals (Pt+Pd), increased by 70% when compared with Pt, and exhibited a 14-fold enhancement when normalized to Pt only. The enhancement could be attributed to the combination effect of strain, arising from the lattice mismatch, and electronic modification. The CO-strippings were used to further characterize surface electronic properties of the Pt-decorated Pd-Fe NP, shown in Figure 4.10.

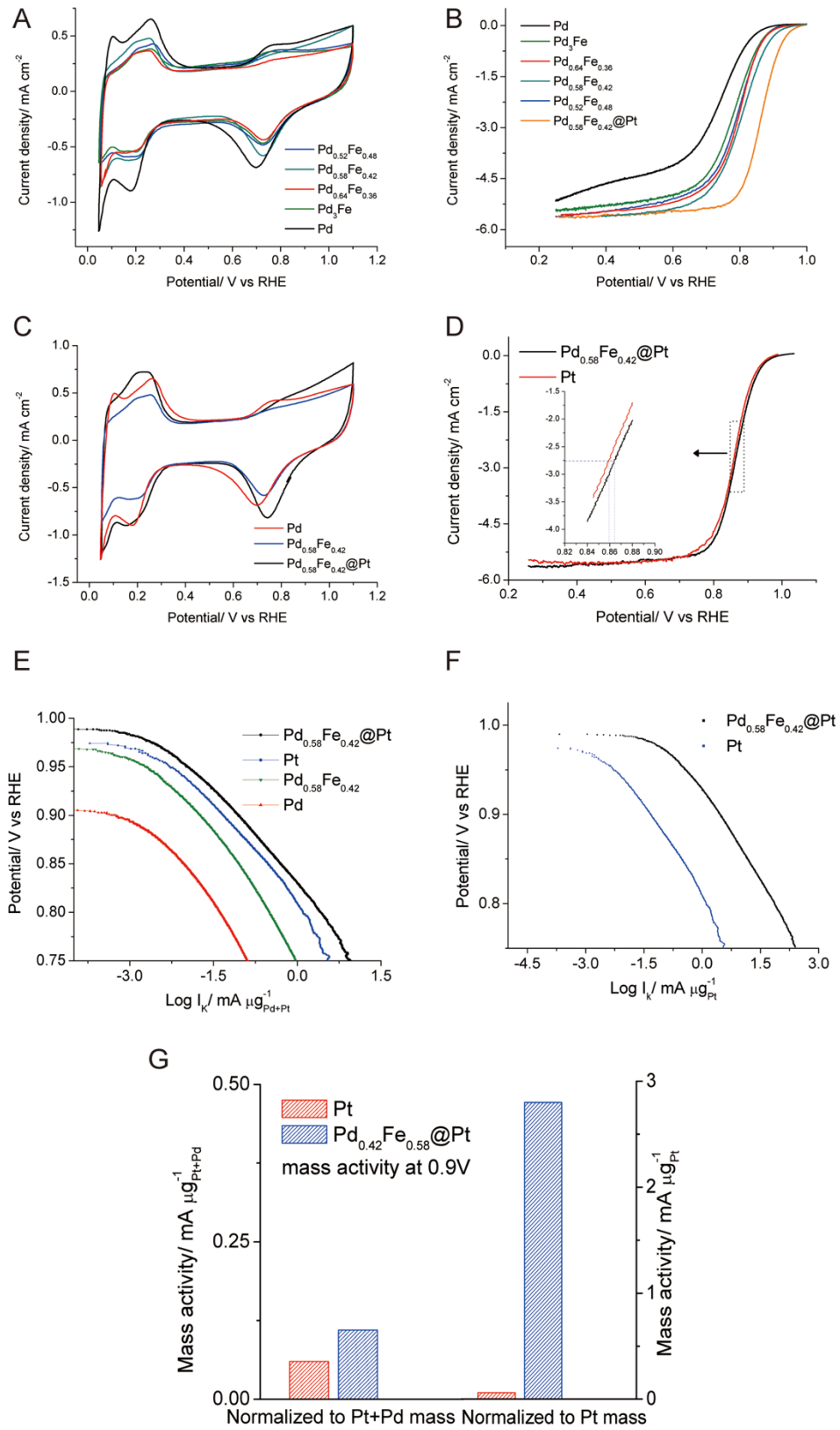
A
Current density/ mA cm-2
Potential/ V vs RHE
Pd0.52Fe0.48
Pd0.58Fe0.42
Pd0.64Fe0.36
Pd3Fe
Pd
B
Current density/ mA cm-2
Potential/ V vs RHE
Pd
Pd3Fe
Pd0.64Fe0.36
Pd0.58Fe0.42
Pd0.52Fe0.48
Pd0.58Fe0.42@Pt
C
Current density/ mA cm-2
Potential/ V vs RHE
Pd
Pd0.58Fe0.42
Pd0.58Fe0.42@Pt
D
Current density/ mA cm-2
Potential/ V vs RHE
Pd0.58Fe0.42@Pt
Pt
E
Potential/ V vs RHE
Log Ik/ mA μg-1Pd+Pt
Pd0.58Fe0.42@Pt
Pt
Pd0.58Fe0.42
Pd
F
Potential/ V vs RHE
Log Ik/ mA μg-1Pt
Pd0.58Fe0.42@Pt
Pt
G
Mass activity/ mA μg-1Pt+Pd
Mass activity/ mA μg-1Pt
Pt
Pd0.42Fe0.58@Pt
mass activity at 0.9V
Normalized to Pt+Pd mass
Normalized to Pt mass

Figure 4.9 Electrocatalytic properties of synthesized Pd-Fe/C and Pd-Fe@Pt/C nanoparticles. (A). Cyclic voltammetry (CV) profiles of synthesized Pd-Fe/C NPs in Ar-saturated 0.1 M $HClO_4$ solution, scanned at a rate of 50 mV/s at room temperature. (B). ORR polarization curves in O_2-saturated 0.1 M $HClO_4$ at a scan rate of 5 mV/s and rotation rate of 1600rpm. (C). CV profiles of Pd/C, $Pd_{0.58}Fe_{0.42}$/C and $Pd_{0.58}Fe_{0.42}$@Pt/C in Ar-purged 0.1 M $HClO_4$ solution at a sweep rate of 50 mV/s. (D). Comparison of ORR polarization curves for Pt/C and $Pd_{0.58}Fe_{0.42}$@Pt/C in O_2-saturated 0.1 M $HClO_4$ solution at a scan rate of 5 mV/s and 1600rpm rotation rate. (E). Tafel plots. Mass activities of different catalysts normalized to the total mass of Pd and Pt. (F). Tafel plots. Mass activity of Pt/C and $Pd_{0.58}Fe_{0.42}$@Pt/C, normalized to the mass of Pt. (G). Comparison of mass activity between Pt/C and $Pd_{0.58}Fe_{0.42}$@Pt/C, at 0.9V vs RHE.

The CO-oxidation peak potential of Pt-decorated $Pd_{0.58}Fe_{0.42}/C$ (0.941 V) was between that of Pd/C (0.959 V) and Pt/C (0.918 V), with a positive shift compared to Pd/C, indicating Pt and Pd can co-exist on the surface of the electrocatalysts with a weakening of the CO adsorption energy related to Pd/C. Durability tests are also conducted for Pt-decorated $Pd_{0.58}Fe_{0.42}/C$ in Ar-saturated 0.1 M $HClO_4$ solution, for 4,000 cycles between 0.05 and 1 V vs. RHE. The CV and ORR polarization curves, before and after testing, are shown in Figure 4.11. While there is a 25 mV negative shift in the half-wave potential, we believe it is due, at least in part, to the loss of electrochemical surface area (ECSA) due to particle aggregation/ coalescence after extensive potential cycling.

Based on the EDX elemental mapping results that indicated Pt surface decoration of the PdFe NPs and the co-existence of Pt and Pd on the surface, from CO stripping, we further investigated what is the effective friction of the Pt layer on this core-shell catalyst from a theoretical perspective. Assuming that Pd-Fe@Pt is a spherical particle, with a diameter of D, and a shell thickness of **x**, the theoretical Pd to Pt atomic ratio (Pd/Pt) will be a function of x as described in the equation in Figure 4.12. The relation between Pd/Pt and shell thickness was systematically studied for both pure Pd cores (solid lines) and bimetallic PdFe cores (dashed lines) with a series of particles of different size (Figure 4.12). The Pd/Pt atomic ratio decays dramatically, as the shell thickness increases, for all different particle sizes, indicating that much more Pt is required for a thicker Pt shell, and thus, the average cost of such a core-shell catalyst will increase significantly. Furthermore, the Pd/Pt atomic ratio also decreases for a constant thickness while the particle size changes from 20 to 5 nm, which indicates that smaller particles will have a larger Pt mole fraction and, thus, a higher average cost of precious metals. For the same particle size,

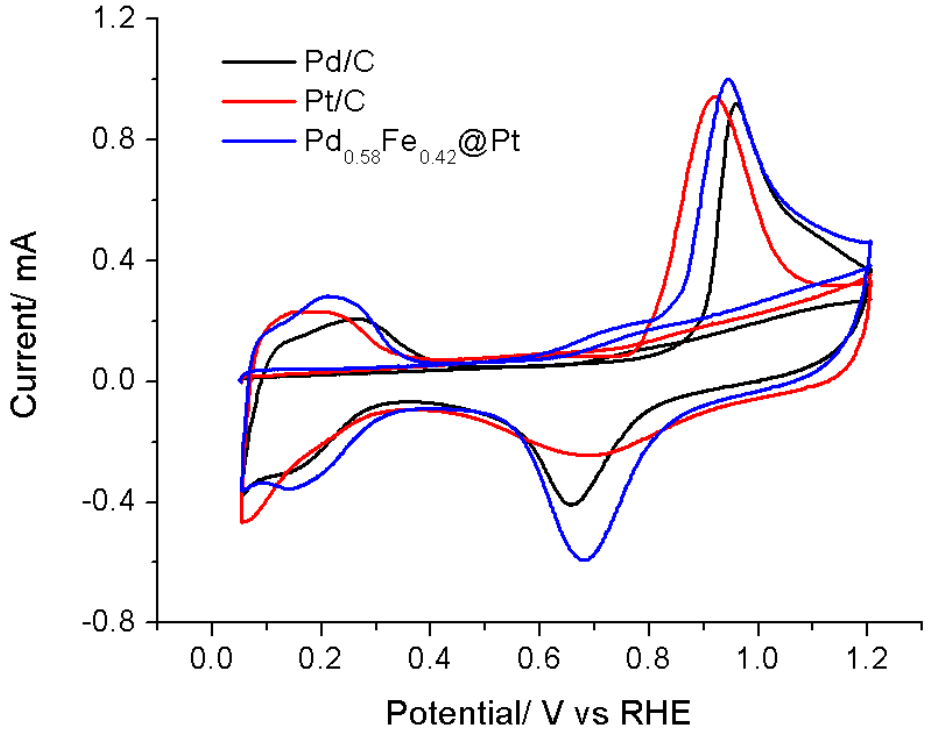

Figure 4.10 The CO stripping voltammetry of Pd/C, Pt/C and Pt-decorated $Pd_{0.58}Fe_{0.42}$/C at a scan rate of 50 mV/s in an Ar-saturated 0.1 M $HClO_4$ solution. Dosing potential of CO adsorption was 0.05 V vs. RHE.

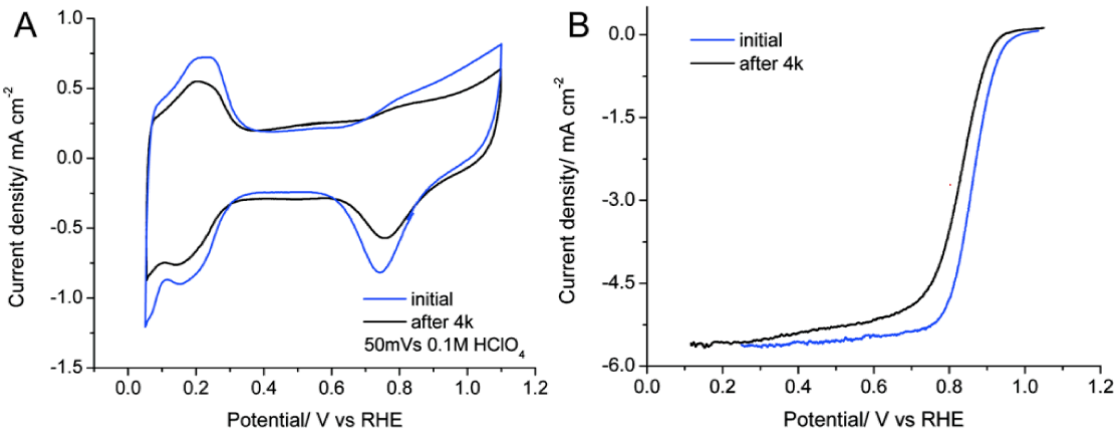

Figure 4.11 (A). Cyclic voltammetry profiles (B). and ORR polarization profiles of Pt decorated $Pd_{0.58}Fe_{0.42}$/C nanoparticles before and after stability test

Pd-Fe@ Pt exhibits a Pd/Pt atomic ratio only about half as large as Pd@Pt because the Pd mole fraction in Pd-Fe core is only 50% of that of a pure Pd core. In summary, overall precious metal loading can be minimized (optimized) if one could design a core-shell catalyst with a thin shell (ideally monolayer), a core with a smaller Pd mole fraction, and a relatively larger particle size. It is worth noting that these design principles need to also accommodate the consideration of the effective electrochemical surface area per mass of core-shell catalyst, and the increasing cost of core materials in a larger particle size. In the case of a 10nm Pd-Fe@Pt particle (red dashed line), Pt/Pd atomic ratio has to be larger than 1:2.7 and thus the Pt mole fractions has to be more than a quarter in total precious metal loading, to achieve a Pt monolayer with 100% coverage. If Pt/Pd ratios can be determined from experiments, such as ICP-AES, one could work out the actual shell thickness, based on the experimental Pt/Pd atomic ratio and compare it with EELS or EDX elemental mapping results. Surprisingly, in this work, the Pt/Pd ratio was determined to be about 1:70 (much smaller than 1:2.7 for a complete Pt monolayer) based on ICP-MS, which would predict a shell thickness far less than a Pt monolayer (about 3 Å). The term 'Pt surface decoration' rather than 'Pt monolayer' was thus used in this work to more rigorously and precisely describe Pd-Fe@Pt. Despite numerous claims in the literature of core-shell structures with 'Pt monolayer/multilayers', based on their EELS or EDX elemental mapping or line profiles (Table 4.1), the measured Pt content was, in fact, insufficient for a fully covered Pt layer, can be readily calculated from this spherical core-shell model[7, 9, 19, 34-38]. Therefore, both core and shell materials are clearly on the surface and can participate in electrocatalysis in many known core-shell electrocatalysts. We believe that the 'back-of-the-envelope' calculations presented in this

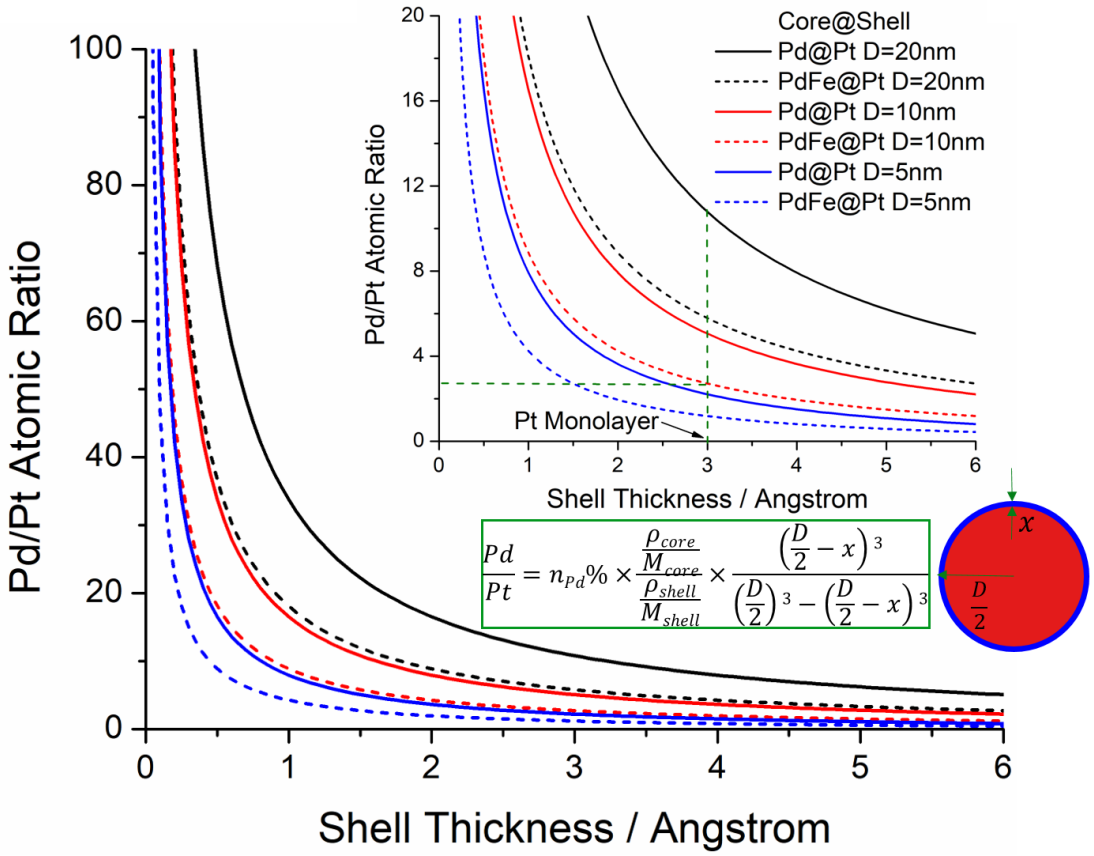

Figure 4.12 Theoretical calculations of the Pd/Pt atomic ratio as a function of the particle size (Diameter, D) and the shell thickness (**x**). The insert shows the magnified diagram with a focus on lower Pd/Pt atomic ratio, i.e., higher relative Pt content. Solid lines are Pd@Pt core-shell particles while dashed lines are PdFe@Pt. The crossing point of the two dashed green lines is for PdFe@Pt with D=10 nm, which has to have a Pt/Pd ratio larger than 1:2.7 to achieve a complete Pt monolayer (3 Å). $n_{Pd}\%$ in the equation is the mole fraction of Pd in the core materials (e.g., $n_{Pd}\%=0.5$ in PdFe). Details of the equation derivation can be found in the supporting information.

work should always be considered before synthesizing core-shell electrocatalysts. The diagram and simple equation developed in Figure 4.12 can be used as a guide to work out the minimal Pt/M ratio in the precursors required to form a complete Pt monolayer or multilayers in the design of M@Pt core-shell electrocatalysts.

4.5 Conclusion

In summary, the Pt-decorated $Pd_{0.58}Fe_{0.42}$/C NPs with tunable core composition and surface Pt decoration have been synthesized via a method involving thermal decomposition, H_2-induced surface segregation and galvanic replacement reaction. The optimal Pd-Fe/C bimetallic nanoparticles exhibited excellent electrochemical performance the towards ORR after surface decoration with ultralow amounts of Pt (around 1 a.t.%). In addition, since non-Pt NPs, with Pt surface decoration and monolayer coating are promising and popular candidates for ORR catalysts. We have also discussed the minimal Pt/Pd required for a monolayer coverage of Pt. For fuel cell catalysts, at the scale of 5-20 nm, a relatively high amount of Pt content is required even for a Pt monolayer. Compared with a full Pt monolayer coating, the use of Pt surface decoration enables an ultralow Pt loading while retaining the high activity of the Pd-Fe@Pd core-shell catalysts. The electrocatalyst also maintained a moderate durability during electrochemical cycles. The experimental design and theoretical calculations described in this work provide a novel approach to design higher-efficiency and lower-cost electrocatalysts for the oxygen reduction reaction.

Ref.	Catalyst composition	Claimed shell : core atomic ratio (ICP-AES)	Claimed average particle size (XRD,TEM)	Claimed shell thickness (EELS, EDX mapping)	Calculated shell thickness based on equations*
This work	PdFe@Pt	Pt:Pd= 1:70	10nm	Pt decoration	0.12 Å
1	Pd_3Co@Pt	Pt:Pd=1:90	15 nm	Pt monolayer	0.25 Å
2	PdCo@Pt	Pt:Pd=1:90	15 nm	Pt monolayer	0.15 Å
3	PdCu@Pt	Pt:Pd=1:9.2	10 nm	Pt monolayer	1.0 Å
4	Pd@Pt	Pt:Pd=1:2.7	4 nm	Pt monolayer	2.1 Å
5	Pd@Pt	Pt:Pd=1:3.0	5 nm	Pt monolayer	2.5 Å
6	Pd@Pt	Pt:Pd=1:2.4	15 nm	5~10 Å	8.5 Å
7	AuCu@Pt	Pt:Au=1:10.4	15 nm	1.5 Pt atomic layers	1.2 Å
8	Au@Pt	Pt:Au=1:14	7 nm	Pt monolayer	0.75 Å

Table 4.1 Detailed information of reports regardining about Pt monolayer-coating NPs. *Equations were derived based on a core-shell spherical particle with a particle diameter D and shell thickness x. Red text indicated that the claimed shell thickness is larger than the calculated one, and thus the particle surfaces cannot have a 100% Pt coverage and the core and shell materials can co-exist on surfaces. Green test indicates the claimed shell thickness is relatively consistent with the calculated one.

References were listed as follows:

1. Wang, D.; Xin, H. L.; Wang, H.; Yu, Y.; Rus, E.; Muller, D. A.; DiSalvo. F. J.; Abruña, H. *Chem. Mat.* **2012**, 24, 2274.
2. Wang, D.; Xin, H. L.; Wang, H.; Yu, Y.; Rus, E.; Muller, D. A.; DiSalvo. F. J.; Abruña, H. *J. Am. Chem. Soc*. **2010**, 132, 17664.
3. Shao, M.; Shoemaker, M.; Peles, A.; Kaneko, K.; Protsailo, L. *J. Am. Chem. Soc*. **2010**, 132, 9253.

4. Zhang, Y.; Hsieh, Y.-C.; Volkov, V.; Su, D.; An, W.; Si, R.; Zhu, Y.; Liu, P.; Wang, J. X.; Adzic, R. R. *ACS Catal.* **2014**, 4, 738.
5. Kongkand, A.; Subramanian, N.; Yu, Y.; Liu, Z.; Igarashi, H.; Muller, D. A. *ACS Catal*., **2016**, 6, 1578.
6. Wang, X.; Vara, M.; Luo, M.; Huang, H.; Ruditskiy, A.; Park, J.; Bao, S.; Liu, J.; Howe, J.; Chi, M.; Xie, Z.; Xia, Y. *J. Am. Chem. Soc*. **2015**, 137, 15036.
7. Wang, G.; Huang, B.; Xiao, L.; Ren, Z.; Chen, H.; Wang, D.; Abruña, H.; Lu, J.; Zhuang, L. *J. Am. Chem. Soc*. **2014**, 136, 9643.
8. Hu, J.; Wu, L.; Kuttiyiel, K.; Goodman, K. R.; Zhang, C.; Zhu, Y.; Vukmirovic, M. B.; White, M. G.; Sasaki, K., Adzic, R. R. *J. Am. Chem. Soc.* **2016**, 138, 9294.

4.6 References

1. Gasteiger, H.; Markovic, N. M. *Science* **2009**, 324, 48.
2. Debe, M. *Nature* **2012**, *486*, 43.
3. Arico, A. S.; Bruce, P.; Scrosati, B.; Tarascon, J. M.; Van Schalkwijk, W. *Nat. Mater.* **2005**, 4, 366.
4. Wang, J.; Zhao, N.; Fang, B.; Li, H.; Bi, X. T.; Wang, H. *Chem. Rev*. **2015**, 115, 3433.
5. Guo, S.; Zhang, S.; Sun, S. Angew. *Chem., Int. Ed*. **2013**, 52, 8526.
6. Zhao, X.; Chen, S.; Fang, Z.; Ding, J.; Sang, W.; Wang, Y.; Zhao, J.; Peng, Z.; and Zeng, J. *J. Am. Chem. Soc*. **2015**, 137, 2804.
7. Wang, D.; Xin, H. L.; Hovden, R.; Wang, H.; Yu, Y.; Muller, D. A.; DiSalvo, F. J.; Abruña, H. D. *Nat. Mater*. **2012**, 12, 81.
8. Strasser, P.; Koh, S.; Anniyev, T.; Greeley, J.; More, K.; Yu, C. F.; Liu, Z. C.; Kaya, S.; Nordlund, D.; Ogasawara, H.; Toney, M. F.; Nilsson, A. *Nat. Chem*. **2010**, 2, 454.
9. Wang, D.; Xin, H. L.; Yu, Y.; Wang, H.; Rus, E.; Muller, D. A.; Abruña, H. D. *J. Am. Chem. Soc.* **2010**, 132, 17664.
10. Oezaslan, M.; Heggen, M.; Strasser, P. *J. Am. Chem. Soc*. **2012**, 134, 514.
11. Wu, Y.; Wang, D.; Niu, Z.; Chen, P.; Zhou, G.; Li, Y. *Angew. Chem., Int. Ed*. **2012**, 51, 12524.
12. Gan, L.; Heggen, M.; Rudi, S.; Strasser, P. *Nano Lett.* **2012**, *12*, 5423.
13. Ruban, A. V.; Skriver, H. L.; Nørskov, J. K. *Phys. Rev. B* **1999**, 59, 15990.
14. Wang, L.-L.; Johnson, D. D. *J. Am. Chem. Soc.* **2009**, 131, 14023.

15. Dubau, L.; Maillard, F.; Chatenet, M.; André, J.; Rossinot, E. *Electrochim. Acta* **2010**, 56, 776.

16. Chen, S.; Gasteiger, H. A.; Hayakawa, K.; Tada, T.; Shao-Horn, Y. J. *Electrochem. Soc.* **2010**, 157, A82.

17. Cui, C.; Gan, L.; Heggen, M.; Rudi, S.; Strasser, P. *Nat. Mat.* **2013**, *12*, 765.

18. Hu, J.; Wu, L.; Kuttiyiel, K.; Goodman, K.; Zhang, C.; Zhu, Y.; Vukmirovic, M.; White, M.; Sasaki, K.; Adzic, R. *J. Am. Chem. Soc.* **2016**, *138*, 9294.

19. Wang, G.; Huang, B.; Xiao, L.; Ren, Z.; Chen, H.; Wang, D.; Abruña, H.; Lu, J.; Zhuang, L. *J. Am. Chem. Soc.* **2014**, *136*, 9643.

20. Zheng, Y.; Zhao, S.; Liu, S.; Yin, H.; Chen, Y.; Bao, J.; Han, M.; Dai, Z. *ACS Appl. Mater. Inter.* **2015**, *7*, 5347.

21. Gao, Q.; Ju, Y.; An, D.; Gao, M.; Cui, C.; Liu, J.; Cong, H.; Yu, S. *ChemSusChem* **2013**, *6*, 1878.

22. Liu, H.; Koenigsmann, C.; Adzic, R.; Wong, S. *ACS Catal.* **2014**, *4*, 2544.

23. Arico, A. S.; Stassi, A.; Modica, E.; Ornelas, R.; Gatto, I.; Passalacqua, E.; Antonucci, V. *J. Power Sources* **2008**, 178, 525.

24. Stamenkovic, V.; Schmidt, T. J.; Ross, P. N.; Markovic, N. M. *J. Phys. Chem. B* **2002**, 106, 11970.

25. Gasteiger, H. A.; Kocha, S. S.; Sompalli, B.; Wagner, F. T. *Appl. Catal., B* **2005**, 56, 9.

26. Zhao, X.; Chen, S.; Fang, Z.; Ding, J.; Sang, W.; Wang, Y.; Zhao, J.; Peng, Z.; Zeng, J. *J. Am. Chem. Soc.* **2015**, 137, 2804.

27. Hu, J.; Kuttiyiel, K.; Sasaki, K.; Su, D.; Yang, T.-H.; Park, G.-G.; Zhang, C.; Chen, G.; Adzic, R. R. *Catalysts* **2015**, 5, 1321.

28. Van der Vliet, D. F.; Wang, C.; Li, D.; Paulikas, A. P.; Greeley, J.; Rankin, R. B.; Strmcnik, D.; Tripkovic, D.; Markovic, N. M.; Stamenkovic, V. R. *Angew. Chem. In. Ed.* **2012**, 51, 3139.

29. Wang, C.; Daimon, H.; Onodera, T.; Koda, T.; Sun, S. *Angew. Chem., Int. Ed*. **2008**, 47, 3588.

30. Niu, W.; Li, L.; Liu, X.; Wang, N.; Liu, J.; Zhou, W.; Tang, Z.; Chen, S. *J. Am. Chem*. *Soc.* **2015**, 137, 5555.

31. Mavrikakis, M.; Hammer, B.; Norskov, J. K. *Phys. Rev. Lett*. **1998**, 81, 2819.

32. Hammer, B.; Hansen, L. B.; Norskov, J. K. *Phys. Rev. B* **1999**, 59, 7413.

33. Bard, A. J.; Faulkner L. R. Electrochemical Methods: Fundamentals and Applications, Wiley: New York, 2001, pp341.

34. Shao, M.; Shoemaker, M.; Peles, A.; Kaneko, K.; Protsailo, L. *J. Am. Chem. Soc*. **2010**,1 32, 9253.

35. Zhang, Y.; Hsieh, Y.-C.; Volkov, V.; Su, D.; An, W.; Si, R.; Zhu, Y.; Liu, P.; Wang, J. X.; Adzic, R. R. *ACS Catal.* **2014**, 4, 738.

36. Kongkand, A.; Subramanian, N.; Yu, Y.; Liu, Z.; Igarashi, H.; Muller, D. A. *ACS Catal*., **2016**, 6, 1578.

37. Wang, X.; Vara, M.; Luo, M.; Huang, H.; Ruditskiy, A.; Park, J.; Bao, S.; Liu, J.; Howe, J.; Chi, M.; Xie, Z.; Xia, Y. *J. Am. Chem. Soc*. **2015**, 137, 15036.

38. Hu, J.; Wu, L.; Kuttiyiel, K.; Goodman, K. R.; Zhang, C.; Zhu, Y.; Vukmirovic, M. B.; White, M. G.; Sasaki, K., Adzic, R. R. *J. Am. Chem. Soc.* **2016**, 138, 9294.

CHAPTER 5

REVEALING THE ATOMIC ORDERING OF BINARY INTERMETALLICS USING IN SITU HEATING TECHNIQUES AT MULTILENGTH SCALES

Reproduced from *Proc. Natl. Acad. Sci.* **2019**. 116 (6) 1974-1983

5.1 Abstract

Ordered intermetallic nanoparticles are promising electrocatalysts with enhanced activity and durability for the oxygen reduction reaction (ORR) in proton-exchange membrane fuel cells (PEMFCs). The ordered phase is generally identified based on the existence of superlattice ordering peaks in powder X-ray diffraction (PXRD). However, after employing a widely used post-synthesis annealing treatment, we have found that claims of "ordered" catalysts were possibly/likely mixed phases of ordered intermetallics and disordered solid solutions. Here, we employed *in situ* heating, synchrotron-based, X-ray diffraction to quantitatively investigate the impact of a variety of annealing conditions on the degree of ordering of large ensembles of Pt_3Co nanoparticles. Monte-Carlo simulations suggest that Pt_3Co nanoparticles have a lower order-disorder phase transition (ODPT) temperature relative to the bulk counterpart. Furthermore, we employed microscopic-level *in situ* heating electron microscopy to directly visualize the morphological changes and the formation of both fully and partially ordered nanoparticles at the atomic scale. In general, a higher degree of ordering leads to more active and durable electrocatalysts. The annealed Pt_3Co/C with an optimal degree of ordering exhibited significantly enhanced durability, relative to the disordered counterpart, in practical membrane electrode assembly (MEA) measurements. The results highlight the importance of understanding the annealing process to maximize the degree of ordering in intermetallics to optimize electrocatalytic activity.

5.2 Introduction

Pt-based intermetallics display superior electrocatalytic activity for the normally sluggish oxygen reduction reaction (ORR), as well as enable a decrease in Pt loading, compared to Pt/C, in proton exchange membrane (PEM) fuel cells.[1-5] As-synthesized, Pt-based alloy (Pt-M; M=Mn, Fe, Co, Ni, etc.) nanoparticles (NPs) generally form as a disordered solid solution in which the occupancy of a given site by Pt or M atoms is random and without local preference. The probability of occupancy by Pt or M is determined only by the stoichiometric ratio of Pt and M in a particular particle. These alloys generally suffer from a rapid loss of activity during electrochemical cycling due to the oxidation and dissolution of the M element and subsequent changes in both the particle morphology and the crystal structures.[15-6] In some systems, such as the Pt-Sn system, partially ordered intermetallic particles can be obtained at room temperature and further improved to fully ordered phase by low temperature annealing (200 ^{o}C).[8] However, in most other cases, post-synthesis annealing at high temperatures is required to transform the disordered solid solution phase into the ordered intermetallic phase. These intermetallic NPs show significantly better durability and improved electrocatalytic activity.[9-29] The enhanced durability of ordered intermetallics can be attributed to a more stable structure, which arises from the stronger heteroatomic Pt-M bond and a greater enthalpy of formation relative to its disordered counterpart. Ordered Pt_3M intermetallics normally have a primitive cubic crystal structure ($AuCu_3$-type, Pm-3m), while ordered PtM intermetallics typically have a tetragonal crystal structure (tcs) of the AuCu-type, P4/mmm. Because ordered intermetallics of Pt_3M and PtM have different crystal symmetry and additional atomic ordering, compared with their

disordered counterparts, they show extra peaks in X-ray diffraction (XRD), which are usually referred to as superlattice ordering peaks.

In studies of ordered intermetallic catalysts, there are two related questions that are of particular interest: Is the ordered intermetallic phase present and what is the phase fraction of the intermetallic? The first question can be quantitatively determined by the existence of superlattice ordering peaks in powder XRD.[11-29] By measuring the relative intensity of the superstructure peaks, information that is important but often neglected, the degree of ordering can be quantified. Having a measure of the degree of ordering is important to understand the intermetallic phase's contribution to catalyst performance and is necessary for understanding and optimizing the synthesis and annealing conditions.

After performing a systematic literature survey on ordered intermetallic nanoparticles, which included the most common Pt-M and Pd-M intermetallics, we realized that most of these studies only qualitatively described the formation of ordered intermetallics, and further quantitative understanding of the degree of ordering was required (Table 5.1).[11-29] For example, in our previous studies on Pt_3Co[2] and PdFe[6], intermetallic nanoparticles were found to be only partially ordered, despite our attempts to optimize the post-synthesis annealing conditions. In our other studies on PtSn[8] and PdZn[20], intermetallic nanoparticles were measured to be fully in the ordered phase. This suggests that it is likely that some claims of "ordered" intermetallic electrocatalysts may, in fact, be mixed phases of ordered intermetallic and disordered solid solution particles. It is possible that, due to high strain and surface energy, for some NP systems, and from a thermodynamic standpoint, only partial order can be achieved, even if a pure phase can be obtained at equilibrium in the bulk. In either case, the synthesized, disordered alloy needs to

overcome energetic barriers and kinetics to nucleate and grow the more stable, ordered intermetallic phase through the annealing treatment. However, the annealing process must be carefully designed/controlled. The newly formed ordered intermetallic phase can revert back to the disordered phase if the temperature surpasses a critical, order-disorder, phase transition (ODPT) temperature (T_c= 750 ^oC for bulk Pt_3Co).[30] The ODPT represents an intriguing process, coupling both kinetic and thermodynamic aspects. Further, nucleation and growth may also be (and likely are) influenced by the composition, morphology and size of each nanoparticle.

It is critical to understand the ODPT behavior of nanoparticles, which will, in turn, enable us to develop better annealing processes to increase the degree of ordering of NP electrocatalysts and, by extension, enhance fuel cell performance. However, mechanistic studies of such processes have been challenging due to the lack of suitable *in situ* techniques capable of tracking the dynamic phase transition and structural changes of metastable intermediates under real-time annealing conditions. Previous studies have only involved *in situ* heating, during XRD, to study the lattice strain of Pt-Cu intermetallics,[31] or have employed microscopic-level, *in situ* heating TEM, to investigate morphological changes of Pt [32] and Pt-based alloys.[33-37] However, to the best of our knowledge, none of them has attempted to quantitatively study the degree of ordering using X-ray diffraction and correlate it with the evolution of particle morphology and the formation of ordered intermetallics, at the atomic scale, using electron microscopy.

In this study, we have investigated the ODPT of Pt_3Co nanoparticles during a temperature annealing treatment, using both *in situ* heating synchrotron-based XRD and *in situ* heating TEM. We have studied, quantitatively, the effects of annealing and cooling

conditions (temperature and time) on the degree of ordering. We further employed *in situ* heating TEM to directly visualize the morphological and structural transition at the atomic-scale, during the thermal annealing treatment. Finally, we have systematically correlated catalyst durability to the degree of ordering, where a higher degree of ordering led to enhanced durability. This mechanistic study, involving both *in situ* heating XRD and *in situ* heating TEM, provides a microscopically detailed picture of post-synthesis processing.

Ref.	Claimed ordered intermetallic catalysts	Crystal Structure	Synthesis/annealing conditions	XRD database PDF number
1	Pt_3Ti	$AuCu_3$, Pm-3m	Pt_3Ti alloy annealed at 600 °C, 12h	03-065-3259
2	Pt_3V	$AuCu_3$, Pm-3m	Pt_3V alloy annealed at 650-700 °C, 24h	01-072-3016
3	Pt_3Cr	$AuCu_3$, Pm-3m	Pt_3Cr alloy annealed at 700 °C, 24h	01-071-7609
4	Pt_3Mn	$AuCu_3$, Pm-3m	$Pt(acac)_2$+$Mn(acac)_2$ OAm/OAc at 200 °C, 0.5h	01-071-9674
5	Pt_3Fe	$AuCu_3$, Pm-3m	Pt-Fe alloy annealed at 700 °C	01-071-5031 01-089-2051
6	Pt_3Co	$AuCu_3$, Pm-3m	Pt_3Co alloy annealed at 700 °C, 2h	01-071-7410
7	PtNi	AuCu,P4/mmm	$Pt(acac)_2$+$Ni(acac)_2$ $KBH(Et)_3$ in THF r.t.	01-072-2524
8	$PtCu_3$	$AuCu_3$, Pm-3m	$PtCu_3$ alloy annealed at 1000 °C, 10h	03-065-3247
9	Pt_3Zn	$AuCu_3$, Pm-3m	$Pt(acac)_2$+$Zn(acac)_2$ PVP in DMF,180°C, 9h	01-072-3028
10	Pt_3Zn	$AuCu_3$, Pm-3m	$Pd(acac)_2$+$Zn(acac)_2$ OAm/OAc at 350°C, 1h	01-072-3028
11	PtZn	AuCu,P4/mmm	Pt/C +Zn chip heated at 500 °C, 8h	01-072-3027
12	Pt_3Sn	$AuCu_3$,Pm-3m	H_2PtCl_6+$SnCl_2$, DDA+HDD,300°C, 0.5h	01-072-2977
13	PdFe	AuCu,P4/mmm	PdFe alloy annealed at 500 °C, 2h	01-089-2051
14	$Au_{10}Pd_{40}Co_{50}$	AuCu, Fm-3m	$Au_{10}Pd_{40}Co_{50}$ alloy annealed at 800 °C, 0.5h	01-071-7394 (PdCo)
15	PdCu	CsCl, Pm-3m	PdCu annealed at 400 °C	01-080-4575
16	PdCu	CsCl, Pm-3m	PdCu alloy, annealed at 375 °C, 1h	01-080-4575
17	PdZn	AuCu,P4/mmm	$Pd_2(dba)_3$+Et_2Zn OAm at 250 °C, 1h	01-072-2936
18	Pd_3Pb	$AuCu_3$, Pm-3m	Pd/C + $Pb(Ac)_2$, EG microwave 300W, 6min	01-089-2062
19	$AuCu_3$	Pm-3m	$Cu(Ac)_2$+Au NPs OAm/OAc at 300 °C	01-088-1731

20	AuCu	P4/mmm	$HAuCl_4$+$CuCl_2$ glycerol at 300 °C, 5h	01-089-2037
21	AuCu	P4/mmm	AuCu alloy annealed at 500 °C, 12h	01-089-2037

Table 5.1 All of the following reported catalysts are nanoparticles supported on carbon substrate.

Pt-M and Pd-M ordered intermetallic compounds:

M can be: Ti, V, Cr, Mn, Fe, Co, Ni, Cu, Zn, Sn, Pb, Bi

Abbreviations:

OAm: oleylamine; OAc: oleic acid; acac: acetylacetonate

Ac: acetate; dba: dibenzylideneacetone; Et: ethyl.

r.t.: room temperature

DDA: dodecylamine; HDD: 1,2-hexadecandiol; EG: ethylene glycol

References

1. Abe H, Matsumoto F, Alden L, Warren S, Abruña HD, DiSalvo FJ (2008) Electrocatalytic performance of fuel oxidation by Pt_3Ti nanoparticles. *J Am Chem Soc* 130:5452-5458.
2. Cui Z, Chen H, Zhao M, Marshall D, Yu Y, Abruña HD, DiSalvo FJ (2014) Synthesis of structurally ordered Pt_3Ti and Pt_3V nanoparticles as methanol oxidation catalysts. *J Am Chem Soc* 136: 10206-10209.
3. Ghosh T, Leonard B, Zhou Q, DiSalvo FJ (2010) Pt alloy and intermetallic phases with V, Cr, Mn, Ni, and Cu: synthesis as nanomaterials and possible applications as fuel cell catalysts. *Chem Mater* 22:2190-2202.

4. Kang Y, Murray C (2010) Synthesis and electrocatalytic properties of cubic Mn−Pt nanocrystals (nanocubes). *J Am Chem Soc* 132:7568-7569.
5. Chung D, Jun S, Yoon G, Kwon S, Shin D, Seo P, Yoo J, Shin H, Chung Y, Kim H, Mun B, Lee K, Lee N, Yoo S, Lim D, Kang K, Sung Y, Hyeon T (2015) Highly durable and active PtFe nanocatalyst for electrochemical oxygen reduction Reaction. *J Am Chem Soc* 137:15478-15485.
6. Wang D, Xin H, Hovden R, Wang H, Yu Y, Muller DA, DiSalvo FJ, Abruña HD (2013) Structurally ordered intermetallic platinum–cobalt core–shell nanoparticles with enhanced activity and stability as oxygen reduction electrocatalysts. *Nat Mater* 12:81-87.
7. Leonard B, Zhou Q, Wu D, DiSalvo F (2011) Facile synthesis of PtNi intermetallic nanoparticles: influence of reducing agent and precursors on electrocatalytic activity. *Chem Mater* 23:1136-1146.
8. Wang D, Yu Y, Xin H, Hovden R, Ercius P, Mundy J, Chen H, Richard J, Muller D, DiSalvo F, Abruña HD (2012) Tuning oxygen reduction reaction activity via controllable dealloying: a model study of ordered Cu_3Pt/C intermetallic nanocatalysts. *Nano Lett* 12:5230-5238.
9. Chen Q, Zhang J, Jia Y, Jiang Z, Xie Z, Zheng L (2014) Wet chemical synthesis of intermetallic Pt_3Zn nanocrystals via weak reduction reaction together with UPD process and their excellent electrocatalytic performances. *Nanoscale* 6:7019-7024.

10. Kang Y, Pyo J, Ye X, Gordon T, Murray C (2012) Synthesis, shape control, and methanol electro-oxidation properties of Pt–Zn alloy and Pt_3Zn intermetallic nanocrystals. *ACS Nano* 6: 5642-5647.
11. Miura A, Wang H, Leonard B, Abruña HD, DiSalvo FJ (2009) Synthesis of intermetallic PtZn nanoparticles by reaction of Pt nanoparticles with Zn vapor and their application as fuel cell catalysts. *Chem Mater* 21:2661-2667.
12. Wang X, Altmann L, Stöver J, Zielasek V, Bäumer M, Al-Shamery K, Borchert H, Parisi J, Kolny-Olesiak J (2012) Pt/Sn intermetallic, core/shell and alloy nanoparticles: colloidal synthesis and structural control. *Chem Mater* 25:1400-1407.
13. Xiong Y; Yang Y; DiSalvo FJ, Abruña HD (2018) Pt-Decorated Composition-Tunable Pd−Fe@Pd/C Core−Shell Nanoparticles with Enhanced Electrocatalytic Activity toward the Oxygen Reduction Reaction. *J Am Chem Soc* 140:7248-7255.
14. Kuttiyiel K, Sasaki K, Su D, Wu L, Zhu Y, Adzic R (2014) Gold-promoted structurally ordered intermetallic palladium cobalt nanoparticles for the oxygen reduction reaction. *Nat Commun* 5:5185.
15. Li G, Kobayashi H, Kusada K, Taylor J, Kubota Y, Kato K, Takata M, Yamamoto T, Matsumura S, Kitagawa H (2014) An ordered bcc CuPd nanoalloy synthesised via the thermal decomposition of Pd nanoparticles covered with a metal–organic framework under hydrogen gas. *Chem Commun* 50:13750-13753.
16. Jiang K, Wang P, Guo S, Zhang X, Shen X, Lu G, Su D, Huang X (2016) Ordered PdCu-based nanoparticles as bifunctional oxygen-reduction and ethanol-oxidation electrocatalysts. *Angew Chem Int Ed* 55:9030 –9035.

17. Cable R, Schaak, R (2007) Solution synthesis of nanocrystalline M-Zn (M: Pd, Au, Cu) intermetallic compounds via chemical conversion of metal nanoparticle precursors. *Chem Mat* 19:4908-4104.
18. Gunji T, Noh S, Tanabe T, Han B, Nien C, Ohsaka T, Matsumoto F (2017) Enhanced electrocatalytic activity of carbon-supported ordered intermetallic palladium–lead (Pd_3Pb) nanoparticles toward electrooxidation of formic acid. *Chem Mater* 29:2906-2913.
19. Chen W, Yu R, Li, L, Wang A, Peng Q, Li Y (2010) A seed-based diffusion route to monodisperse intermetallic CuAu Nanocrystals. *Angew Chem Int Ed* 49:2917-2921.
20. Wang G, Huang B, Xiao L, Ren Z, Chen H, Wang D, Abruña HD, Lu J, Zhuang L (2014) Pt skin on AuCu intermetallic substrate: a strategy to maximize Pt utilization for fuel cells. *J Am Chem Soc* 136:9643-9649.
21. Sra A, Schaak R (2004) Synthesis of atomically ordered AuCu and $AuCu_3$ nanocrystals from bimetallic nanoparticle precursors. *J Am Chem Soc* 126:6667-6672.

5.3 Experimental Section

5.3.1 Preparation of Pt_3Co/C Catalysts

The Pt_3Co/C catalysts were prepared by an impregnation method. In a typical synthesis, 0.1 mmol (51.8 mg) $H_2PtCl_6 \cdot 6H_2O$ and 7.9 mg (0.034 mmol) $CoCl_2 \cdot 6H_2O$ were dissolved in deionized water, with 86 mg of Vulcan XC-72 carbon support dispersed later to make the mass loading of Pt_3Co nanoparticles to be ~ 20%. After ultrasonic mixing for 30 min, the suspension was heated under magnetic stirring to evaporate extra moisture and form a smooth and thick slurry. The slurry was then dried in an oven at 60 ^oC. After being ground in an agate mortar, the resulting dark and free-flowing powder was heated in a tube furnace at 300 ^oC under flowing forming gas (5% H_2, 95% N_2) for 2 h. The high-temperature treated samples were prepared by annealing the as-synthesized Pt_3Co/C alloy at specific temperatures for 2 h under forming gas. Powder XRD of Pt_3Co/C was performed using a Rigaku Ultima VI X-ray diffractometer, which was measured from 10^o to 90^o at a scan rate of 2^o/min.

5.3.2 Electrochemical Characterizations

Electrochemical activity and durability were measured at room temperature in a 0.1M $HClO_4$ solution using a Solartron potentiostat. 5 mg of the 20 wt.% Pt_3Co/C intermetallic catalyst were mixed with 2 mL of 0.05 wt.% Nafion/ethanol solution and sonicated subsequently to form a well-dispersed catalyst ink. 10 µL of the resulting catalyst ink were loaded onto a glassy carbon electrode (D = 5.0 mm), followed by the thermal evaporation of the ethanol solvent. The mass loading of Pt_3Co on the electrode was calculated to be 22 µg/cm^2. A coiled Pt wire was used as the counter electrode and a Ag/AgCl in saturated KCl served as the reference electrode. ORR measurements were

carried out using a rotating disk electrode (RDE, Pine Instruments) in an oxygen-saturated 0.1M $HClO_4$ solution at a rotation rate of 1600 rpm and a sweep rate of 5 mV/s. ORR polarization profiles were obtained after 50 cycles over the potential range from 0.05 to 1.1 V at 50 mV/s in 0.1M $HClO_4$ to remove surface contamination. Cyclic voltammetry (CV) was performed to obtain the electrochemical surface area (ECSA) by integrating the charge over the hydrogen adsorption/desorption region from 0.05 V to +0.4 V vs RHE. We used a conversion factor of 200 $\mu C/cm^2$, according to recent results from Feliu.[50-51] Durability tests were carried out by continuous CV scanning for 2,000 cycles over the potential range between 0.6 to 1 V vs RHE. ECSA measurements and ORR profiles were also obtained after cycling to evaluate the electrocatalytical durability.

5.3.3 MEA Measurements

Fuel cell evaluations of each catalyst were done in a membrane-electrode assembly (MEA) with the electrocatalyst of interest at the cathode. The active area of the fuel cell single cell was 53 cm^2. The metal weight percent on carbon black-supported electrocatalysts was approximately 25%. 2.8 g of catalyst were mixed with 3.4 g of perfluorosulfonic acid (PFSA) ionomer (900 equivalent weight) in a 60 g water-propanol solution, then coated on a gas-diffusion carbon paper to fabricate a gas-diffusion electrode (GDE). The electrode Pt loadings were 0.1 and 0.025 $mgPt/cm^2$ for the cathode and anode, respectively. The MEA was then fabricated by hot pressing an 18 μm thick PFSA-based membrane between the cathode and anode GDEs at 146°C, 3 MPa for 4 min. Detailed fabrication procedures have been discussed elsewhere.[52] Catalyst accelerated stability tests (AST) recommended by the U.S. Department of Energy (DOE) were used in this study (https://www.energy.gov/sites/prod/files/2017/05/f34/fcto_myrdd_

fuel_cells.pdf). The AST consisted of 30,000 trapezoidal voltage cycles between 0.6 and 0.95 V, at 80°C, 100% relative humidity, and ambient pressure. The dwell time at each voltage was 2.5 s and the ramp time was 0.5 s and each cycle took 6 s. The fuel cell performance, electrochemically active surface area (ECSA), and oxygen reduction reaction (ORR) mass activity were measured after 0, 10,000 and 30,000 cycles during the AST. ORR activity was reported at 0.9 VRHE at 80°C, 100% relative humidity, and 1 bar of O_2.1 Pt ECSA was measured by CO stripping in an MEA.[53] Fuel cell current-voltage and power density characteristics were evaluated under the following operating conditions in the order of anode/cathode: H_2/air, 94°C, 65/65% RH, 250/250 kPaabs, outlet, reactant stoichiometries of 1.5/2.

5.3.4 *In situ* Heating Synchrotron-based X-ray Diffraction (XRD) Setup

The *in situ* X-ray diffraction measurements were performed at the A1 station of the Cornell High Energy Synchrotron Source (CHESS) using a customized setup. The sample was heated, *in-situ*, using a SabreTube furnace (Absolute Nano, Wixom, MI) which consists of a resistively heated strip of single crystal Si inside a quartz tube. The furnace was fitted with a customized quartz tube with two Kapton windows to allow the incident X-ray beam to reach the sample and the diffracted beam to reach the detector. The furnace was continually purged with forming gas (5% H_2, 95% N_2) to prevent the oxidation of the sample. Sample holders were lithographically fabricated from a double side polished Si wafer by etching 200 μm deep wells using KOH. The holder had a nitride coating to prevent current from passing through the sample holder. The sample powder was mixed with acetone before being pressed into the well to help in forming a stable powder compact. The furnace temperature was measured by a thermo couple pushed up against

the bottom of the heating element. The linear offset between the thermocouple and sample temperature was characterized by the observation of the melting point of several metals (Fig. S1). During diffraction, the sample was held at a fixed angle to the incident beam.

5.3.5 *In Situ* Heating Synchrotron-based XRD Measurements

XRD experiments were performed at the A1 station (X-ray energy = 19.6 keV, λ = 0.63 Å) in CHESS. A Pilatus 100K (Dectris, Switzerland) pixel array detector was used to collect the X-ray signal, and the temperature calibration of the setup was conducted by measuring the melting point of metal powders (Al, Sn and Zn) with a purity > 99.99% by tracking their changes in the XRD pattern with increasing temperature. The temperature difference between the measured and real values was 4 °C (Figure 5.2A). Directly measured d-spacing data were converted to the standard 2θ values when using Cu Kα radiation (λ =1.5406Å). The 2θ values of the XRD were calibrated based on a CeO_2 reference sample. The 2θ resolution was also measured using CeO_2 powder and was found to be at least 0.1°.

5.3.6 Monte-Carol Simulation

Monte Carlo (MC) simulations, using N-body potentials, provide an efficient means to quickly simulate the equilibrium and kinetic properties of large atomic systems (~10,000 particles). We employ a commonly used semi-empirical atomistic potential derived in the framework of the second moment approximation of the density of states in a tight-binding model (TB-SMA).[1] The potential energy at any given site *i*, is comprised of two distinct parts: an attractive band-term (N-body interaction) given by E_i^b,

$$E_i^b = -\sqrt{\sum_{j, r_{ij} < r_{\alpha\beta}^{cut1}} \xi_{\alpha\beta}^2 \exp\left[-2q_{\alpha\beta}\left(\frac{r_{ij}}{r_{\alpha\beta}^0} - 1\right)\right]}$$

and a Born-Mayer type (pair-wise) repulsive term given by E_i^r,

$$E_i^r = \sum_{j, r_{ij} < r_{\alpha\beta}^{cut1}} A_{\alpha\beta} \exp\left[-2p_{\alpha\beta}\left(\frac{r_{ij}}{r_{\alpha\beta}^0} - 1\right)\right]$$

And so, the total system energy, E_N, where N is the total number of 'sites' or atoms in the system is given by,

$$E_N = \sum_{i=1}^{N} \left(E_i^b + E_i^r\right)$$

The parameter set used is the same as the one used in Ref. 2. The nanoparticle (NP) cluster is carved out from an equilibrated snapshot of the simulated bulk system. The values of the chosen radii correspond to multiples of the lattice vector of the equilibrated bulk phase. The stoichiometric ratio (Pt:Co) is kept as close to 3 as possible, without inducing defects. The potential is cut-off at the third-nearest neighbor distance ($r_{\alpha\beta}^{cut1} = \sqrt{3} r_{\alpha\beta}^0$) and extended up to the fourth-nearest neighbor distance ($r_{\alpha\beta}^{cut2} = 2r_{\alpha\beta}^0$) using a tail correction that replaces the exponential functions with a fifth-order polynomial function.

To simulate the NP clusters with N particles, MC simulations are performed in the constant temperature, constant volume (NVT) ensemble without periodic boundaries. Each MC cycle consists of N translational moves (to allow thermal relaxation), and N/3 exchange moves between random Co and Pt atoms (to facilitate faster equilibration of the

spatial compositional distribution). The bulk system was simulated in an isothermal-isobaric (NPT) ensemble with periodic boundaries, with each MC cycle consisting of N (N=864) translational, N/3 exchange and N/30 volume moves.[3] Each NP cluster is initially equilibrated by gradually ramping up the number of exchange moves per MC cycle from zero to N/3 over ~25,000-50,000 MC cycles. This is done to allow the NP to smoothly transition from its bulk lattice environment to vacuum.

To characterize the local order in the system, a Warren-Cowley[4] type short-range order parameter (SROP) is calculated as

$$SROP = 1 - \frac{m_i - m_{i,0}}{c_j - m_{i,0}} = \frac{m_i - c_j}{m_{i,0} - c_j}$$

where *i, j (i≠j)* refer to species (Co/Pt), m_i is the average number of heterogeneous first-neighbor bonds in the system keeping species *i* at the center, $m_{i,0}$ is the value of m_i in the corresponding fully ordered state, c_j is the mole fraction of the other species. For the $L1_2$ phase, $m_{Co,0} = 1$ and $m_{Pt,0} = 4/12$. First-neighbor bonds are defined as all the bonds within the first coordination sphere; i.e., a sphere of radius equal to 1.2 times the distance to the first peak of the radial distribution function, $g(r)$.

Similarly, to measure global order, the long-range order parameter (LROP).[5] is also evaluated for the $L1_2$ phase as

$$LROP = c^{\alpha} + c^{\beta} + c^{\gamma} - \frac{c^{\delta}}{3} - 2$$

where $\alpha, \beta, \gamma, \delta$ are assigned to label the four simple cubic sub-lattices (in decreasing order of c, such that $c^{\alpha} > c^{\beta} > c^{\gamma} > c^{\delta}$) that comprise the face-centered cubic (FCC) lattice, and c denotes the fractional sub-lattice occupation by Pt atoms, i.e. c = (total number of Pt atoms on the sub-lattice)/(total number of atoms on the sub-lattice). As with

the SROP, by definition, LROP of 0 and 1 represent completely disordered and perfectly ordered lattices. The transition temperatures are estimated by performing serial heating runs (with temperature increments of 5˚C, and averaging over 32 independent trajectories) and locating the inflexion point of the LROP and SROP curves.

Since the model parameterization used underestimates the ODT temperature (when compared to the experimentally calculated value[6]) by about 500˚C , the results are rigidly shifted to match the experimental ODT temperature as detected by the OPs ($T_{ODT}\sim 500K$). Despite this quantitative shortcoming of the model, it is expected to be able to capture the relative trends in physical behavior.

Simulation References:

1. Rosato, V., Guillope, M. & Legrand, B. Thermodynamical and structural properties of f.c.c. transition metals using a simple tight-binding model. *Philos. Mag. A* **59,** 321–336 (2006).

2. Front, A., Legrand, B., Tréglia, G. & Mottet, C. Bidimensional phases in Co–Pt surface alloys: A theoretical study of ordering and surface segregation. *Surface Science* **679,** 128–138 (2019).

3. Parrinello, M. & Rahman, A. Polymorphic transitions in single crystals: A new molecular dynamics method. *J. of Appl. Phys.* **52,** 7182–7190 (1981).

4. Cowley, J. M. Short- and Long-Range Order Parameters in Disordered Solid Solutions. *Phys. Rev.* **120,** 1648 (1960).

5. Lopes, A., Tréglia, G., Mottet, C. & Legrand, B. Ordering and surface segregation in Co1−cPtc nanoparticles: A theoretical study from surface alloys to nanoalloys. *Phys. Rev. B* **91,** 035407 (2015).

6. Okamoto, H. Co-Pt (Cobalt-Platinum). *J. Phase Equilib.* **22,** 591 (2001).

5.3.7 Electron Microscopy Characterizations

Ex situ atomic-scale STEM images were recorded using an aberration-corrected FEI Titan Themis STEM operated at 300 keV with a convergence angle of 30 mrad. *In situ* heating STEM experiments were conducted in a FEI Tecnai F20 with a Schottky field emission gun at 200 keV with a convergence angle of about 9.8 mrad. An annular, dark field detector was used to collect the image signal with high collection angles to achieve better atomic number sensitivity. The temperature was controlled using a Protochips Aduro heating holder with the sample powder dispersed on a model E-AHA21 Protochips E-chip, which has an amorphous carbon film that covered the viewing window. The temperature was pre-calibrated before use. The particle size distribution was calculated from STEM images using an automated procedure implemented in MATLAB. A light Gaussian smoothing was applied to each image to reduce noise, and the uneven background of the carbon support was estimated and removed using a gray-scale morphological opening operation with a 30 nm radius, spherical, structure element. The Pt_3Co particles were then segmented using an active contour with the Chan-Vese method.[54] The active contour segmentation began with an initial estimate from threshold segmentation and operated on the square root of the background-subtracted STEM image to reduce the impact of thickness variations from particles of different sizes. After the Pt_3Co nanoparticles were segmented, their size distribution was calculated using a procedure that estimated the local radius of particle sub-regions. This provided a more robust estimate of size than a simple spherical-particle approximation for particles that had irregular shapes or were overlapping in the STEM images. Particles were separated into sub-regions using a watershed transform, and the local radius for each sub-region

was calculated as the maximum distance from the particle edge in that sub-region. The sub-regions were weighted according to their projected area in the image for inclusion in the particle size distribution and for estimation of the specific surface area (SSA). Palladium acetylacetonate ($Pd(acac)_2$), iron acetylacetonate ($Fe(acac)_3$), triethylene glycol, 1,2-hexadecanediol, sodium hydroxide, potassium tetrachloroplatinate(II) (K_2PtCl_4) and Nafion (5% wt) were purchased from Sigma-Aldrich. All chemicals were used as received without further purification. Vulcan XC-72 carbon black was from Cabot Corporation.

5.4 Result and Discussion

5.4.1 *In Situ* Heating Synchrotron-based X-ray Diffraction

Pt_3Co/C disordered alloys were synthesized using an impregnation method[2] in which precursors were reduced under forming gas at 300 °C and the as-synthesized Pt_3Co/C catalysts were subsequently annealed further at high temperatures under forming gas. The XRD patterns of the as-synthesized Pt_3Co/C and Pt_3Co/C annealed at 700 °C in a conventional tube furnace were first measured in the *in situ* heating XRD stage to verify the reliability of the set-up (Figure 5.1A). After annealing, the sample exhibited multiple superlattice ordering peaks: (100) at 23°, (110) at 32.5°, (210) at 53.5°, (211) at 59°, (300) at 74.3° and (310) at 79°, which match well with XRD reference of ordered intermetallic Pt_3Co (PDF #04-006-8057), confirming the formation of ordered phase. In this experiment the orientation of the crystallites should be random both at the nanoparticle (NP) level, and within the NP/C mixture. Beyond this assumption, the data itself provide assurance that the orientations of the crystallites are sufficiently random. First, data were

collected using a 2D detector and integrated to generate the 1D data sets. The detector image of the as-prepared Pt_3Co intermetallic NPs collects a portion of the ring, as shown Figure 5.2B. It can be seen, particularly in the smallest ring, that there is no change in intensity as a function of position along the ring, indicating a random orientation of grains. The peak positions were consistent with the standard database of bulk Pt_3Co-ordered intermetallics (PDF # 04-004-5243) (Figure 5.1B). After subtracting the background, by selecting three points to form the baseline (Figure 5.1C, inset), the XRD pattern was analyzed further to quantify the relative content of the ordered phase. We employed the intermetallic peak (110) at 32.5° for analysis. It is the second strongest intermetallic peak, yielding a sufficient signal-to-noise ratio for further analysis. While the strongest intermetallic peak is the (100), it is located within the diffuse scattering ring from the carbon support, making it difficult to accurately extract the integrated intensity of this peak, precluding an accurate intensity analysis. Because there was some overlap between the (111) and (200) peaks, due to the broadening of the peaks by the relatively small domain/crystallite size, the ratio of the integrated area under the (110) peak (red) to that of the sum of the areas under the (111) and (200) peaks (blue), $I_{(110)}/(I_{(111)}+I_{(200)})$, was used so as to yield a more accurate quantitative evaluation. The theoretical value of $I_{(110)}/(I_{(111)}+I_{(200)})$, based on the structure factor, for Pt_3Co is 0.078, as calculated using the XRD database of ordered Pt_3Co. This corresponds to a 100 % of fully ordered intermetallic Pt_3Co particles (Figure 5.1D). The relative fraction of the ordered phase

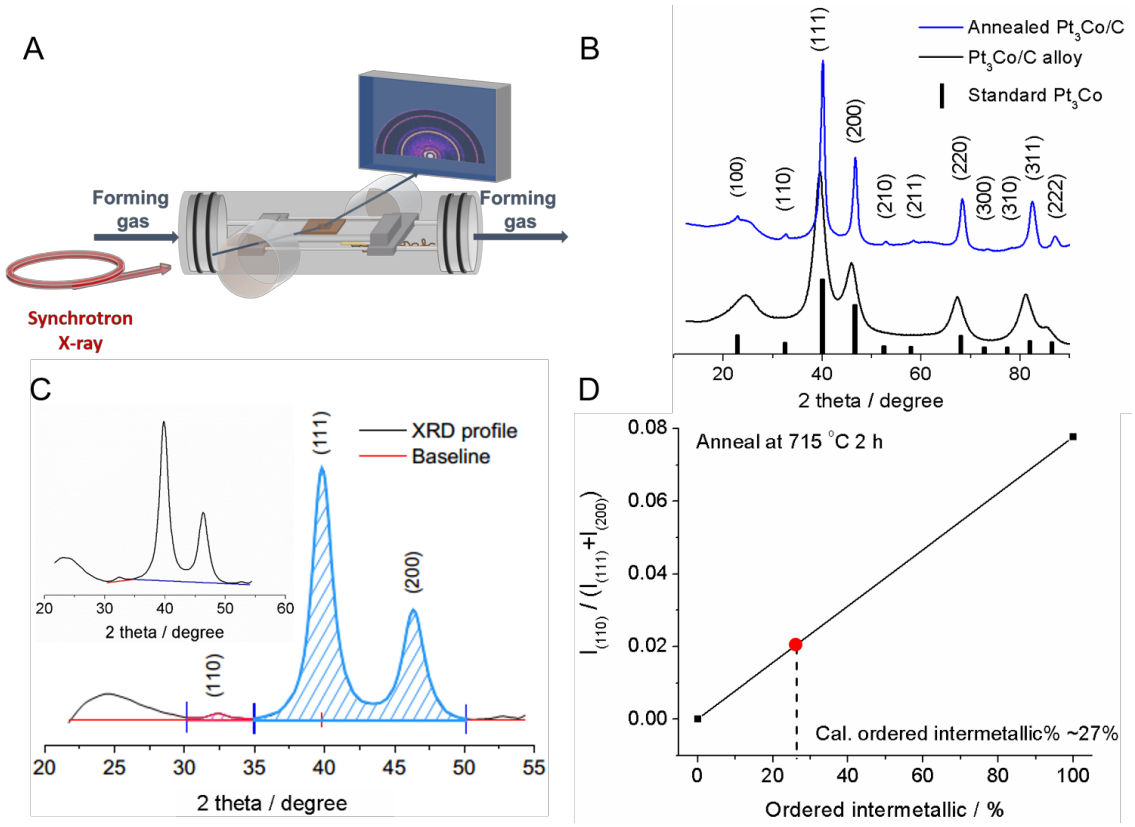

Figure 5.1 (A) Schematic illustration of the home-made device for the *in situ* synchrotron-based, X-ray diffraction (XRD) study. (B) XRD patterns of the as-synthesized Pt_3Co/C alloy and Pt_3Co/C after further annealing at 700 °C in the in-situ heating cell. (C) Quantitative analysis of the peak integral of the (110) ordering peak, and the (111) and (200) major peaks. Inset: illustration of background subtraction. (D) Quantitative calculations of the relative content of ordered intermetallic based on the assumption of a linear relationship between the ratio of the integrated areas of the ordered intermetallic peak at (110) to the sum of the (111) and (200) peaks.

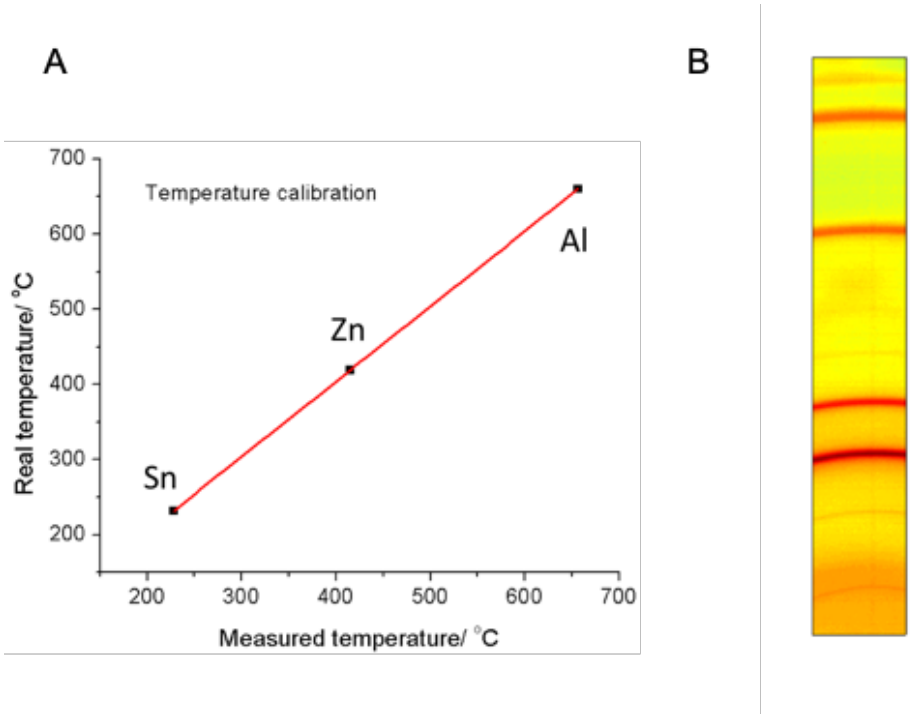

Figure 5.2 (A) Temperature calibration of the *in situ* heating stage (Si substrate). The Y axis is the theoretical melting temperature of metals and the X axis is the measured melting temperature from the heating stage. The plot shows a linear offset between the measured temperature and the actual temperature (B) XRD pattern of as-synthesized annealed Pt_3Co collected from 2D detector.

exhibits a linear relationship with $I_{(110)}/(I_{(111)}+I_{(200)})$. This approach is valid since the intensity of the (111) and (200) peaks, the fundamental reflections, are constant for both ordered and disordered phases since the average electron density for these planes is fixed, assuming a fixed composition. For example, we found that Pt_3Co/C annealed at 715 °C had a peak ratio of 0.020, and therefore we calculated that the phase fraction of nanoparticles adopting the ordered phase was approximately 26%.[2]

To better understand the changes in XRD patterns as a function of the annealing temperature, the as-synthesized Pt_3Co/C alloy catalysts were annealed at different temperatures, for 2 h each, in flowing forming gas (Figure 5.3A). After the two-hour anneal, the intensity of the (110) superstructure peak at ~33° was compared to the fundamental (111) reflections. We found that the ratio, $I_{(110)}/(I_{(111)}+I_{(200)})$, increased with annealing temperature over the 600 °C to 750 °C range. The increased ordering is likely due to the enhanced ability to overcome the nucleation and diffusion barriers with increasing temperature. The maximum relative superstructure peak intensity at 750 °C was 0.023, corresponding to an ordered intermetallic phase fraction of about 30%. When annealed at 825 °C for 2 h, the relative fraction of the ordered phase went to zero, within the signal to noise level, consistent with the presence of only the disordered phase which is stable when $T > T_c$ (750 °C) in the bulk Pt-Co phase diagram. Similar changes at different temperatures were also observed in the powder XRD under the same conditions during the post-synthesis annealing treatment in a traditional tube furnace. (Figure 5.4).

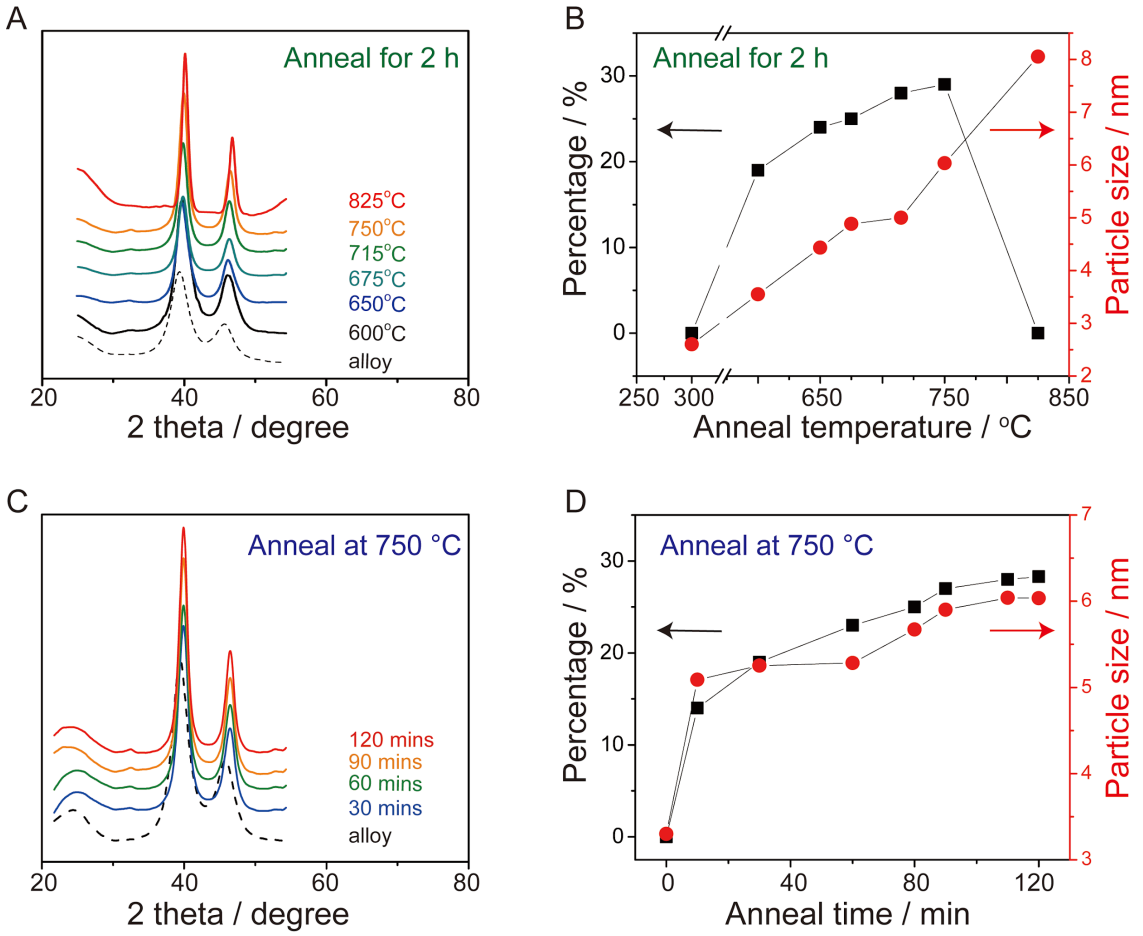

Figure 5.3 (A) *In situ* heating XRD patterns of Pt_3Co/C annealed at various temperatures. The dashed line represents the as-synthesized Pt_3Co/C alloy. (B) Calculated relative content of ordered intermetallic Pt_3Co/C formed and particle size (calculated from the width of the (111) peak). (C) *In situ* heating XRD patterns of Pt_3Co/C at 750 °C, the optimal temperature, as a function of annealing time. (D) Calculated relative content of ordered Pt_3Co/C formed, and particle size.

There are several factors that may influence the behavior of an ensemble of particles during annealing. The first is the diffusion rate, both intra- and inter-particle, which increases with increasing temperature. Overall, diffusion will drive the composition to be spatially uniform. After sufficient time, all particles will be alike. Concomitantly, the average particle size will grow. Further, higher diffusion rates will allow the NP's to reach their equilibrium state faster. During the cooling process, the driving force for nucleation increases and the diffusion rate decreases as the temperature falls below the phase transition temperature. The next consideration is the stoichiometric ratio of the components (Pt to M). The stoichiometric ratio may vary from particle to particle due to the randomness of aggregation of Pt and M to a growing particle. The average ratio, of course, will be determined by the ratio of reagents used in a particular synthesis procedure. Particle size and morphology may also play a factor in the overall behavior. Finally, even at thermodynamic equilibrium, the degree of ordering will likely be less than 100 % due to strain and finite size effects. Since thermal equilibrium is reached by diffusion, low temperature anneals may not result in nucleation nor subsequent growth.

We observed a sharper (111) peak at the higher annealing temperatures (Figure 5.3A). The average domain size of each ensemble of particles was estimated by the Scherrer equation using the full width at half maximum (FWHM) of the (111) peak, which is fairly consistent with the particle size determined from our TEM analysis (*vide infra*). After a 2 h annealing process, the average domain size of Pt_3Co/C increased from 3.5 nm to 6 nm with increasing annealing temperature from 600 ^oC to 750 ^oC, and it became as large as 8 nm when the temperature was 825 ^oC. The (111) diffraction peak also shifted gradually to higher angles, indicating that the corresponding lattice d-spacing decreased

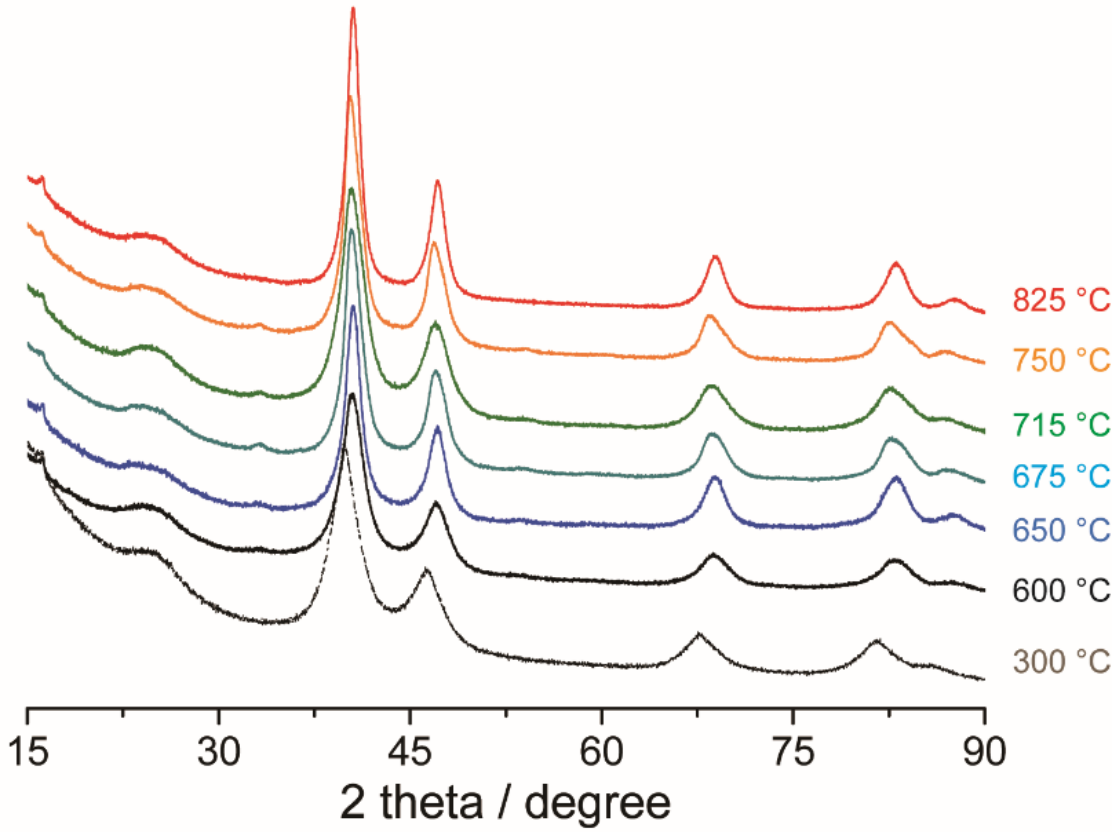

Figure 5.4 Powder XRD patterns of Pt_3Co/C annealed at various temperatures for 2h in a flow furnace in the lab. The change in ordering peak at ~33° is fairly consistent with Figure 5.3 A.

from 2.29 Å, before annealing, and reached a value as low as 2.24 Å after a 2h anneal at 825 °C. The d-spacing approached the theoretical value of ordered bulk Pt_3Co, 2.21 Å, (Figure 5.5A). The relative content of the ordered phase and the particle size, both increased with increasing temperatures when the temperature was 600~750 °C (Figure 5.3B). The above behavior is similar to that of bulk $AuCu_3$ and PtCo nanoparticles.[38-42]

At 750 °C, which was the optimal annealing temperature for the highest degree of ordering achieved in this experiment, the XRD patterns were tracked dynamically as a function of annealing time (Figure 5.3C). The (110) ordering peak became more pronounced, and the (111) peak became sharper and shifted to higher angles with longer annealing times. The calculated phase content of ordered Pt_3Co/C and domain sizes exhibited a similar trend; they both increased rapidly during the first half hour, and gradually approached a relatively stable plateau (Figure 5.3D). This suggested that 2 h was sufficient time to achieve a steady state (or possibly equilibrium) and optimal contents of the ordered phase at such temperatures. After 2 h of annealing at 750 °C, Pt_3Co/C had an average domain size of 6 nm and a (110) ordered peak intensity of 30% relative to the maximum possible, if ordering was complete. In addition, the d-spacing decreased during the first 30 mins and approached a plateau (Figure 5.5B), indicating that the lattice contracted during annealing as the average order increased.

To investigate quantitatively the influence of Pt_3Co particle size (3~8 nm) on the onset of disorder, we used Monte-Carlo simulations to calculate the degree of substitutional ordering at thermodynamic equilibrium at various temperatures from the average atomic occupation of the lattice sites.[38-41] The order-disorder transition (ODT) was characterized

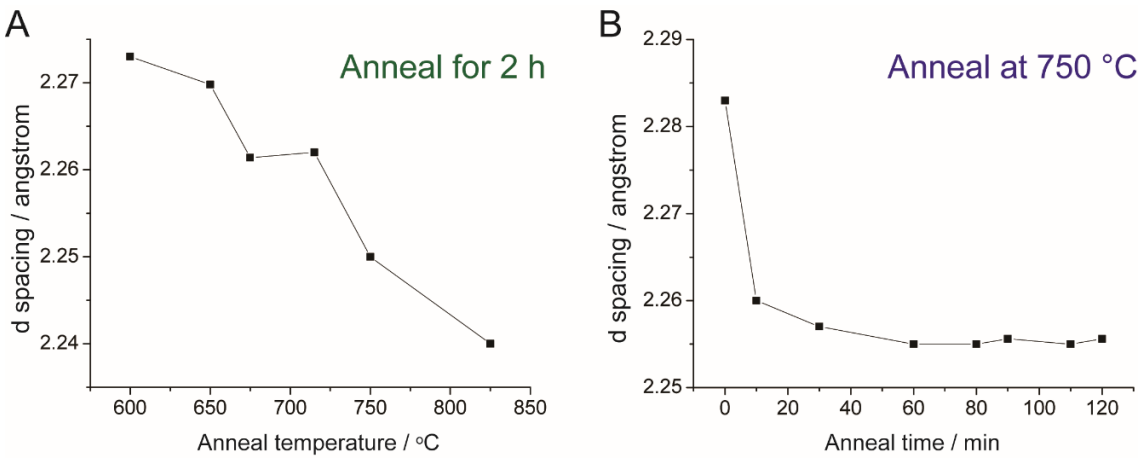

Figure 5.5 (A) Measured d-spacing of Pt_3Co/C after 2 h annealing at various temperatures. (B) Measured d-spacing of Pt_3Co/C at different annealing times at 750 °C.

by both the (long-range order parameter) LROP and the (short-range order parameter) SROP and plotted as a function of temperature in Figure 5.6 for two NP sizes (2.9 and 5.2 nm) and the bulk system (see calculation details in the supporting information). For each system, the temperature at which the LROP and SROP curves exhibit inflexion points is roughly the same and marks the ODT temperature, T_{ODT}. At T_{ODT}, the system undergoes a transition from the $L1_2$ phase (Figure 5.6B) to a disordered phase via an intermediate, transient $D0_{22}$ phase (Figure 5.6C). The $D0_{22}$ phase also possesses global long-range order with lower crystal symmetry but is not captured by the LROP used (Figures 5.6B-C). The T_{ODT} of the NPs is significantly lower than that of the bulk system (750 ºC), and there is a clear trend of a decrease in T_{ODT} with a decrease in NP size. This indicates that for a certain range of temperatures (below the bulk T_{ODT}) one could observe larger NPs maintaining higher degree of substitutional order than smaller NPs, which is consistent with our experimental observations in Figure 5.3B.

To dynamically track the evolution of the superlattice ordering peaks during the annealing process, the XRD patterns of Pt_3Co/C were obtained by increasing the temperature at a very slow rate of 0.5 ºC/min from 620 ºC to 830 ºC (Figure 5.7A). Because each diffraction scan took less than 2 min, the temperature resolution was within 1 ºC. With higher annealing temperatures, the (110) peak became more pronounced and attained a maximum at 720-750 ºC, while the absolute intensity of the (111) peak decreased, due to additional disordering in the lattice above the transition temperature as well as to Debye-Waller effects.[43-44] The relative magnitude of the peak intensity ratio of (110) to (111), with the maximum ratio normalized to 100%, was employed as a simple (and reliable) metric to represent the relative amount of the ordered phase (Figure 5.7B).

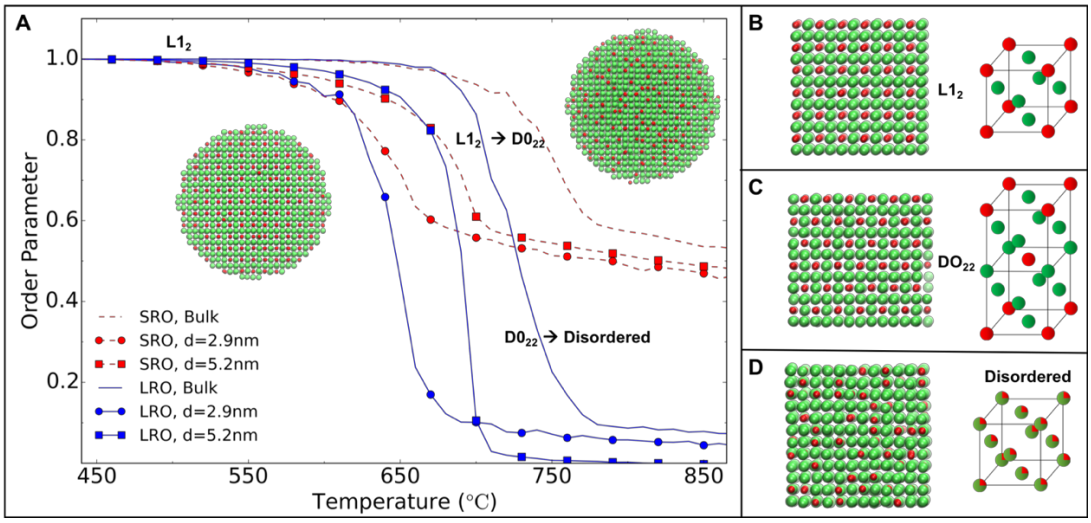

Figure 5.6 (A) Simulation results for the SROP (red, dashed line) and LROP (blue, solid line) as a function of temperature for bulk (N=864, no marker) and spherical NPs with diameter d=2.9 nm (N=800, circles) and d=5.2 nm (N=4800, squares, with snapshots shown at temperatures just before the ODT on the left, and just after the ODT on the right). The temperatures are rigidly shifted so as to match the simulation results to the experimental Bulk order-disorder transition (ODT) temperature. As the size of the NP is reduced, the ODT temperature for the NPs also decreases. Snapshots of the bulk trajectory taken at increasing temperatures showing (B) ordered intermetallic phase, $L1_2$, (C) $D0_{22}$ state with global long-range order and lower crystal symmetry, and (D) disordered solid solution phase. The green and red atoms represent Pt and Co, respectively.

Because the annealing treatment of binary intermetallics during synthesis must be accompanied by cooling of the catalysts down to room temperature, the cooling procedure, after the *in situ* annealing process, was also investigated. Pt_3Co/C powders, annealed at 715 °C for 2 h were used as a baseline to measure the effect of different cooling rates (Figure 5.8A). After annealing at 715 °C for 2 h, and cooling to room temperature, the (111) peak shifted to higher angle, indicating that the lattice had contracted further. Cooling experiments were conducted at two different cooling rates after 2 h of annealing (Figure 5.8B). The first was a slow rate of 6 °C/min, and in the second, the sample was cooled by turning off the electric heater and allowing the gas in the device to cool naturally at a rate of ~30 °C/min. At the slower cooling rate, the relative contents of the ordered Pt_3Co/C phase increased, which was ascribed to the extended period for the atomic rearrangement to the thermodynamically-favored state. The sample cooled at a higher rate showed only a slight increase in ordered phase content.

In summary, the effects of the annealing and cooling processes at different annealing temperatures and times on the ordered intermetallic content, were investigated. We conclude that the optimal annealing conditions were to anneal Pt_3Co/C at 750 °C for 2 h and then to cool to room temperature at a slow rate (e.g., 6 °C/min). Other cooling procedures may lead to an even larger fraction of ordered particles. Such processing parameters are used to manufacture heat-resistant CorningWare glass, and in toughening metals by age precipitation hardening, for example.

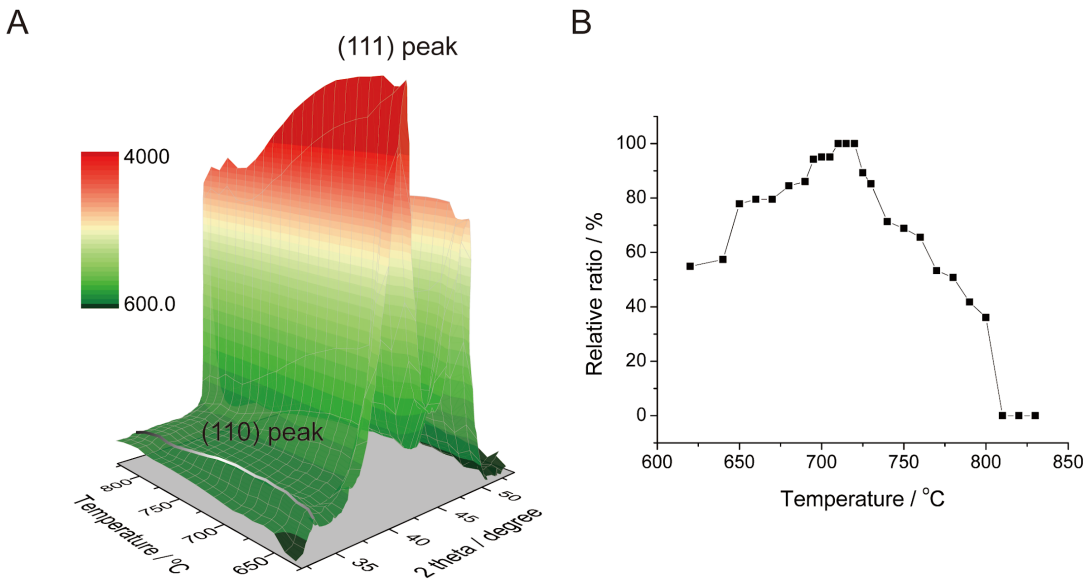

Figure 5.7 (A) *In situ* heating XRD patterns of Pt_3Co/C annealed from 620 °C to 830 °C at a slow temperature ramping rate of 0.5 °C/min (B) Relative peak integral ratio of the (110) to (111) peaks (with the maximum ratio normalized to 100%) at a series of temperatures.

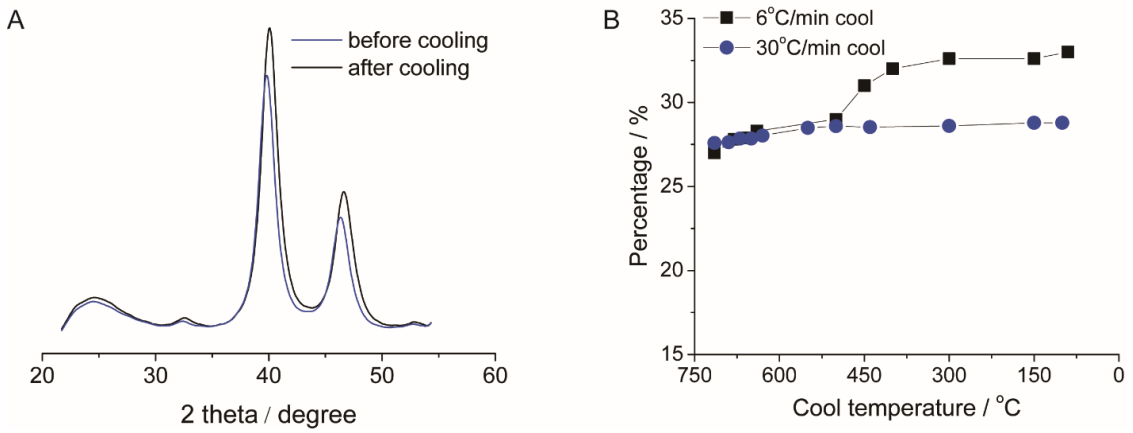

Figure 5.8 (A) XRD patterns of Pt_3Co after annealing at 715 °C for 2 h, and after cooling down to room temperature. (B) Relative contents of ordered intermetallic Pt_3Co/C under two different cooling rates. X-axis represents the monitored temperatures during the cooling process.

5.4.2 *In Situ* Heating STEM

In addition to enabling structured ordering, the thermal annealing process can also alter the morphology of the Pt_3Co nanoparticles. The most important morphological change was coarsening of the Pt_3Co particles, which increased their size and decreased the catalysts' active surface area. To observe these morphological changes, we conducted *in situ* annealing experiments in a scanning transmission electron microscope (STEM).

A Pt_3Co/C alloy specimen was annealed at 750°C for 2 hours in an *in situ* STEM specimen holder in vacuum to approximate the conditions of a typical annealing protocol. Images were acquired alternately in three separate regions of the specimen to provide a more robust and representative measurement of changes in the specimen (Figure 5.9). Figures 5.9A-C show a broad area of the sample before the annealing procedure and after 22 minutes and 2 hours of heating at 750 °C, respectively. An overall coarsening of the particles was evident throughout the region, especially during the first 22 minutes. Figures 5.9D-I show a smaller sub-region, in detail, to highlight the observed particle coalescence, which appeared to be the primary coarsening mechanism. Significant particle mobility on the carbon support was also observed, with some particles moving more than 10 nm and growing significantly in size from collisions and coalescence with other particles. Note that several ~2 nm particles remained fixed near their initial positions throughout the experiment with no noticeable change in size. This observation argues against Ostwald ripening as being a significant contributor to the particle coarsening. Dynamic movements of particles can be seen in the supplementary video.

Additional insights can be gained by calculating the statistical distribution of particle sizes and considering their change during the experiment (Figure 5.9J). The particle size

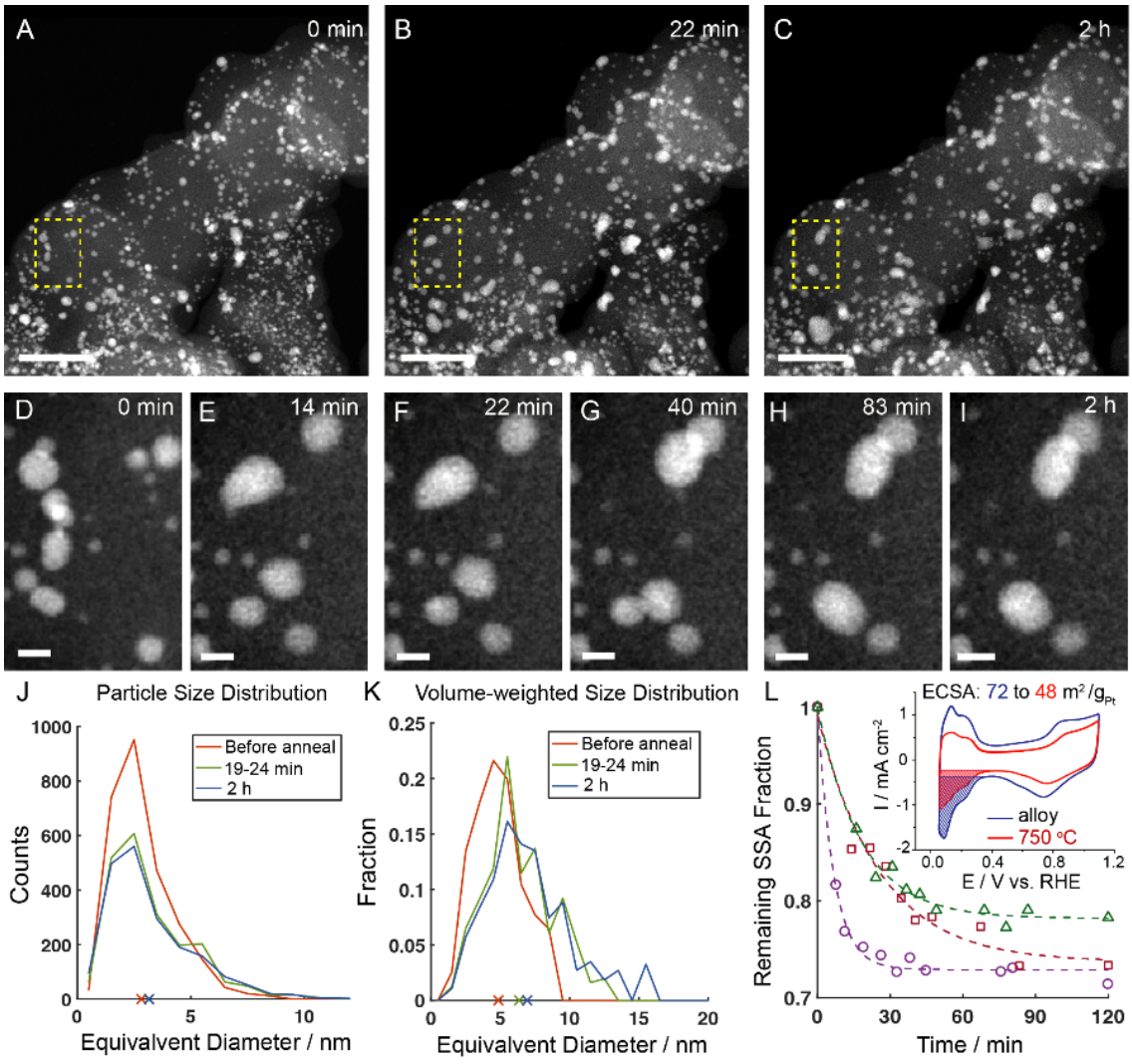

Figure 5.9 *In situ* heating STEM enabling tracking of the morphological changes of Pt_3Co/C annealed at 750°C. (A-C) Pt_3Co/C before annealing, annealed for 22 min, and annealed for 2h, respectively. (D-I) A specific region was magnified to illustrate particle migration and coalescence during a continuous 2 h annealing process. (J) Measured distribution of particle sizes of thousands of particles from Figure 5.7A at different annealing times at 750°C. Cross marks on the X-axis represent the corresponding average particle sizes. (K) Volume-weighted, particle size distribution, which reflects the relative

contribution of larger particles more clearly, as shown by the more pronounced tails for particle sizes above 8 nm. Cross marks on the X-axis represent the corresponding volume-weighted, average particle sizes. (L) Specific surface area (SSA) (m^2/g_{Pt}) estimated from STEM images of three different regions at different annealing times. Inset: Electrochemical surface area (ECSA) for Pt_3Co/C before and after annealing at 750 ^oC for 2 h, measured from the coulometric charge associate with hydrogen adsorption (H_{ads}) regions in the cyclic voltammograms. Details of statistical analysis of particle sizes and SSA calculations can be found in the experimental section. Scale bars in Figures A-C are 50 nm, and scale bars in Figures D-I are 5 nm.

distribution approximately followed a lognormal form, with smaller 2-3 nm particles being the most common with a substantial tail of larger particles. After annealing, the count of smaller particles decreased, while the distribution tail of larger particles grew more pronounced. This change in the shape of the distribution is also consistent with coarsening by particle coalescence, when a subset of smaller particles merge to form larger particles.[45-46] By contrast, an Ostwald ripening mechanism would have resulted in a more uniform shift in the distribution. The most significant change in the distribution occurred prior to the end of 19-24 min frame, though more subtle changes in the distribution occurred during the remainder of the annealing process. The growth in the number of large particles is more readily observed in the volume-weighted size distribution (Figure 5.9K), which shows that larger particles, formed by coalescence, accounted for a significant fraction of the Pt_3Co volume, even though large particles were relatively few in number.

The consequences of coarsening that occurred during the annealing process, on the electrochemical surface area (ECSA) of the Pt_3Co particles were examined by estimating the specific surface area (SSA) of the particles from the images in each region of the specimen (Figure 5.9L). The overall estimated SSA loss was approximately 20-30% and it varied among the three different locations in the specimen. This was similar in magnitude to the 33% loss in ECSA that we calculated from the cyclic voltammograms (CV) of Pt_3Co/C annealed for 2 h at 750°C in forming gas as discussed below. (Figure 5.9L, inset) In each specimen region, the SSA tended to decrease in approximately an exponential manner, and decayed towards a lower (but non-zero) value with a time-constant that varied from 7-25 min among the three different regions. This confirmed

previous observations that the most significant changes in the distribution of particle sizes occurred very early in the annealing process. The variation between the total SSA loss and the decay rate likely reflect differences in the strength of the bonding between Pt_3Co particles and the carbon support, suggesting that the structure of the carbon support can be quite heterogeneous.

5.4.3 Atomic-Scale *Ex Situ* HAADF-STEM Imaging

To directly observe the crystal structure of ordered intermetallics at the atomic-scale, we employed aberration-corrected scanning transmission electron microscopy (STEM) to study the Pt_3Co/C after the annealing and cooling processes. We used the high-angle annular dark-field (HAADF) STEM imaging mode, which provides intensities that scale with the atomic number ($I \propto Z^{1.7}$) so that Pt atoms appear much brighter than Co atoms. $L1_2$ intermetallic ordering in Pt_3Co nanoparticles can be recognized by the presence of unique, superlattice-ordered unit cells. The atomic-scale STEM image of a Pt_3Co particle along the [100] zone axis exhibits a periodic square array of dimmer Co atom columns at the center, surrounded by brighter Pt columns at the corners (Figure 5.10A). The square symmetry is consistent with the projected crystal model along the same [100] zone axis in ordered Pt_3Co intermetallics, where four pure Pt atom columns (red), at the corners, surround the pure Co atom columns (green) at the center (PDF # 01-072-9179) (Figure 5.10C). However, another single-crystal Pt_3Co nanoparticle (Figure 5.10B), which was viewed along the [100] zone axis, exhibited only a partially ordered intermetallic phase, as only parts of the NP showed a similar variation in the intensity as the crystal model suggested (Figure 5.10C). Other parts of the NP showed atoms at the center that were as bright as atoms at the corners, indicating that only a short-range, atom ordering existed

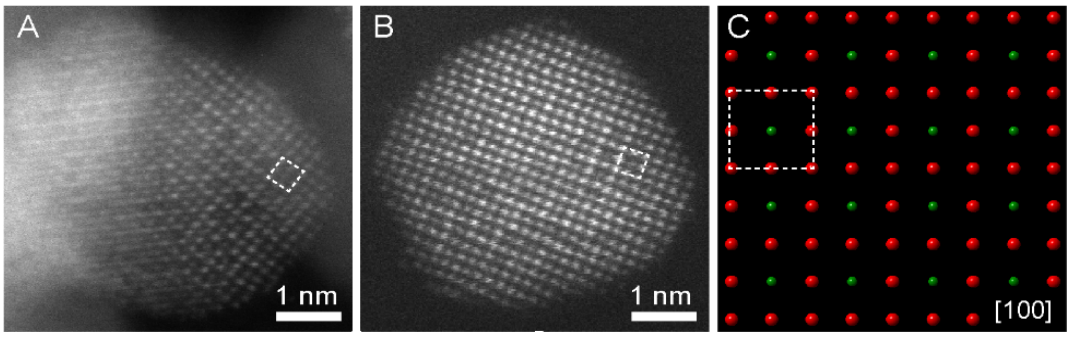

Figure 5.10 Atomic-scale *ex situ* HAADF-STEM images of Pt_3Co/C after annealing. (A) An ordered intermetallic Pt_3Co particle on the [100] zone axis. Brighter atoms at corners of squares are Pt, and dimmer atoms at the center are Co. (B) A partially ordered intermetallic particle on the [100] zone axis. Both brighter and dimmer atoms exist at the center of the squares. (C) Corresponding projected crystal model along [100]. Red and green atoms are Pt and Co, respectively. Crystal models were built based on the ordered intermetallic Pt_3Co (PDF # 01-072-9179).

in such Pt_3Co nanoparticles. Figures 5.10A-B indicate that both fully and partially ordered intermetallics exist in the Pt_3Co nanoparticles after the annealing process.

5.4.4 **Correlation of the Degree of Ordering to the Catalyst's Durability**

The above mechanistic studies involving both *in situ* heating XRD and *in situ* heating TEM yield a fuller picture of the order- disorder phase transition and provide further practical guidance for the design of ORR catalysts with enhanced durability. The electrochemical properties of the electrocatalysts annealed at different temperatures in a tube furnace were studied systematically to correlate the degree of ordering to the catalyst's durability (Figure 5.11). The powder XRD patterns of annealed Pt_3Co/C (Figure 5.4) exhibited a similar trend as the *in situ* heating XRD patterns in Figure 5.3. The mass-specific activity (MA), the surface area-specific activity (SA), and the electrochemical surface area (ECSA) of the Pt_3Co/C alloy electrocatalysts, that were annealed at different temperatures, were measured and calculated initially and after stability cycling, which involved potential cycling at 50 mV/s in 0.1M $HClO_4$ over the potential range of 0.6 to 1.0 V vs. the reversible hydrogen electrode (RHE) (Figures 5.12-13). Figure 5.11A presents the ECSA, MA (mass activity) and SA (specific activity) of Pt_3Co/C annealed at various temperatures. The ECSA exhibited a minimal decrease from 650 to 750 °C while both of MA and SA improved with the degree of ordering and reached a maximum at 750 °C. After stability tests, similar trends in MA and SA were evident However, in all cases, the activity decreased dramatically when the annealing temperature

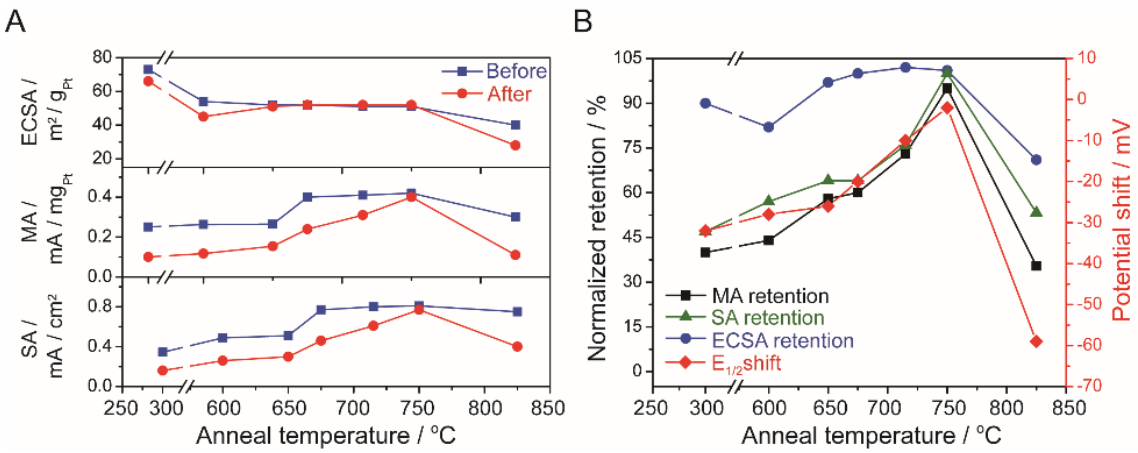

Figure 5.11 (A) Calculated ECSA, mass-specific activity (MA) and surface-specific activity (SA) at 0.9V vs. RHE of Pt_3Co/C before and after stability tests, after a series of annealing temperatures for 2h. (B) Normalized retention of mass-specific activity (MA), surface area-specific activity (SA), and electrochemical surface area (ECSA) on the left axis, and half-wave potential shift on the right axis of Pt_3Co/C after annealing at different temperatures. Normalized retention was calculated based on the ratio of the initial activity/surface areas to that after durability tests (2000 cycles in cyclic voltammetry at 100 mV/sec in 0.1M $HClO_4$ over the potential at the range from 0.6 to 1.0 V vs RHE). The best durability was achieved at around 750 ºC, corresponding to the optimal degree of ordering.

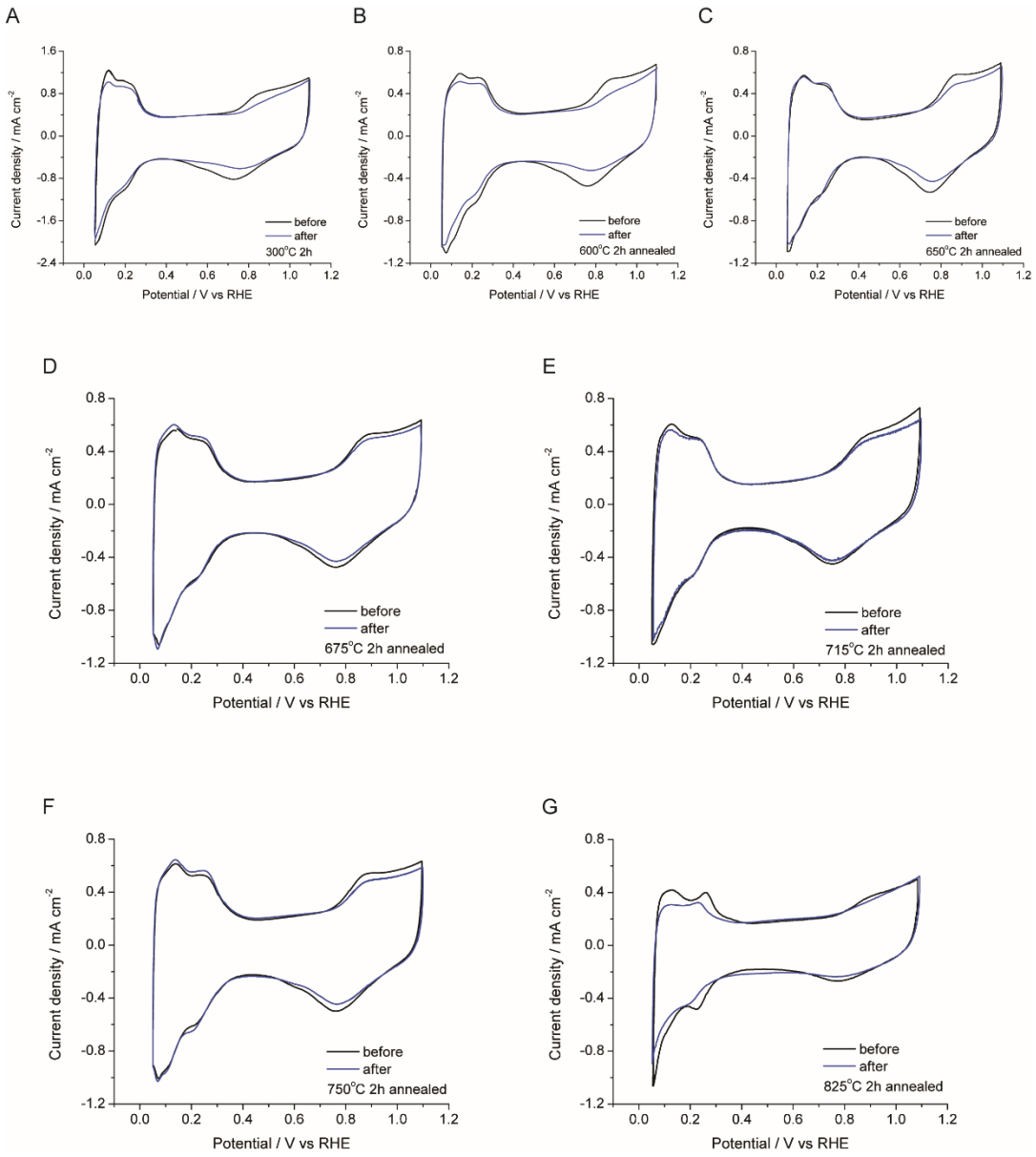

Figure 5.12 CV profiles of as-synthesized Pt_3Co/C and Pt_3Co/C annealed at different temperatures, before and after stability tests. (All CV profiles were obtained at a sweep rate of 50 mV/sec in oxygen-saturated a 0.1M $HClO_4$ solution over the potential range from 0.05 to 1.1 V vs RHE.)

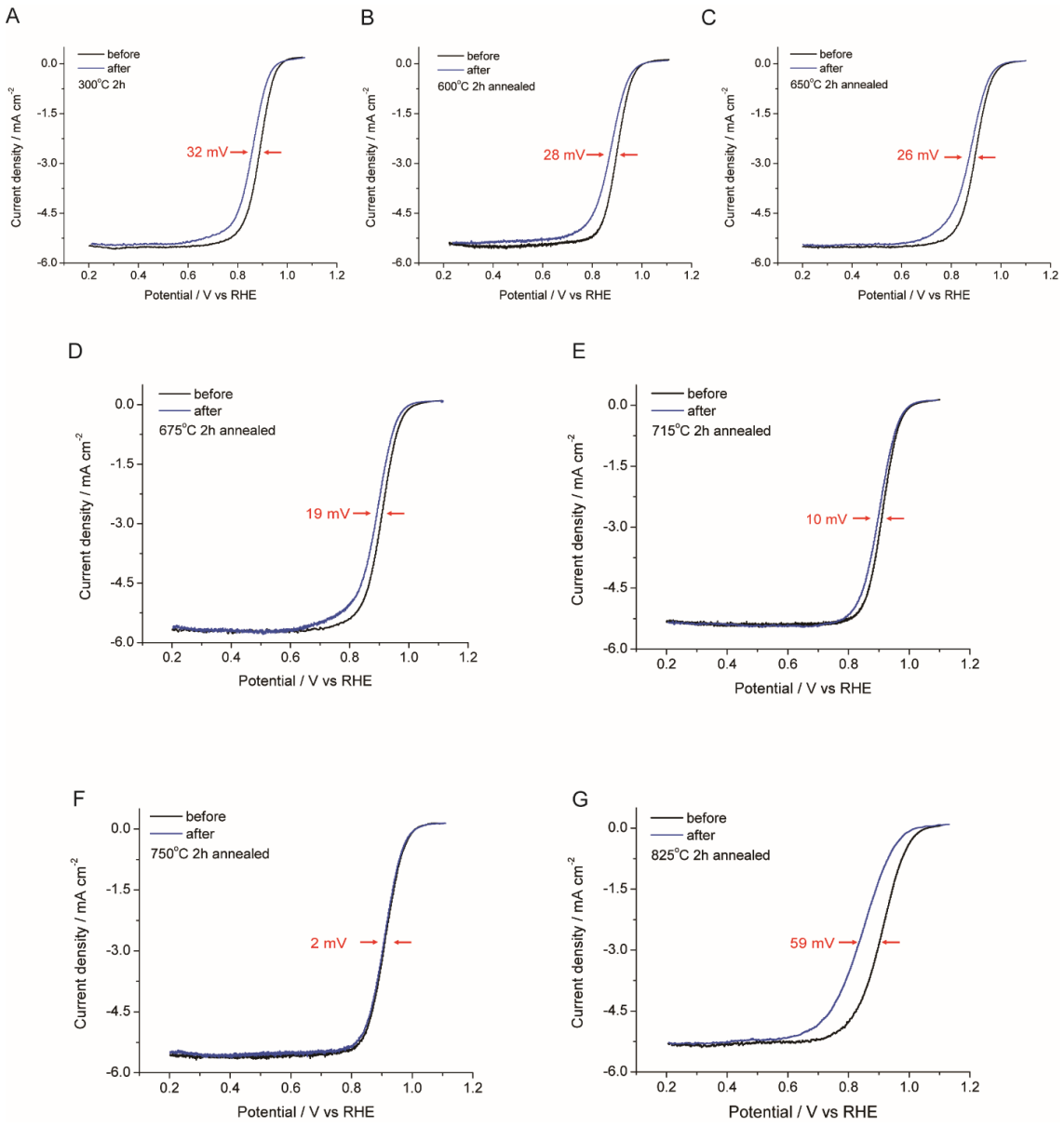

Figure 5.13 RDE polarization curves of as-synthesized Pt_3Co/C and Pt_3Co/C annealed at different temperatures, before and after stability tests. (All RDE polarization curves were obtained at a sweep rate of 5 mV/sec in oxygen-saturated a 0.1M $HClO_4$ solution at a rotation rate of 1600 rpm.)

exceeded 750 °C, as would be anticipated. Furthermore, their relative retentions were calculated from the ratio between the initial activity/surface areas to that after the durability tests (Figure 5.11A and Table 5.2). With increasing annealing temperature, the retention of the SA and MA improved continuously until reaching the highest values of 94% and 95%, respectively, at 750 °C. However, they dramatically decreased when the annealing temperature was increased to 825 °C. The trends in retention of SA and MA were quite consistent with the degree of ordering of the intermetallics, which indicated that the more ordered atomic structure improved the durability of the Pt_3Co/C nanoparticles. ECSA retention reached a maximum plateau at 725-750 °C with nearly no decay, with respect to its initial value, suggesting that a higher degree of ordering suppressed the loss of Pt surface area. It should be noted that the as-synthesized Pt_3Co/C (reduced at 300 °C) had a slightly higher ECSA than Pt_3Co/C that was annealed at 600 °C, likely because the as-synthesized Pt_3Co/C contained particles that were smaller than those annealed at 600 °C. This may have counteracted, or even surpassed, the benefit of the higher degree of ordering at 600 °C.

The shift in the half-wave potential ($E_{1/2}$), which is considered as an indicator of the intrinsic electrocatalytic activity in a more straightforward way, was also evaluated for its stability. The $E_{1/2}$ exhibited a trend similar to the SA and MA, with the least negative shift (< 5mV) observed at the optimal annealing temperature of 750 °C. The improvement in the stability of the Pt_3Co with the highest ordered degree, comes from the stable intermetallic Pt, Co arrangement in the core and the Pt rich shell. In the stability test of Pt_3Co alloy or intermetallics, the degradation of the electrocatalyst comes mainly from the loss of Co and the leached Co ions in the electrolyte, in turn contaminating the Pt

Temp. (°C)	ECSA (m^2/g_{Pt})		ECSA retention (%)	MA ($mA/\mu g_{Pt}$)		MA Retention (%)	SA (mA/cm^2_{Pt})		SA Retention (%)	$E_{1/2}$ (V vs. RHE)		$E_{1/2}$ Shift (mV)
	Before	After		Before	After		Before	After		Before	After	
300	73	66	90	0.251	0.1	40	0.344	0.16	47	0.886	0.854	-32
600	54	45	82	0.263	0.117	44	0.488	0.26	53	0.899	0.871	-28
650	52	51	97	0.265	0.154	58	0.51	0.30	59	0.902	0.876	-26
675	52	52	100	0.4	0.24	60	0.77	0.46	60	0.909	0.89	-19
715	51	52	102	0.41	0.31	73	0.80	0.61	76	0.912	0.904	-8
750	51	52	102	0.42	0.4	95	0.82	0.77	94	0.915	0.912	-3
825	40	28	70	0.3	0.11	36	0.75	0.40	53	0.904	0.845	-59

Table 5.2 The calculated ECSA, MA, SA at 0.9 V and half-wave potential ($E_{1/2}$) for different Pt_3Co/C samples before and after stability tests. ECSA and Mass activity retentions were calculated from the ratio of hydrogen adsorption region between its initial values to that after stability test. Since all the catalysts have the same mass loading of Pt_3Co, SA will have a value of MA divided by ECSA.

surface. The intermetallic nanoparticle with the highest ordered degree had the most uniform and regular atomic structure, so the Co was mostly bonded and surrounded by Pt.

Also, the stable and ordered structure maintained the robust atomic structure, retaining the highest ECSA after the cycling process. As a result, it yielded a large improvement in the $E_{1/2}$ during the stability test. This enhancement is not only observed from the RDE experiments, but also demonstrated in the membrane electrode assembly results (see below). To the best of our knowledge, this study represents the first successful attempt to systematically correlate the degree of ordering of binary alloy catalysts to the durability of electrocatalysts towards the oxygen reduction reaction in fuel cells, which will provide valuable insights and strategies in the future design of novel, ordered intermetallic electrocatalysts.

5.4.5 Real-World Stability Evaluation

For practical applications in PEMFCs, it is important to confirm that the findings in the laboratory can be translated to real-world (practical) improvement. The annealed, ordered, Pt_3Co/C electrocatalysts prepared in this work were evaluated in a fuel cell membrane-electrode assembly (MEA) and compared to one of the most active and durable state-of-the-art PtCo/C catalysts (Figure 5.13) .[47-48] The disordered Pt_3Co/C used for comparison was made by chemically dealloying a PtCo/C precursor. The disordered Pt_3Co/C had already exhibited excellent activity and stability in MEA results and had surpassed the U.S. Department of Energy (DOE) targets (initial ORR mass activity >0.44 A/mg_{Pt} and <40% loss after stability test) (Figure 5.13B). In this study, the disordered Pt_3Co was further processed through the aforementioned optimal annealing conditions to achieve a

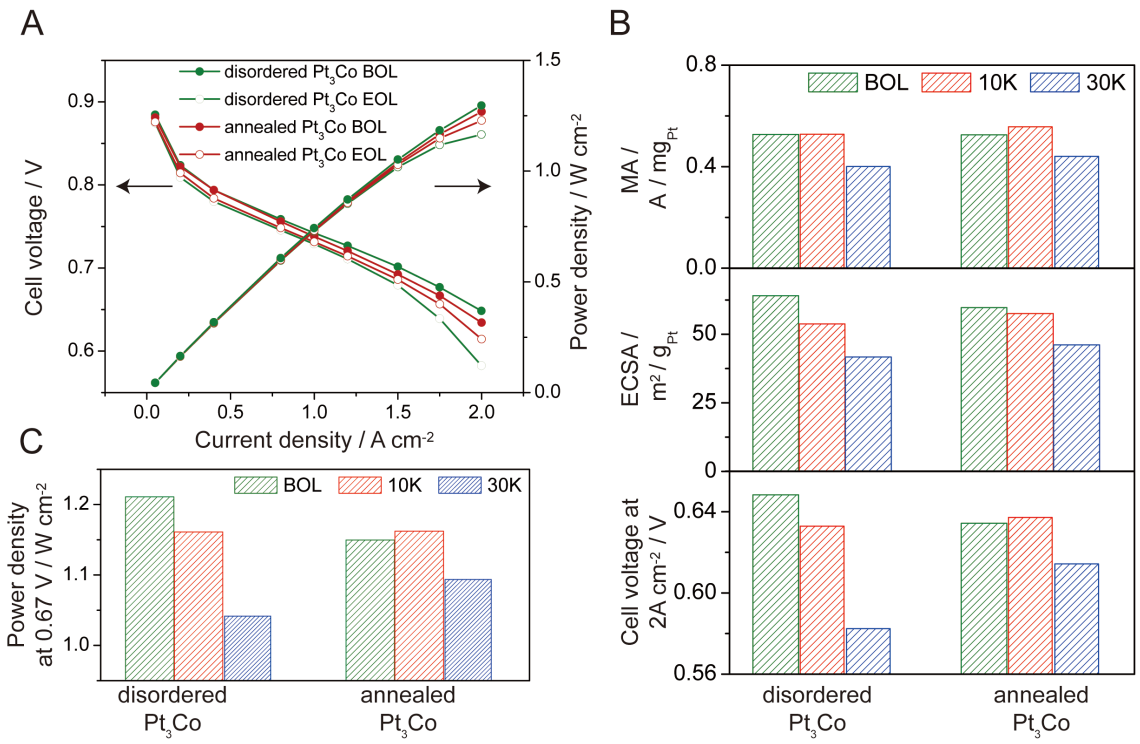

Figure 5.13 Fuel cell performance comparison of disordered and annealed Pt_3Co/C before and after stability testing. BOL and EOL represent beginning-of-life (initial performance) and end-of-life (after 30,000 cycles), respectively. (A) MEA performance at Pt loadings of 0.025 and 0.10 mg_{Pt}/cm^2 on anode and cathode, respectively. Cell operation conditions are in the order of anode/cathode: H_2/air, 94 °C, 65/65%RH, 250/250 $kPa_{abs,outlet}$, stoichiometries of 1.5/2. (B) Mass-specific activity (MA) measured at 0.9 V vs. RHE; ECSA of Pt measured by CO stripping in MEA; Voltage measured at a high current density of 2 A/cm^2. (C) Power density at 0.67 V under the same condition as (A).

maximum degree of ordering. The annealed Pt_3Co/C showed comparable initial ORR activity and Pt ECSA to the disordered catalyst, however, it had about a 40% lower loss after the stability test (Figure 5.13B middle plot). This is an impressive achievement over an already-very-stable, high performing electrocatalyst. These results support the findings of the above-described *in situ* experiments on Pt_3Co, that ordered intermetallic phases represent a promising path to develop stable, high performance fuel cell electrocatalysts. The initial high-current-density (HCD) performance (Figure 5.13B lower plot and 5.13C) of the ordered catalyst, although quite respectable by industry standards, is still slightly lower than our well-optimized baseline disordered Pt_3Co/C catalyst. The development of MEA electrodes for HCD for new catalysts generally takes several months and large amount of materials to optimize the ionomer, catalyst, and pore distribution within the electrode. Taking the mass activity and ECSA of the ordered catalyst into account, we predict that once optimized, the initial performance of the ordered phase Pt_3Co electrocatalyst will surpass that of the disordered Pt_3Co/C catalyst.[49]

The greatest value of the stability improvement of this catalyst is especially evident at HCD, as the durability under HCD performance is the leading factor determining the cost of a fuel cell stack.[49] The annealed Pt_3Co/C catalyst showed significantly smaller losses compared to the disordered catalyst after 30,000 cycles; only 20 mV vs. 66 mV (Figure 5.13B lower plot). This is due to the better retention of ORR activity and ECSA of the ordered catalysts as discussed above. To practically meet the U.S. DOE heat rejection target ($Q/\Delta T$ of <1.45), the voltage must be higher than the 0.67 V under the operating conditions used in this work (94°C).[48] As shown in Figure 5.13C, the annealed Pt_3Co/C exhibited only a 5% loss in power density at 0.67 V after 30,000 cycles, relative to a 14%

loss for the disordered Pt_3Co/C electrocatalyst. To the best of our knowledge, these results represent a cathode catalyst in PEMFCs with the highest performance and stability published to date. While we employed an accelerated stability test and yet require performing a long-term durability validation in this study, the advancement projects progress toward meeting the US DOE durability target of less than 10% performance loss after 8,000 h of automotive drive cycle.

5.5 Conclusion

In summary, this work represents the first time that both *in situ* heating synchrotron-based XRD for large ensembles of nanoparticles and *in situ* heating TEM at microscopic level have been used to quantitatively study the dynamics of the order-disorder phase transition and morphological and structural changes of binary intermetallics during a thermal annealing treatment. We have studied the impact of the annealing temperature and cooling conditions (temperature and time) comprehensively, on the degree of ordering, particle size, and lattice strain of Pt_3Co intermetallics. Through Monte Carlo simulations, we have also found that Pt_3Co nanoparticles have a lower order-disorder phase transition temperature than their bulk counterpart (by up to ~100 ^oC for 3-5 nm nanoparticles). At the optimal annealing temperature (750 ^oC), the total content of ordered intermetallic phase peaks at about 30%, reflecting the presence of both fully and partially ordered nanoparticles and a correlation between intermetallic order and particle size. To directly visualize the morphological and structural transitions during the annealing treatment, we further employed *in situ* heating STEM to study the mechanism of

nanoparticle migration and growth, and we quantitatively investigated the evolution of particle size distribution and the specific surface area during the annealing process. We achieved a direct visualization of both fully ordered and partially ordered individual Pt_3Co nanoparticles at the atomic scale. Finally, we have built a structure-activity correlation in which the Pt_3Co/C catalysts, with a higher degree of ordering, exhibited significantly enhanced durability. We further demonstrated that the annealed Pt_3Co/C with optimal degree of ordering exhibited remarkable long-term durability in practical MEA measurements in PEMFCs. This systematic and in-depth study, which involved both *in situ* heating XRD and *in situ* heating TEM, will have a broad impact on the further development of ordered intermetallic electrocatalysts for fuel cell applications.

5.6 References

1. Cano ZP, Banham D, Ye S, Hintennach A, Lu J, Fowler M, Chen Z (2018) Batteries and fuel cells for emerging electric vehicle markets. *Nat Energy* 3:279-289.
2. Wang D, Xin H, Hovden R, Wang H, Yu Y, Muller DA, DiSalvo FJ, Abruña HD (2013) Structurally ordered intermetallic platinum–cobalt core–shell nanoparticles with enhanced activity and stability as oxygen reduction electrocatalysts. *Nat Mater* 12:81-87.
3. Stamenkovic V, Mun B, Arenz M, Mayrhofer K, Lucas C, Wang G, Ross P, Markovic N (2007) Trends in electrocatalysis on extended and nanoscale Pt-bimetallic alloy surfaces. *Nat Mater* 6:241-247.
4. Cui C, Gan L, Heggen M, Rudi S, Strasser P (2013) Compositional segregation in shaped Pt alloy nanoparticles and their structural behaviour during electrocatalysis. *Nat Mater* 12:765-771.
5. Shao M, Chang Q, Dodelet J, Chenitz R (2016) Recent advances in electrocatalysts for oxygen reduction reaction. *Chem Rev* 116:3594-3657.
6. Xiong Y, Yang Y, DiSalvo FJ, Abruña HD (2018) Pt-decorated composition-tunable Pd−Fe@Pd/C core−shell nanoparticles with enhanced electrocatalytic activity toward the oxygen reduction reaction. *J Am Chem Soc* 140:7248-7255.
7. Han B, Carlton C, Kongkanand A, Kukreja R, Theobald B, Gan L, O'Malley R, Strasser P, Wagner F, Shao-Horn Y (2015) Record activity and stability of dealloyed bimetallic catalysts for proton exchange membrane fuel cells. *Energy Environ Sci* 8:258-266.

8. DeSario DY, DiSalvo FJ (2014) Ordered intermetallic Pt−Sn nanoparticles: Expl oring ordering behavior across the bulk phase diagram. *Chem Mater* 26:2750-27 57.
9. Yan Y, Du J, Gilroy K, Yang D, Xia Y, Zhang H (2017) Intermetallic nanocryst als: syntheses and catalytic applications. *Adv Mater* 29:1605997.
10. Luo M, Sun Y, Wang L, Guo S (2017) Tuning multimetallic ordered intermetalli c nanocrystals for efficient energy electrocatalysis. *Adv Energy Mater* 7:160207 3.
11. Abe H, Matsumoto F, Alden L, Warren S, Abruña HD, DiSalvo FJ (2008) Electr ocatalytic performance of fuel oxidation by Pt_3Ti nanoparticles. *J Am Chem Soc* 130:5452-5458.
12. Cui Z, Chen H, Zhao M, Marshall D, Yu Y, Abruña HD, DiSalvo FJ (2014) Syn thesis of structurally ordered Pt_3Ti and Pt_3V nanoparticles as methanol oxidation catalysts. *J Am Chem Soc* 136:10206-10209.
13. Ghosh T, Leonard B, Zhou Q, DiSalvo FJ (2010) Pt alloy and intermetallic phas es with V, Cr, Mn, Ni, and Cu: Synthesis as nanomaterials and possible applicati ons as fuel cell catalysts. *Chem Mater* 22:2190-2202.
14. Kang Y, Murray C (2010) Synthesis and electrocatalytic properties of cubic Mn −Pt nanocrystals (nanocubes). *J Am Chem Soc* 132:7568-7569.
15. Chung D, Jun S, Yoon G, Kwon S, Shin D, Seo P, Yoo J, Shin H, Chung Y, Kim H, Mun B, Lee K, Lee N, Yoo S, Lim D, Kang K, Sung Y, Hyeon T (2015) Hig hly durable and active PtFe nanocatalyst for electrochemical oxygen reduction re action. *J Am Chem Soc* 137:15478-15485.

16. Leonard B, Zhou Q, Wu D, DiSalvo FJ (2011) Facile synthesis of PtNi intermeta llic nanoparticles: Influence of reducing agent and precursors on electrocatalytic activity. *Chem Mater* 23:1136-1146.
17. Wang D, Yu Y, Xin H, Hovden R, Ercius P, Mundy J, Chen H, Richard J, Mulle r DA, DiSalvo FJ, Abruña HD (2012) Tuning oxygen reduction reaction activity via controllable dealloying: A model study of ordered Cu_3Pt/C intermetallic nan ocatalysts. *Nano Lett* 12:5230-5238.
18. Chen Q, Zhang J, Jia Y, Jiang Z, Xie Z, Zheng L (2014) Wet chemical synthesis of intermetallic Pt_3Zn nanocrystals via weak reduction reaction together with UP D process and their excellent electrocatalytic performances. *Nanoscale* 6:7019-7 024.
19. Kang Y, Pyo J, Ye X, Gordon T, Murray C (2012) Synthesis, shape control, and methanol electro-oxidation properties of Pt–Zn alloy and Pt_3Zn intermetallic nan ocrystals. *ACS Nano* 6:5642-5647.
20. Miura A, Wang H, Leonard B, Abruña HD, DiSalvo FJ (2009) Synthesis of inte rmetallic PtZn nanoparticles by reaction of Pt nanoparticles with Zn vapor and th eir application as fuel cell catalysts. *Chem Mater* 21:2661-2667.
21. Wang X, Altmann L, Stöver J, Zielasek V, Bäumer M, Al-Shamery K, Borchert H, Parisi, J, Kolny-Olesiak, J (2013) Pt/Sn intermetallic, core/shell and alloy nan oparticles: Colloidal synthesis and structural control. *Chem Mater* 25:1400-1407
22. Kuttiyiel K, Sasaki K, Su D, Wu L, Zhu Y, Adzic R (2014) Gold-promoted struc turally ordered intermetallic palladium cobalt nanoparticles for the oxygen reduc tion reaction. *Nat Commun* 5:5185.

23. Li G, Kobayashi H, Kusada K, Taylor J, Kubota Y, Kato K, Takata M, Yamamo to T, Matsumura S, Kitagawa H (2014) An ordered bcc CuPd nanoalloy synthesi sed via the thermal decomposition of Pd nanoparticles covered with a metal–org anic framework under hydrogen gas. *Chem Commun* 50:13750-13753.
24. Jiang K, Wang P, Guo S, Zhang X, Shen X, Lu G, Su D, Huang X (2016) Ordere d PdCu-based nanoparticles as bifunctional oxygen-reduction and ethanol-oxidat ion electrocatalysts. *Angew Chem Int Ed* 55:9030-9035.
25. Cable R, Schaak R (2007) Solution synthesis of nanocrystalline M-Zn (M: Pd, A u, Cu) intermetallic compounds via chemical conversion of metal nanoparticle pr ecursors. *Chem Mat* 19: 4098-4104.
26. Gunji T, Noh S, Tanabe T, Han B, Nien C, Ohsaka T, Matsumoto F (2017) Enha nced electrocatalytic activity of carbon-supported ordered intermetallic palladiu m–lead (Pd_3Pb) nanoparticles toward electrooxidation of formic acid. *Chem Mat er* 29:2906-2913.
27. Chen W, Yu R, Li L, Wang A, Peng Q, Li Y (2010) A seed-based diffusion rout e to monodisperse intermetallic CuAu nanocrystals. *Angew Chem Int Ed* 49:291 7-2921.
28. Wang G, Huang B, Xiao L, Ren Z, Chen H, Wang D, Abruña HD, Lu J, Zhuang L (2014) Pt skin on AuCu intermetallic substrate: a strategy to maximize Pt utili zation for fuel cells. *J Am Chem Soc* 136:9643-9649.
29. Sra A, Schaak R. (2004) Synthesis of atomically ordered AuCu and $AuCu_3$ nano crystals from bimetallic nanoparticle precursors. *J Am Chem Soc* 126:6667-6672.

30. Okamoto H (2001) Co-Pt (cobalt-platinum). *J Phase Equilib* 22:591.

31. Oezaslan M, Hasché F, Strasser P (2011) *In situ* observation of bimetallic alloy n anoparticle formation and growth using high-temperature XRD. *Chem Mater* 23: 2159-2165.

32. Avanesian T, Dai S, Kale M, Graham G, Pan X, Christopher P (2017) Quantitati ve and atomic-scale view of CO-induced Pt nanoparticle surface reconstruction a t saturation coverage via DFT calculations coupled with *in situ* TEM and IR. *J A m Chem Soc* 139:4551-4558.

33. van der Vliet D, Wang C, Tripkovic D, Strmcnik D, Zhang X, Debe M, Atanasos ki R, Markovic N, Stamenkovic V (2012) Mesostructured thin films as electrocat alysts with tunable composition and surface morphology. *Nat Mater* 11:1051-10 58.

34. Dubau L, Nelayah J, Moldovan S, Ersen O, Bordet P, Drnec J, Asset T, Chattot R, Maillard F (2016) Defects do catalysis: CO monolayer oxidation and oxygen reduction reaction on hollow PtNi/C nanoparticles. *ACS Catal* 6:4673-4684.

35. Dai S, You Y, Zhang S, Cai W, Xu M, Xie L, Wu R, Graham G, Pan X (2017) I n situ atomic-scale observation of oxygen-driven core-shell formation in Pt_3Co n anoparticles. *Nat Commun* 8:204.

36. Chi M, Wang C, Lei Y, Wang G, Li D, More K, Lupini A, Allard L, Markovic N, Stamenkovic V (2015) Surface faceting and elemental diffusion behaviour at at omic scale for alloy nanoparticles during *in situ* annealing. *Nat Commun* 6:8925.

37. Xin H, Alayoglu S, Tao R, Genc A, Wang C, Kovarik L, Stach E, Wang L, Sal meron M, Somorjai G, Zheng H (2014) Revealing the atomic restructuring of Pt –Co nanoparticles. *Nano Lett*. 14:3203-3207.

38. Alloyeau D, Ricolleau C, Mottet C, Oikawa T, Langlois C, Le Bouar Y, Braidy N, Loiseau A (2009) Size and shape effects on the order–disorder phase transitio n in CoPt nanoparticles. *Nat Mater* 8:940-946.

39. Keating DT, Warren BE (1951) Long-range order in beta-brass and Cu_3Au. *J Ap pl Phys* 33:286-290.

40. Yasuda H, Mori H (1996) Effect of cluster size on the chemical ordering in nano meter-sized Au-75at%Cu alloy clusters. *Z Phys D* 37:181-186.

41. Front A, Legrand B, Trélia, G, Mottet, C (2019) Bidimensional phases in Co–Pt surface alloys: A theoretical study of ordering and surface segregation. Surf Sci 679: 128–138.

42. Rosato V. Guillope M, Legrand B (1989) Thermodynamical and structural prope rties of f.c.c. transition metals using a simple tight-binding model. *Phil Mag A* 5 9:321-336.

43. Warren BE (2014) X-Ray Diffraction. (Dover Publications, New York).

44. Flinn P, McManus G, Rayne J (1961) Effective X-ray and calorimetric Debye te mperature for copper. *Phys Rev* 123:809-812.

45. Granqvist CG, Buhrman, RA (1976) Size distributions for supported metal catal ysts: Coalescence growth versus Ostwald ripening. *J Catal* 42:477–479.

46. Xin HL, Mundy JA, Liu Z, Cabezas R, Hovden R, Kourkoutis LF, Zhang J, Subr amanian NP, Makharia R, Wagner FT, Muller DA (2011) Atomic-resolution spe

ctroscopic imaging of ensembles of nanocatalyst particles across the life of a fue l cell. *Nano Lett* 1:490-497.

47. Han B, Carlton CE, Kongkanand A, Kukreja RS, Theobald BR, Gan L, O'Malle y R, Strasser P, Wagner FT, Shao-Horn Y (2015) Record activity and stability of dealloyed bimetallic catalysts for proton exchange membrane fuel cells. *Energy Environ Sci* 8:258–266.
48. Yarlagadda V, Carpenter MK, Moylan TE, Kukreja RS, Koestner R, Gu W, Tho mpson L, Kongkanand A (2018) Boosting fuel cell performance with accessible carbon mesopores. *ACS Energy Lett* 3:618-621.
49. Kongkanand A, Mathias MF (2016) The priority and challenge of high-power pe rformance of low-platinum proton-exchange membrane fuel cells. *J Phys Chem Lett* 7:1127–1137.
50. Vidal-Iglesias F, Arán-Ais R, Solla-Gullón J, Herrero E, Feliu J (2012) Electroc hemical characterization of shape-controlled Pt nanoparticles in different support ing electrolytes. *ACS Catal* 2:901-910.
51. Chen Q, Solla-Gullón J, Sun S, Feliu J (2010) The potential of zero total charge of Pt nanoparticles and polycrystalline electrodes with different surface structure: The role of anion adsorption in fundamental electrocatalysis. *Electrochim Acta* 55:7982–7994.
52. Gasteiger HA, Kocha SS, Sompalli B, Wagner FT, (2005) Activity benchmarks and requirements for Pt, Pt-alloy, and non-Pt oxygen reduction catalysts for PEM FCs. *Appl Catal B Environ* 56:9–35.

53. Garrick TR, Moylan TE, Carpenter MK, Kongkanand A (2017) Electrochemical ly active surface area measurement of aged Pt alloy catalysts in PEM fuel cells b y CO stripping *J Electrochem Soc* 164: F55–F59.
54. Chan T, Vese L (2001) Active contours without edges. *IEEE Trans Image Proce ss* 10:266-277.

CHAPTER 6

A STRATEGY FOR INCREASING THE EFFICIENCY OF THE OXYGEN REDUCTION REACTION IN MN-DOPED COBALT FERRITES

Reproduced from *J. Am. Chem. Soc*. **2019**, 141, 10, 4412-4421

.6.1 Abstract

Alkaline fuel cells have drawn increasing attention as next-generation energy-conversion devices for electrical vehicles, since high pH enables the use of non-precious metal catalyst. Herein, we report on a family of rationally designed Mn-promoting cobalt ferrite (MCF) spinel nanocrystals, with an optimal composition, $Mn_{0.8}(CoFe_2)_{0.73}O_4$ (MCF-0.8), that are effective electrocatalysts for the oxygen reduction reaction (ORR). MCF-0.8 exhibits a half-wave potential ($E_{1/2}$) of 0.89 V vs. RHE in 1M NaOH, only 0.02 V less than that of commercial Pt/C under identical testing conditions, and to the best of our knowledge, is one of the highest recorded values in the literature. Moreover, MCF-0.8 exhibits remarkable durability ($\Delta E_{1/2}$=0.014 V) after 10,000 electrochemical cycles. *In situ* X-ray absorption spectroscopy (XAS) reveals that the superior performance of the trimetallic MCF-0.8 originates from the synergistic catalytic effect of Mn and Co, While Fe helps preserve the spinel structure during cycling. We employed *in situ* XAS to track the evolution of the oxidation states and the metal-oxygen distances under not only constant applied potentials (steady state) but also during dynamic cyclic voltammetry (CV) (non-steady state). The periodic conversion between Mn(III, IV)/Co(III) and Mn(II, III)/Co(II) as well as the essentially constant oxidation state of Fe during the CV suggest collaboration efforts among Mn, Co and Fe. Mn and Co serve as the synergistic co-active sites to catalyze the oxygen reduction, apparently resulting in the observed high activity, while Fe works to maintain the integrity of the spinel structure, likely contributing to the remarkable durability of the catalyst. These findings provide a mechanistic understanding of the electrocatalytic processes of trimetallic oxides under real-time fuel cell operating

conditions. and This approach provides a new strategy to design high-performance non-precious metal electrocatalysts for alkaline fuel cells.

6.2 Introduction

The increasing need for clean, renewable energy continuously stimulates the development of fuel cells, which can exhibit energy conversion efficiency about three times higher than that of internal the combustion engine (ICE). However, the sluggish kinetics of the oxygen reduction reaction (ORR) at the cathode remains as one of the key challenges.[1-2] To date, state-of-the-art Pt and Pd-based electrocatalysts are recognized as the most efficient commercial candidates for the ORR in acidic media, but their high cost and scarcity still hinder the widespread large-scale application of proton exchange membrane fuel cells (PEMFCs).[4-8] Alternatively, alkaline polymer electrolyte fuel cells (APEFCs) have attracted tremendous attention since they enable the use of non-precious and earth-abundant materials as electrocatalysts, but they are only resistant to corrosion in alkaline media.[10-13] To lower the ORR overpotential in alkaline media, considerable effort has been devoted to investigating and designing various non-precious metal catalysts, such as nitrogen-doped carbon,[14-15] transition metal oxides,[16-23] and metal oxynitrides/carbides.[24-25] Recently, Zhuang group, together with our effort, has reported on an adenosine-derived Fe/N/C catalyst with atomic Fe-N_4 catalytic sites. This material, under the appropriate conditions, achieved a volume-specific activity comparable to commercial Pt/C in rotating-disk electrode experiments and yield a high peak power density above 450 mW/cm^2 in APEFC.[15] Dai et al. substituted Co in Co_3O_4 with Mn to form covalent hybrid spinel oxides, $MnCo_2O_4$ loaded on N-doped reduced graphene

oxide. Their material dramatically enhanced the ORR kinetics, which, they claimed, was due to a covalent coupling effect between spinel oxide nanoparticles and the graphene support.[16-17] Recently, we have reported on a synergistic Mn-Co spinel catalyst with a significantly enhanced ORR activity, when compared to the monoxide counterparts.[21] Li et al. utilized a high-pressure pyrolysis process to encapsulate hollow spheres of iron carbide nanoparticles in graphitic layers. The synthesized material exhibited promising ORR activity and stability in both acidic and alkaline medias.[25]

Among all of those catalysts, spinel metal oxides represent one of the most promising candidates, due to their high activity, long durability and low cost. Particularly, spinel metal oxides containing Mn cations have demonstrated to be auspicious as ORR electrocatalysts.[16-23] The electrocatalytic activity of Mn-containing spinel oxides is highly dependent on the nominal content of Mn and structural variations. Several reports have found that the ORR performance could be tuned, by progressively substituting Mn in $Mn_xM_{3-x}O_4$ (M = Co, Fe or Cu) spinel oxides.[26-28] Besides, $Co_xFe_{3-x}O_4$, with a cubic spinel structure, has also achieved excellent electrocatalytic activity toward the ORR.[29-30] Despite the substantial progress that has been achieved in the design of more active spinel oxide catalysts, a detailed understanding of the mechanism of oxygen-reduction catalysis using metal oxides remains elusive. Catalysts, normally characterized *ex situ*, may not maintain the same catalytic properties as those under real-time electrochemical conditions, which calls for *in situ* spectroscopy techniques to unveil/ identify the true electrocatalytic sites for the ORR.[21]

Herein, we have synthesized a series of manganese cobalt ferrite nanoparticles with the spinel structure of $Mn_x(CoFe_2)_yO_4$(x ranges from 0 to 1.2, described as MCF-x below).

The materials with an optimized composition (MCF-0.8 when x=0.8), exhibits excellent electrocatalytic performance, and remarkable durability after 10,000 CV cycles. A variety of characterization tools, including powder XRD (X-ray diffraction), STEM (Scanning transmission electron microscopy) imaging, electron energy loss spectroscopy (EELS) elemental mapping, and energy dispersive spectroscopy (EDX) analysis have been systematically utilized to examine the crystal structures, morphology and elemental distribution at the atomic scale. Furthermore, *in situ* X-ray absorption spectroscopy (XAS) studies have been carried out to track the changes in the local electronic structures under both steady state and dynamic non-steady state conditions. These studies strongly suggest that Mn and Co serve as synergistic electrocatalytic sites while Fe acts as a structurally stabilizing element that contributes to the long-term durability of the MCF catalysts.

6.3 Experimental Section

6.3.1 Materials

Iron acetate ($Fe(OAc)_2$), cobalt acetate tetrahydrate ($Co(OAc)_2 \cdot 4H_2O$), manganese acetate tetrahydrate ($Mn(OAc)_2 \cdot 4H_2O$), sodium hydroxide (AR), ammonium hydroxide (25 wt.%), nitric acid (HNO_3, 70 wt.%) and Nafion (5 wt.%) were purchased from Sigma-Aldrich. Carbon-supported Pt/C (20 wt.%) nanoparticles (NPs) were supplied by Johnson Matthey. Carbon nanotubes were purchased from Carbon Nanotube Plus. All chemicals were used as received without further purification, except carbon nanotubes, which were treated by soaking in nitric acid overnight and washing eleven times with deionized water.

6.3.2 Material Synthesis

MCF nanoparticles, including $CoFe_2O_4$ (MCF-0), $Mn_{0.3}(CoFe_2)_{0.9}O_4$ (MCF-0.3), $Mn_{0.6}(CoFe_2)_{0.8}O_4$(MCF-0.6), $Mn_{0.8}(CoFe_2)_{0.73}O_4$ (MCF-0.8), $Mn_1(CoFe_2)_{0.66}O_4$ (MCF-1) and $Mn_{1.2}(CoFe_2)_{0.6}O_4$ (MCF-1.2) were prepared by a facile hydrothermal method. In a typical synthesis, $Fe(OAc)_2$ (0.25 mmol, 44 mg) and $Co(OAc)_2 \cdot 4H_2O$ (0.125 mmol, 31 mg) were suspended in 20 mL deionized water, followed by sonicating and stirring for 15 mins, respectively. Then, 0.5 mL $NH_3 \cdot H_2O$ was added dropwisely into the solution under magnetic stirring for another 15 mins. A stoichiometric amount of $Mn(OAc)_2 \cdot 4H_2O$ was dissolved in 10 mL of deionized water, ultrasonicated for 10 mins, and dropped into the Fe/Co precursor solution. The mixture suspension was maintained at 60 ^oC in an oil bath for 20 hr with constant stirring, and was subsequently transferred to a Teflon autoclave, at 130 ^oC for 3 hr. The resulting product was isolated by centrifuging and washed with acetone and isopropanol for three times, respectively. The as-synthesized nanoparticles were dried in an oven at 60 ^oC overnight and mixed with carbon nanotubes to achieve a 40% mass loading of the metal oxides. The mixture was homogenized by ball milling for 20 minutes. Finally, the carbon supported nanoparticles were annealed under Ar at 500 ^oC for 2 hr.

6.3.3 Structural Characterizations

The crystal structure of all the synthesized NPs was confirmed by powder X-ray diffraction (XRD) using a Rigaku Ultima IV Diffractometer. Diffraction patterns were collected at a scan rate of 2° min^{-1} at 0.02° steps from 20° to 80°. Scanning transmission electron microscopy (STEM) images and elemental electron energy loss spectroscopy (EELS) maps were acquired on a fifth-order aberration-corrected STEM (Cornell Nion UltraSTEM) operated at 100 keV with a beam convergence semi-angle of 30 mrad. Sub-

Ångström spatial resolution is achievable under such operating conditions. STEM images were processed using Richard-Lucy deconvolution (3 iterations) (Figure 6.1). EELS spectral images were acquired with a 0.25 eV/channel energy dispersion in a Gatan spectrometer with a size of 100×100 pixels and an acquisition time of 20 ms/pixel. The Mn, Co and Fe elemental maps were extracted using their sharp L_3 edges from EELS spectral images (Figure 6.2) and processed using principal component analysis (PCA, 3 components) and the linear combination of power law (LCPL) to subtract the background in ImageJ software. The crystal models were generated using Crystal Maker software.

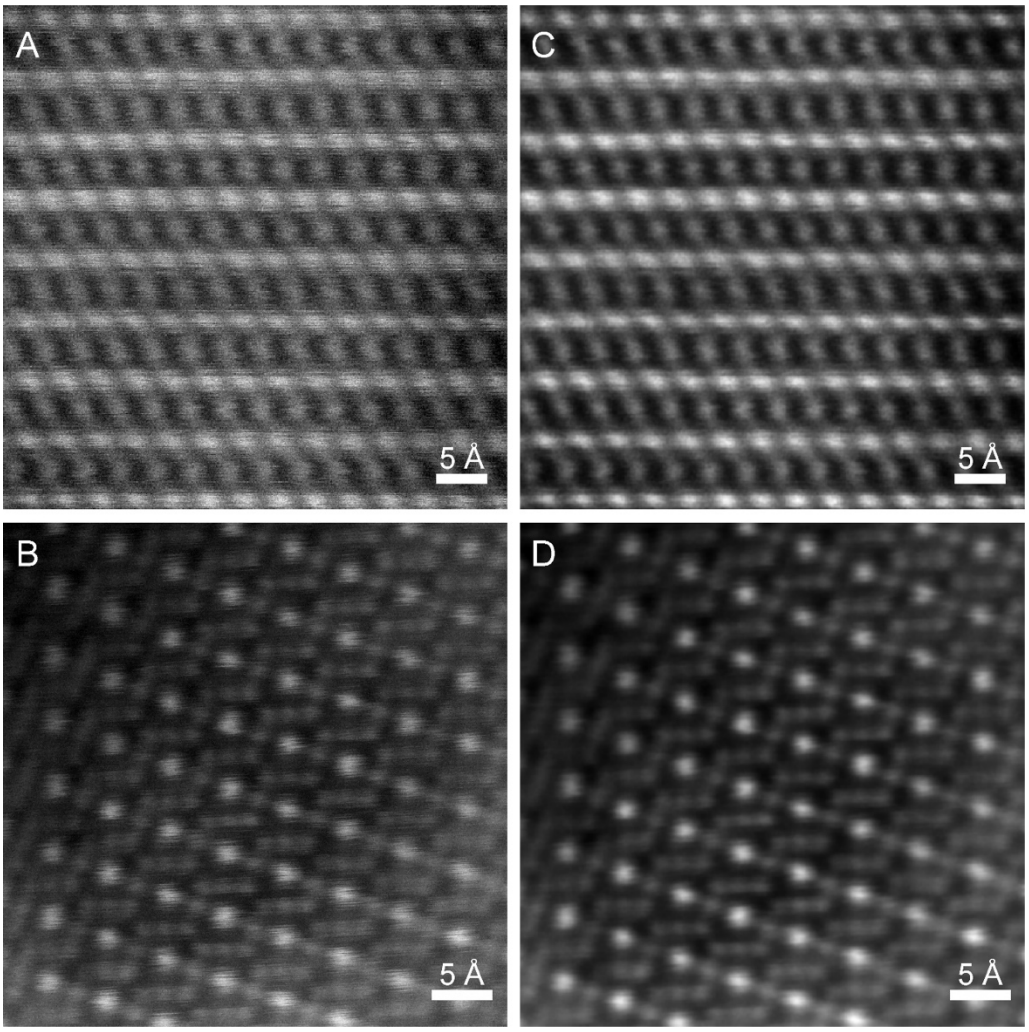

Figure 6.1 STEM images process. (A-B) raw atomic-scale STEM images. (C-D) images in (A-B) filtered by using the Richard-Lucy deconvolution (3 iterations). The deconvolution was processed in ImageJ software assuming an Airy disk (100 kV, α_{max}=28 mrad) convolved with a 0.8 Å Gaussian source.

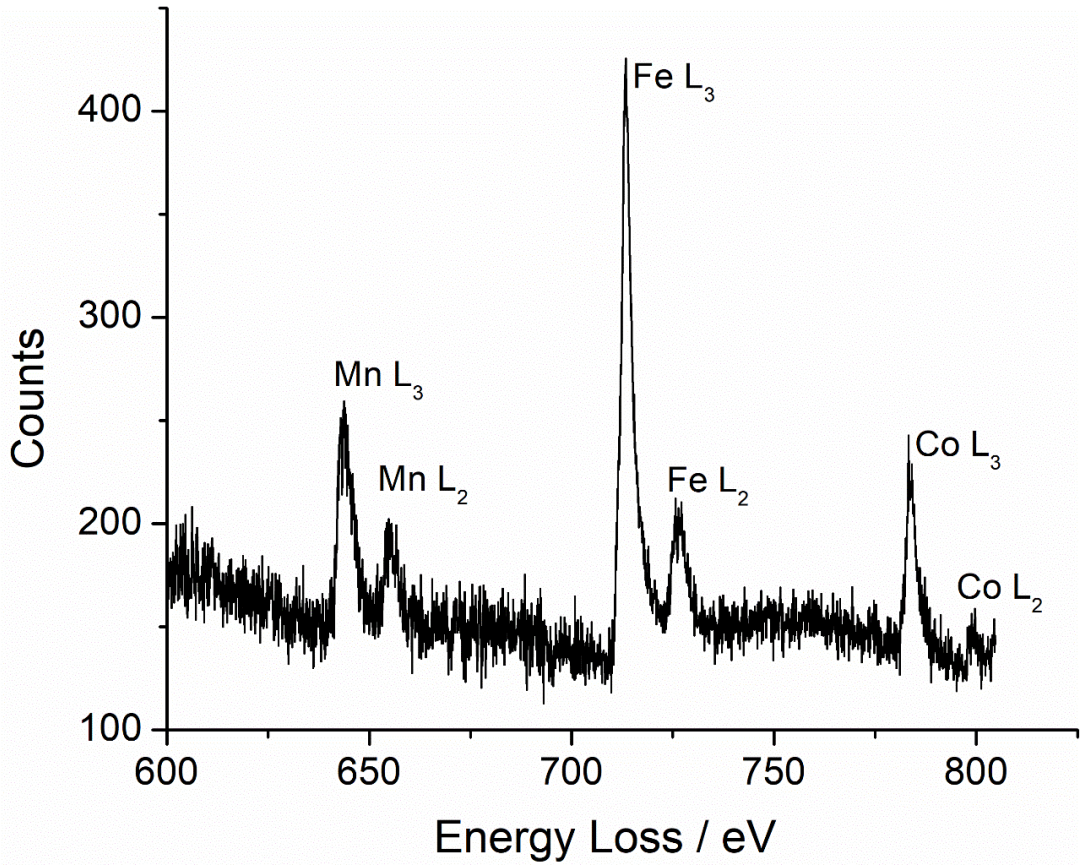

Figure 6.2 EELS spectrum of MCF-0.8 acquired from the particle shown in Figure 6.6A

6.3.4 Electrochemical Characterization

Electrochemical measurements were performed in 1M NaOH on a Solartron potentiostat. In all electrochemical measurements, 5 mg of the prepared catalyst was mixed with 2 mL of 0.05 wt% Nafion/ethanol solution and subsequently sonicated for approximately 30 minutes. 20 μL of the resulting catalyst ink were loaded onto a 5 mm diameter glassy carbon (GC) electrode, achieving a metal oxide loading of 0.1 mg cm^{-2}, followed by thermal evaporation of the solvent under infrared light. The mass loading of Pt on GC was 25 μg cm^{-2}, a common value, for comparison in fuel cell tests.[8] A graphite rod was used as the counter electrode and Ag/AgCl, in a 1M KCl solution, served as the reference electrode. ORR measurements were carried out with a rotating disk electrode (RDE) in oxygen-saturated 1M NaOH solution at room temperature (23 ^{o}C) (Bubbling with O_2 for 15 mins before scanning). All cyclic voltammetric profiles were obtained between 0.15 V to 1.2 V vs. a reversible hydrogen electrode (RHE) at 5 mV/s in Ar-saturated 1M NaOH. The ORR profiles were obtained at 5 mV/s and 1600 rpm after 50 CV cycles from 0.15 to 1.2 V at 50 mVs^{-1} to remove the surface contamination and activate the catalyst. The background capacitive current measured in Ar-saturated 1M NaOH solution was subtracted to process and plot the ORR profiles. Durability tests were carried out by continuously cycling the potential from 0.6 V to 1.0 V at 100 mV/s for 10,000 cycles. The ORR profiles after 10,000 cycles were measured in a fresh 1M NaOH solution.

6.3.5 *In situ* X-ray Absorption Measurements

Mn, Co and Fe K-edge X-ray absorption near edge structure (XANES) spectra were acquired at the F-3 beamline of the Cornell High Energy Synchrotron Source (CHESS)

from 150 eV below the metal edge out to 550 eV above edge using nitrogen filled ion chambers. XANES and EXAFS (extended X-ray absorption fine structure) spectra were calibrated using metal foils and analyzed using the ATHENA software package.[31] Fourier transformed EXAFS spectra were plotted by applying Hanning window from 3 to 10 $Å^{-1}$ with k^2-weighting and no phase correction. *In situ* non-steady state results were obtained by taking transmission measurements for two seconds at the chosen energy. A shutter was used to minimized potential beam damage by blocking the X-ray beam for one second in between data acquisition. Briefly, MCF-0.8 (40 wt. %) was dispersed in a Nafion/ethanol (0.05 wt. %) solution. Carbon paper (190 μm thick, Fuel Cell Store, AvCarb MGL190) was cut into 1×5 cm^2 pieces and used as the catalyst support. The catalyst-ionomer mixture was sprayed on one end of the carbon paper (1×1 cm^2) with a metal oxide mass loading of 6 mg/cm^2 using an airbrush and the rest, 1×4 cm^2, served as a non-active conductor with negligible effects on the catalytic current.

As described in our previous cell design[21] (Figure 6.3), the electrochemical cell includes two pieces of Teflon, which is chemically inert in the strong base conditions of 1M NaOH saturated. A Teflon U-shaped sealing ring was placed between the two Teflon pieces whose distance could be adjusted to make the electrolyte thickness less than 200 μm. On top of the electrochemical cell, a Teflon cap with one gas inlet and another gas outlet was used to bubble N_2 gas to minimize the influence of trace amounts of O_2 during electrochemical testing. Inside the electrochemical cell, the section of the carbon paper with the catalyst layer was immersed into the electrolyte near the window for X-ray transmission measurements. A carbon rod was used as the counter electrode (CE) and placed near the working electrode (WE). Ag/AgCl (1M KCl) was used as the reference

electrode (RE) and was placed (via a salt bridge) at the bottom of the cell so that the distance between the WE and RE could be minimized. This, in turn, minimized the IR drop during electrochemical testing. All three electrodes were connected to a potentiostat (Biologic SP-200) during *in-situ* X-ray data acquisition.

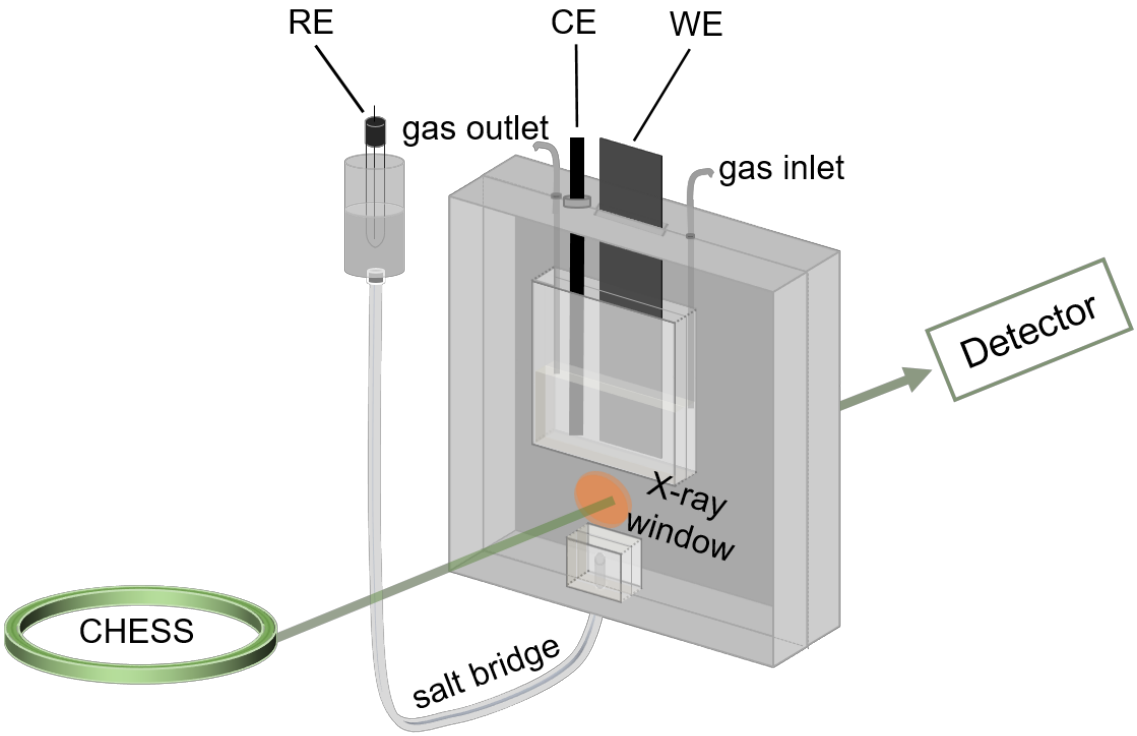

Figure 6.3 Schematic of the *in situ* XAS electrochemical cell. Working electrode (WE, catalyst on carbon paper) and counter electrode (CE, carbon rod) were immersed in 1M NaOH solution. Reference electrode (RE, Ag/AgCl in saturated KCl) was connected to the cell by a salt bridge and the distance between the RE and the catalysts at the end of the carbon paper was minimized to reduce IR drops caused by the resistance in the thin electrolyte layer ($\leq$ 200 μm) in the X-ray window. Details of the cell design and operation was reported in our previous study[3].

6.4 Results and Discussion

A family of MCF was prepared using a facile hydrothermal method followed by a high-temperature treatment. Their crystal structures were examined by powder XRD, as presented in Figure 6.4. All of the prepared samples, named as $CoFe_2O_4$ (MCF-0), $Mn_{0.3}(CoFe_2)_{0.9}O_4$ (MCF-0.3), $Mn_{0.6}(CoFe_2)_{0.8}O_4$(MCF-0.6), $Mn_{0.8}(CoFe_2)_{0.73}O_4$ (MCF-0.8), $Mn_1(CoFe_2)_{0.66}O_4$ (MCF-1), and $Mn_{1.2}(CoFe_2)_{0.6}O_4$ (MCF-1.2), possess cubic spinel structures. The broad peak at around 25° in the XRD belongs to carbon, and the remaining of diffraction peaks matched well with the standard cubic spinel $CoFe_2O_4$ (PDF # 01-077-0426, a=b=c=8.401 Å) and $MnFe_2O_4$ (PDF # 01-073-3820, a=b=c=8.498 Å). There is a progressive shift to lower 2θ angle at higher Mn contents, corresponding to the gradual substitution of Co and Fe by Mn with larger atomic size. The average domain size of all MCF samples, as estimated from XRD measurements, was found to be around 10-15 nm, which is consistent with STEM images (Figure 6.5).

The crystal structure of $Mn_{0.8}(CoFe_2)_{0.73}O_4$/C (MCF-0.8) with optimal activity was further examined at the atomic scale using high-angle annular dark-field (HAADF) scanning transmission electron microscopy (STEM) imaging at 100 keV (Cornell Nion UltraSTEM). Since $CoFe_2O_4$ (a=8.401 Å) shares a very similar cubic spinel crystal structure to $MnFe_2O_4$ (a=8.498 Å), the crystal structure of MCF-0.8 from STEM imaging analysis can be built based on the structure of $CoFe_2O_4$ (PDF # 01-077-0426). Figures 6.6A-B present the atomic-scale lattice image of MCF-0.8 and the corresponding crystal model viewed along the $[11\bar{2}]$ zone axis. Two perpendicular d-spacings were measured

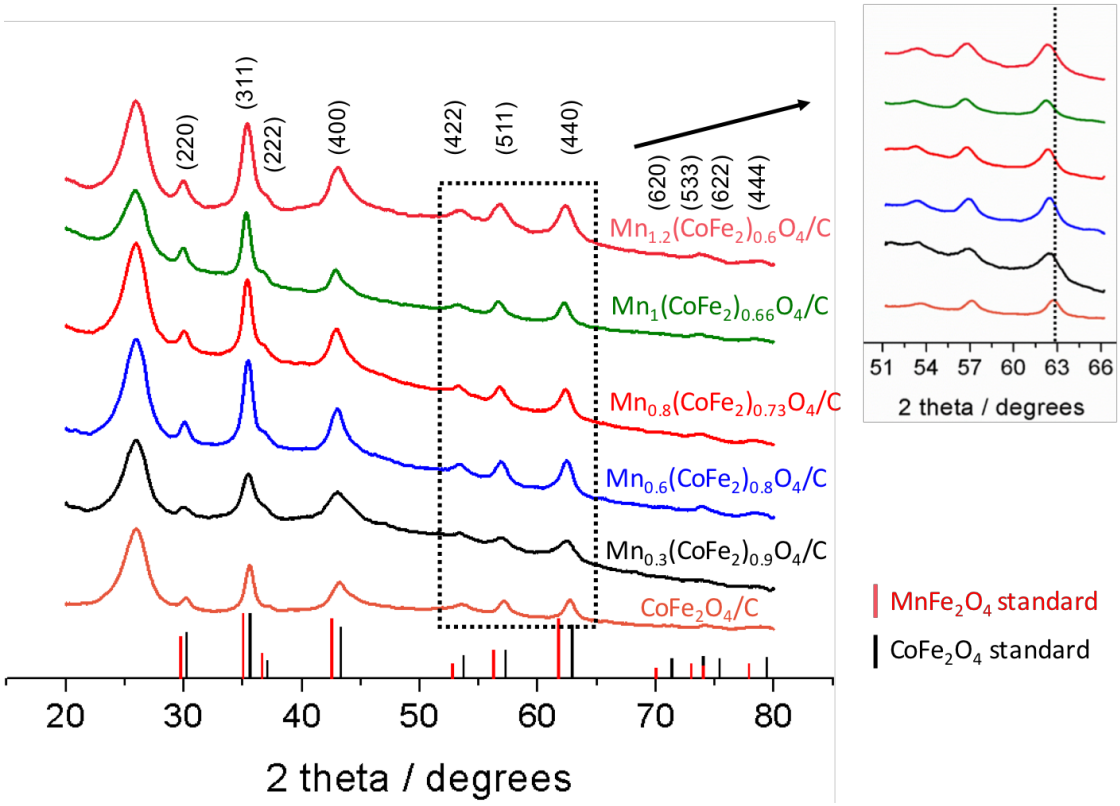

Figure 6.4 XRD patterns of as-synthesized MCF cubic spinel nanoparticles: $CoFe_2O_4$, $Mn_{0.3}(CoFe_2)_{0.9}O_4$, $Mn_{0.6}(CoFe_2)_{0.8}O_4$, $Mn_{0.8}(CoFe_2)_{0.73}O_4$, $Mn_1(CoFe_2)_{0.66}O_4$ and $Mn_{1.2}(CoFe_2)_{0.6}O_4$. The red and black vertical lines correspond to standard $CoFe_2O_4$ (PDF # 01-077-0426) and $MnFe_2O_4$ (PDF # 01-073-3820) XRD patterns, respectively; inset represents the enlarged region of the $CoFe_2O_4$ (440) diffraction peak.

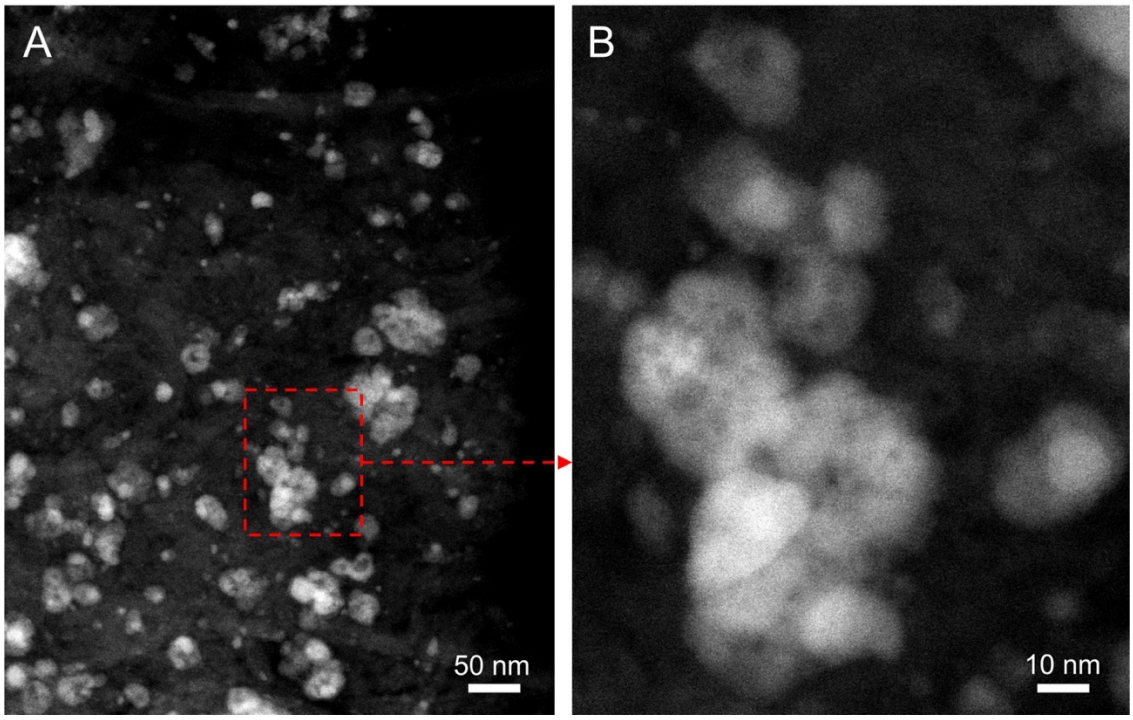

Figure 6.5 (A) STEM image of as-synthesized MCF-0.8 catalysts. (B) STEM image from one region magnified in (A) (red dashed box), showing particles composed of smaller sub-domains with domain sizes of around 15 nm.

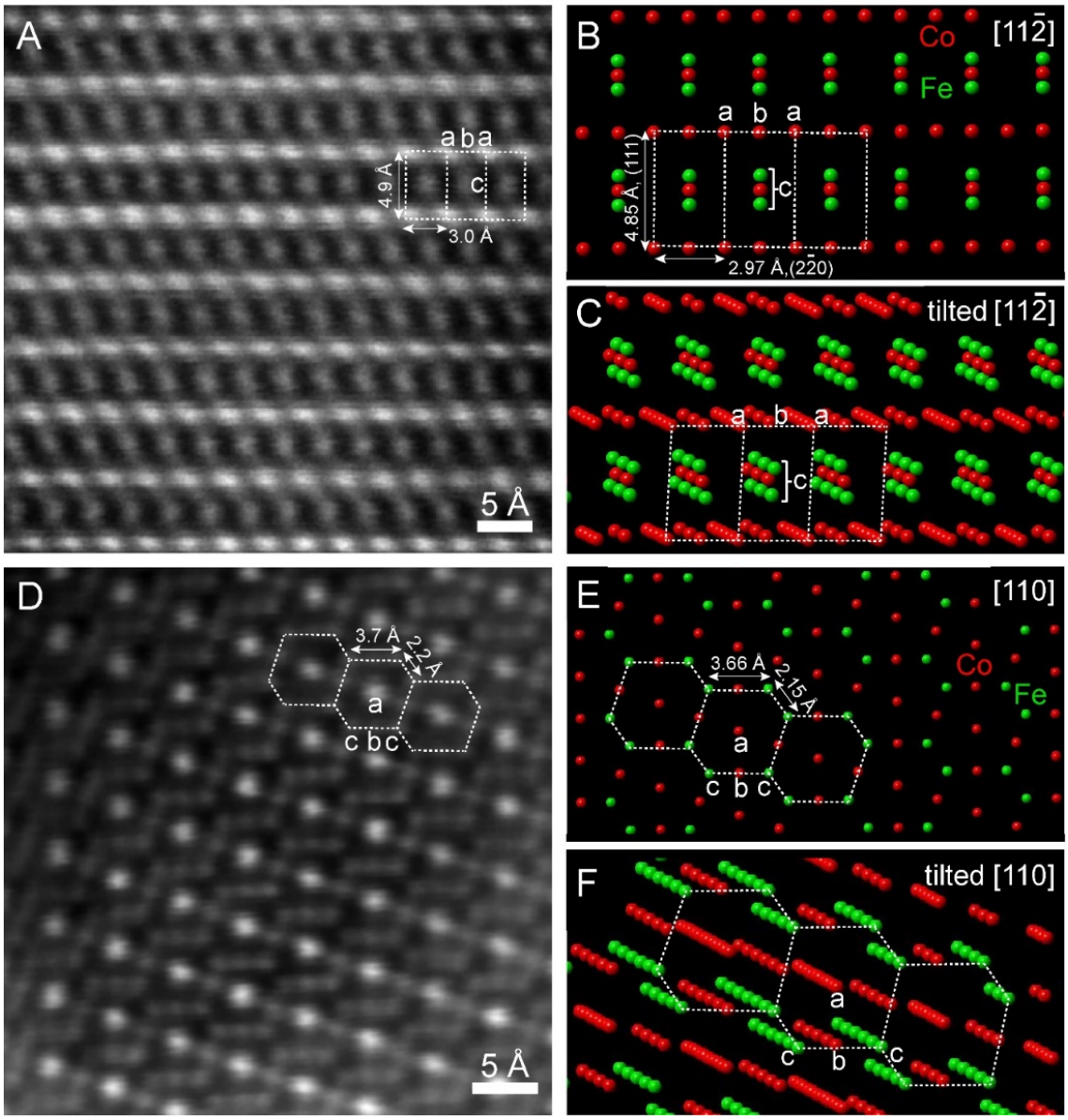

Figure 6.6 Atomic-scale HAADF-STEM images of MCF-0.8. (A-B) atomic-scale image and the corresponding crystal model on the [11$\bar{2}$] zone axis. Two lattice d-spacings were measured to be 4.9 and 3.0 Å, which matched well with the theoretical values of (111), 4.85 Å and (2$\bar{2}$0), 2.97 Å, respectively. Atom columns, **a**, at the corner of the lattice image, exhibit a brighter intensity than atom columns, **b**, on the side, because **a** has higher atom density than that of **b** and **c** in the crystal model. Atom columns, **c**, at the center of the

lattice image, are elongated in the (111) direction, which are actually composed of three atom columns next to each other. (C) The crystal model on the [11$\bar{2}$] zone axis slightly tilted to reveal the underneath atom columns. (D-E) Another atomic-scale image and the corresponding crystal model on the [110] zone axis. Hexagonal repeating unit cells with two nearby sides of 3.7 and 2.2 Å were observed, which matched the theoretical values of 3.66 and 2.15 Å, respectively, in the crystal model. Atom columns, **a**, at the center of the lattice image, exhibit a brighter intensity than that of columns **b** and **c** on the side, because **a** has a higher atom density than **b** and **c**. Atom columns, **b** and **c** show little difference in the image intensity, since they are Co and Fe atoms, with very similar atomic numbers, 27 and 26, respectively. The crystal model was established based on the cubic spinel structure of $CoFe_2O_4$. (F) The crystal model on the [110] zone axis was slightly tilted to reveal the underneath atom columns.

to be 4.9 and 3.0 Å, well consistent with the theoretical (111), 4.85 Å and ($2\bar{2}0$), 2.97 Å lattice planes, respectively. Since the intensity of a HAADF-STEM image is proportional to the atomic number ($I \propto Z^{1.7}$), it is intriguing to observe in Figure 6.6A that atom columns, **a**, at the corner, exhibit a higher intensity related to that of atom columns, **b**, on the side, even though they are supposed to be the same element, according to the 2D projected crystal model in Figure 6.6B. This apparent inconsistence can be resolved by deliberately tilting the [$11\bar{2}$] zone axis (Figure 6.6C) to reveal the atom columns underneath. Despite being the same element, atom columns, **a**, clearly have a higher atom density than that of atom columns, **b**, resulting in a higher image intensity as observed in Figure 6.6A. It is also observed that atom columns, **c**, at the center of the lattice image in Figure 6.6A seem to be elongated in the (111) direction, which, in fact, corresponds to an assembly of three atom columns next to each other. The distances among the three of them are too short and beyond the spatial resolution of STEM images.

Figures 6.6D-E exhibit another atomic-scale lattice image of MCF-0.8 and the corresponding crystal model on the more basic [110] zone axis. Hexagonal repeating unit cells are indicated in the dashed boxes with two nearby sides of 3.7 and 2.2 Å with an angle of 125°, which are consistent with the theoretical values of 3.66 and 2.15 Å, respectively, with an angle of 126°. Similar to Figure 6.6A, atom columns, **a**, at the center of the lattice image in Figure 6.6D, exhibit a higher intensity than that of atom columns, **b** and **c**, on the side. The intensity variations also come from the fact that atom columns, **a**, have higher atoms density than that of **b** and **c**, as shown in the tilted [110] zone axis (Figure 6.6F). Noticeably, atom columns **b** and **c**, exhibit no significant difference in image intensity, although they could be different element combinations, Co and Fe or Mn

and Fe. Given that Mn, Fe and Co have very similar atomic numbers, the image intensity variations are likely below the noise level threshold of the electron detector. In summary, the aforementioned atomic-scale STEM imaging analysis directly visualized and confirmed the cubic spinel crystal structure of MCF-0.8.

The chemical composition of MCF-0.8 nanoparticles was investigated using electron energy loss spectroscopy (EELS) elemental mapping. Figure 6.7A shows a typical MCF-0.8 nanoparticle composed of multiple sub-domains. The region in the dashed box was magnified in Figure 6.7E to show the lattice image, which is on the [001] zone axis with the perpendicular (220) and ($2\bar{2}0$) lattice planes (3.1 Å). Figures 6.7B-D present the EELS elemental maps of Mn (red), Fe (green) and Co (blue) for the particle in Figure 6.7A. Figures 6.7F-H show the composite EELS maps of Mn vs. Fe, Mn vs. Co and Fe vs. Co. The composite EELS map of Mn vs. Fe suggests a homogenous elemental distribution in which Mn and Fe are intimately mixed on a nearly atomic scale. The composite EELS maps of Mn vs. Co and Fe vs. Co exhibit a relatively homogenous elemental distribution with a local enrichment of Co at the edge of the particle. This EELS chemical mapping study combined with the previous analysis of atomic-scale STEM images in Figure 6.6, unambiguously demonstrate that MCF-0.8 has a cubic spinel crystal structure with a relatively homogenous elemental distribution of Mn, Co and Fe.

The cyclic voltammetric profiles (CVs) of all MCF NPs, with different Mn content were obtained in an Ar-saturated 1 M NaOH solution at a scan rate of 5 mV/s from 0.15 to 1.2 V vs. RHE, and all shown in Figure 6.8A. To identify the redox couples more accurately, the CVs of MCF, together with $CoFe_2O_4$ and $MnFe_2O_4$ were investigated and

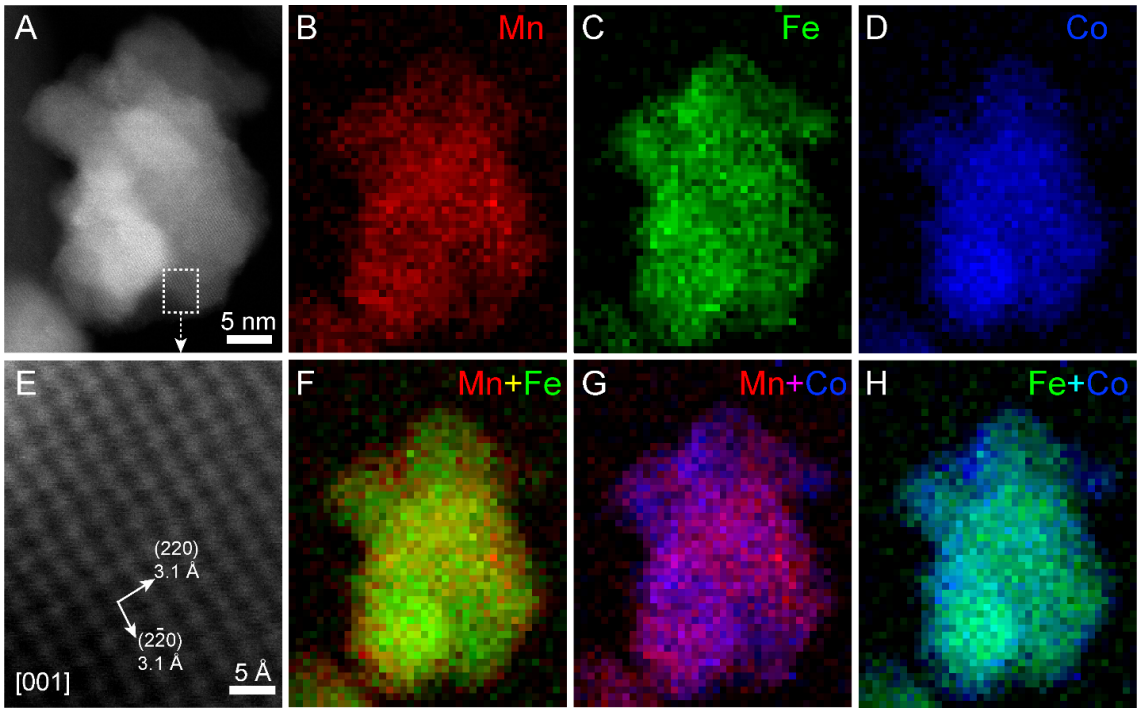

Figure 6.7 EELS elemental maps of MCF-0.8. (A) HAADF-STEM image of a typical nanoparticle composed of smaller sub-domains. The lattice image in the dashed box was magnified in (E) to show (220) and (2$\bar{2}$0) with same d-spacing values of 3.1 Å on the zone axis of [001]. (B-D) EELS elemental maps of Mn (red), Fe (green) and Co (blue), respectively. (F-H) EELS elemental composite maps of Mn vs. Fe, Mn vs. Co and Fe vs. Co, respectively.

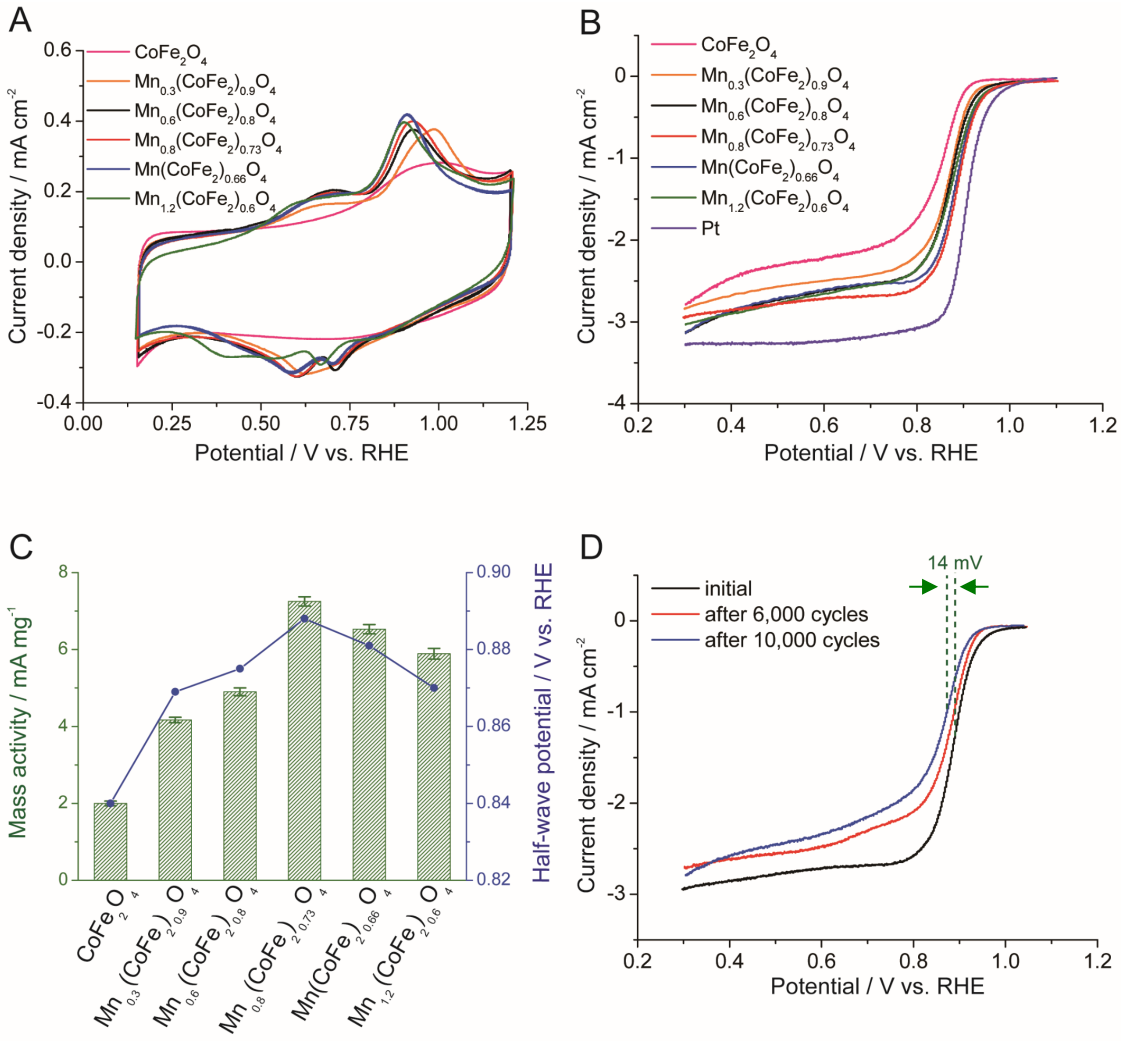

Figure 6.8 Electrocatalytic properties of as-synthesized MCF nanoparticles. (A) Cyclic voltammetry (CV) profiles of synthesized MCF NPs in Ar-saturated 1 M NaOH solution, scanned at a rate of 5 mV/s at room temperature. (B) ORR polarization curves in O_2-saturated 1 M NaOH at a scan rate of 5 mV/s and rotation at a rate of 1600 rpm. (C) Comparison of mass activity and half-wave potential of different MCFs at 0.9 V vs. RHE. (D) Polarization profiles of MCF-0.8 after 10,000 cycles of stability testing.

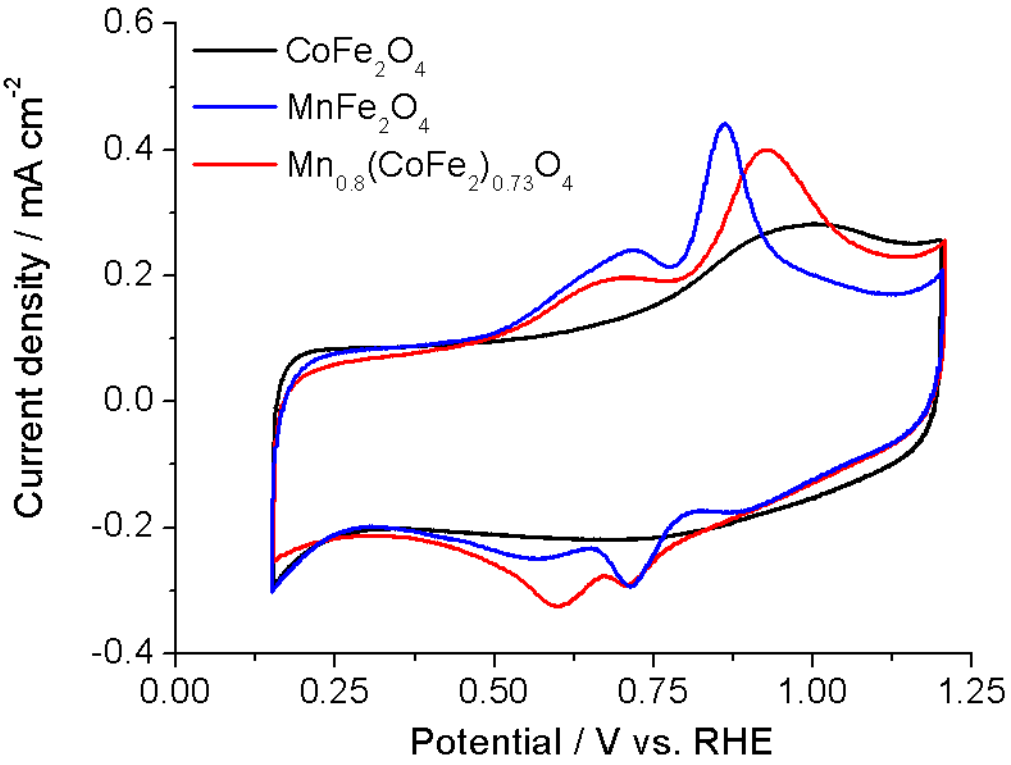

Figure 6.9 Cyclic voltammetric profiles of $CoFe_2O_4$, $MnFe_2O_4$ and $Mn_{0.8}(CoFe_2)O_4$ in Ar-saturated 1M NaOH, at 5 mV/s scan rate.

as presented in Figure 6.9. There are two redox couples in the 0.15-1.2V potential window for all Mn-containing oxides. Mn exhibits two oxidative peaks in the positive potential scanning direction, at around 0.68 and 0.91 V respectively, corresponding to the gradual evolution from Mn (II) to higher valence states (Mn (III, IV)). Conversely, two reductive peaks were observed at 0.72 and 0.6 V repeatedly indicating the conversion back to Mn (II). Co (III) exhibited a single oxidative peak at around 0.97 V, which overlapped with the more pronounced features from Mn. With increasing Mn and decreasing Co contents, the first peak at higher potential shifts gradually from 0.97 to 0.91 V, which is consistent with the compositional variation. No redox couples from Fe were observed in the CV profiles, as its redox reactions typically occur at more negative potentials.[32-33]

Rotating disk electrode (RDE) voltammetry was employed to assess the ORR activity of all MCF electrocatalysts. The polarization curves shown in Figure 6.8B were obtained in 1 M O_2-saturated NaOH solution, at 5 mV/s and 1600 rpm. The half-wave potential ($E_{1/2}$) exhibited a correlation between the electrochemical activity and the Mn content following the order of MCF-0 (0.84 V) < MCF-0.3 (0.868 V) < MCF-0.6 (0.875 V) < MCF-1.2 (0.87 V) < MCF-1 (0.88 V) < MCF-0.8 (0.888 V), as shown in Figure 6.8C (right Y-axis). With increased Mn content, the kinetics were enhanced at first, and then decreased to higher Mn content, with an optimal performance at MCF-0.8, suggesting a "volcano trend". The mass-specific activity (MA) of the MCFs at 0.9 V was calculated by normalizing the kinetic current to the catalyst mass from the Koutecky−Levich equation,[34] (Figure 6.8C, left Y-axis). MCF-0.8 exhibited the highest MA value of 7.25 mA mg_{oxide}^{-1}, outperforming its counterparts with other Mn contents. To gain further insight into the long-term durability of MCF-0.8, a stability test was carried in Ar-

saturated 1M NaOH solution for 6,000 and 10,000 cycles between 0.6 to 1.0 V, the typical working potential region of APEFCs.[11] There was a progressive negative shift in the polarization curve after 6,000 and 10,000 cycles and the diffusion limiting current decreased slightly, especially in the high polarization region. The degradation of the electrocatalysts after 10,000 cycles was ascribed to the loss of active material upon extended cycling. This was further confirmed by comparing the CV profiles before and after potential cycles (Figure 6.10), where the Mn/Co redox peaks gradually faded and broadened as an indication of losing Mn and Co active sites in addition to possible particle aggregation. Despite this minor degradation after durability testing, the MCF-0.8 still exhibited a remarkable ORR electrocatalytic activity, with an $E_{1/2}$ of 0.874 V and $\Delta E_{1/2}$ of only 14 mV (Figure 6.8D).

To further understand the degradation mechanism(s), STEM imaging and EDX spectroscopy were employed to investigate the structural and chemical evolution after cycling. As shown in Figure 6.11, a STEM image of MCF-0.8 nanoparticles, after electrochemical cycles, clearly indicated particle aggregation/coalescence when compared to the as-synthesized MCF-0.8 in Figure 6.5. STEM-EDX was used to quantitatively analyze the relative amounts of Co, Fe and Mn before and after electrochemical cycles. Relative amounts of Co, Fe and Mn were calculated from the EDX spectra, where the intensity of Fe was normalized to 1 for comparison (Figure 6.12). It is clear that the Mn loss is nearly 50%, relative to its original content, Co lost around 30%, while the Fe content was stable during the cycling process. The quantitative results are shown in Tables 6.1-3. The relative atomic percentages of as synthesized MCF-0.8 were 29.2, 23.8 and 47.0 % for Mn, Co and Fe, respectively, which is quite consistent

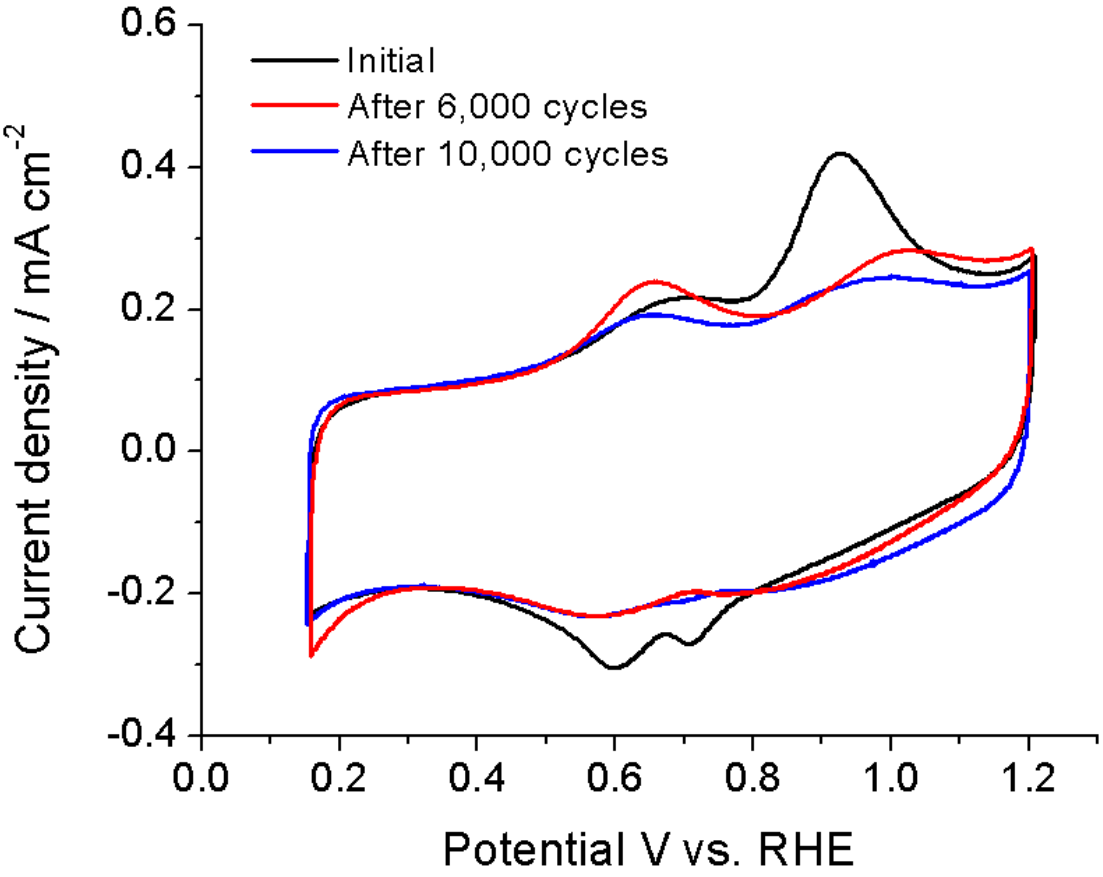

Figure 6.10 Cyclic voltammetric profiles between 0.15 to 1.2V of MCF-0.8 ($Mn_{0.8}(CoFe_2)_{0.73}O_4$) in Ar-saturated 1M NaOH, at 5 mV/s scan rate. The black line is the initial CV, and the red and blue lines are after stability testing of 6,000 and 10,000 cycles, respectively, at 100 mV/s between 0.6 to 1.0 V vs. RHE.

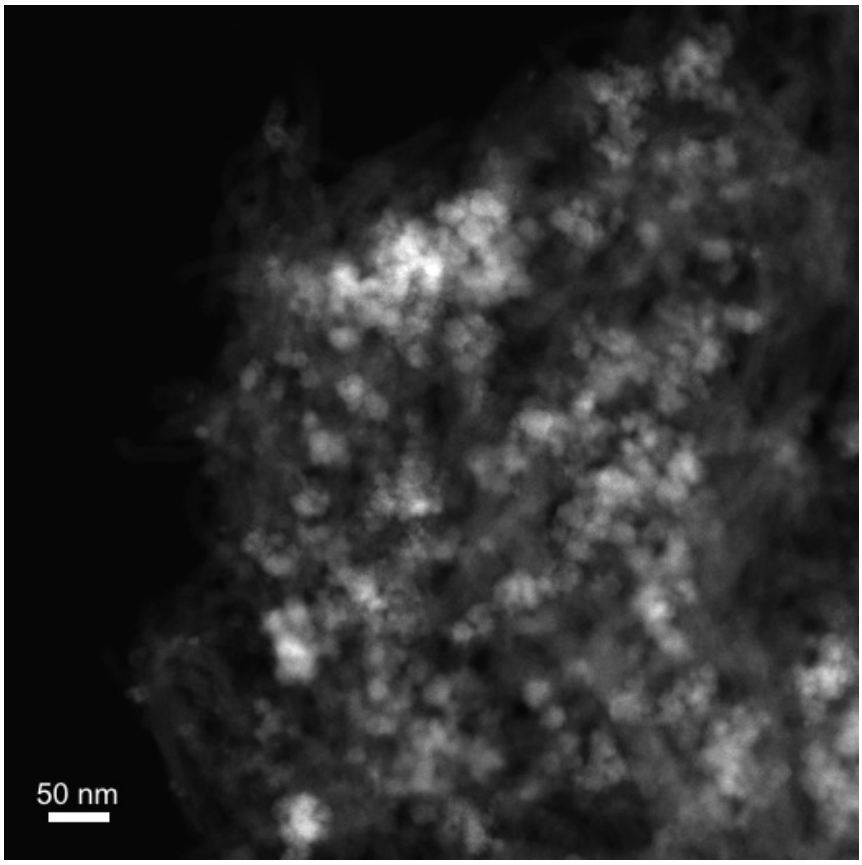

Figure 6.11 STEM image of MCF-0.8 catalyst after 10,000 electrochemical cycles. The observed particle aggregation is likely responsible, at least input, for the degradation in electrochemical activity.

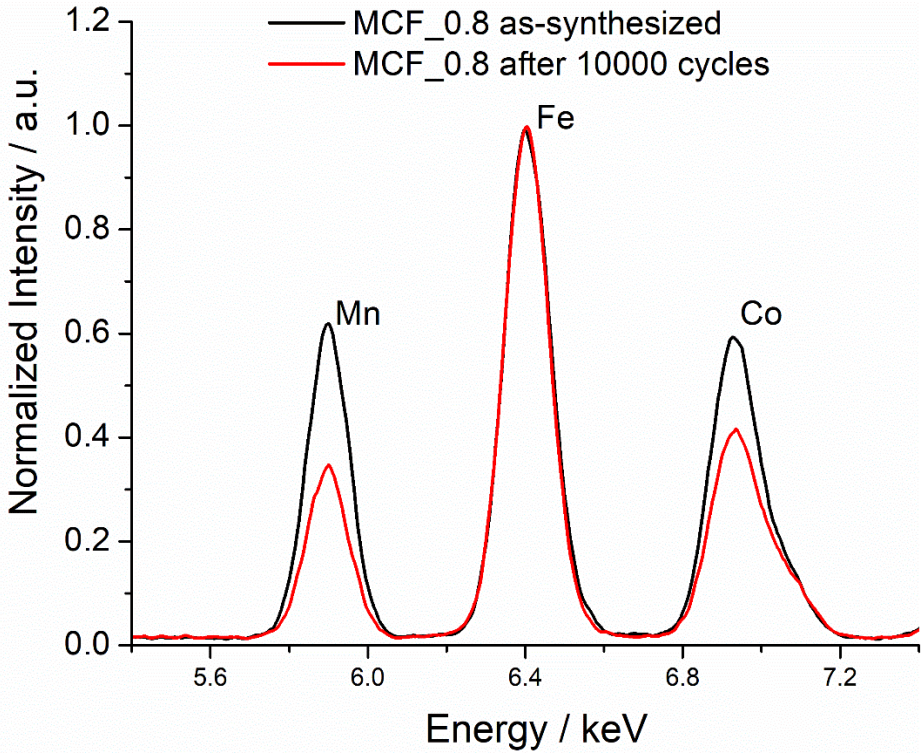

Figure 6.12 EDX spectra of MCF-0.8 before and after electrochemical cycles. The X-ray intensities were normalized to the value of Fe Kα edge for comparisons. It should be noted that the Mn major Kα edge is at 5.89 keV and the Mn minor Kβ edge at 6.49 keV overlaps with Fe's major Kα edge(6.40 keV). Fe's minor Kβ edge at 7.05 keV overlaps with Co's major Kα edge at 6.93 keV, which explains why Fe and Co peaks have small shoulder peaks on the right side of their peaks.

MCF_0.8	Mn at.%	Co at.%	Fe at.%
As-synthesized	29.2	23.8	47.0
After CV cycles	20.2	18.3	61.5

Table 6.1 EDX quantitative analysis of MCF_0.8 catalysts before and after electrochemical cycles. Relative amounts of Mn, Co and Fe are average results from seven different regions in EDX measurements. The relative error using one standard deviation (Sd) was estimated to around 1 at.%. Accurate calculations of relative contents of Mn, Co and Fe were discussed as below.

Based on the Cliff-Lorimer thin-film criterion,[4] if the sample is assumed to be a thin foil so that the X-ray absorption or fluorescence can be safely ignored, the elemental concentration of two elements can be proportional to the X-ray intensity ratio (peak integral): $\frac{C1}{C2} = k_{12}\frac{I1}{I2}$, where k_{12} is a constant.

Mn, Co and Fe relative contents were calculated by integrating their K edge peaks and taking into account their k-factors. The results were summarized in the following table.

MCF_0.8	Mn at.%	Co at.%	Fe at.%
As-synthesized	26.4	28.2	45.4
After CV cycles	18.3	23.8	57.9

Table 6.2 EDX quantitative analysis of MCF_0.8 catalysts before and after electrochemical cycles without considering the overlap between Mn Kβ and Fe Kα and between Fe Kβ and Co Kα.

Considering Mn Kβ overlaps with Fe Kα and Fe Kβ overlaps with Co Kα, the above table overestimates the relative contributions of Fe and Co. The intensity ratio of Kβ/Kα is 17/150 for Mn, Co and Fe.[5] Assuming the actual relative contents of Mn, Fe and Co are x at.%, y at.% and z at.%, three following equations were set to solve the actual relative contents.

$$1.\ x + y + z = 100$$

$$2.\ \frac{\frac{17}{150}x+y}{x} = \frac{45.4}{26.4}$$

$$3.\ \frac{\frac{17}{150}y+z}{y} = \frac{28.2}{45.4}$$

Solving equations results in the actual relative contents of Mn (29.2 at.%), Co (23.8 at.%) and Fe (47.0%), which is more consistent with the ideal relative contents of Mn (26.7% at.%), Co (24.3 at.%) and Fe (48.6 at.%) in $Mn_{0.8}(CoFe_2)_{0.73}O_4$ catalysts (MCF_0.8). The actual relative contents of MCF_0.8 after electrochemical cycles were also calculated using the same strategy and summarized in the following table together with that of as-synthesized MCF_0.8.

MCF_0.8	Mn at.%	Co at.%	Fe at.%
As-synthesized	29.2	23.8	47.0
After CV cycles	20.2	18.3	61.5

Table 6.3 More accurate EDX quantitative analysis of MCF_0.8 catalysts before and after electrochemical cycles after considering the overlap between Mn Kβ and Fe Kα and between Fe Kβ and Co Kα.

with the theoretical ratio of reactants of 27, 24 and 49 %. After electrochemical cycling, the relative amounts of Mn and Co dropped from 29.2 to 20.2 % and from 23.8 to 18.3 %, respectively, while the content of Fe increased from 47.0 to 61.5 %.

The superior ORR activity and durability of the trimetallic oxide MCF-0.8 over both $CoFe_2O_4$/C and $MnFe_2O_4$/C, suggest that the underlying catalytic mechanism involves multiple metal active sites catalyzing the reduction of oxygen. *In situ* synchrotron-based XAS was employed to investigate the catalytic mechanism of MCF-0.8 under real-time electrochemical conditions. We have designed a customized electrochemical cell for *in situ* XAS measurements in our previous report[21]. The cell consisted of a working electrode of a MCF-0.8 catalyst loaded on porous carbon paper, a Ag/AgCl (1M KCl) reference electrode and a carbon rod counter electrode. Details of the cell design can be found in Figure 6.3. To investigate the structural evolution of the Co-Mn oxide catalysts at steady state, the applied potential was held constant while *in situ* XAS spectra were acquired, after the current had dropped to background levels. According to the CV profile of the catalysts at a scan rate of 1 mV/s in the home-made cell (Figure 6.13A, inset), constant applied electrochemical potentials (E) of 1.2 V, 1.0 V and 0.8 V vs. RHE correspond to the oxidation peak and its two onset potentials while values of 0.8 V, 0.6 V and 0.4 V vs. RHE correspond to the reduction peak and its two onset potentials. E value of 0.2 V vs. RHE was also included to investigate the electrochemical behavior of MCF-0.8 in a strongly reducing environment. Figure 6.13A exhibits the *in situ* XANES spectra of the Mn K-edge of MCF-0.8 at various applied potentials, suggesting systematic changes in the local electronic structure. Mn XANES spectra were calibrated, based on the characteristic absorption edge of elemental Mn (metal foil) at 6539.0 eV, which

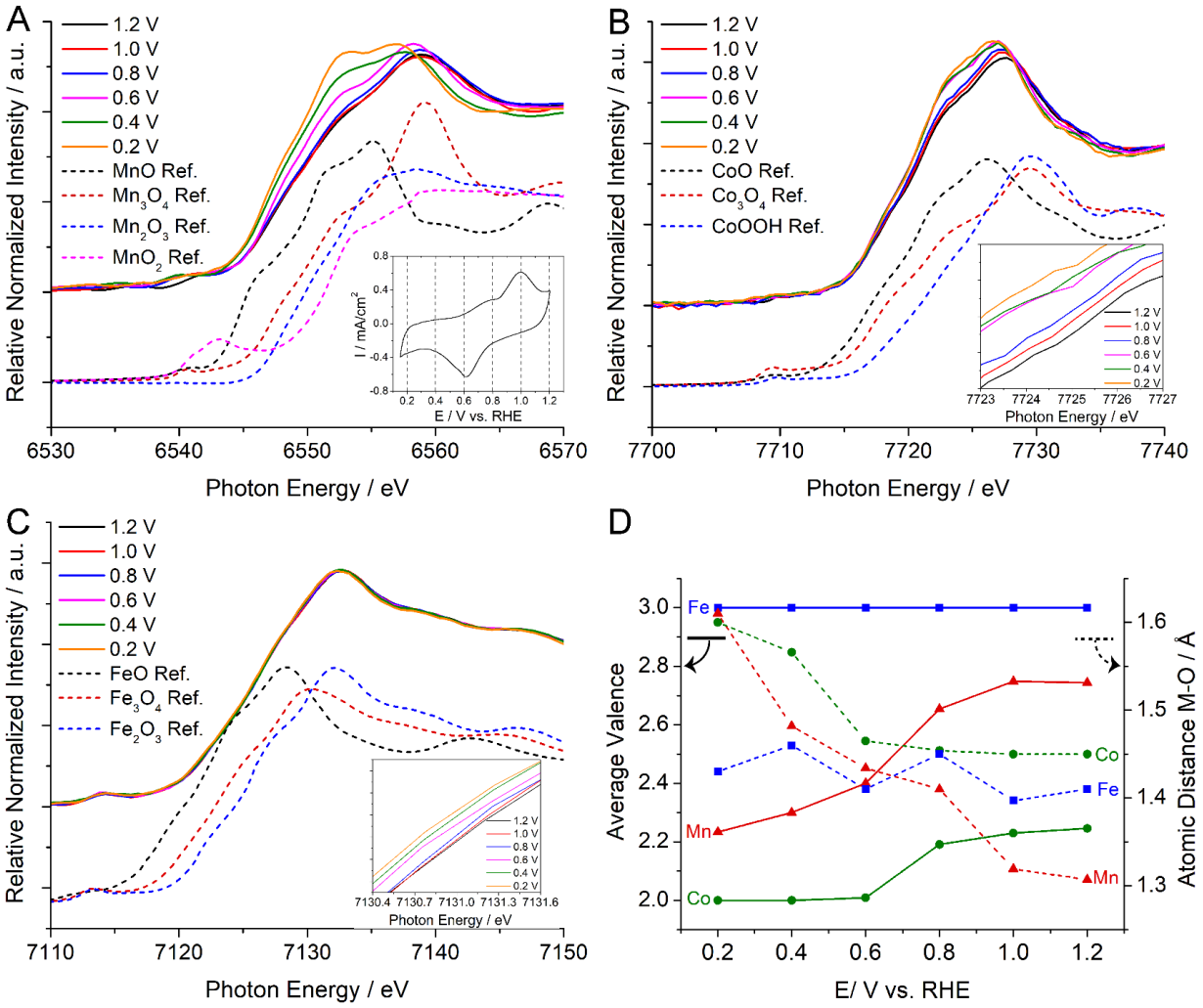

Figure 6.13 *In situ* XANES spectra of the Mn, Co and Fe K-edges of MCF-0.8 and the evolution of the average metal valence and metal-oxygen atomic distance at a series of applied potentials. (A) *In situ* XANES spectra at the Mn K-edge of the MCF-0.8 (solid lines) and the reference manganese oxides (dashed lines). Inset shows the selected applied potential from the CV profile at a scan rate of 1mV/s in the home-made electrochemical cell at which signals were detected. (B) *In situ* XANES spectra at the Co K-edge of the MCF-0.8 (solid lines) and the reference cobalt oxides (dashed lines). Inset shows the gradual shift of the Co K-edge to lower photon energies with changing in intensity. (C)

In situ XANES spectra at the Fe K-edge of the MCF-0.8 (solid lines) and the reference iron oxides (dashed lines). Inset shows the incremental shift of Fe K-edge to lower photon energies with a change in intensity. (D) Calculated average metal valence (solid lines, left Y-axis) as a function of potential based on the linear combination fitting using XANES spectra of reference metal oxides. Measured metal-oxygen (M-O) atomic distance as a function of potential (dashed lines, right Y-axis) based on the *in situ* EXAFS analysis.

corresponds to the excitation of electrons from the Mn 1s orbital. The white line in these Mn spectra, near 6559 eV, originates from an electronic transition from 1s to 4p orbitals, since the 4p are the lowest allowed unoccupied orbitals of 3d transition metals based on the dipole selection rule, $\Delta l = \pm 1$. The shoulder peak at 6553 eV shows a gradual increase in the peak intensity and a small shift to lower energies when the applied potential decreases from 1.2 to 0.2 V, indicating a lower Mn valence state at more negative potentials. More specifically, this peak at 6553 eV exhibited no significant changes when the potential varies from 1.2 to 0.8 V and became pronounced when *E* decreased from 0.8 to 0.6 V. When the potential was below 0.4V, it became more prominent and similar to the feature in the MnO (II) reference, qualitatively suggesting a larger contribution from a lower-valence Mn.

In order to study the gradual changes in the Mn valence more quantitatively, linear combination fitting (LCF) analysis was performed using pure manganese oxides, MnO (II), Mn_3O_4 (II, III), Mn_2O_3 (III) and MnO_2 (IV) as reference spectra. As shown in Figure 6.14, the LCF fits well the experimental Mn XANES spectra and enables the reliable calculation of the relative contributions in of the different Mn oxide references. Figure 6.14B further demonstrates the evolution of the relative contents of Mn oxide references as *E* varies from 1.2 to 0.2 V, as derived from the LCF analysis. When *E* decreased from 1.2 V to 0.8V, the relative contents of different metal oxides remained relatively unchanged, corresponding to the little change in the XANES spectra (Figure 6.13A). When *E* continues to decrease from 0.8 V to 0.2 V, the relative contents of MnO_2 (IV) and Mn_2O_3 (III) quickly dropped from 7%, 10%, respectively, to nearly 0 % and the

relative contents of Mn_3O_4 (II, III) dropped from 60% to 35%. Concomitantly, the relative contents of

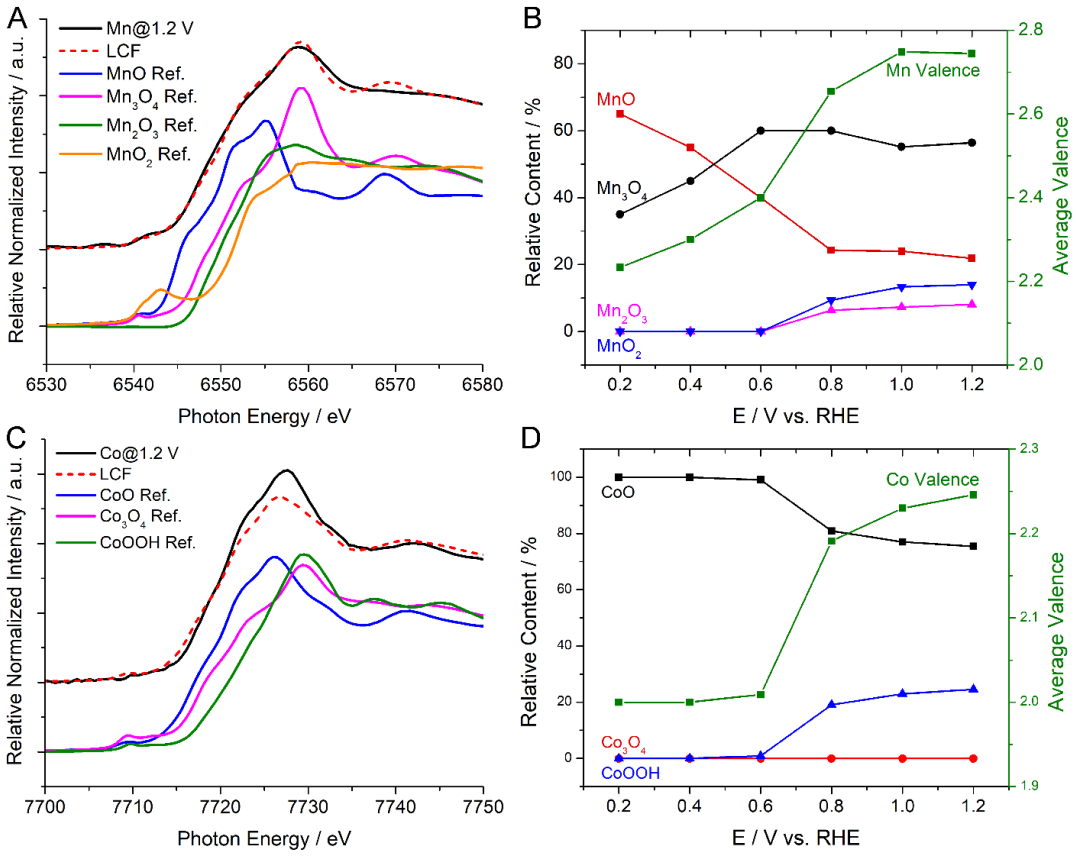

Figure 6.14 (A) Valence analysis of Mn K-edge at 1.2 V vs. RHE. Linear combination fitting (LCF) (red dashed line) indicates the relative content of MnO (22%), Mn_3O_4 (56%), Mn_2O_3 (8.1%) and MnO_2 (14%) at 1.2 V. This LCF has a small R-factor of 0.00276 and reduced χ^2 of 0.000710, indicating a good fitting quality. (B) Average Mn valence at a series of applied potential, which was calculated from the relative contribution of four manganese oxide references. (C) Valence analysis of Co K-edge at 1.2 V. Linear combination fitting (LCF) (red dashed line) indicates the relative content of CoO (75.5%), Co_3O_4 (0%) and Co_2O_3 (24.5%) at 1.2 V. This LCF has a small R-factor of 0.0179 and reduced χ^2 of 0.00517, indicating a reasonable fitting quality. (D) Average Co valence at

a series of applied potential, which was calculated from the relative contribution of three cobalt oxide references.

MnO (II) increased dramatically from 23% to 65%, corresponding to the more dominant features of MnO (II) in XANES spectra of MCF-0.8 at lower potentials. The calculated average valence of Mn decreased substantially and continuously from 2.58 to 2.23 when *E* decreased from 1.2 to 0.2 V, as shown in Figure 6.14B (green line). A lower Mn valence at lower applied potentials would suggest a longer Mn-O chemical bond and weaker binding strength to oxygen, which are clearly confirmed by the corresponding *in situ* EXAFS spectra in Figure 6.15A. The Mn-O atomic distance increased continuously from 1.31 to 1.61 Å when *E* decreased from 1.2 to 0.2 V, as shown in Figure 6.15A (black dashed line). This systematic evolution of the Mn valence and the M-O atomic distance strongly indicate that various Mn species can serve as the active site to catalyze the oxygen reduction reaction.

Co K-edge XANES spectra exhibited similar changes to those of Mn in the MCF-0.8 electrocatalyst. (Figure 6.13B). Co XANES spectra were calibrated based on the characteristic absorption edge of elemental Co (metal foil) at 7709.0 eV. The *in situ* Co XANES spectra and the magnified inset in Figure 6.13B, exhibit a gradual increase in the peak intensity at around 7725 eV, and a continuous shift to lower energies when *E* decreased from 1.2 to 0.2 V, indicating lower Co valences at lower applied potentials. The absorption edge of Co had the most significant changes when *E* dropped from 0.8 to 0.6 V, indicating an abrupt change in its oxidation state and electronic environment. LCF analysis was also employed to quantitatively study the Co valence with CoO (II), Co_3O_4 (II, III) and CoOOH (III) as cobalt oxide references (Figure 6.14C). When *E* varied from

1.2 V to 0.6 V, the relative contents of CoOOH decreased from 24% to nearly 0% while that of CoO increased from 76% to nearly 100%, corresponding to the abrupt change in XANES spectra in Figure 6.13B. The XANES spectra of Co remained essentially unchanged with 100 % CoO when the applied *E* further was decreased from 0.6 to 0.2 V. In contrast to changes of relative contents of Mn_3O_4, the relative contents of Co_3O_4 were calculated to be consistently zero at various potentials, suggesting a negligible contribution from Co_3O_4. The calculated average valence of Co decreased from 2.246 to 2.0 when *E* varied from 1.2 to 0.6 V, and stayed at 2.0 from 0.6 to 0.2V, as shown in Figure 6.14D (green line). *In situ* EXAFS of Co further revealed that the Co-O atomic distance gradually became longer, from 1.45 to 1.60 Å, when *E* shifted from 1.2 to 0.2 V, as shown in Figure 6.15B (black dashed line). This is consistent with the lower Co valence at lower applied potentials, suggesting a weaker Co binding strength to oxygen. Although the gradual evolution of the average Co valence and Co-O atomic distance at various applied potentials were less pronounced than for Mn, the changes in the valence state of Co and Mn shared a similar pattern, suggesting that Co and Mn could serve as co-active sites to catalyze the reduction of oxygen.

Contrary to Co and Mn, the *in situ* XANES of Fe at the K-edge indicated no significant changes during the entire potential range from 1.2 to 0.2 V (Figure 6.13C). The magnified inset exhibits a small increase in the peak intensity at around 7131 eV and a slight shift to lower energies. Further LCF analysis of the Fe valence suggests a 100% contribution from Fe_2O_3 (III) at 1.2 V (Figure 6.16). The Fe valence remained unchanged over the entire *E* range, from 1.2 to 0.2 V, when considering the small statistical error of the LCF analysis (reduced $\chi^2 < 0.001$). The *in situ* EXAFS spectra around the Fe K-edge in Figure

16 suggest that the Fe-O atomic distance remained relatively stable at 1.43 Å with no more than ± 0.05 Å variation when *E* decreased from 1.2 to 0.2 V. Given the above analysis of the average Fe valence and the Fe-O inter atomic distance, unlike Co and Mn, the local electronic structure of Fe stays relatively unchanged over a wide potential range from 1.2 to 0.2 V, indicating that Fe can serve as a "stabilizing agent" in MCF-0.8, and at least in part, contribute to the remarkable durability of MCF-0.8 even after 10,000 electrochemical cycles.

Figure 6.13D serves as a compact summary of the dynamic evolution of average metal valence (solid lines, left Y-axis) and metal-oxygen (M-O) inter atomic-distance (dashed lines, right Y-axis) at various applied potentials. The average Mn and Co valences share a similar decreasing trend at lower applied potentials (red and green solid lines), but some differences in the details can be noted. The Mn-O distance continuously and dramatically decreased from 2.581 to 2.233 Å while the Co-O distance decreased from 2.246 to 2.000 Å when *E* varied from 1.2 to 0.6 V and remained at 2.000 Å even when *E* was below 0.6 V. Considering that the typical working voltages of the membrane electrode assembly (MEA) in alkaline fuel cells are from 0.6 to 1.0 V,[11] the dynamic changes of the valence of Mn and Co suggested that both could serve as active sites and catalyze the reduction of oxygen. The Mn-O atomic distance increased at lower potentials which is consistent with the decrease of Mn valence at lower potentials, suggesting a weaker binding energy of Mn towards oxygen. Changes of the Co-O inter atomic distance followed a similar pattern through with less pronounced changes than for Mn at various potentials (dashed green line). The Co-O inter atomic distance continuously increased when *E* was below 0.6V while the Co valence mainly remained at 2.0, indicating that other factors in the

electronic structure and local chemical environment may also influence the binding energy of Co towards oxygen. The lack of significant changes in the Fe valence and the

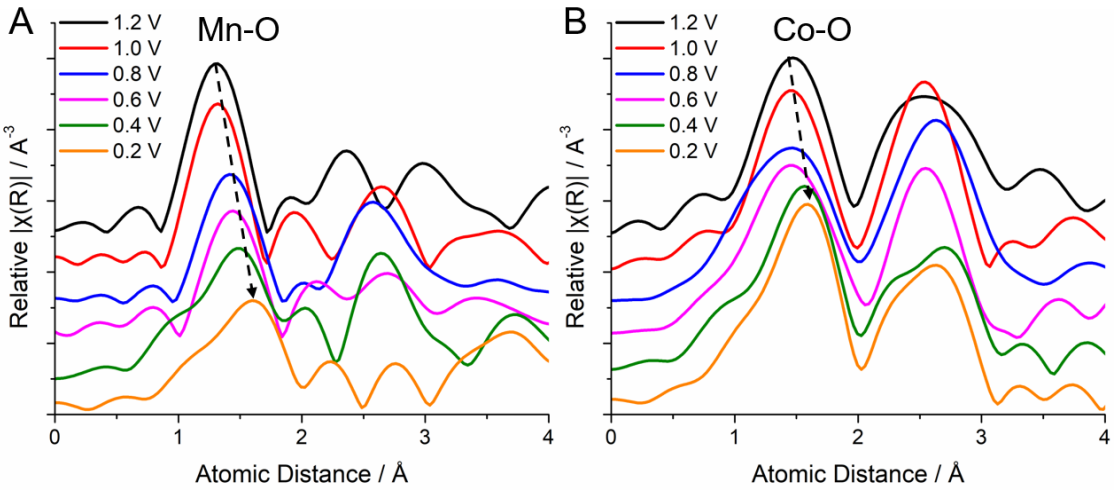

Figure 6.15. *In situ* EXAFS of Mn (A) and Co (B) at a series of applied potential. The Metal-oxygen (M-O) bond distance increases as the applied potential decreased from 1.2 to 0.2 V, corresponding to a lower metal valence and weaker binding strength to oxygen. EXFAS spectra were processed by setting the background value (Rbkg) to 1.2 in Athena software with the FT-window set to 3 to 10 $Å^{-1}$ and no phase correction.

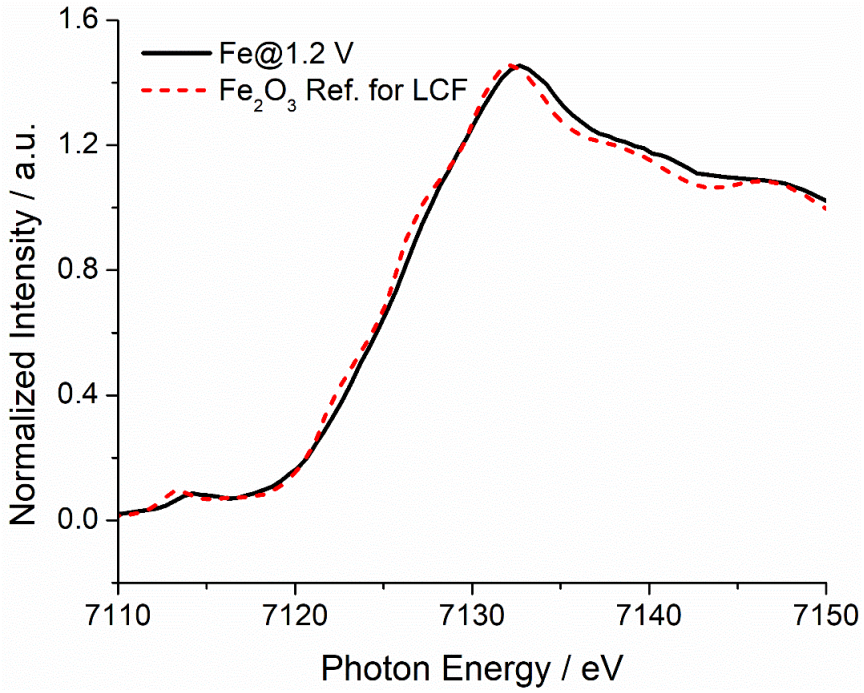

Figure 6.16 Valence analysis of Fe K-edge at 1.2 V. Linear combination fitting (LCF) (red dashed line) indicates the relative content of FeO (0%), Fe_3O_4 (0%) Fe_2O_3 (100%) at 1.2 V. This LCF has a small R-factor of 0.00317 and reduced χ^2 of 0.000922, indicating a good fitting quality. The Fe valence is thus +3 and stays the same when E decreases from 1.2 to 0.2 V, based on the LCF analysis.

Fe-O inter atomic distance (solid and dashed blue lines) suggest that Fe could serve as a stabilizing core element to maintain the integrity of the spinel structure and enhance the long-term durability.

We investigated the evolution of the local electronic structures of Mn, Co and Fe using *in situ* XANES and EXAFS under steady state, constant applied potential conditions. We then explored the dynamic changes in the valence state of the metal active sites during cyclic voltammetry (CV). Such experiments require a non-conventional strategy to enable fast recording of absorption differences, of transmitted X-rays, down to the level of seconds, so as to enable following the relatively potential fast changes during CV. This strategy was first reported in our previous study[21] and employed in this work to enable understanding the synergistic effects of the multi-active sites in MCF-0.8. Instead of acquiring a full XAS spectrum over a time long period (20-30 min). The absorbed X-ray intensity variations were recorded within seconds, at a characteristic energy where the largest changes in the intensity of absorption occurred in the above mentioned steady-state measurements (Figure 6.13A). The X-ray absorption intensity was calculated as $ln(I_1/I_2)$ where I_1 and I_2 are the incident and transmitted X-ray beam intensities, respectively. In this particular case, the characteristic energy values of Mn, Co and Fe were determined to be 6553, 7225 and 7131 eV, respectively. A scan rate of 1mV/s, combined with a X-ray acquisition time of 3s, indicates that the X-ray signal will be averaged over a 3mV potential range, closely approximating to non-steady (dynamic) measurements. From the CV profile at 1 mV/s in the upper inset of Figure 6.17, we

observed that the oxidation currents (positive values) and the reduction currents (negative values) were divided by two boundary potentials, 1.12 and 0.28V. One would expect that the oxidation/reduction currents will reflect metal active sites being converted into higher/lower valence states, and that a periodic change of the metal valence will follow the triangular potential scan (*vide infra*).

Figure 6.17 reveals the periodic changes in the relative X-ray intensity, $ln(I_1/I_2)$, as a cyclic potential scan is applied. When the applied potential starts at the upper boundary value, 1.12 V and is scanned to the lower limit, 0.15 V, the relative X-ray intensity of Mn increases dramatically, and keeps increasing to the maximum intensity until the potential passes the lower limit, 0.15 V and reaches the lower boundary potential, 0.28 V. Higher X-ray intensities, as shown in Figure 6.13A, indicate higher contents of lower Mn valence since the selected energy is closer to the Mn (II) white line energy. The processes from 1.12 to 0.28 V represent the conversion from Mn (III, IV) to Mn (II, III). Symmetrically, when the potential varies from the lower boundary potential, 0.28 V to the upper limit, 1.2 V, the X-ray intensity keeps decreasing to the minimum values until the potential first passes the upper limit, 1.2 V and reaches the upper boundary potential, 1.12 V. The processes from 0.28 V to 1.12 V represent for the conversion from Mn (II, III) to Mn (III, IV). Mn valences change in a periodic fashion in the subsequent two cyclic potential scans. This is fully consistent with the boundary potentials (0.28 V, 1.12 V) of oxidation and reduction currents in the CV discussed before, unveiling a real-time glimpse of an intriguing electrocatalytic mechanism of Mn active sites in MCF-0.8.

Compared to the changes of Mn, the relative X-ray intensity of Co at 7225 eV also increases as the potential drops from 1.12 V, but reaches a relatively stable plateau at around 0.6 V, which is consistent with the dramatic changes in the Co XANES spectra

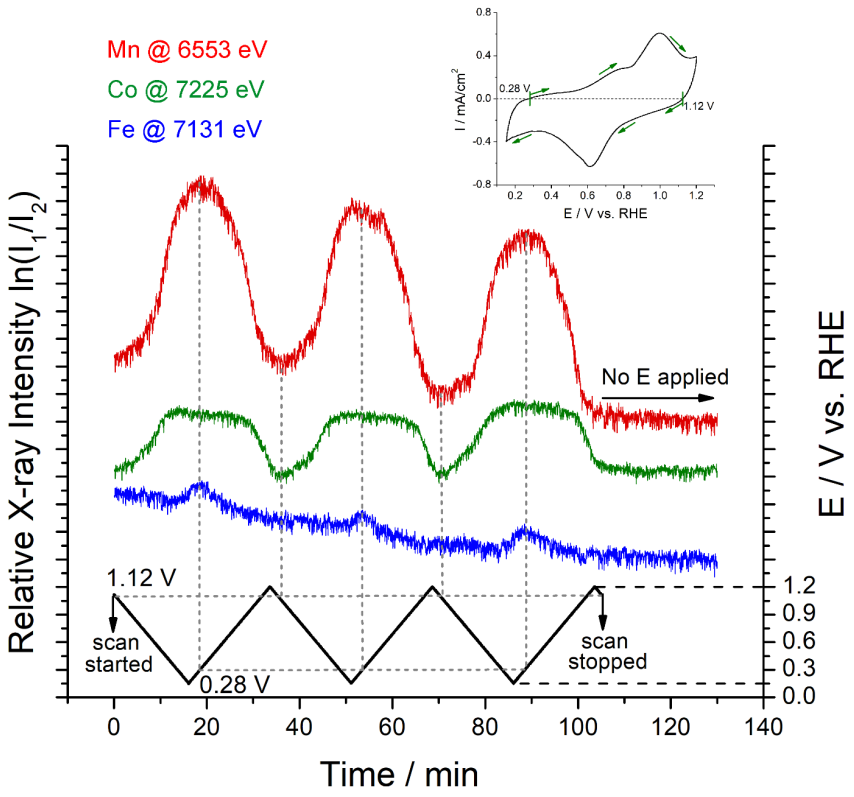

Figure 6.17 Periodic changes of the relative X-ray intensities ($ln(I_1/I_2)$) at 6553 eV (Mn K-edge, red lines), 7225 eV (Co K-edge, green lines) and 7131 eV (Fe K-edge, blue lines), respectively, as a function of the cyclic potential sweep at 1 mV/s from 1.2 to 0.15 V vs. RHE. Intensity variations at 6553, 7225 and 7131 eV reflect the conversion among Mn(IV), Mn(III) and Mn(II), between Co(III) and Co (II), and Fe(III) and Fe(II), respectively. Relative X-ray intensity increases, suggesting a conversion of the metal from higher valence to lower valence as the applied potential goes from 1.2 to 0.15 V, and reach a maximum value at 0.28 V. Concomitantly, the relative X-ray intensity decreased as the applied potential goes from 0.15 to 1.2 V and reach a maximum value at

1.12 V. The upper inset shows the corresponding CV at 1 mV/s over the potential range of 0.15-1.2 V vs. RHE. Oxidation and reduction currents in the CV are divided by two boundary potentials, 0.28V and 1.12 V vs. RHE.

from 1.2 to 0.6 V with little, if any, changes below 0.6 V (Figure 6.14B). During the cyclic potential scan, the periodic behavior of the relative X-ray intensity of Co correspond to the reversible conversion between Co(III) at high *E* to Co(II) at lower *E*. In sharp contrast to the patterns of Mn and Co, the relative X-ray intensity of Fe at 7131 eV, remains essentially unchanged during the cyclic potential scan, suggesting no significant changes in the Fe valence. A smaller X-ray intensity variation of Fe evident at very negative potentials at around 0.15~0.28 V may suggest a slight reduction from Fe(III) to Fe(II), which is consistent with the incremental increase in the X-ray intensity of the Fe K-edge XANES (Figure 6.14C). Such a small conversion from Fe(III) to Fe(II) may not be revealed in the change of Fe valence, considering the statistical error of LCF analysis.

The relative changing X-ray intensities of Mn, Co and Fe following repeating patterns during three continuous cyclic potential scans, suggest a reproducible and stable electrochemical behavior of the three metal active sites under electrochemical operating conditions. To rigorously exclude other factors, such as X-ray generated photoelectrons, which may result in periodic patterns of X-ray intensity variations, a control experiment was performed by recording the X-ray signal without an applied potential. A stable background in the X-ray intensity indicates that the periodic changes of Mn and Co valences primarily arise from the applied cyclic potential scan. In summary, the periodic patterns of Mn and Co valence changes in MCF-0.8 are in sync with each other, which strongly suggests a synergistic effect existing between Mn and Co for the electrocatalysis

towards the reduction of oxygen. Fe, in contrast, maintains a stable electronic structure and serves as a supportive core element, which may contribute to the long-term durability.

6.5 Conclusion

In summary, a new class of MCF nanoparticle electrocatalysts for the ORR have been rationally designed and prepared via hydrothermal reaction and subsequent heat treatment. Their electrochemical activity demonstrates a "volcano trend" correlation with continuously increasing Mn content. The MCF-0.8, had the most active composition, exhibiting an ORR activity with a $E_{1/2}$ of 0.89 V, nearly same as Pt/C and a robust durability with a $\Delta E_{1/2}$ of 0.014 V after 10,000 potential cycles. A thorough mechanistic picture emerged from the *in situ* XAS experiment, suggesting that the Mn and Co cations serve as the active sites, with Fe stabilizing the spinel oxide structure. Additionally, the comprehensive STEM-EDX quantitative analysis provided additional evidence of the synergistic effect towards the oxygen reduction reaction, and possible explanations for the degradation process. The work outlined here shed light on the strategic design of trimetallic spinel oxides as ORR electrocatalysts in alkaline fuel cells and advance our understanding of the catalytic mechanism using *operando* spectroscopic methods.

6.6 References

1. Debe, M. K. Electrocatalyst Approaches and Challenges for Automotive Fuel Cell s. *Nature* **2012**, *486*, 43-51.
2. Xiong, Y.; Yang, Y.; Joress, H.; Padgett, E.; Gupta, U.; Yarlagadda, V.; Agyeman-B udu, D. N.; Huang, X.; Moylan, T. E.; Zeng, R.; Kongkanand, A.; Escobedo, F. A.; Brock, J. D.; DiSalvo, F. J.; Muller, D. A.; Abruña, H. D. Revealing the Atomic Ord ering of Binary Intermetallics Using in Situ Heating Techniques at Multilength Scal es. *Proc. Natl. Acad. Sci. U.S.A*. **2019**, DOI: 10.1073/pnas.1815643116.
3. Gasteiger, H. A.; Kocha, S. S.; Sompalli, B.; Wagner, F. T. Activity Benchmarks an d Requirements for Pt, Pt-alloy, and Non-Pt Oxygen Reduction Catalysts for PEMF Cs. *Appl. Catal. B: Environ*. **2005**, 56, 9-35.
4. Shao, M.; Chang, Q.; Dodelet, J.-P.; Chenitz. R. Recent Advances in Electrocatalyst s for Oxygen Reduction Reaction. *Chem. Rev*. **2016**, 116, 3594-3657.
5. Chung, H. T.; Cullen, D. A.; Higgins, D.; Sneed, B. T.; Holby, E. F.; More, K. L.; Z elenay, P. Direct Atomic-level Insight into the Active Sites of a High-Performance P GM-Free ORR Catalyst. *Science* **2017**, 357, 479-484.
6. Stamenkovic, V. R.; Mun, B. S.; Arenz, M.; Mayrhofer, K. J.; Lucas, C. A.; Wang, G..; Ross, P. N.; Markovic, N. M. Trends in Electrocatalysis on Extended and Nanos cale Pt-Bimetallic Alloy Surfaces. *Nat. Mater*. **2007**, 6, 241-247.
7. Wang, D.; Xin, H. L.; Hovden, R.; Wang, H.; Yu, Y.; Muller, D. A.; DiSalvo, F. J.; Abruña, H. D. Structurally Ordered Intermetallic Platinum–Cobalt Core–Shell Nano particles with Enhanced Activity and Stability as Oxygen Reduction Electrocatalyst s. *Nat. Mater*. **2013**, 12, 81-87.

8. Xiong, Y.; Yang, Y.; DiSalvo, F. J.; Abruña, H. D. Pt-Decorated Composition-Tunable Pd-Fe@ Pd/C Core-Shell Nanoparticles with Enhanced Electrocatalytic Activity towards the Oxygen Reduction Reaction. *J. Am. Chem. Soc*. **2018**, 140, 7248-7255.
9. Xiong, Y.; Xiao, L.; Yang, Y.; DiSalvo, F. J.; Abruña, H. D. High-Loading Intermetallic Pt_3Co/C Core–Shell Nanoparticles as Enhanced Activity Electrocatalysts toward the Oxygen Reduction Reaction (ORR). *Chem. Mater*. **2018**, 30, 1532-1539.
10. Lima, F. H. B.; Zhang, J.; Shao, M.; Sasaki, K.; Vukmirovic, M. B.; Ticianelli, E. A.; Adzic, R. R. Catalytic Activity-d-Band Center Correlation for the O_2 Reduction Reaction on Platinum in Alkaline Solutions. *J. Phys. Chem. C*, **2007**, 111, 404-410.
11. Lu, S.; Pan, J.; Huang, A.; Zhuang, L.; Lu, J. Alkaline Polymer Electrolyte Fuel Cells Completely Free from Noble Metal Catalysts. *Proc. Natl. Acad. Sci. U. S. A*. **2008**, 105, 20611-20614.
12. Wang, Y.-J.; Qiao, J.; Baker, R.; Zhang, J. Alkaline Polymer Electrolyte Membranes for Fuel Cell Applications. *Chem. Soc. Rev*. **2013**, 42, 5768−5787.
13. Ge. X.; Sumboja, A.; Wuu, D.; An, T.; Li, B.; Thomas Goh, F. W.; Andy Hor, T. S.; Zong, Y.; Liu, Z. Oxygen Reduction in Alkaline Media: from Mechanisms to Recent Advances of Catalysts. *ACS Catal*., **2015**, 5, 4643-4667.
14. Jiang, W.-J.; Gu, L.; Li, L.; Zhang, Y.; Zhang, X.; Zhang, L.-J.; Wang, J.-Q.; Hu, J.-S.; Wei, Z.; Wan, L.-J. Understanding the High Activity of Fe–N–C Electrocatalysts in Oxygen Reduction: Fe/Fe_3C Nanoparticles Boost the Activity of $Fe–N_x$. *J. Am. Chem. Soc*., **2016**, 138, 3570-3578.
15. Ren, H.; Wang, Y.; Yang, Y.; Tang, X.; Peng, Y.; Peng, H.; Xiao, L.; Lu, J.; Abruña, H. D.; Zhuang, L. Fe/N/C Nanotubes with Atomic Fe sites: A Highly Active Cathod

e Catalyst for Alkaline Polymer Electrolyte Fuel Cells. *ACS Catal*. **2017**, 7, 6485-6492.

16. Liang, Y.; Li, Y.; Wang, H.; Zhou, J.; Wang, J.; Regier, T.; Dai, H. Co_3O_4 Nanocrystals on Graphene as a Synergistic Catalyst for Oxygen Reduction Reaction. *Nat. Mater*. **2011**, 10, 780-786.
17. Liang, Y.; Wang, H.; Zhou, J.; Li, Y.; Wang, J.; Regier, T.; Dai, H. Covalent Hybrid of Spinel Manganese–Cobalt Oxide and Graphene as Advanced Oxygen Reduction Electrocatalysts. *J. Am. Chem. Soc.*, **2012**, 134, 3517-3523.
18. Cheng, F.; Shen, J.; Peng, B.; Pan, Y.; Tao, Z.; Chen, J. Rapid Room-Temperature Synthesis of Nanocrystalline Spinels as Oxygen Reduction and Evolution Electrocatalysts. *Nat. Chem*. **2011**, 3, 79-84.
19. Li, C.; Han, X.; Cheng, F.; Hu, Y.; Chen, C.; Chen, J. Phase and Composition Controllable Synthesis of Cobalt Manganese Spinel Nanoparticles towards Efficient Oxygen Electrocatalysis. *Nat. Commun*. **2015**, 6, 7345.
20. Zhao, Q.; Yan, Z.; Chen, C.; Chen, J. Spinels: Controlled Preparation, Oxygen Reduction/Evolution Reaction Application, and Beyond. *Chem. Rev*. **2017**, 117, 10121-10211.
21. Yang, Y.; Wang, Y.; Xiong, Y.; Huang, X.; Shen, L.; Huang, R.; Wang, H.; Pastore, J. P.; Yu, S.-H.; Xiao, L.; Brock, J. D.; Zhuang, L.; Abruña, H. D. In Situ X-ray Absorption Spectroscopy of a Synergistic Co−Mn Oxide Catalyst for the Oxygen Reduction Reaction. *J. Am. Chem. Soc*. **2019**, 141, 1463-1466.
22. Meng, Y.; Song, W.; Huang, H.; Ren, Z.; Chen, S.-Y.; Suib, S. L. Structure–Property Relationship of Bifunctional MnO_2 Nanostructures: Highly Efficient, Ultra-Stable

Electrochemical Water Oxidation and Oxygen Reduction Reaction Catalysts Identified in Alkaline Media *J. Am. Chem. Soc*. **2014**, 136, 11452-11464.

23. Lee, J. W.; Hall, A. S.; Kim, J. D.; Mallouk, T. E. A Facile and Template-Free Hydrothermal Synthesis of Mn_3O_4 Nanorods on Graphene Sheets for Supercapacitor Electrodes with Long Cycle Stability. *Chem. Mater*. **2012**, 24, 1158-1164.
24. Miura, A.; Rosero-Navarro, C.; Masubuchi, Y.; Higuchi, M.; Kikkawa, S.; Tadanaga, K. Nitrogen-Rich Manganese Oxynitrides with Enhanced Catalytic Activity in the Oxygen Reduction Reaction. *Angew. Chem., Int. Ed.* **2016**, 55, 7963-7967.
25. Hu, Y.; Jensen, J.; Zhang, W.; Cleemann, L.; Xing, W.; Bjerrum, N.; Li, Q. Hollow Spheres of Iron Carbide Nanoparticles Encased in Graphitic Layers as Oxygen Reduction Catalysts. *Angew. Chem., Int. Ed.* **2014**, 126, 3749-375.
26. Zhu, H.; Zhang, S.; Huang, Y.-X.; Wu, L.; Sun, S. Monodisperse $M_xFe_{3-x}O_4$ (M = Fe, Cu, Co, Mn) Nanoparticles and Their Electrocatalysis for Oxygen Reduction Reaction. *Nano Lett*. **2013**, 13, 2947-2951.
27. Restovic, A.; Ríos, E.; Barbato, S.; Ortiz, J.; Gautier, J. Oxygen Reduction in Alkaline Medium at Thin $Mn_xCo_{3-x}O_4$ ($0 \leq x \leq 1$) Spinel Films Prepared by Spray Pyrolysis. Effect of Oxide Cation Composition on the Reaction Kinetics. *J. Electroanal. Chem.* **2002**, 522, 141-151.
28. Ríos, E.; Abarca, S.; Daccarett, P.; Cong, H. N.; Martel, D.; Marco, J.; Gancedo, J.; Gautier, J. Electrocatalysis of Oxygen Reduction on $Cu_xMn_{3-x}O_4$ ($1.0 \leq x \leq 1.4$) Spinel Particles/Polypyrrole Composite Electrodes. *Int. J. Hydrog. Energy*. **2008**, 33, 4945−4954.

29. Indra, A.; Menezes, P.; Sahraie, N.; Bergmann, A.; Das, C.; Tallarida, M.; Schmeiße r, D.; Strasser, P.; Driess, M. Unification of Catalytic Water Oxidation and Oxygen Reduction Reactions: Amorphous Beat Crystalline Cobalt Iron Oxides. *J. Am. Chem. Soc.* **2014**, *136*, 17530-17536.

30. Wu, G.; Wang, J.; Ding, W.; Nie, Y.; Li, L.; Qi, X.; Chen, S.; Wei, Z. A strategy to Promote the Electrocatalytic Activity of Spinels for Oxygen Reduction by Structure Reversal. *Angew. Chem.* **2016**, *128*, 1362-1366.

31. Ravel, B. & Newville, M. ATHENA, ARTEMIS, HEPHAESTUS: Data Analysis fo r X-ray Absorption Spectroscopy Using IFEFFIT. *J. Synchrotron Rad*. **2005**, 12, 53 7.

32. Castro, P.; Vago, E.; Calvo, E. Surface Electrochemical Transformations on Spinel I ron Oxide Electrodes in Aqueous Solutions. *J. Chem. Soc. Faraday Trans.* **1996**, *92*, 3371.

33. Zhou, Y.; Xi, S.; Wang, J.; Sun, S.; Wei, C.; Feng, Z.; Du, Y.; Xu, Z. J. Revealing th e Dominant Chemistry for Oxygen Reduction Reaction on Small Oxide Nanoparticl es. *ACS Catal*., **2018**, 8, 673–677.

34. Bard, A. J.; Faulkner L. R. Electrochemical Methods: Fundamentals and Applicatio ns, Wiley: New York, **2001**, pp341.

CHAPTER 7

MOF-DERIVED CO-FE BIMETALLIC OXYGEN REDUCTION ELECTROCATALYSTS FOR ALKALINE FUEL CELLS

Reproduced from *J. Am. Chem. Soc.***2019**, 141 (27) 10744-10750

.7.1 Abstract

The oxygen reduction reaction (ORR) is considered the cornerstone for regenerative energy conversion devices involving fuel cells and electrolyzers. The development of non-precious-metal electrocatalysts is of paramount importance for their large-scale commercialization. Here, Co-Fe binary alloy embedded bimetallic organic frameworks (BMOF)s based on carbon nanocomposites have been designed with a compositionally optimized template, by a facile host-guest strategy, for the ORR in alkaline media. The electrocatalyst exhibits promising electrocatalytic activity for the ORR with a half-wave potential of 0.89 V in 0.1 M NaOH; comparable to state-of-the-art Pt/C electrocatalysts. More importantly, it exhibits robust durability after 30,000 potential cycles. Scanning transmission electron microscopy (STEM) and quantitative energy-dispersive X-ray (EDX) spectroscopy suggest that the Co-Fe alloy nanoparticles have a homogenous elemental distribution of Co and Fe at the atomic-scale with optimized BMOF and Co/Fe ratio of 9:1. The long-term durability is attributed to its ability to maintain its structural and compositional integrity after the cycling process, as evidenced by STEM-EDX analysis. This work provides valuable insights into the design and fabrication of novel PGM-free highly active ORR electrocatalysts in alkaline media.

7.2 Introduction

The continuing consumption of non-renewable fossil fuels and increased aspiration for a global sustainable energy technology landscape, has stimulated the development of novel fuel cell technologies.[Error! Reference source not found.-Error! Reference source not found.] The regenerative energy conversion concept, targeting low-carbon or carbon-free fuels, makes

it a promising approach to lower CO_2 emissions.[3-4] The challenge to accelerate the sluggish oxygen reduction reaction (ORR) at the cathode in fuel cell applications, will require novel materials and architectures. Platinum-group-metals (PGM) based materials are still considered to be the state-of-the-art electrocatalysts towards the ORR.[5-7] However, their large-scale application in fuel cells is still precluded by cost and limited stability.[8-9] Thus, there is a clear need to design and develop cost effective alternatives with high electrocatalytic activity and robust long-term stability. Alkaline polymer electrolyte fuel cells (APEFCs) have attracted a great deal of interest in the recent past because they can enable the use of non-precious metals as electrocatalysts for the ORR.[10] In this context, extensive investigations have focused on non-PGM materials, including transition metal oxide[11-18], ranging from monometallic to trimetallic oxides, and PGM-free nitrogen doped carbon materials.[19-21] Dai and co-workers have reported on Mn-Co oxides loaded on N-doped reduced graphene oxide, which significantly enhanced the electrocatalytic activity by the covalent coupling effect between the support and the oxide nanoparticles.[22] Yang et al. studied perovskite-based oxides, applying them for both oxygen reduction and evolution reactions.[23] Zelenay and Dodelet have utilized nitrogen-containing organic molecules incorporating earth-abundant Co or Fe, to prepare metal-nitrogen-carbon (M-N-C) materials through high-temperature pyrolysis. The resulting materials have exhibited promising performance in membrane electrode assemblies (MEAs), providing further impetus to the industrial application of PGM-free electrocatalyst materials. [24-27] Furthermore, Lu et al., Peng et al. and Sa et al. have fabricated a variety of non-PGM catalysts, including carbonaceous materi-al derived from halloysite, CoOx nanohybrids

and Fe, N doped carbon materials, respectively. They are adapted in APEFCs and demonstrated excellent performance.[28-30]

Recently, metal organic frameworks (MOFs), (containing metal centers and organic linkers), have generated a great deal of attention as scaffolds and precursors for novel families of carbon nanocomposites.[31-32] As representatives of MOFs, zeolitic imidazolate frameworks (ZIFs) such as ZIF-67 and ZIF-8, with available metal centers and highly abundant carbon and nitrogen, have emerged as promising precursors as electrocatalysts.[33-34] The nitrogen species can bond to non-noble-metal nanoparticles as a means to yield N-doped carbon materials.[35] Nitrogen atoms can generate positively charged sites that are conducive to O_2 adsorption or splitting, which is believed to help expedite the kinetics of the oxygen reduction reaction.[36-37] There have been numerous reports on these context. Lou et al. employed ZIF-67 to produce porous hollow carbon polyhedra, comprised of N-doped carbon nanotubes (CNTs), as bifunctional electrocatalysts towards the ORR and OER.[38] Song et al. used ZIF-8 as a sacrificial framework that was pyrolyzed and activated with NH_3 for optimized N configuration/doping to boost electrocatalytic activity.[39] ZIF-67-derived materials feature N-doped mesoporous graphitic carbon with a stable structure, as well as high electronic conductivity and Co decoration for the generation of active sites. ZIF-8 provides a hollow framework with high surface area, promoting rapid diffusion kinetics during electrocatalysis. Jiang and coworkers, Su and coworkers and others, have employed bimetallic mixtures of ZIF-67 and ZIF-8 as templates, further doped with phosphate anions, to fabricate electrocatalytically active nanocarbon materials after pyrolysis in Ar.[40-41]

7.3 Experimental Section

7.3.1 Materials

Zinc nitrate ($Zn(NO_3)_2 \cdot 6H_2O$), cobalt nitrate ($Co(NO_3)_2 \cdot 6H_2O$), 2-methylimidazole, 1-methylimidazole, sodium hydroxide (AR), sulfuric acid, methanol, ethanol, hexane and Nafion (5 wt.%) were purchased from Sigma-Aldrich. Carbon-supported Pt/C (20 wt.%) nanoparticles (NPs) were supplied by Johnson Matthey. All chemicals were used as received without further purification.

7.3.2 Synthesis of BMOFs Zn_xCo_y Derived Carbon Materials

In a typical synthesis, a mixture of $Co(NO_3)_2 \cdot 6H_2O$ and zinc nitrate hexahydrate ($Zn(NO_3)_2 \cdot 6H_2O$) with different molar ratios of Co^{2+}/Zn^{2+} was dissolved in a mixed solvent of 40 mL ethanol and 40 mL methanol, where the total molar amounts of Zn and Co were 6 mmol with stoichiometric number represented by x and y in moles. Another mixture of 2-methylimidazole (1.97 g) and 1-methylimidazole (0.97 g) with 40 mL methanol and 40 mL ethanol was then added under magnetic stirring. The solution was kept static for 48 h at room temperature. The formed precipitate was collected by centrifugation, washed with isopropanol and dried in an oven at 60 ^oC. The as-synthesized BMOF particles were dispersed in a ceramic boat and heated in flowing forming gas (5% H_2, 95% N_2). The temperature of the furnace was first adjusted to 300 ^oC over 1.5 h and further ramped up to 800 ^oC at 5 ^oC/min and held there for an additional 2 h. The furnace was subsequently turned off and the system allowed to cool. The carbon materials that remained were treated in 0.5 M sulfuric acid solution for 10 h. The resulting samples were

collected by centrifugation, repeatedly washed with DI water until neutral and dried at 60 ^{o}C.

7.3.3 Synthesis of BMOF_Zn_6Co_Fe Derived Carbon Materials

150 mg of agglomerated crystals of BMOF_Zn_6Co were suspended in 20 mL hexane and sonicated for 1 h. Then 2 mL of $Fe(acac)_3$ (2 mg/mL) were added in a dropwise fashion while magnetically stirring. The suspension was sonicated for 1 h and stirred at room temperature for 12 h. The impregnated BMOF_Zn_6Co_Fe sample was centrifuged and dried overnight. The resulting powder sample was treated with the same thermal and acid treatments as mentioned above and dried at 600 ^{o}C for 1 h.

7.3.4 Structural Characterizations

The crystal structures of all the synthesized BMOF related materials were confirmed by powder X-ray diffraction (XRD) using a Rigaku Ultima IV Diffractometer. Diffraction patterns were collected at a scan rate of 2^{o} min^{-1} at 0.02^{o} steps from 10 to 80^{o} two theta. The N_2 sorption isotherms were collected using a Micromeritics ASAP 2020 system at liquid-nitrogen temperature. Raman spectra are collected using a Renishaw System 1000 micro-Raman spectroscope (Renishaw). Morphologies were characterized by a field-emission scanning electron microscopy (Zeiss Gemini 500, 0.75 eV). Scanning transmission electron microscopy (STEM) images and elemental electron energy loss spectroscopy (EELS) maps were acquired on a fifth-order aberration-corrected STEM (Cornell Nion UltraSTEM) operated at 100 keV with a beam convergence angle of 30 mrad. STEM images were processed using Richard-Lucy deconvolution (3 iterations). EELS (electron energy loss spectro-mapping) spectral images were acquired with a 0.25 eV/channel energy dispersion in a Gatan spectrometer with a size of 100×100 pixels and

an acquisition time of 10 ms/pixel. The Co and Fe elemental maps were extracted using their sharp L_3 edges from the EELS spectrum image and processed using principal component analysis (PCA, 3 components) and the linear combination of power law (LCPL) to subtract the background, in ImageJ software. STEM-EDX spectra were collected in a FEI Tecnai F-20 electron microscope equipped with an Oxford X-Max detector. Possible beam damage was routinely checked before and after EELS and EDX mapping. Under the conditions mentioned above, no damage was observed.

7.3.5 Electrochemical Characterization

Electrochemical measurements were performed in 0.1M NaOH on a Solartron potentiostat. In all electrochemical measurements, 5 mg of the prepared catalyst was mixed with 1 mL of 0.05 wt% Nafion/ethanol solution and subsequently sonicated for approximately 30 minutes. 20 μL of the resulting catalyst ink were loaded onto a 5 mm diameter glassy carbon (GC) electrode, achieving a catalyst loading of 0.5 mg cm^{-2}, followed by thermal evaporation of the solvent under infrared light. The mass loading of Pt on GC was 25 μg cm^{-2}, a common value, for comparison in fuel cell tests. A graphite rod was used as the counter electrode and Ag/AgCl, in a 1M KCl solution, served as the reference electrode. ORR measurements were carried out with a rotating disk electrode (RDE) in oxygen-saturated 0.1M NaOH solution at room temperature (23 ^oC) (Bubbling with O_2 for 15 mins before scanning). All cyclic voltammetric profiles were obtained between 0.05 V to 1.1 V vs. a reversible hydrogen electrode (RHE) at 5 mV/s in Ar-saturated 0.1M NaOH. The ORR profiles were obtained at 5 mV/s and 1600 rpm after 50 CV cycles from 0.05 to 1.1 V at 50 mVs^{-1} to remove the surface contamination and activate the catalyst. The background capacitive current measured in Ar-saturated 0.1M

NaOH solution was subtracted to process and plot the ORR profiles. Durability tests were carried out by continuously cycling the potential from 0.6 V to 1.0 V at 100 mV/s for 30,000 cycles. The ORR profiles after 30,000 cycles were measured in the 0.1M NaOH electrolyte.

7.4 Results and Discussion

Herein, we report on a group of optimized bimetallic MOFs (BMOFs) derived from a Co-Fe alloy embedded in a carbon nanocomposite, which when compositionally optimized, exhibit highly stable electrocatalytic activity towards the ORR (detailed experiments can be found in Experimental Section). In ZIF-8, volatile Zn metal centers can evaporate, generating a carbon structure with high surface area and porosity. The resulting cavities served as hosts to encapsulate Fe ions to form a Co-Fe alloy with cobalt derived from the ZIF-67 or with externally added $Fe(acac)_3$. The resulting nanocomposite exhibited ORR electrocatalytic activity comparable to commercial Pt, as well as high stability for the ORR in alkaline media as evidenced by its compositional and structural integrity. A family of Co-Zn bimetallic MOFs (BMOFs) precursors was synthesized by a facile one-step solvothermal method at room temperature, through the self-assembly of Co^{2+}/Zn^{2+} with 1/2-methyimidazole in a solvent mixture of ethanol and methanol. Their compositions were varied systematically and labeled as BMOF-Co, $ZnCo_3$, ZnCo, Zn_3Co, Zn_6Co, $Zn_{11}Co$, $Zn_{20}Co$ and Zn, representing the fraction of the Co^{2+} salt ($Co(NO_3)_2$) as 100%, 75%, 50%, 14%, 8%, 5% and 0%, respectively. The powder X-ray diffraction (XRD) patterns of the resulting BMOFs are shown in Figure 7.1, where those of BMOF_Co and Zn were consistent with the simulated XRD patterns of ZIF-67 and ZIF-

8, respectively. The intermediate XRD patterns, were analogous to ZIF-67 and ZIF-8, indicating the successful synthesis of the BMOFs. Their morphologies were characterized via scanning electron microscopy (SEM) and transmission electron microscopy (TEM), shown in Figure 7.2 and Figure 7.3, indicating a uniform distribution and smooth surfaces. The BMOF crystal sizes decreased at higher Zn/Co ratios in the metal precursors with less metallic Co nanoparticles remained. The crystal size decreased from the BMOF-Co sample, with an average edge length of around 2 μm, to around 1 μm in BMOF_ZnCo, and eventually to <100 nm in BMOF_Zn. As expected, there exists a correlation between the diminution in the crystal size and the increasing fraction of Co in the salt precursors. The formed polyhedra were pyrolyzed under forming gas at 800°C for 2 h, followed by a sulfuric acid wash to remove any leachable metallic Co. As shown in Figure 7.4A-H, the polyhedral morphology of the crystals was retained after the heat-treatment and acid wash. It is generally accepted that CNTs (carbon nanotubes) would likely grow on most transition metals at elevated temperatures and under a sufficiently high H_2 pressure.[42] The nanocomposites with higher Co content yielded rougher surfaces, suggesting the formation of a higher amount of carbon nanotubes. Figure 7.5 shows the XRD patterns of the carbonized BMOFs, in which all materials exhibited two peaks at 25° and 44° indexed to the (002) and (101) peaks of carbon, and XRD peaks at 44° and 51° ascribed to the (111) and (200) peaks of metallic Co in a face-centered cubic structure. At higher Co contents, metallic Co peaks became more pronounced. The generated Zn oxide was expected to be reduced in the forming gas atmosphere or by carbon, which subsequently vaporized at high temperature. Thus, there were no diffraction peaks from Zn. The TGA measurements in Figure 7.6A were used to confirm the complete removal of Zn. The

residual mass of pyrolyzed BMOFs was precisely proportional to the amount of Co precursors, and the Co-free material had nearly a 100% mass loss after acid leaching. The

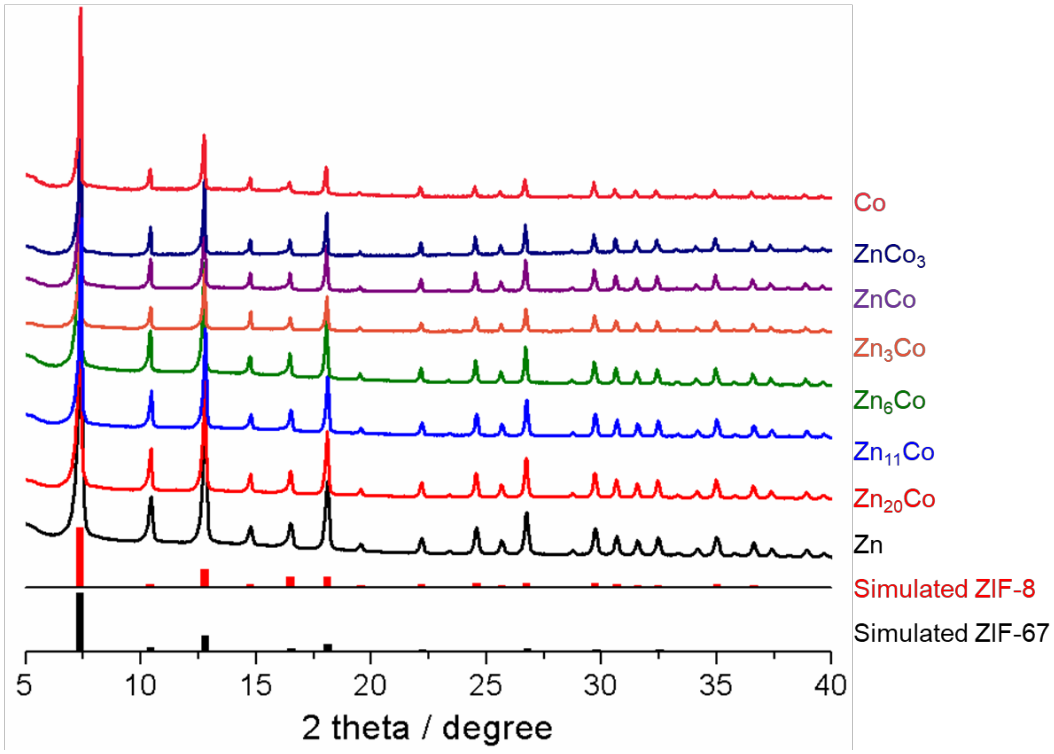

Figure 7.1 X-ray diffraction patterns of as-synthesized BMOFs with different ratios of Co and Zn precursors.

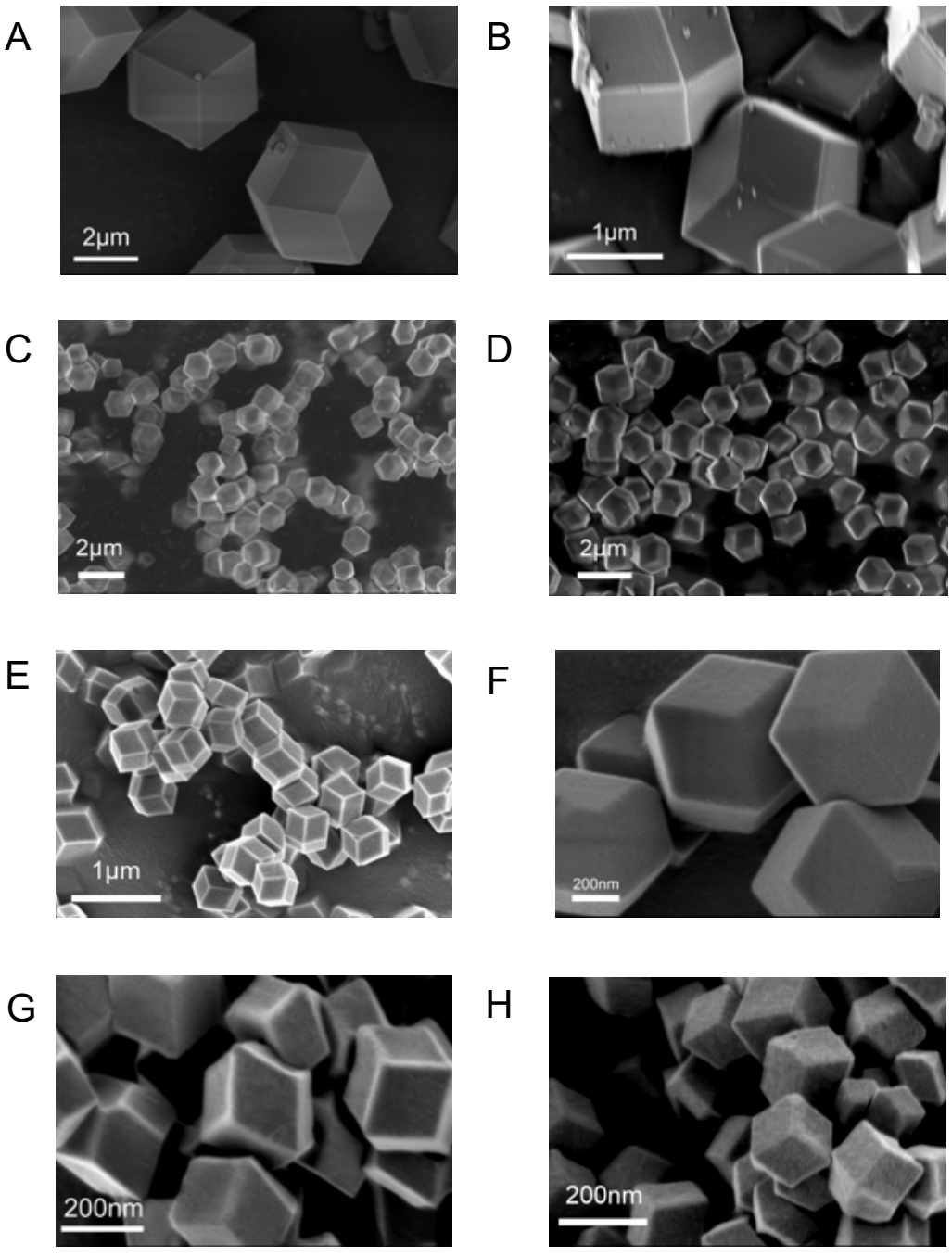
A
2μm
B
1μm
C
2μm
D
2μm
E
1μm
F
200nm
G
200nm
H
200nm

Figure 7.2 SEM images of as-prepared BMOFs synthesized at room temperature (A) BMOF_Co (B) BMOF_$ZnCo_3$ (C) BMOF_ZnCo (D) BMOF_Zn_3Co (E) BMOF_Zn_6Co (F) BMOF_$Zn_{11}Co$ (G) BMOF_$Zn_{20}Co$ (H) BMOF_Zn

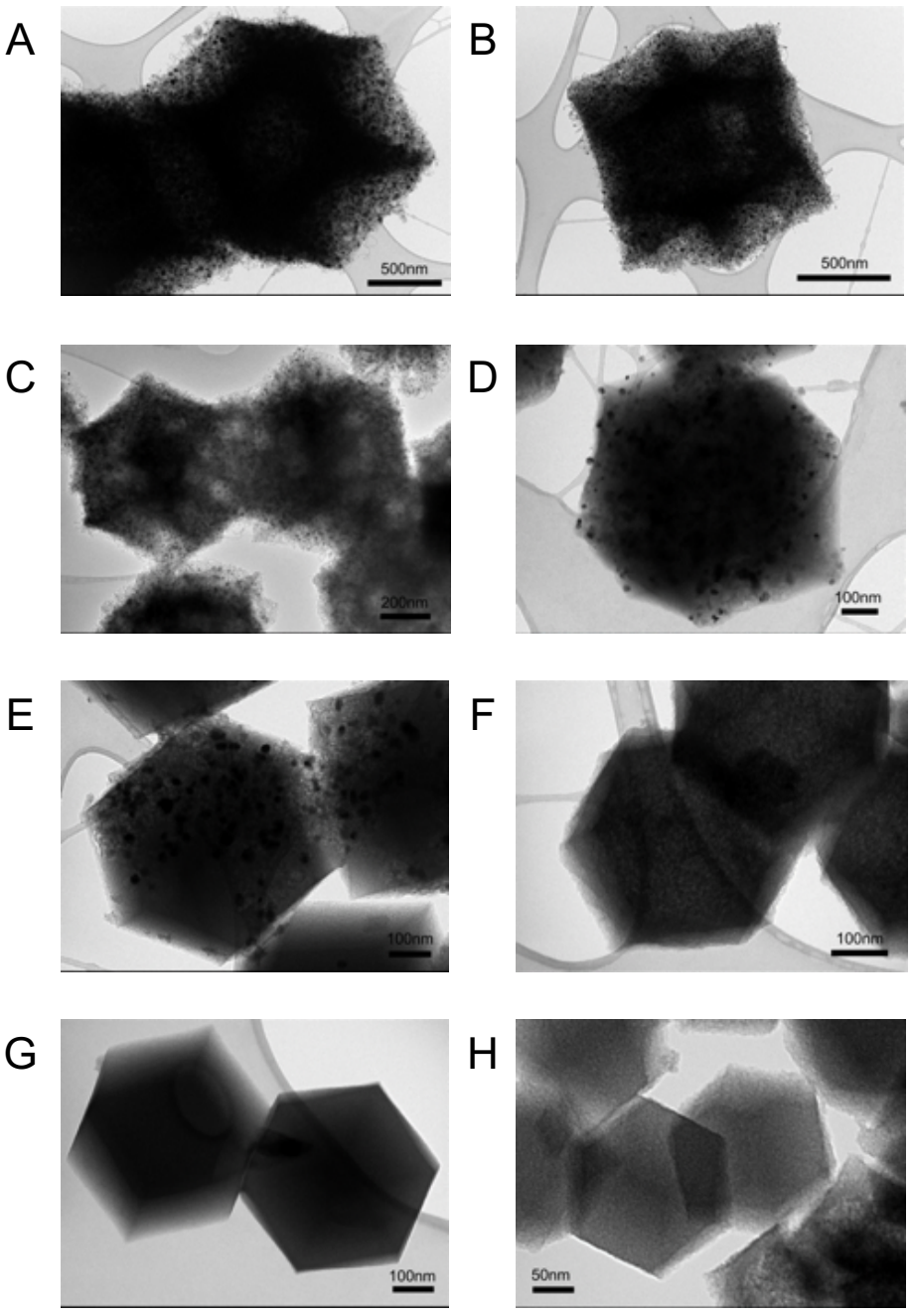

Figure 7.3 TEM images of pyrolyzed BMOFs at 800°C under forming gas (A) BMOF_Co (B) BMOF_$ZnCo_3$ (C) BMOF_ZnCo (D) BMOF_Zn_3Co (E) BMOF_Zn_6Co (F) BMOF_$Zn_{11}Co$ (G) BMOF_$Zn_{20}Co$ (H) BMOF_Zn

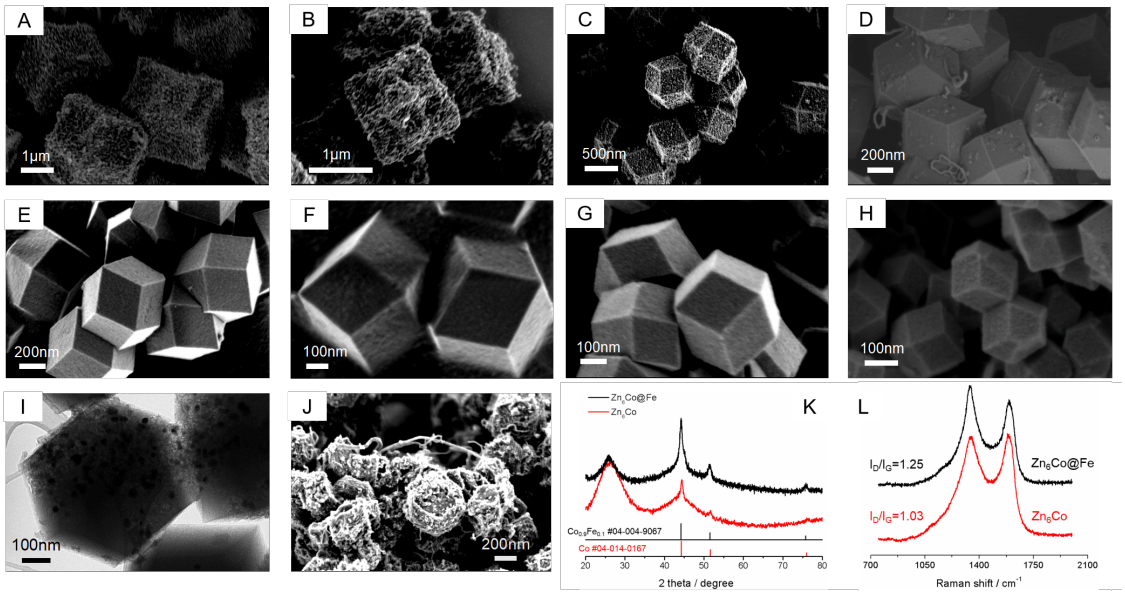

Figure 7.4 (A-H) SEM images of pyrolyzed BMOF_Co, BMOF_$ZnCo_3$, BMOF_ZnCo, BMOF_Zn_3Co, BMOF_Zn_6Co, BMOF_$Zn_{11}Co$, BMOF_$Zn_{20}Co$ and BMOF_Zn at 800°C in forming gas (95% N_2 and 5% H_2) (I) TEM image of the pyrolyzed Zn_6Co (J) SEM image of the pyrolyzed Zn_6Co_Fe (K) XRD patterns of Zn_6Co and Zn_6Co_Fe (L) Raman spectrum of Zn_6Co and Zn_6Co_Fe

BMOF material derived from the Zn_6Co composite, was further used as the scaffold to encapsulate the Fe^{3+} in its cavities/pores via the double solvent method.[43-44] The Fe^{3+} moieties were immobilized in the pores of the Zn_6Co network and reduced simultaneously with their neighboring Co atoms, creating the bimetallic active sites after carbonization and acid leaching.

Figures 7.7A-B show the morphology of BMOF_Zn_6Co before and after thermal treatment and acid leaching, confirming that neither of the two processes affected the overall morphology. The TEM image of the pyrolyzed BMOF_Zn_6Co in Figure 7.4I demonstrates that the polyhedral scaffold of carbon was embedded with metallic Co nanoparticles. With the incorporation of Fe, the resulting carbon nanocomposite, derived from Zn_6Co (labeled as Zn_6Co_Fe), had abundant carbon nanotubes, covering the surface of the polyhedral crystals (Figure 7.4J). The XRD patterns of pyrolyzed Zn_6Co and Zn_6Co_Fe revealed that, metallic Co and bimetallic $Co_{0.9}Fe_{0.1}$ were formed in the reducing atmosphere during carbonization and were retained after the acid wash. The diffraction pattern of the pyrolyzed Zn_6Co_Fe in Figure 7.4K, exhibited a slight shift to lower angles compared with the non-Fe counterpart, consistent with the larger atomic radius of Fe. There were two peaks observed in the Raman spectrum shown in Figure 7.4L, illustrating the D and G band features of carbon.[45] The Raman peaks located at 1350 and 1600 cm^{-1} were attributed to sp^2 graphitic and defects in the carbon, respectively. The defects could come from the heteroatom substitution, vacancies, and grain boundaries, which are commonly considered to be more active in electrocatalysis than the basal

plane.[45] The D/G band ratio increased from 1.03 to 1.25 following the addition of Fe, indicating the formation of more defect sites facilitating electrocatalysis.

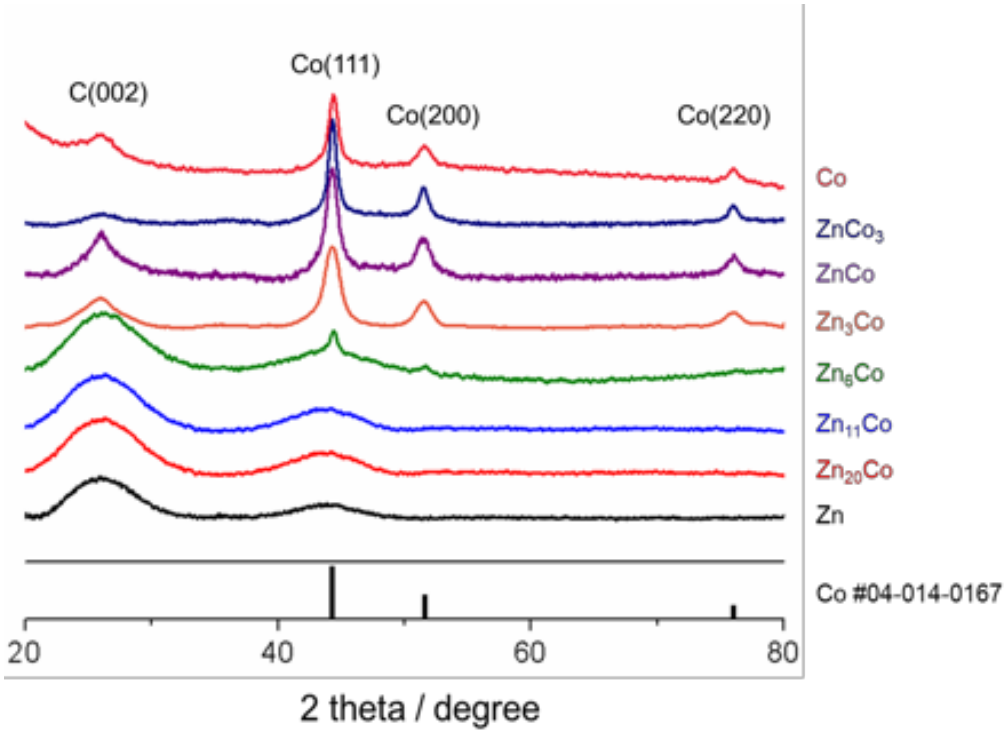

Figure 7.5 Powder XRD patterns of BMOFs after pyrolysis at 800°C in forming gas

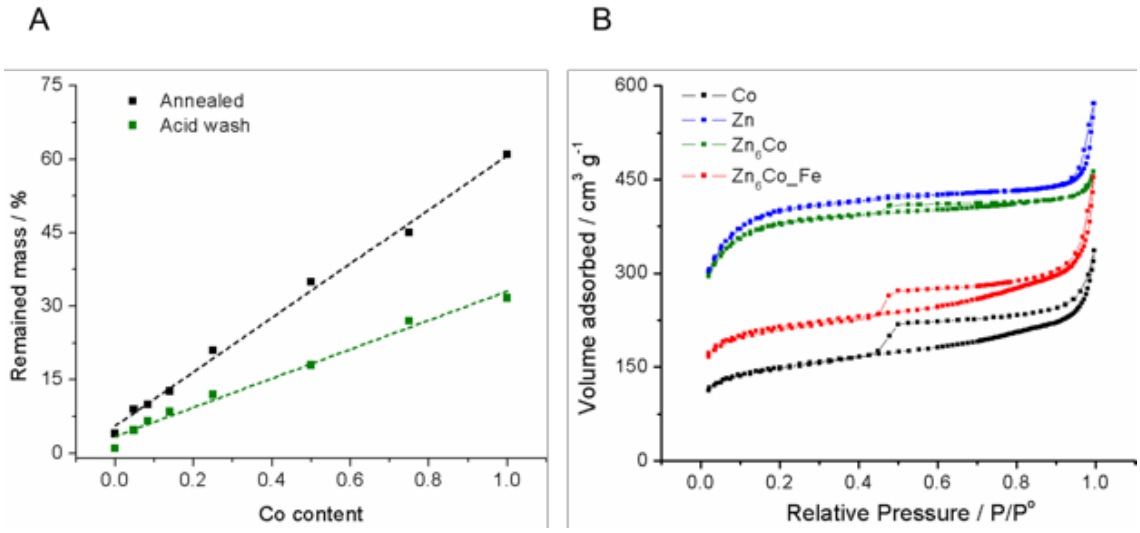

Figure 7.6 (A) TGA results of annealed BMOFs before and after acid wash, in air and (B) BET N_2 adsorption/desorption isotherms of BMOFs derived carbon nanocomposites.

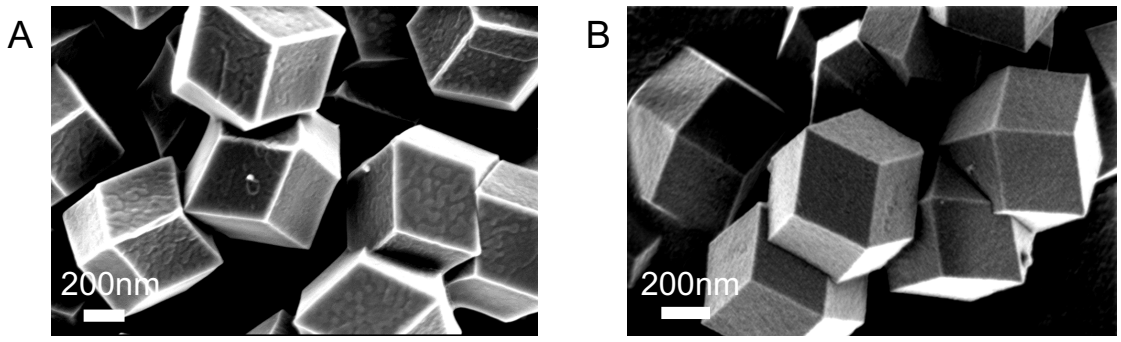

Figure 7.7 Morphology and structural characterization of BMOFs. (A) SEM image of the as-prepared BMOF_Zn_6Co (B) SEM image of the pyrolyzed Zn_6Co.

It was speculated that the volatile Zn would substantially increase the surface area. The BET surface areas of four representative samples, the carbon nanocomposites from Co, Zn_6Co, Zn and Zn_6Co_Fe were measured to be 520, 1310, 1400 and 745 m^2/g, respectively. The high surface area allowed the exposure of active sites and was deemed beneficial to the rapid transport of O_2 and relevant species during the electrocatalysis processes (Figure 7.6B).

The atomic structure of the $Co_{0.9}Fe_{0.1,}$ embedded in the carbon nanocomposite, derived from Zn_6Co_Fe, was further examined by high-angle annular dark-field (HAADF) STEM imaging. Since STEM image intensity is proportional to the atomic number ($I \propto Z^{1.7}$), the $Co_{0.9}Fe_{0.1}$ alloy particles will be significantly brighter than the carbon support. As shown in Figure 7.8A, $Co_{0.9}Fe_{0.1}$ bimetallic nanoparticles (NPs) were uniformly distributed and embedded in the MOF-derived porous carbon matrix. $Co_{0.9}Fe_{0.1}$ NPs exhibited narrow particle size distribution (PSD) of 8 ± 2 nm (average $\pm$ one standard deviation, S_d), (Figure 7.8B) based on an analysis of more than 300 nanoparticles from Figures 7.8A and Figure 7.9. The crystal structure was further examined by STEM images at the atomic scale. Figure 7.8C shows a single-crystal nanoparticle with a d-spacing value of 0.20 nm, which is consistent with the theoretical radius of $Co_{0.9}Fe_{0.1}$ {111} facets, 0.2048 nm (PDF # 04-004-9067). Another $Co_{0.9}Fe_{0.1}$ nanoparticle was found to have five sub-domains of {111} d-spacings on the same zone axis of [110] (Figures 7.8D and Figure 7.10). Domain boundaries were marked with red dashed lines, and the hexagonal symmetry of [110] in each domain was clearly resolved from the atom arrangements. The Fourier transform of

this nanoparticle showed the corresponding fives pairs of diffraction spots with the same d-spacing values.

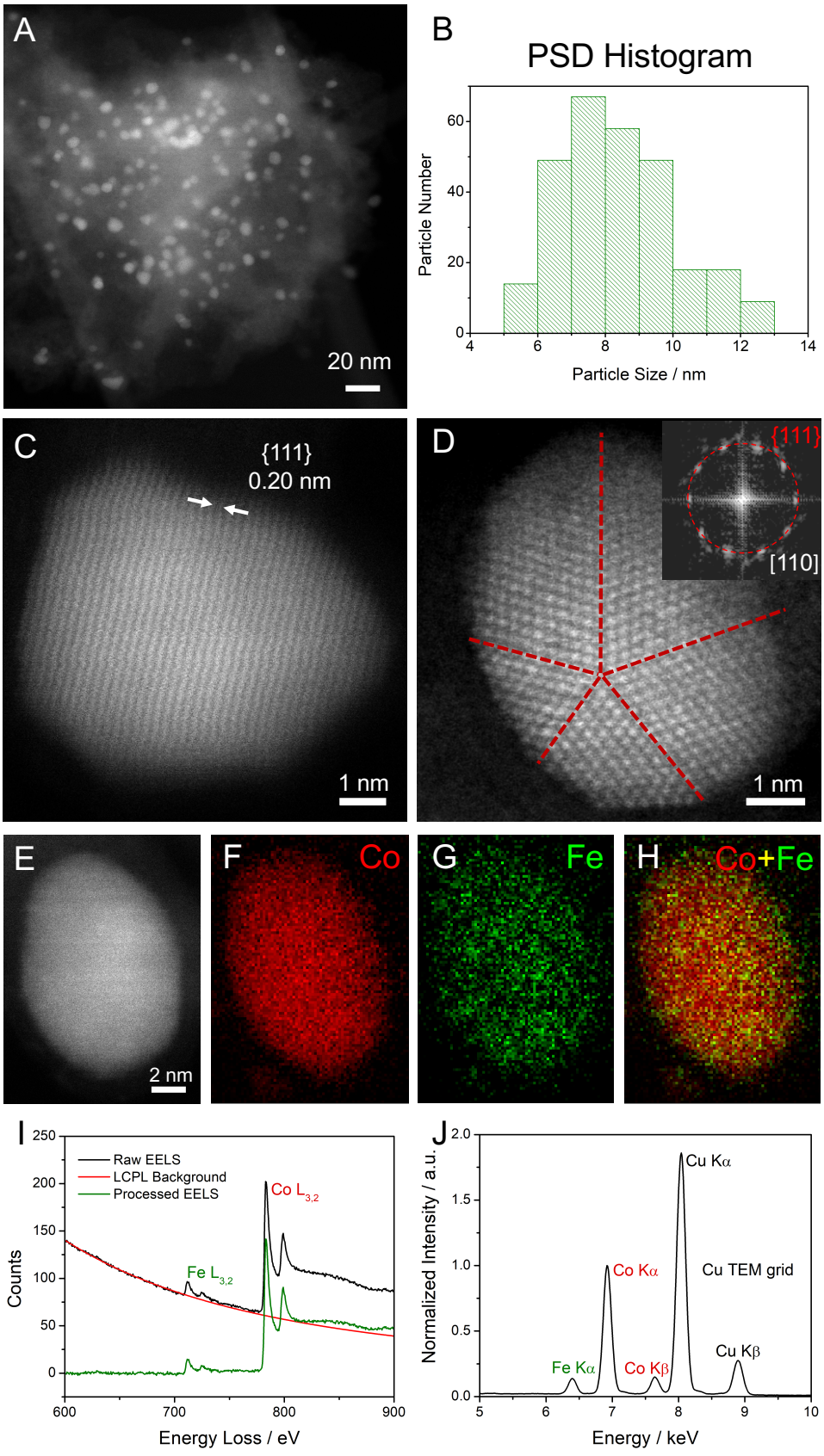
A
20 nm
B
PSD Histogram
Particle Number
Particle Size / nm
C
{111}
0.20 nm
1 nm
D
{111}
[110]
1 nm
E
2 nm
F
Co
G
Fe
H
Co+Fe
I
Raw EELS
LCPL Background
Processed EELS
Co L3,2
Fe L3,2
Counts
Energy Loss / eV
J
Cu Kα
Co Kα
Cu TEM grid
Fe Kα
Co Kβ
Cu Kβ
Normalized Intensity / a.u.
Energy / keV

Figure 7.8 HAADF-STEM images of $Co_{0.9}Fe_{0.1}$ bimetallic nanoparticles embedded in a MOF-derived porous carbon matrix (BMOF). (A) low-magnification STEM image of BMOF (B) particle size distribution (PSD) histogram of about 300 particles analyzed from (A) and Figure S4. (C) Atomic-scale STEM image of a single crystal with a d-spacing value of 0.20 nm, indicating {111} facets of Co0.9Fe0.1. (D) Atomic-scale STEM image of a nanoparticle with five sub-domains on the [110] zone axis and the domain boundaries indicated as the red dashed lines. Inset shows the corresponding Fourier transform with five pairs of {111} diffraction spots; Chemical composition of a $Co_{0.9}Fe_{0.1}$ bimetallic nanoparticle. (E-H) STEM image and the corresponding EELS elemental maps of Co (red), Fe (green) and the composite map (Co vs. Fe). (I) Processed EELS spectrum with pronounced Fe and Co L3,2 edges (J) STEM-EDX spectrum with Fe Kα and Co Kα,β edges. Quantitative EDX analysis suggests Fe, Co contents of 89.2 at.% and 10.8 at.%, respectively.

Figure 7.8I shows the pronounced Co and Fe $L_{3,2}$ edges at around 790 and 710 eV, respectively, which were used to extract 2D EELS elemental mapping. Figure 7.8E-F presents a 10 nm $Co_{0.9}Fe_{0.1}$ nanoparticle with EELS maps of Co (red) and Fe (green). The EELS composite map of Co vs. Fe in the upper right of Figure 7.8E-F suggested a relatively homogenous distribution of Co and Fe, which was further evidenced by similar EELS maps in Figure 7.11. This provides convincing and compelling evidence of the formation of a Co-Fe alloy at the atomic-scale, which is consistent with the observation from the XRD of $Co_{0.9}Fe_{0.1}$ in Figure 7.8K. Besides the elemental distribution from EELS, EDX also served as a quantitative tool to analyze the local atomic ratio (Figure 7.8J). Co and Fe Kα edges at 6.9 and 6.4 keV, respectively, were employed to calculate the relative atomic contents of Fe and Co, based on the Cliff-Lorimer equation.[46] Co and Fe were found to have relative contents of 89.2% and 10.8%, respectively, which is consistent with the designed stoichiometry of Co/Fe (9:1) and ICP-MS results, which indicated that the atomic ratio of Co to Fe was around 9:1. The relative error was defined as one S_d of 0.6 %, based on a random selection of five different regions on the TEM grid. The strong Cu signal in Figure 7.8J came from the Cu TEM grid. STEM-EDX elemental maps of several $Co_{0.9}Fe_{0.1}$ NPs also yielded a similar homogenous distribution of Co and Fe to that obtained from EELS mapping (Figure 7.11). In summary, microscopic-level STEM-EELS mapping, combined with quantitative EDX analysis, unambiguously indicate that the $Co_{0.9}Fe_{0.1}$ alloy nanoparticles have a homogenous distribution of Co and Fe at the atomic scale with the designed Co/Fe ratio of 9:1.

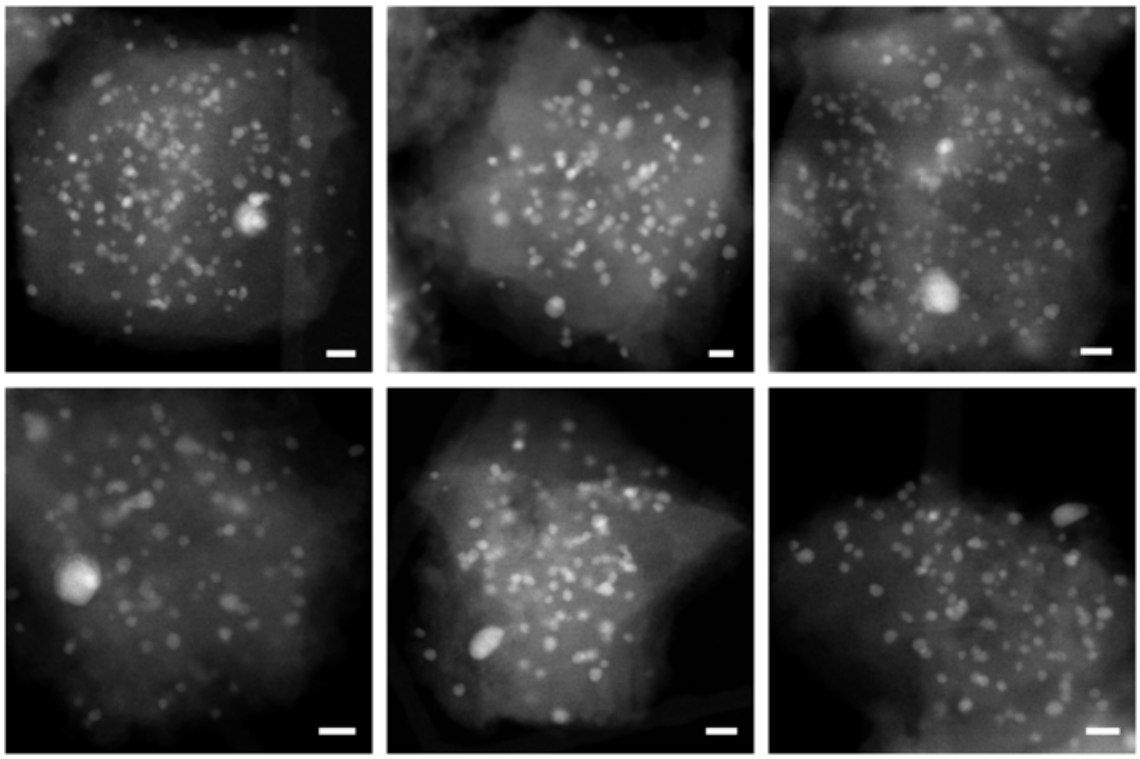

Figure 7.9 Collection of low-magnification STEM images of $Co_{0.9}Fe_{0.1}$ bimetallic nanoparticles embedded in a MOF-derived porous carbon matrix (BMOF) (scale bar, 20 nm). Around 300 nanoparticles were counted and analyzed for the PSD histogram in Figure 7.8B. Very few particles larger than 15 nm were not included in the PSD histogram.

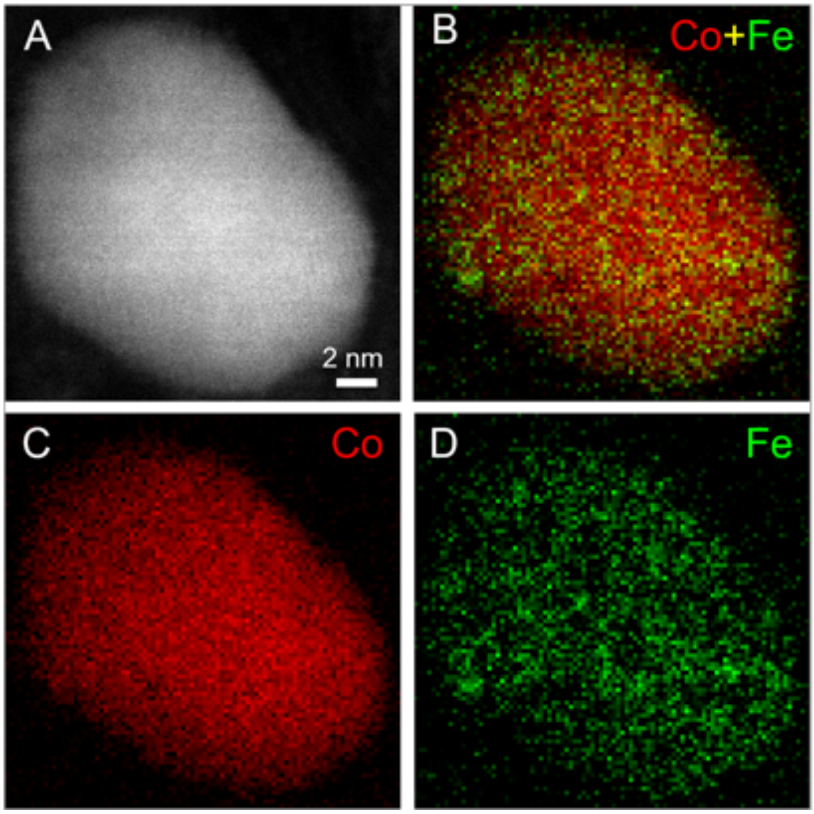

Figure 7.10 STEM image of a $Co_{0.9}Fe_{0.1}$ bimetallic nanoparticle and the corresponding EELS maps of Co (red), Fe (green) and the composite map (Co vs. Fe).

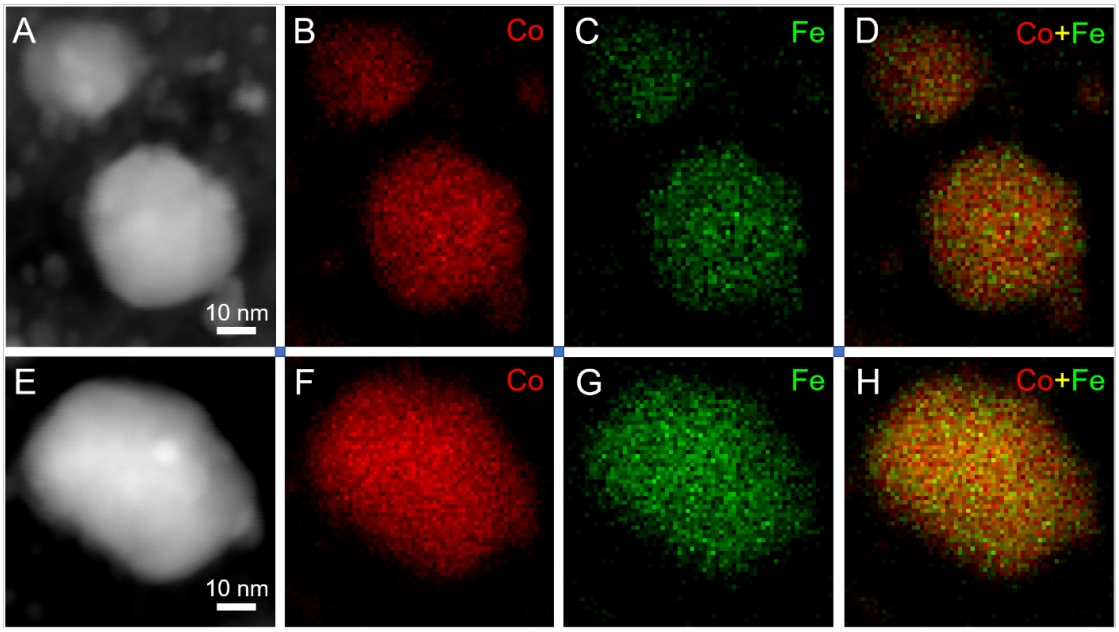

Figure 7.11 (A-D) and (E-H) STEM images of $Co_{0.9}Fe_{0.1}$ bimetallic nanoparticles and the corresponding EDX elemental maps of Co (red), Fe (green) and the composite map (Co vs. Fe), extracted using Co and Fe Kα edges from spectrum images. The corresponding EDX spectra can be found in Fig. 4D. Co and Fe had X-ray counts of no less than 50 and 10 counts/pixel, respectively, and the beam dose was ~ 0.8 e/(Å·s). Large nanoparticles were selected for mitigating sample drift during long-time high-quality EDX elemental mapping acquisition.

With the desirable structural information discussed above, the electrocatalytic performance of these materials, towards the ORR, was assessed in alkaline media. Shown in Figure 7.12A, all the polarization curves of all BMOFs derived carbon nanocomposites collected in a conventional three-electrode system at 1600 rpm, in an O_2-saturated 0.1M NaOH electrolyte, at a scan rate of 5 mV/s and a rotation rate of 1600 rpm. The mass activities at 0.85 V and the half-wave potentials are summarized in Figure 7.12B. The Zn-derived material showed the lowest onset potential and the slowest kinetics in the mixed diffusion-kinetics control region. In sharp contrast, with a minimal amount of Co incorporated, the electrocatalytic performance of the $Zn_{20}Co$-derived sample had a dramatically enhanced increase of 200% in mass activity, and a 30 mV positive shift in the half-wave potential. This dramatic improvement indicated that Co provided critical active sites for ORR electrocatalysis. With additional increases in the Co loading, there were further increases in the mass activity, although the additional relative enhancement gradually decreased with higher Co contents. Contrary to such behavior, in the case of Zn_6Co to Co, the electrocatalytic activity decreased in increasing levels of Co. As a result, Zn_6Co proved to be the best ORR candidate derived from BMOFs precursors. We ascribe this to its high surface area, accessible Co-based active sites and N dopants. Furthermore, the Co-Fe bimetallic alloy derived from Zn_6Co, namely Zn_6Co_Fe, exhibited an electrocatalytic activity that surpassed those of Zn_6Co and commercial Pt/C, in terms of the half-wave potential (Figure 7.12C). Stability was assessed for carbon nanocomposites derived from both Zn_6Co and Zn_6Co_Fe in an Ar-saturated 0.1M NaOH solution at a scan rate of 100 mV/s for 30,000 cycles (Figure 7.12D), where the carbon derived from Zn_6Co_Fe proved extraordinarily stable.

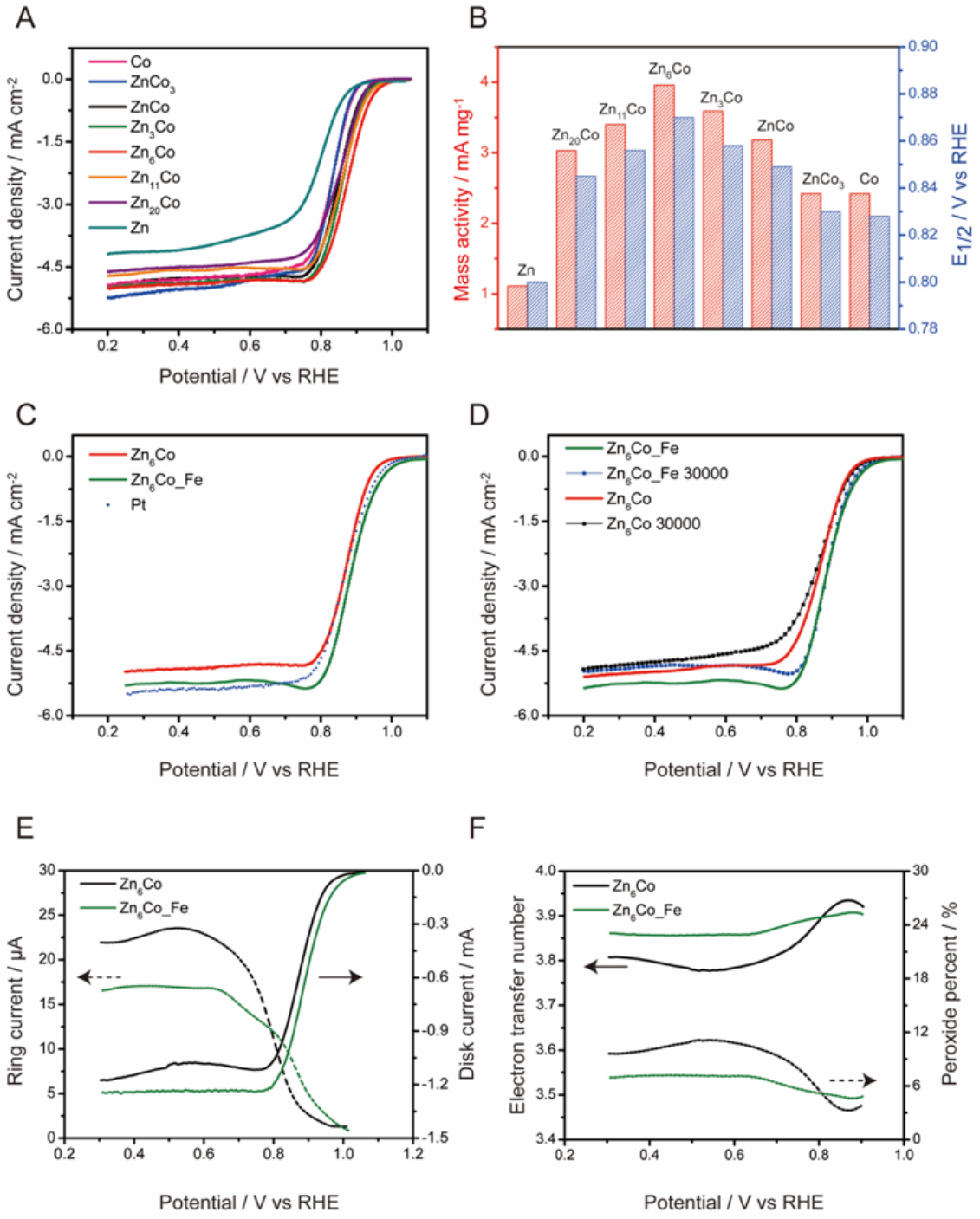

Figure 7.12 Degradation mechanism investigation of BMOF electrocatalysts during durability tests. (A) ORR polarization profiles of BMOF electrocatalysts at 1600 rpm and 5 mV/s after 10,000, 20,000 and 30,000 potential cycles from 0.6 to 1.0 V at 100 mV/s.

(B) EDX spectra of BMOF at the initial state and after 30,000 cycles, showing a relatively stable Fe/Co atomic ratio. (C) STEM image of BMOF after 30,000 cycles, showing a majority of small particles as well as aggregated larger particles. (D) PSD histogram of BMOF after 30,000 cycles, analyzed from (C) and Figure 7.13, showing an increasing number of larger particles, relative to the initial state in Figure 7.12B.

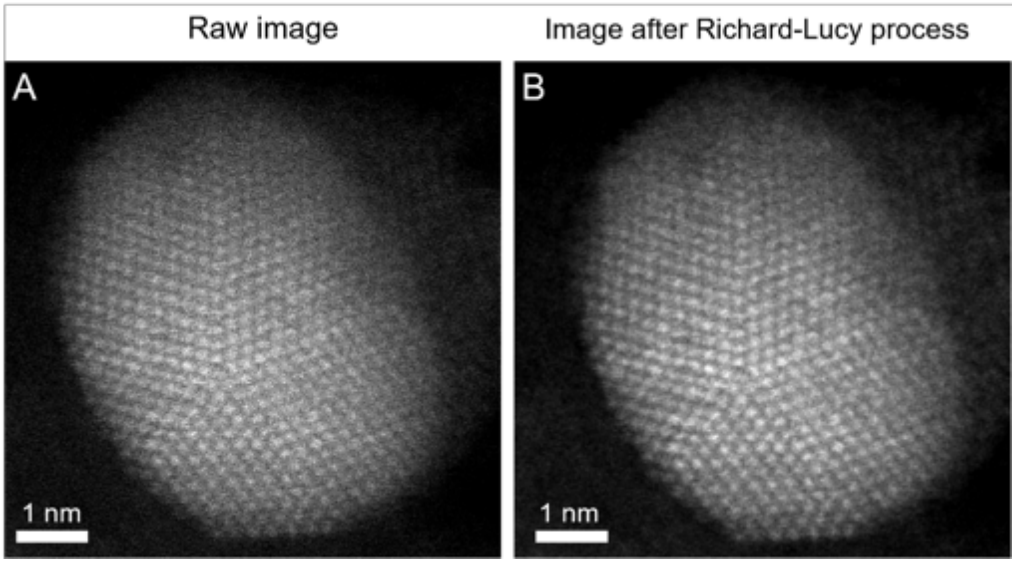

Figure 7.13 STEM image processing. (A) raw atomic-scale STEM image of a $Co_{0.9}Fe_{0.1}$ bimetallic nanoparticle. (B) image in (A) filtered using Richard-Lucy deconvolution (3 iterations). The deconvolution was processed in ImageJ software assuming an Airy disk (100 kV, αmax=28 mrad) convolved with a 0.8 Å Gaussian source.[1-2]

1. Kirkland, E. Advanced Computing in Electrons Microscopy. Springer: New York, **2010**.

2. Wang, D.; Xin, H.; Hovden, R.; Wang, H.; Yu, Y.; Muller, D.; DiSalvo, F.; Abruña, H. Structurally Ordered Intermetallic Platinum-Cobalt Core-Shell Nanoparticles with Enhanced Activity and Stability as Oxygen Reduction Electrocatalysts. *Nat. Mater*. **2012**, 12, 81.

After 30,000 CV cycles, there was virtually no loss in the potential region between 0.8 to 1.0 V, and the electrocatalytic activity still outperformed that of Zn_6Co carbon. To better evaluate the selectivity of the oxygen reduction process, the rotating ring-disk electrode (RRDE) method was employed to measure the peroxide yield, corresponding to the undesirable $2e^-$ process. Figure 7.12E presents the ring and disk currents obtained for Zn_6Co and Zn_6Co_Fe. Zn_6Co_Fe exhibited a higher disk current, while its ring current decreased by 30%, when compared to Zn_6Co, suggesting a dominant four-electron transfer reaction. The electron transfer number (n) and peroxide yield values are presented in Figure 7.12F. For the Zn_6Co_Fe carbon, the n-value was determined to be above 3.9 over the potential region between 0.2 V to 0.9 V, and the generated peroxide was below 7%; a value that is about half, when compared to the 12% H_2O_2 generation from Zn_6Co. The peroxide yield is relatively low when compared to other reported values in the literature. Our results are, in fact, comparable to other state-of-the-art catalysts. To make a better comparison, we have prepared a table that summarizes the peroxide yield of various materials in table S1.[28-30, 47-55]. Lowering down the peroxide yield would be most beneficial since it is well understood that peroxide can diffuse into the membrane and chemically break down to hydroxyl radicals. These radicals, in return, will react with perfluorosulfonic ionomers in the electrode and the membrane to produce hydrofluoric acid HF leading to the degradation of the MEA[56]. To address the disadvantage from produced peroxide, it requires collaborative efforts, also from the design of peroxide-tolerant membranes[57].

In order to implement Pt-free cathodes for industrial applications in alkaline membrane exchange fuel cells (AMEFCs), non-precious ORR electrocatalysts need to not only

satisfy the requirements of high initial ORR activity, but also address long-term durability concerns.[58] The durability and the possible degradation mechanisms of ORR electrocatalysts need to not only satisfy the requirements of the BMOF electrocatalysts were investigated using STEM imaging and quantitative EDX analysis. As shown in Figure 7.14A, the halfwave potentials of BMOF electrocatalysts shifted slightly positively after 10,000 and 20,000 cycles, indicating an initial catalyst activation. After 30,000 cycles, the $E_{1/2}$ shifted in the negative direction by less than 5 mV, indicating a remarkable activity retention. The continuous decrease in I_d from -5.4 to -5.0 mA/cm^2, suggests a loss of electrochemical surface area (ECSA). EDX quantitative analysis and STEM images were employed to investigate the changes in microstructures and local chemical composition. EDX spectra of BMOF electrocatalysts, at the initial state and after 30,000 cycles, were normalized to the Co Kα edge (783 eV) and showed little, if any, changes in the Fe Kα edge (712 eV). (Figure 7.14B) Quantitative analysis suggested that the relative contents of Co, and Fe changed from 89.2% and 10.8% (± 0.6%) at the initial state to 88.5% and 11.5% (± 0.8%) after 30,000 cycles, respectively. Given the relative error of EDX measurements, no significant changes in composition ratio was detected. STEM images of BMOF electrocatalysts after 30,000 cycles showed that the majority of the small particles were able to remain embedded in the carbon matrix with only a few aggregated larger particles evident. (Figure 7.14C). Around 300 $Co_{0.9}Fe_{0.1}$ nanoparticles in Figures 7.14C and Figure 7.15 were analyzed to form the particle size distribution (PSD) histogram in Figure 7.14D. It suggests that $Co_{0.9}Fe_{0.1}$ NPs have a larger average particle size of 10-15 nm and a broader PSD after 30,000 cycles, when compared to the initial state in Figure 7.8, which may partially explain the decrease in I_d in Figure

7.14A. Initially, nearly all O2 could be fully reduced to H2O via either the direct 4-electron transfer reaction or in a two-step process in which the generated peroxide is fully reduced (to water) by nearby sites before escaping the catalyst layer. After potential cycling process, some of active sites dissolved so that their density is lower. In this case, the peroxide has a higher possibility of diffusing into the bulk electrolyte causing a decrease in the limiting current. The E1/2 does not shift too much, in the kinetic-diffusion region, indicating that the kinetics is relatively fast. In In summary, the excellent durability of BMOF derived electrocatalysts after 30,000 cycles was ascribed to their capability to maintain a stable local chemical composition as well as a reasonably small particle size, highlighting the close interactions between $Co_{0.9}Fe_{0.1}$ NPs and the MOF-derived carbon matrix.

Here, we attributed the stability of our Co-Fe BMOF catalysts to the highly porous structure arising from the use of Zn as a sacrificial template in the reducing atmosphere and to the in-situ formation of the Co-Fe bimetallic nanoparticles. The annealing processes was deliberately conducted at H2 flowing rates, known to promote the formation of carbon nanotubes on the surface of transition metals, like Co and Fe in this case, that help immobilize active sites. At the same time, Co and Fe are reduced and alloyed at the elevated temperatures employed during the formation of these CNTs and are subsequently wrapped in these tubes. In addition, the 1/2-immidazole ligands in the BMOF precursors bring N dopants in the carbon structure, which are able to not only provide additional cata-lytic pathways, but also bind and coordinate the metallic nanoparticles thus enhancing stability from both chemical and physical prospective. The porous structure of our materials is maintained after extensive cycling, as evidenced by

TEM. To-gether with the minimal compositional difference between a fresh sample and a sample after 30k cycles, it is reasonable to expect that the excellent stability derives from the structural and chemical integrity.

In addition, based on the Pourbaix diagram, the surface of the bimetallic Co-Fe nanoparticle is highly likely to be partially oxidized, in the form of Co and Fe oxide/hydroxide. It is possible/likely that, under working conditions (applied potential), there is a mixture of $Co(OH)_2$ and $Co(OH)_3$ (or Co_2O_3, Co_3O_4 and CoO) for Co on the surface. Similarly, Fe likely exists as a mixture of $Fe(OH)_2$ and $Fe(OH)_3$ (or Fe_2O_3 and Fe_3O_4). The average valence state is likely to be potential de-pendent; closer to +3 in the higher potential region (near 1V vs RHE) and near +2 when the applied potential is lower (near 0V vs RHE). Those two metals on the surface, simultaneously and synergistically catalyze the ORR reaction efficiently and stably.

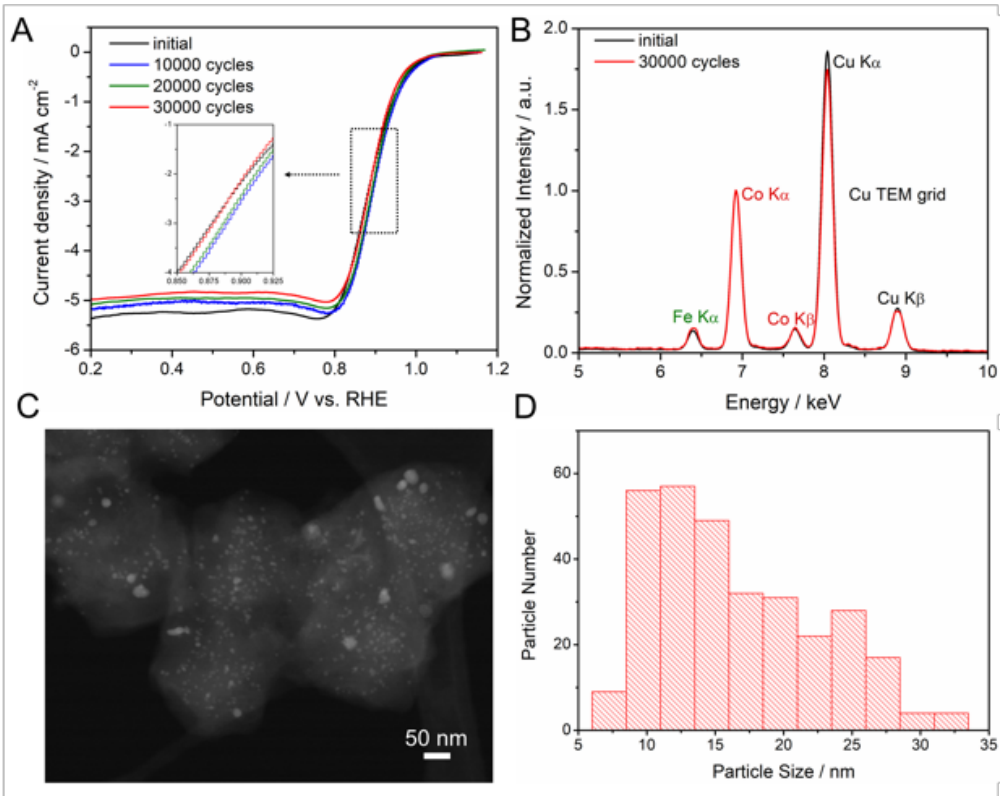

Figure 7.14 Degradation mechanism investigation of BMOF electrocatalysts during durability tests. (A) ORR polarization profiles of BMOF electrocatalysts at 1600 rpm and 5 mV/s after 10,000, 20,000 and 30,000 potential cycles from 0.6 to 1.0 V at 100 mV/s. (B) EDX spectra of BMOF at the initial state and after 30,000 cycles, showing a relatively stable Fe/Co atomic ratio. (C) STEM image of BMOF after 30,000 cycles, showing a majority of small particles as well as aggregated larger particles. (D) PSD histogram of BMOF after 30,000 cycles, analyzed from (C) and Figure 7.13, showing an increasing number of larger particles, relative to the initial state in Figure 7.12B.

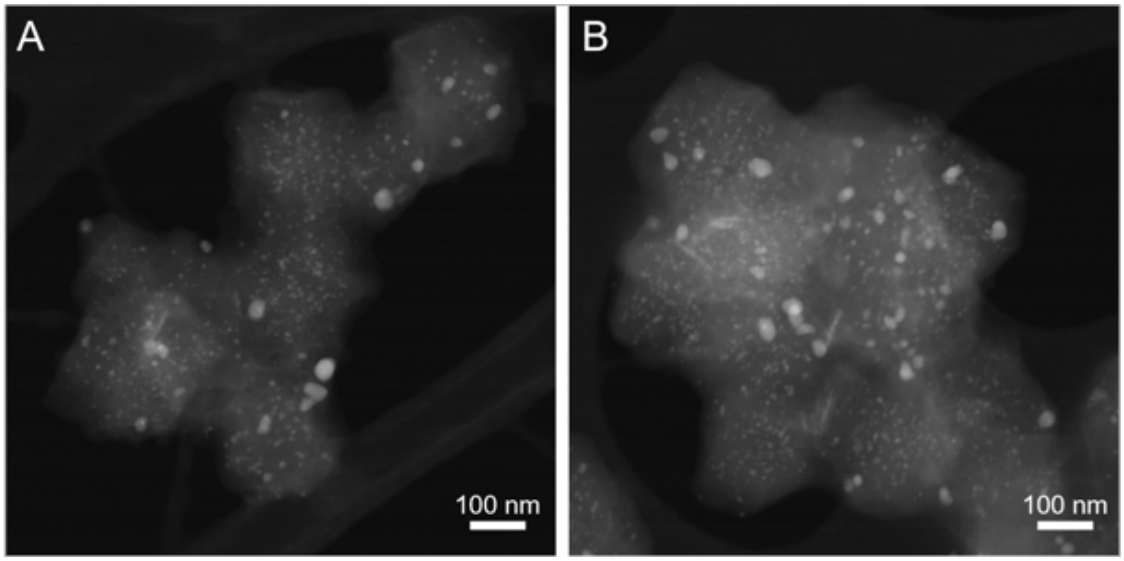

Figure 7.15 (A-B) low-magnification STEM images of BMOFs after 30000 potential cycles. Around 300 nanoparticles were counted and analyzed for the PSD histogram in Figure 7.9.

7.5 Conclusion

In summary, we have designed a family of BMOF derived Co-Fe alloys embedded in a carbon nanocomposite through the combination of the conventional self-assembly of MOFs and a guest-host strategy. Zn_6Co proved to be the compositionally-optimized template and substrate, for the encapsulation of exterior Fe to generate the bimetallic nanoparticles-carbon composite. This nanocomposite, composed of porous carbon with high surface area and uniform distribution of $Co_{0.9}Fe_{0.1}$ bimetallic nanoparticles, exhibited superior electrocatalytic activity towards the ORR, as well as robust stability after 30,000 cycles, owing to its structural and compositional integrity, as confirmed by STEM and EDX measurement. The synthesis strategy and optimization process presented here may provide with new pathways to push forward the substitution of Pt with more cost-effective electrocatalysts for fuel cell applications.

7.6 References

1. Chu, S.; Majumdar, A. Opportunities and challenges for a sustainable energy fut ure. *Nature* **2012**, 488, 294.
2. Xiong, Y.; Yang, Y.; Joress, H.; Padgett, E.; Gupta, U.; Yarlagadda, V.; Agyema nBudu, D.; Huang, X.; Moylan, T. E.; Zeng, R.; Kongkanand, A.; Escobedo, F. A.; Brock, J. D.; DiSalvo, F. J.; Muller, D. A.; Abruña, H. D. Revealing the atom ic ordering of binary intermetallics using *in situ* heating techniques at multilengt h scales. *Proc. Natl. Acad. Sci. U.S.A*. **2019**, 116, 1974.
3. Dresselhaus, M.; Thomas, I. Alternative energy technologies. *Nature* **2001**, 414, 332.
4. Dunn, B.; Kamath, H.; Tarascon, J. Electrical energy storage for the grid: A batt ery of choices. *Science* **2001**, 334, 928.
5. Kongkanand, A.; Mathias, M. The priority and challenge of high-power perform ance of low-platinum proton-exchange membrane fuel cells. *J. Phys. Chem. Lett*. **2016**, 7, 1127.
6. Xiong, Y.; Yang, Y.; DiSalvo, F. J.; Abruña, H. D. Pt-decorated composition-tun able Pd–Fe@Pd/C core–shell nanoparticles with enhanced electrocatalytic activi ty toward the oxygen reduction reaction *J. Am. Chem. Soc*. **2018**, 140, 7248.
7. Xiong, Y.; Xiao, L.; Yang, Y.; DiSalvo, F. J.; Abruña, H. D. High-loading inter metallic Pt_3Co/C core–shell nanoparticles as enhanced activity electrocatalysts to ward the oxygen reduction reaction (ORR). *Chem. Mater*. **2018**, 30, 1532.

8. Meier, J.; Katsounaros, I.; Galeano, C.; Bongard, H.; Topalov, A.; Kostka, A.; K arschin, A.; Schüth, F.; Mayrhofer, K. Stability investigations of electrocatalysts on the nanoscale. *Energy Environ. Sci*. **2012**, 5, 9319.
9. Liu, X.; Park, M.; Kim, M.; Gupta, S.; Wu, G.; Cho, J. Integrating NiCo alloys w ith their oxides as efficient bifunctional cathode catalysts for rechargeable zinc-a ir batteries. *Angew. Chem. Int. Ed*. **2015**, 54, 9654.
10. Wang, Y.; Qiao, J.; Baker, R.; Zhang, J. Alkaline polymer electrolyte membrane s for fuel cell applications. *Chem. Soc. Rev*. **2013**, 42, 5768.
11. Yang, Y.; Wang, Y.; Xiong, Y.; Huang, X.; Shen, L.; Huang, R.; Wang, H.; Past ore, J. P.; Yu, S.-H.; Xiao, L.; Brock, J. D.; Zhuang, L.; Abruña, H. D. In situ X-ray absorption spectroscopy of a synergistic Co−Mn oxide catalyst for the oxyge n reduction reaction. *J. Am. Chem. Soc.* **2019**, 141, 1463.
12. Xiong, Y.; Yang, Y.; Feng, X.; DiSalvo, F. J.; Abruña, H. D. A strategy for incre asing the efficiency of the oxygen reduction reaction in Mn-doped cobalt ferrites. *J. Am. Chem. Soc*. **2019**, 141, 10, 4412.
13. Wang, J.; Cui, W.; Liu, Q.; Xing, Z.; Asiri, A.; Sun, X. Recent progress in cobalt -based heterogeneous catalysts for electro-chemical water splitting. *Adv. Mater.* **2015**, 28, 215.
14. Zhu, Y.; Ma, T.; Jaroniec, M.; Qiao, S. Self-templating synthesis of hollow Co_3O_4 microtube arrays for highly efficient water electrolysis. *Angew. Chem. Int. Ed.* **2016**, 56, 215.

15. Cheng, F.; Shen, J.; Peng, B.; Pan, Y.; Tao, Z.; Chen, J. Rapid room-temperature synthesis of nanocrystalline spinels as oxygen reduction and evolution electroca talysts. *Nat. Chem*. **2010**, 3, 79.

16. Jiao, F.; Frei, H. Nanostructured cobalt oxide clusters in mesoporous silica as eff icient oxygen-evolving catalysts. *Angew. Chem. Int. Ed*. **2009**, 48, 1841.

17. Yeo, B.; Bell, A. Enhanced activity of gold-supported cobalt oxide for the electr ochemical evolution of oxygen. *J. Am. Chem. Soc*. **2011**, 133, 5587.

18. Li, T.; Xue, B.; Wang, B.; Guo, G.; Han, D.; Yan, Y.; Dong, A. Tubular monola yer superlattices of hollow Mn_3O_4 nanocrystals and their oxygen reduction activi ty. *J. Am. Chem. Soc*. **2017**, 139, 12133.

19. Ren, H.; Wang, Y.; Yang, Y.; Tang, X.; Peng, Y.; Peng, H.; Xiao, L.; Lu, J.; Abr uña, H. D.; Zhuang, L. Fe/N/C nanotubes with atomic Fe sites: A highly active c athode catalyst for alkaline polymer electrolyte fuel cells. *ACS Catal*. **2017**, 7, 64 85.

20. Gong, K.; Du, F.; Xia, Z.; Durstock, M.; Dai, L. Nitrogen-doped carbon nanotub e arrays with high electrocatalytic activity for oxygen reduction. *Science* **2009**, 3 23, 760.

21. Liang, H.; Wei, W.; Wu, Z.; Feng, X.; Müllen, K. Mesoporous metal–nitrogen-d oped carbon electrocatalysts for highly efficient oxygen reduction reaction. *J. A m. Chem. Soc*. **2013**, 135, 16002.

22. Liang, Y.; Wang, H.; Zhou, J.; Li, Y.; Wang, J.; Regier, T.; Dai, H. Covalent hyb rid of spinel manganese-cobalt oxide and graphene as advanced oxygen reductio n electrocatalysts. *J. Am. Chem. Soc*. **2012**, 134, 3517.

23. Suntivich, J.; Gasteiger, H.; Yabuuchi, N.; Nakanishi, H.; Goodenough, J.; Shao-Horn, Y. Design principles for oxygen-reduction activity on perovskite oxide cat alysts for fuel cells and metal-air batteries. *Nat. Chem*. **2011**, 3, 546.

24. Wu, G.; More, K.; Johnston, C.; Zelenay, P. High-performance electrocatalysts f or oxygen reduction derived from polyaniline, iron, and cobalt. *Science* **2011**, 33 2, 443.

25. Chung, H.; Cullen, D.; Higgins, D.; Sneed, B.; Holby, E.; More, K.; Zelenay, P. Direct atomic-level insight into the active sites of a high-performance PGM-free ORR catalyst. *Science* **2017**, 357, 479.

26. Proietti, E.; Jaouen, F.; Lefèvre, M.; Larouche, N.; Tian, J.; Herranz, J.; Dodelet, J. Iron-based cathode catalyst with enhanced power density in polymer electroly te membrane fuel cells. *Nat. Commun*. **2011**, 2, 416.

27. Lefèvre, M.; Proietti, E.; Jaouen, F.; Dodelet, J. Iron-based catalysts with improv ed oxygen reduction activity in polymer electrolyte fuel cells. *Science* **2009**, 324, 71.

28. Lu, Y.; Wang, L.; Preuß, K.; Qiao, M.; Titirici M.-M.; Varcoe, J.; Cai, Q. *J. Pow er Sources* **2017**, 372, 82.

29. Peng, X.; Omasta, T.; Magliocca, E.; Wang, L.; Varcoe, J.; Mustain, W. Angew. Chem., 2018, 131, 1058.

30. Sa, Y.; Seo, D.; Woo, J.; Lim, J.; Cheon, J.; Yang, S.; Lee, J.; Kang, D.; Shin, T.; Shin, H.; Jeong, H.; Kim, C.; Kim, M.; Kim, T.; Joo, S., J. Am. Chem. Soc. 201 6, 138, 15046.

31. Venna, S.; Jasinski, J.; Carreon, M. Structural evolution of zeolitic imidazolate fr amework-8. *J. Am. Chem. Soc.* **2010**, 132, 18030.

32. Banerjee, R.; Phan, A.; Wang, B.; Knobler, C.; Furukawa, H.; O'Keeffe, M.; Yag hi, O. High-throughput synthesis of zeolitic imidazolate frameworks and applica tion to CO_2 capture. *Science* **2008**, 319, 939.

33. Tang, J.; Salunkhe, R.; Liu, J.; Torad, N.; Imura, M.; Furukawa, S.; Yamauchi, Y. Thermal conversion of core-shell metal-organic frameworks: A new method f or selectively functionalized nanoporous hybrid carbon. *J. Am. Chem. Soc*. **2015**, 137, 1572.

34. Li, Y.; Jia, B.; Fan, Y.; Zhu, K.; Li, G.; Su, C. Bimetallic zeolitic imidazolite fra mework derived carbon nanotubes embedded with Co nanoparticles for efficient bifunctional oxygen electrocatalyst. *Adv. Energy Mater*. **2017**, 8, 1702048.

35. Furukawa, H.; Cordova, K. E.; O'Keee, M.; Yaghi, O. M. The chemistry and app lications of metal-organic frameworks. *Science* **2013**, 341, 1230444.

36. Zhao, Y.; Yang, L.; Chen, S.; Wang, X.; Ma, Y.; Wu, Q.; Jiang, Y.; Qian, W.; H u, Z. Can Boron and nitrogen Co-doping improve oxygen reduction reaction acti vity of carbon nanotubes? *J. Am. Chem. Soc.* **2013**, 135, 1201.

37. Sharifi, T.; Hu, G.; Jia, X.; Wågberg, T. Formation of active sites for oxygen red uction reactions by transformation of nitrogen functionalities in nitrogen-doped c arbon nanotubes. *ACS Nano* **2012**, 6, 8904.

38. Xia, B.; Yan, Y.; Li, N.; Wu, H.; Lou, X.; Wang, X. A metal-organic framework -derived bifunctional oxygen electrocatalyst. *Nat. Energy* **2016**, 1, 15006.

39. Wu, M.; Wang, K.; Yi, M.; Tong, Y.; Wang, Y.; Song, S. A facile activation stra tegy for an MOF-derived metal-free oxygen re-duction reaction catalyst: Direct a ccess to optimized pore structure and nitrogen species. *ACS Catal*. **2017**, 7, 6082.

40. Chen, Y.; Wang, C.; Wu, Z.; Xiong, Y.; Xu, Q.; Yu, S.; Jiang, H. From bimetalli c metal-organic framework to porous carbon: High surface area and multicompo nent active dopants for excel-lent electrocatalysis. *Adv. Mater*. **2015**, 27, 5010.

41. Li, Y.; Jia, B.; Fan, Y.; Zhu, K.; Li, G.; Su, C. Bimetallic zeolitic imidazolite fra mework derived carbon nanotubes embedded with Co nanoparticles for efficient bifunctional oxygen electrocatalyst. *Adv. Energy Mater*. **2017**, 8, 1702048.

42. Behr, M.; Gaulding, E.; Mkhoyan, K.; Aydil, E. Effect of hydrogen on catalyst n anoparticles in carbon nanotube growth. *J. Appl. Phys*. **2010**, 108, 053303.

43. Park, K.; Ni, Z.; Cote, A.; Choi, J.; Huang, R.; Uribe-Romo, F.; Chae, H.; O'Kee ffe, M.; Yaghi, O. Exceptional chemical and thermal stability of zeolitic imidazo late frameworks. *Proc. Natl. Acad. Sci*. **2006**. 103, 10186.

44. Huang, X.; Lin, Y.; Zhang, J.; Chen, X. Ligand-directed strategy for zeolite-type metal-organic frameworks: Zinc(II) imidazolates with unusual zeolitic topologie s. *Angew. Chem. Int. Ed*. **2006**, 45, 1557.

45. Meng, F.; Wang, Z.; Zhong, H.; Wang, J.; Yan, J.; Zhang, X. Reactive multifunc tional template-induced preparation of Fe-N-doped mesoporous carbon microsph eres towards highly efficient electrocatalysts for oxygen reduction. *Adv. Mater.* **2 016**, 28, 7948.

46. Cliff, G.; Lorimer, G. The quantitative analysis of thin specimens. *J. Microsc*. **19 75**, 103, 203.

47. Singh, S.; Kashyap, V.; Manna, N.; Bhange, S.; Soni, R.; Boukherroub, R.; Szun erits, S.; Kurungot, S. ACS Catal. 2017, 7, 6700.

48. Fu, G.; Yan, X.; Chen, Y.; Xu, L.; Sun, D.; Lee, J.; Tang, Y. Adv. Mater. 2018, 30, 1704609.

49. Wu, M.; Wang, K.; Yi, M.; Tong, Y.; Wang, Y.; Song, S. ACS Catal. 2017, 7, 6 082.

50. Wang, Y.; Yang, Y.; Jia, S.; Wang, X.; Lyu, K.; Peng, Y.; Zheng, H.; Wei, X.; R en, H.; Xiao, L.; Wang, J.; Muller, D.; Abruña, H.; Hwang, B.; Lu, J.; Zhuang, L. Nat. Comm. 2019, 10.

51. Sun, J.; Lowe, S.; Zhang, L.; Wang, Y.; Pang, K.; Wang, Y.; Zhong, Y.; Liu, P.; Zhao, K.; Tang, Z.; Zhao, H. Angew. Chem. Int. Ed. 2018, 130, 16749.

52. Wang, J.; Liu, W.; Luo, G.; Li, Z.; Zhao, C.; Zhang, H.; Zhu, M.; Xu, Q.; Wang, X.; Zhao, C.; Qu, Y.; Yang, Z.; Yao, T.; Li, Y.; Lin, Y.; Wu, Y.; Li, Y. Energy Environ. Sci. 2018, 11, 3375.

53. Li, S.; Cheng, C.; Liang, H.; Feng, X.; Thomas, A. Adv. Mat. 2017, 29, 170070 7.

54. Hu, C.; Dai, L. Adv. Mat. 2016, 29, 1604942.

55. Xiang, Z.; Xue, Y.; Cao, D.; Huang, L.; Chen, J.; Dai, L. Angew. Chem. Int. Ed. 2014, 126, 2465.

56. Sethuraman, V.; Weidner, J.; Haug, A.; Motupally, S.; Protsailo, L. J. Electroche m. Soc. 2008, 155, B50.

57. Kim, Y.; Moh, L.; Swager, T. ACS Appl. Mater. Interfaces 2017, 9, 42409.

58. Gasteiger, H.; Kocha, S.; Sompalli, B.; Wagner, F. Activity benchmarks and req uirements for Pt, Pt-alloy, and on-Pt oxygen reduction catalysts for PEMFCs. *Ap pl. Catal. B*, **2005**, 56, 9.